A LONG-TERM SPACE ASTROPHYSICS RESEARCH PROGRAM

AN X-RAY PERSPECTIVE OF THE COMPONENTS AND STRUCTURE OF GALAXIES

NASA Grant NAGW-2681

Performance Report No. 7

For the Period 1 May 1994 through 30 April 1995

Principal Investigator
Dr. G. Fabbiano

April 1995

Prepared for:

National Aeronautics and Space Administration
Washington, DC 20546

Smithsonian Institution
Astrophysical Observatory
Cambridge, Massachusetts 02138

The Smithsonian Astrophysical Observatory is a member of the Harvard-Smithsonian Center for Astrophysics

The NASA Technical Officer for this grant is S. New, Code: SZE, National Aeronautics and Space Administration, Washington, DC 20546.

Contents

1 Activities at SAO

1.1 ROSAT PSPC pipeline

Version 3 of a ROSAT X-ray data reduction and analysis pipeline has been completed in February 1995. The pipeline operates on pointed PSPC observations that exist in the U.S. ROSAT Archive. This pipeline is substantially different from the recently released WGACAT and ROSAT SRC point source catalogues.

Specifically, the pipeline 1) fully corrects PSPC observations for instrumental effects, 2) uses source detection algorithms (both PROS LDETECT and Wavelets) to identify BOTH point source and extended sources, 3) does automatic XSPEC spectral fitting to a subset of sources, 4) computes fluxes for detected sources based on 3 standard spectral laws, 5) produces contour maps and surface brightness profiles for extended sources, 6) automatically loads pipeline results into SYBASE database management system (DBMS) for later access and analysis use.

Status: Version 4 (V4) is under construction, which will be the final working version of the pipeline. We expect completion in early May.

It will contain 1) slight science modifications based on V3 science testing results, 2) the addition of optical full field and subimages of PSPC fields and extended sources from the recently completed STScI Guide Star Survey CD-ROM set. X-ray subimage contours will be overlayed onto greyscale optical fields. 3) the addition of source obscuration information, 4) fluxes or upper limits for all sources that exist in the PSPC F.O.V. that exist in a Master Catalogue (MC) of 43 selected X-ray, EUV, optical, IR and radio catalogues of point and extended sources, 5) perform source identification based on positional matches with the STScI Guide Star Catalogue and MC.

Reference:

Rhode, K.L., Fabbiano, G., and Mackie, G. 1994, "An IRAF-Based Pipeline for Reduction and Analysis of Archived ROSAT Data", In: Astronomical Data Analysis Software and Systems III, ASP Conference Series, vol 61, p371.

1.2 X-ray sources in nearby Sc galaxies

Mackie completed optical (B, I and Halpha+[NII]) CCD imagery of 3 Sculptor (D=2.5Mpc) Sc galaxies in November 1994 at CTIO. Work is continuing on an optical-X-ray study of the X-ray sources in these, the closest group of galaxies outside the Local Group.

1.3 Optical-X-ray-Radio study of an ongoing merger

During the November 1994 CTIO CCD observing run, Mackie also obtained very deep B and Halpha+[NII] images of NGC1316. This galaxy is the archetypical E/SO merger. We discovered a large, extended region of Halpha+[NII] coincident with the position of an optical tidal tail, which is the stellar remnant of the progenitor merger galaxy that is interacting with NGC1316. The region is most likely shock excited, consistent with its position on the

edge of extended X-ray emission S of NGC1316. The discovery has important implications in the understanding of merger dynamics, and the origin of the ISM in elliptical galaxies.

Reference:

NOAO newsletter, June 1995, in prep.
Mackie, G., Fabbiano, G. 1995 (in preparation.)

1.4 A radio, Far-Infrared, Optical and X-ray Study of the Sc galaxy NGC247.

VLA HI and 1.49GHz, IRAS 60 and 100micron, optical B, I and Halpha+[NII], and ROSAT PSPC X-ray images are combined to investigate the multi-wavelength properties of the close Sc galaxy, NGC247.

Reference:

Mackie, G., Fabbiano, G., Ikebe, Y., and Kim, D.-W. 1995, In: IAU Symposium 164, "Stellar Populations", ed. G.Gilmore, P. van der Kruit (Kluwer)

1.5 A Multiparametric Analysis of the Einstein Sample of Early-Type Galaxies

We have completed and submitted to Ap. J. three papers reporting the results of multivariate statistical analysis of the Einstein Observatory sample of E and S0 galaxies. Two papers have been published (Ap. J. Suppl. and Ap. J.), the third is in press (Ap. J.).

I. Luminosity and ISM parameters – In this paper we study correlations between Hot (X-ray), cold (HI, and far IR) ISM indicators, stellar indicators (near IR, and B), and nuclear activity (6cm) in E and S0s.

II. Galaxy Formation History and Properties of the ISM – We compare emission properties of E and S0 galaxies with structural properties which measure the depth of the potential (σ_v, Mg_2), and its shape (axial ratio, boxiness). We find that the ability of retening a hot ISM is correlated with both depth and shape of the potential. We explore the implications of our results in terms of galaxy formation scenarios.

III. Comparisons with the κ parameters – We have extended our work to a set of parameters that define the fundamental plane of early-type galaxies. This work confirms that mass and M/L are strongly responsible for the present day X-ray properties of early-type galaxies.

References:

Eskridge, P. B., Fabbiano, G., and Kim, D.-W. 1995, Ap. J. Supp., 97, 141.
Eskridge, P. B., Fabbiano, G., and Kim, D.-W. 1995, Ap. J., 442, 523.
Eskridge, P. B., Fabbiano, G., and Kim, D.-W. 1995, Ap. J., in press.

1.6 Other papers based on ROSAT and ASCA data

We have studied the ROSAT PSPC observation of NGC 507, the central galaxy of a small group and an extremely luminous X-ray source. These data allow us to measure the mass of the system (M/L of about 100 in solar units), reveal central cooling, and also suggest the presence of several clums of emission in the outer halo, way in excess of what we would expect from serendipitous sources in the field. We need to follow-up this observation with higher resolution ones to confirm and study these clumps. This paper has been published in Ap. J. (Kim and Fabbiano 1995)

We have studied the X-ray properties of two dynamically young early-type galaxies, which may be the product of recent mergers. These galaxies turn out to be X-ray faint (Ap. J. in press, Fabbiano and Schweizer).

We have discovered evidence of thermal confinement of the radio source in the elliptical galaxy NGC 1399, and submitted a paper to Ap. J. (Kim et al).

We have studied the ASCA data of the X-ray faint S0 NGC 4382. These data confirm a multicomponent emission for this galaxy (Kim et al, Ap. J. submitted).

References:

Kim, D.W., and Fabbiano, G. 1995, Ap. J., 441, 182.

Fabbiano, G., and Schweizer, F. 1995, Ap. J., in press.

Kim, D.-W., Fabbiano, G., Mackie, G., and Norman, C. 1995, Ap. J. Submitted.

Kim, D.-W, Fabbiano, G., Matsumoto, H., Koyama, K., and Trinchieri, G. 1995, Ap. J., submitted.

1.7 Talks by G. Fabbiano

G. Fabbiano has delivered several talks, reviewing the results of this work.

'The Hot ISM of Galaxies', to appear in 'The Physics of the Interstellar and Intergalactic Medium' (A. Ferrara, C. Heiles, C.F. McKee, and P.Shapiro, eds.) PASP Conference Series.

'From X-ray Observations to Galaxy Formation' to appear in the Proceedings of the XVII Texas Symposium.

'The X-ray Properties of Early Type Galaxies' presented at the Puebla meeting on early type galaxies.

'The X-ray Properties of E and SO galaxies: Facts and Myths', CfA Colloquium.

2 Activities at MIT

Activities included continued analysis of observations with ROSAT, and ASCA, and continued development of new approaches to spectral analysis with ASCA and AXAF. Also, a new method for characterizing structure in clusters was developed and applied to ROSAT images of a large sample of clusters.

2.1 ROSAT Data Analysis

We completed a detailed analysis of our ROSAT PSPC observation of the flattened elliptical galaxy NGC1332. The paper was submitted this fall and very recently received back from the referee. Revisions are in progress. Evidence for flattened, dark matter halos is present, though more limited than for the previous study of NGC720 because of the poorer signal to noise and smaller size of NGC1332. However, in the process of performing the analysis, the techniques were significantly improved over previous versions. The technique of shape analysis wass also tested, for the case of galaxy clusters, using models from N-body/hydro codes. Results are in press. The same analysis was also applied to ROSAT images of clusters previously analyzed using Einstein data.

2.2 ASCA

We participated in planning and execution of several galaxy and cluster observations. Results on the Centaurus cluster were published. Centaurus is one of a few clusters that show abundance gradients. An analysis of hard X-ray emission from several bright elliptical galaxies was also published. We have begun analyzing M87 data with the intent of reconciling spectral information from ASCA and all previous missions.

2.3 Spectral Analysis

We have continued our efforts to develop new methods for fitting ASCA spectra that will be less model dependent and yield better results than the tradiationsl method of simply fitting isolthermal "Raymond-Smith" models. These would also be applicable to XMM and AXAF. The method was applied to several ASCA spectra, but we are still attempting to sort out fitting problems vs. problems with atomic physics input.

2.4 Power Ratio Method

We have developed a quantitative method for characterizing the structure of a cluster from it's X-ray image using ratios of the power in various multipole moments. The technique was tested using simulated data and also applied to a large sample of ROSAT images. One paper is in press and a second is nearing completion.

2.5 Future Plans

1. Continue analysis of ROSAT data: The HRI observations of NGC 720 are being fully analyzed and will be completed during the next year. Also do more detailed modeling

of constraints on the shape of the dark matter in these systems. We also intend to obtain improved optical observations, including long slit spectra, to better model the potential.

2. We will continue exploration of alternative spectral fitting approaches with specific application to ASCA data. We are participating in the organization of a workshop on plasma codes and spectral fitting to be held in July.

3. We will continue our analysis of M87 using ASCA plus other past spectral measurements. We also have an approved ASCA observation of NGC 720.

4. We will continue exploring the efficacy of the power ratio method, including its relevance for distinguishing cosmological models using cluster evolutionary properties.

5. We have been awarded time for HST FOS observations to search for UV absorption lines against the nucleus of M87.

2.6 Relevant Publications:

Mergers, Cooling Flows and Evaporation Revisted, C.R. Canizares, A. Fabian and H. Bohringer, Ap.J., 425, 40, 1994.

Geometrical Evidence for Dark Matter: X-ray Constraints on the Mass of the Elliptical Galaxy NGC 720, D. Buote and C.R. Canizares, Ap. J., 427, 86, 1994.

ROSAT PSPC Observations of NGC 4636: Interaction with Virgo Gas? G. Trinchieri, D.-W. Kim, G. Fabbiano, and C. R. C. Canizares, Ap. J., 428, 555, 1994.

Dark Matter in Clusters of Galaxies, Claude R. Canizares, Procedings from IAU Symposium 164 on Stellar Popluations, (in press) August 1994.

Metal Concentration and X-ray Cool Spectral Component in the Central Region of the Centarurus Cluster of Galaxies, Y. Fukazawa, T. Ohashi, A.C. Fabian, C.R. Canizares, Y. Ikebe, K. Makishima, R. Mushotsky and K. Yamashita, Publications of the Astronomical Society of Japan, Initial Results from ASCA, 46, No. 3,, L55, 1994.

Detections of Hard X-ray Emissions from Bright Early-Type Galaxies with ASCA, K. Matsushita, K. Makishima, H. Awaki, C.R. Canizares, A.C. Fabian, Y. Fukazawa, M. Loewenstein, H. Matsumoto, T. Mihara, R.F. Mushotzky, T. Ohashi, G.R. Ricker, P.J. Serlemitsos, T. Tsuru, Y. Tsusaka, and T. Yamazaki, Ap. J. (Letters) , 436, L41, 1994.

Buote, D. A., & Canizares, C. R. 1995, X-ray Constraints on the Intrinsic Shape of the Lenticular Galaxy NGC 1332, The Astrophysical Journal, in press

Buote, D. A., & Canizares, C. R. 1995, X-ray Constraints on the Intrinsic Shapes and Baryon Fractions of Five Abell Clusters, The Astrophysical Journal, submitted

Buote, D. A., & Tsai, J. C. 1995, The Reliability of X-ray Constraints of Intrinsic Cluster Shapes, The Astrophysical Journal, 439, 29

Buote, D. A., & Tsai, J. C. 1995, Quantifying the Morphologies and Dynamical Evolution of Galaxy Clusters. I. The Method, The Astrophysical Journal, in press

Buote, D. A., & Tsai, J. C. 1995, Quantifying the Morphologies and Dynamical Evolution of Galaxy Clusters. II. The Data, The Astrophysical Journal, submitted

A Preprints

THE ASTROPHYSICAL JOURNAL SUPPLEMENT SERIES, 97:141–184, 1995 March

A MULTIPARAMETRIC ANALYSIS OF THE *EINSTEIN* SAMPLE OF EARLY-TYPE GALAXIES. I. LUMINOSITY AND ISM PARAMETERS

PAUL B. ESKRIDGE[1] AND GIUSEPPINA FABBIANO
Harvard-Smithsonian Center for Astrophysics, 60 Garden Street, Cambridge, MA 02138; paul@hera.astr.ua.edu, pepi@cfa.harvard.edu

AND

DONG-WOO KIM
Harvard-Smithsonian Center for Astrophysics, 60 Garden Street, Cambridge, MA 02138; and Department of Astronomy and Space Science, Chungnam National University, Taejon, 305-764, South Korea; kim@cfa.harvard.edu
Received 1994 May 16; accepted 1994 July 28

ABSTRACT

We have conducted bivariate and multivariate statistical analysis of data measuring the luminosity and interstellar medium of the *Einstein* sample of early-type galaxies (presented by Fabbiano, Kim, & Trinchieri 1992). We find a strong nonlinear correlation between L_B and L_X, with a power-law slope of 1.8 ± 0.1, steepening to 2.0 ± 0.2 if we do not consider the Local Group dwarf galaxies M32 and NGC 205. Considering only galaxies with $\log L_X \leq 40.5$, we instead find a slope of 1.0 ± 0.2 (with or without the Local Group dwarfs). Although E and S0 galaxies have consistent slopes for their L_B-L_X relationships, the mean values of the distribution functions of both L_X and L_X/L_B for the S0 galaxies are lower than those for the E galaxies at the 2.8 σ and 3.5 σ levels, respectively. We find clear evidence for a correlation between L_X and the X-ray color C_{21}, defined by Kim, Fabbiano, & Trinchieri (1992b), which indicates that X-ray luminosity is correlated with the spectral shape below 1 keV in the sense that low-L_X systems have relatively large contributions from a soft component compared with high-L_X systems. We find evidence from our analysis of the 12 μm *IRAS* data for our sample that our S0 sample has excess 12 μm emission compared with the E sample, scaled by their optical luminosities. This may be due to emission from dust heated in star-forming regions in S0 disks. This interpretation is reinforced by the existence of a strong L_{12}-L_{100} correlation for our S0 sample that is not found for the E galaxies, and by an analysis of optical-IR colors. We find steep slopes for power-law relationships between radio luminosity and optical, X-ray, and far-IR (FIR) properties. This last point argues that the presence of an FIR-emitting interstellar medium (ISM) in early-type galaxies is coupled to their ability to generate nonthermal radio continuum, as previously argued by, e.g., Walsh et al. (1989). We also find that, for a given L_{100}, galaxies with larger L_X/L_B tend to be stronger nonthermal radio sources, as originally suggested by Kim & Fabbiano (1990). We note that, while L_B is most strongly correlated with L_6, the *total* radio luminosity, both L_X and L_X/L_B are more strongly correlated with L_{6cc}, the *core* radio luminosity. These points support the argument (proposed by Fabbiano, Gioia, & Trinchieri 1989) that radio cores in early-type galaxies are fueled by the hot ISM.

Subject headings: galaxies: elliptical and lenticular, cD — galaxies: general — galaxies: ISM — X-rays: galaxies

1. INTRODUCTION

The classic view of early-type (E and S0) galaxies, as put forth in the preface to the Hubble Atlas (Sandage 1961) is that of pure Population II stellar systems, with little or (ideally) no optical signatures of an interstellar medium (ISM). It was already clear by then that a significant fraction of luminous early-type galaxies do indeed possess some quantity of optical emission-line gas (Mayall 1939; Humason, Mayall, & Sandage 1956). Furthermore, as the angular resolution of radio telescopes improved throughout the 1950s and 1960s, it also became clear that many early-type galaxies are powerful radio continuum sources (e.g., Maltby & Moffet 1962). It was thus obvious that they contain relativistic electrons, moving under the influence of magnetic fields (e.g., Hoyle 1960). By the 1970s, a few early-type galaxies were also known to have some amount of H I gas, based on 21 cm line observations (e.g., Bottinelli & Gouguenheim 1977; Gallagher et al. 1977; Whiteoak & Gardner 1977; Knapp, Gallagher, & Faber 1978; Fosbury et al. 1978). However, all available evidence pointed toward very small mass fractions for the ISM in early-type galaxies.

That this was, in fact, a serious problem was pointed out in a landmark paper by Faber & Gallagher (1976). They noted that the stellar populations of early-type galaxies are dominated by old stars, and that stars lose a significant amount of mass in the course of stellar evolution. Thus a typical early-type galaxy ($L_B \approx 10^{10}\ L_\odot$) *should* contain $\approx 10^9\ M_\odot$ of ISM if this material were not either converted into new stars (not considered a major sink either then or now) or swept from the system by some internal or external process.

For a number of years, theoretical work focused on the latter possibility, the main mechanisms considered being ram-pressure stripping due to interactions of the early-type galaxies with the intracluster medium of their host clusters (Gunn & Gott 1972; Gisler 1976; Frank & Gisler 1976) and galactic winds generated by energy input from supernovae (Johnson & Ax-

[1] Current address: Department of Physics and Astronomy, University of Alabama, Tuscaloosa, AL 35487.

ford 1971; Mathews & Baker 1971). Indeed, cluster effects do appear to be a significant contributor to the overall state of the ISM in at least some early-type galaxies (e.g., Forman et al. 1979; Forman, Jones, & Tucker 1985; Trinchieri, Fabbiano, & Canizares 1986; Trinchieri & di Serego Alighieri 1991). But the crucial development required to address the problem of the ISM in early-type galaxies turned out to be technological: the invention of ~arcminute resolution X-ray imaging devices (Giacconi et al. 1979).

Among the most important results from the *Einstein Observatory,* the first satellite to contain such devices, was the observation that many early-type galaxies contain significant amounts (10^8–10^9 $M_\odot$) of gas at temperatures of 10^6–10^7 K (Forman et al. 1979). Once it became clear that this material was often the dominant phase of the ISM in early-type galaxies, the problem posed by Faber & Gallagher (1976) was largely resolved, and work became focused on exploring the nature of this newly discovered phase of the ISM (see Fabbiano 1989 and references therein).

In the meantime, improvements in detector technology in other wave bands led to detections of, or increasingly strict upper limits on, characteristic emission from all other phases of the ISM in early-type galaxies (e.g., Knapp, Turner, & Cunniffe 1985, and Wardle & Knapp 1986 for H I; Knapp et al. 1989 for FIR; Sage & Wrobel 1989 and Thronson et al. 1989 for CO). By the mid-1980s it became possible to begin truly multivariate studies of the ISM from statistically significant (for astronomers!) samples of early-type galaxies (Fabbiano et al. 1987; Fabbiano et al. 1989, hereafter FGT).

The final catalog and atlas of *Einstein* observations of galaxies (Fabbiano et al. 1992, hereafter P0) contains X-ray data on 148 normal early-type galaxies. Until a comparable study of results from *ROSAT* become available, this will be the largest-extent sample of X-ray observations of normal early-type galaxies. We have therefore undertaken a multiparametric analysis of the optical, ISM, and structural properties of this sample. In § 2 we describe our sample construction. In § 3 we address the L_X-L_B relationship. We move in § 4 to explore the relationships between X-ray emission and infrared and radio emission. We summarize our results, and discuss possible areas for future research in § 5. Analysis of the structural and stellar data for our sample will be presented in subsequent papers.

2. SAMPLE CONSTRUCTION

As noted above, the *Einstein* galaxy catalog (P0) provides X-ray fluxes or upper limits for 148 early-type (S0 and earlier) galaxies. This represents the largest body of data currently available on the X-ray properties of early-type galaxies. A number of earlier papers have examined the relationships between X-ray emission and other properties of early-type galaxies using smaller samples (e.g., Fabbiano et al. 1987; FGT; Bregman, Hogg, & Roberts 1992). We have undertaken the current study to reexamine the conclusions of these earlier works, and to address a more complete set of properties describing the current physical conditions in early-type systems. Our X-ray data are from P0. The sources of the (B-band) optical data and assumed distances to our sample are also given in P0. We have included all published information from the *IRAS* survey on our sample. The *IRAS* data are 91% complete (134 of 148 at 12 μm, and 135 of 148 at the remaining wavelengths). Five of the systems in our sample are in regions of the sky not well sampled by *IRAS*. We have also included all published 6 cm radio data for our sample. Fluxes or upper limits are available for 90% (133 of 148) of the galaxies. High-resolution data, providing information on the core radio flux, are available for 67% (99 of 148) of our sample. Measurements of the 21 cm H I line flux (or upper limit) are available for 79% (117 of 148) of our sample. Axial ratios are included and have been taken from de Vaucouleurs et al. (1991, hereafter RC3). All these data are summarized, with references, in Table 1.[2] The X-ray and optical data in Table 1 are taken from P0. Sources for the remaining data are given in the table.

We use luminosities (or luminosity ratios) including both detections and upper limits for our analysis of these data below. Arguments regarding the validity of this approach are presented in detail in a number of previous papers (Fabbiano et al. 1987; Fabbiano, Gioia, & Trinchieri 1988; FGT). We note that the lack of any a priori flux limits in our sample will minimize the possibility of any significant effect due to a Malmquist-like bias.

3. THE L_X-L_B RELATIONSHIP

There have been a number of previous attempts at determining the relationship between the X-ray and optical luminosities of early-type galaxies (e.g., FGT; Donnelly, Faber, & O'Connell 1990; Bregman et al. 1992). We have reinvestigated this relationship, examining correlations between L_X, L_B, L_X/L_B, and C_{21} (an X-ray color, defined in Kim et al. 1992b, that gives the ratio between the emission in the 0.8–1.36 keV band and that in the 0.16–0.8 keV band). We also investigate the use of subsamples based on high- and low-luminosity cutoffs and on morphology, breaking the sample into E and S0 subsets.

3.1. *The Full Sample*

3.1.1. *Correlations over the Full Range in Luminosity*

In Figure 1 we plot L_X against L_B for our sample. Because of the upper limits in L_X, standard statistical tests for correlation are invalid. We have instead applied the correlation tests available for censored data sets discussed by Isobe, Feigelson, & Nelson (1986) and LaValley, Isobe, & Feigelson (1992). For samples with censoring in one variable, such as the L_X-L_B data set, the three available tests are the Cox-Hazard model, the modified Kendall's τ-test, and the modified Spearman rank test. The result of each of these tests is that the probability that the X-ray and optical luminosities are uncorrelated is $P < 10^{-4}$. These results are presented in Table 2A. Various regression algorithms are available for data sets with censoring in only one variable. These are the expectation and maximization (E-M) algorithm, the Buckley-James (B-J) algorithm (see Isobe et al. 1986), and Schmitt's binning method (Schmitt 1985). We have used all of them. The results of this regression analysis are shown in Table 3A and, along with the data, in Figure 1. All methods give the result $L_X \propto L_B^{1.8\pm0.1}$.

When performing any regression, one is required to make decisions about the nature of one's data. The central question

[2] These data will be made available to the community via EINLINE.

TABLE 1A

FLUX DATA

Name	B_T^0	Type	log(a/b) RC3	f_X[a] 10^{-13} cgs	σ_X	D Mpc	f_{12} mJy	σ_{12}	f_{25} mJy	σ_{25}	f_{60} mJy	σ_{60}	f_{100} mJy	σ_{100}	f_6 mJy	σ_6	$f_{6,co}$ mJy	$\sigma_{6,co}$	f_{HI}[a] Jy km/sec	σ_{HI} mJy	References
NGC 127	14.68	-2	0.16	< 4.27		80.0															6
NGC 128	12.63	-2	0.52	< 4.17		82.6	0	42	220	61	750	41	1550	115	0	6.67			1.5		1,11,41
NGC 130	14.78	-3	0.31	< 4.36		88.9															6
NGC 205	8.60	-3	0.30	< 17.88		0.7	110	31	130	22	570	37	3130	102	0	0.33			3.3		1,4,10,41
NGC 221	8.79	-6	0.13	9.21		0.7	480	36	220	33	0	87	0	1260	0	0.33			0	18.0	11,41
NGC 315	12.20	-3	0.20	9.69	0.54	99.9	0	31	0	49	320	52	360	90	1045.2		554	33.5	< 1.33		1,10,24,42
NGC 499	12.64	-3	0.10	30.01	1.19	88.6	0	29	0	23	0	40	0	112	60	20			< 1.16		1,14,42
NGC 507	11.76	-2	0.00	93.95	2.32	99.3	0	23	0	37	0	39	0	141	0	20	0	10	< 5.1		1,14,33,42
NGC 533	12.75	-5	0.21	31.42	4.82	107.9	0	44	0	53	0	44	0	96	12						1,21
NGC 584	11.20	-2	0.26	< 2.89		37.6	0	44	0	62	0	41	520	90	0	0.33	0	0.33	0	4.0	1,10,31,41
NGC 596	11.88	-5	0.19	< 2.44		38.2	0	33	0	50	0	26	0	100	0	0.33	0	0.32			1,11,31
NGC 720	11.15	-5	0.29	17.02	1.60	32.6	90	28	0	33	0	42	0	56	0	0.34	0	0.29	0	3.0	1,10,31,41
NGC 984	14.70	-2	0.17	< 4.54		87.5	0	24	0	45	140	37	120	106	78.7	0.11			7.8		1,10,42
NGC 1044	14.00	-3	0.00	< 1.41		122.5									320	10	17				19,35
NGC 1052	11.53	-3	0.16	5.28	0.56	28.6	220	18	510	37	900	31	1400	60	1270.0	40.0	1230	40	5.6		1,11,25,41
NGC 1167	12.79	-3	0.07	< 3.03		99.9	0	30	0	37	120	28	930	133	911.8	0.98	0	243	13.32	0.66	1,10,36,42
NGC 1172	13.00	-2	0.11	< 1.59		29.4	0	26	0	31	0	41	0	72					0	6.9	1,41
NGC 1201	11.56	-2	0.23	< 5.70		32.5	0	38	0	28	0	35	0	72	0	4.00			0	17.0	1,11,41
NGC 1316	9.32	-2	0.15	19.86	0.99	27.2	310	39	270	20	3160	30	14200	3000	6600		90	10	< 1.27		1,10,26,42
NGC 1332	11.29	-2	0.51	6.72	0.66	28.4	90	17	100	23	520	27	1610	51	0	0.33			0	5.4	1,10,41
NGC 1387	11.83	-2	0.00	6.43	1.32	27.2	160	31	170	24	2370	28	6030	44	0	4.00					1,11
NGC 1389	12.39	-2	0.22	< 2.60		27.2	0	24	0	25	0	28	0	89	0	0.33	0	0.33			1,11,37
NGC 1395	11.18	-5	0.12	11.14	1.07	32.1	130	26	50	27	50	26	300	42	2.0	0.2	2.02	0.17			1,10,38
NGC 1399	10.79	-5	0.03	215.72	5.82	27.2	90	23	0	18	0	32	270	72	230.4		110		0	3.1	1,10,27,41
NGC 1404	11.06	-5	0.05	33.22	2.00	27.2	90	41	0	23	0	28	240	49	0	0.23	0	0.23			1,11,37
NGC 1400	12.08	-3	0.06	< 4.98		8.0	0	36	100	23	760	40	2920	129	2.0	0.12			0	13.0	1,10,41
NGC 1407	10.93	-5	0.03	14.18	1.50	34.7	110	29	0	27	140	30	430	65	44.0	4.00			0	3.3	1,11,41
NGC 1497	14.20	-2	0.17	< 2.06		122.6			0	167	0	167	0	500	39.7	0.14	8.17	0.11	0.37		7,10,44
NGC 1510	13.24	-6	0.26	< 4.20		16.6	0	93	0	97	3100	372	10820	1298	0	7			1.61	0.14	6,20,42
NGC 1553	10.36	-2	0.20	14.36	3.28	21.5	170	16	130	26	570	24	1010	51	0	4.00			0	21.2	1,11,41
NGC 1574	11.13	-2	0.04	< 7.01		21.5	100	14	70	17	370	22	590	64	0	3.95					1,10
NGC 1600	12.01	-5	0.17	9.19	1.97	90.3	0	14	0	25	100	27	170	65	22.0	3.00			0	9.0	1,11,41
NGC 1947	11.75	-2	0.07	< 4.45		19.4	140	32	90	20	1100	24	4270	50	18.0	3.00					1,11
NGC 2314	12.83	-5	0.09	< 3.01		84.6	0	24	0	27	70	22	300	55	700.0	233	8.0	0.13	0	4.0	1,10,14,41
NGC 2300	11.99	-5	0.14	10.85	1.68	49.8	90	18	0	28	0	25	0	81	0.7	0.12	0.7	0.12	0	6.0	1,10,11,41
NGC 2444	13.43	-2	0.16	< 5.17		86.4	0	83	530	64	3390	407	6320	758	0	11			0	6.0	6,17,42
NGC 2562	13.37	-1	0.18	< 3.07		102.4	0	31	0	47	170	51	360	161	0	4.3			< 0.53		1,21,42
NGC 2563	12.92	-2	0.14	12.00	1.05	96.1	0	18	0	54	0	27	0	187	0	0.11			< 0.55		1,10,42
NGC 2629	13.30	-2	0.07	< 2.20		80.8	0	21	0	19	100	31	410	109	50.8	0.15	45.2	0.18			8,10
NGC 2685	11.85	-2	0.28	< 3.53		26.0	100	31	0	37	370	42	1660	100	3.3	0.16			32.3		1,10,41
NGC 2694	14.96	-5	0.01	< 3.56		107.5									0	60					14
NGC 2693	12.70	-5	0.16	< 3.40		103.7	0	29	0	32	210	37	790	114	1.7	0.10	1.4	0.14	0	8.0	1,10,41
NGC 2716	12.90	-1	0.10	< 1.50		73.7	140	34	0	28	310	37	920	102	0	3.33					1,16
NGC 2832	12.39	-5	0.10	22.85	2.75	142.3	80	26	0	43	440	27	1330	137	0	11.0			0	2.2	2,11,41
NGC 2859	11.75	-2	0.05	< 1.20		40.8	0	28	0	36	320	31	830	72	0	0.33	0	0.17	0	1.0	1,11,34,41
NGC 2911	12.53	-2	0.11	< 3.76		69.2	0	28	0	36	290	28	560	79	120.0	5.00	163	7	4.4		1,11,25,41
NGC 2974	11.68	-5	0.23	3.32	0.79	45.8	0	21	0	27	430	33	1690	47	7.3	0.10	9.6	0.10	6.0		1,10,41
NGC 3078	11.92	-5	0.08	4.30	0.73	53.7									167.0	5.00	123.5	1.00	0	3.1	3,10,11,41
NGC 3065	12.81	-2	0.01	7.88	1.85	50.3	0	26	290	19	1550	25	1780	88:					7.8		1,41
NGC 3115	9.89	-2	0.47	< 6.41		10.8	290	40	150	33	140	36	0	159	0	0.11			0	1.8	8,10,41
NGC 3222	13.39	-2	0.08	< 2.58		117.2									0	4.3			< 4.72		21,42
NGC 3258	12.48	-5	0.07	7.02	1.36	60.3	0	22	0	34	160	38	640	149	52.0	5.00	3.7		0	1.2	1,11,37,41
NGC 3377	11.10	-5	0.24	< 1.36		13.0	100	33	0	67	140	46	310	57	0	0.20	0	0.20	0	0.3	1,10,31,41
NGC 3379	10.33	-5	0.05	< 6.62		13.0	250	39	0	47	0	42	0	96	2.0		0.8	0.08	0	0.2	1,10,41
NGC 3384	10.70	-2	0.34	< 3.76		13.0	180	28	0	56	0	39	400	75	0	3.9	0	0.17	0	0.5	1,21,34,41
NGC 3458	13.15	-2	0.20	< 3.92		47.4	0	21	0	38	0	33	0	80			0	0.17	0	4.0	1,34,41
NGC 3516	12.34	-2	0.11	30.80	1.30	62.5	390	18	940	14	1900	29	1890	197	15.5	1.70	15.5	1.70	0	4.1	1,11,34,41
NGC 3585	10.81	-3	0.26	1.63	0.35	34.7	110	33	200	28	160	42	0	78	0	0.40			0	16.0	1,10,41
NGC 3607	11.08	-2	0.30	6.19	0.53	32.0									3.9	0.09	2.9	0.12	0	0.5	3,10,41
NGC 3608	11.88	-5	0.09	1.87	0.32	37.6									0.9	0.09	0	0.22	0	0.3	3,10,31,41
NGC 3818	12.79	-5	0.22	< 4.86		40.3	0	45	0	28	0	49	0	85	0	0.33	0	0.22	0	10.0	1,15,31,41
NGC 3894	12.90	-5	0.21	4.93	1.05	74.7	0	22	120	26	140	60	430	140	522.2		577	0.90			1,10,45
NGC 3923	10.79	-3	0.18	10.96	1.19	41.5	120	36	0	27	0	35	0	120	4.5	1.00	0	0.29	0	12.0	1,11,31,41
NGC 3990	13.11	-3	0.24	< 2.98		27.3	0	23	0	26	0	44	410	90							1
NGC 3998	11.50	-2	0.08	59.88	3.92	34.7	130	23	120	21	570	27	1020	110	92.0	3.00	59.4	0.22	6.4		1,10,11,41
NGC 4105	11.76	-2	0.13	3.58	0.77	43.6	0	21	0	36	270	40	740	135	3.7	0.08			11.7		1,10,42
NGC 4168	12.21	-5	0.08	2.26	0.57	27.0	0	42	0	37	0	37	590	139:	4.0		4.5	0.2			1,11,34
NGC 4203	11.62	-2	0.03	31.42	2.55	15.6	0	39	170	26	610	30	1920	71	14.6	0.14	11.6	0.11	27.4		1,10,41
NGC 4215	13.04	-2	0.42	< 2.04		56.4	0	35	0	26	0	31	0	92	0	3.3	0	0.17	0	1.3	1,21,34,41
NGC 4251	11.62	-2	0.39	< 1.22		15.6	0	32	0	42	120	39	0	80	0	0.40	0	0.17	0	0.7	1,11,34,41
NGC 4261	11.38	-5	0.05	13.18	0.94	56.4	170	44	80	60	80	35	130	43	8300.0		315	5	0	7.2	1,11,31,42
NGC 4267	11.78	-2	0.03	< 2.23		27.0	0	26	0	40	190	35	1030	36	0	11	0	0.17	0	0.9	1,21,34,41
NGC 4291	12.26	-5	0.08	8.24	0.64	47.2	0	16	0	19	0	30	0	44	0	0.10	0	0.17			1,10,34
NGC 4340	11.93	-2	0.10	< 2.37		27.0	0	24	310	51	90	25	330	55			0	0.17	0	0.7	1,34,41
NGC 4350	11.88	-2	0.32	< 1.64		27.0	140	43	0	37	370	35	970	74	0	3.1	0	0.17	0	0.8	1,21,34,41

TABLE 1A—*Continued*

Name	B_T^a	Type	log(a/b) RC3	f_X[a] 10^{-13} cgs	σ_X	D Mpc	f_{12} mJy	σ_{12}	f_{25} mJy	σ_{25}	f_{60} mJy	σ_{60}	f_{100} mJy	σ_{100}	f_6 mJy	σ_6	$f_{6,CO}$ mJy	$\sigma_{6,CO}$	f_{HI}[a] Jy km/sec	σ_{HI} mJy	References
NGC 4365	10.60	-5	0.14	2.99	0.41	27.0	150	30	0	43	0	45	580	116	0	0.17	0	0.15	0	0.3	1,11,31,41
NGC 4386	12.53	-2	0.26	< 1.01		45.2	0	20	50	16	120	23	0	79			0	0.17	0	5.0	1,34,41
NGC 4374	10.23	-5	0.06	16.43	0.70	27.0	210	35	180	39	510	27	1030	109	2880.0	240	178.0	0.70	< 7.6		1,10,11,42
NGC 4382	10.10	-2	0.11	6.02	0.48	27.0	0	40	0	59	0	30	0	70	0	0.33	0	0.17	0	0.6	1,10,34,41
NGC 4387	12.75	-5	0.21	< 3.89		27.0	0	33	0	43	0	53	0	158	0	0.33	0	0.18	< 0.34		1,12,31,42
NGC 4406	10.02	-3	0.19	198.81	4.83	27.0	150	35	0	56	110	35	290	59	0	0.20	0	0.18	1.3		1,11,31,41
NGC 4417	12.07	-2	0.41	< 13.13		27.0	0	30	0	77	0	44	0	106	0	3.1	0	0.13	0	0.8	1,21,22,41
NGC 4425	12.79	-2	0.47	< 2.05		27.0	0	33	0	49	0	60	0	146	0	3.0	0	0.17	0	0.7	1,21,34,41
NGC 4435	11.72	-2	0.14	< 3.80		27.0	120	45	210	50	2050	44	4160	106:			1.2	0.1	0	0.7	1,34,41
NGC 4458	12.70	-5	0.04	1.91	0.54	27.0	90	25	0	58	0	34	0	126	0	0.33	0	0.17	< 0.35		1,12,31,42
NGC 4459	11.49	-2	0.12	< 2.87		27.0	330	27	0	90	1920	67	4280	119	2.4	0.80	0.8	0.1	0	1.3	1,11,34,41
NGC 4467	15.18	-5	0.10	< 0.56		27.0															
NGC 4472	9.32	-3	0.09	130.89	2.80	27.0	190	35	0	45	0	66	0	94	248.7		58.1	0.10	0	0.2	1,10,41
NGC 4473	11.07	-5	0.25	3.76	0.95	27.0	270	51	470	50	0	62	0	95	0	0.25	0	0.39	0	0.6	1,10,31,41
NGC 4474	12.70	-2	0.22	< 1.99		27.0	0	37	0	42	0	48	0	80	0	2.9	0	0.17	0	1.2	1,21,34,41
NGC 4479	13.21	-2	0.08	< 1.43		27.0	0	33	0	52	0	25	0	134			0	0.17	< 0.8		1,34,42
NGC 4526	10.59	-2	0.48	1.57	0.36	27.0	440	39	530	49	5720	47	21000	270			3.1	0.2	0	0.5	1,34,41
NGC 4507	12.80	-1	0.10	< 8.35		72.5	460	55	1410	169	4580	733	5600	896					11.0		5,42
NGC 4550	12.33	-3	0.55	< 1.83		27.0	0	29	0	63	140	31	220	80	0	0.25	0	0.17	0	1.5	1,10,34,41
NGC 4551	12.65	-5	0.10	< 2.77		27.0	0	28	0	69	0	38	0	137	0	0.33	0	0.17	0.13		1,12,31,42
NGC 4552	10.80	-2	0.04	9.60	0.74	27.0	120	52	0	49	160	47	470	52	108.0	2.00	107	3	0	0.5	1,11,25,41
NGC 4564	11.87	-5	0.38	< 1.79		27.0	0	35	0	43	0	61	0	168	0	0.25	0	0.17	0	0.4	1,10,34,41
NGC 4578	12.04	-2	0.13	< 2.78		27.0	0	40	0	38	0	34	0	98	0	4.1	0	0.17	0	0.4	1,21,34,41
NGC 4589	11.81	-5	0.09	< 1.65		48.2	0	31	0	21	210	31	590	136	23.5	0.12	21.0	0.7	0	6.0	1,10,34,41
NGC 4621	10.67	-5	0.16	< 3.10		27.0	220	41	0	40	0	51	0	83	6.0		0	0.23	0	1.0	1,10,31,41
NGC 4638	12.05	-2	0.21	1.91	0.56	27.0	0	21	0	32	0	45	0	66	0	0.33	0	0.17	0	0.9	2,10,34,41
NGC 4636	10.50	-3	0.11	108.94	5.91	27.3	190	48	0	52	140	43	0	152	45.0	9.00	27.3		0	1.0	1,11,28,41
NGC 4649	9.83	-2	0.09	46.98	1.83	27.0	360	80	360	68	900	65	2300	270	23.8	2.00	18.4		0	1.6	1,10,28,41
NGC 4645	12.56	-5	0.21	< 1.20		74.6	0	36	0	29	300	60	1490	227	0	4.00					1,11
NGC 4697	10.11	-5	0.19	5.58	0.76	37.4	270	38	0	38	470	23	1100	67	0	0.20	0	0.21	0	16.0	1,11,31,41
NGC 4754	11.41	-2	0.27	< 1.54		27.0	0	26	0	43	0	45	0	102			0	0.17	0	0.9	1,34,41
NGC 4753	10.85	-2	0.33	1.71	0.37	24.3	340	42	310	71	2640	60	8010	176	0	0.10	0	0.13	0	16.0	1,10,39,41
NGC 4756	13.28	-5	0.10	12.16	1.15	88.4	0	30	0	60	0	43	0	135	14.0	3.4					1,20
NGC 4762	11.26	-2	0.72	3.79	0.58	27.0	140	50	0	33	0	48	0	71	0	0.67	0	0.10	0	0.6	1,22,41
NGC 4782	12.75	-5	0.02	6.89	1.51	84.7	0	37	0	75	0	33	0	288	2540.0	75.0	1472		0	32.3	1,11,35,42
IC 3896	12.37	-5	0.12	< 5.87		48.5	0	26	0	30	0	70	0	242	0	4.00					1,11
NGC 4880	12.57	-2	0.11	< 2.73		25.2	0	17	0	57	0	34	0	129	0	0.33			0	0.3	1,11,41
NGC 5044	11.87	-5	0.00	315.01	9.56	62.5	140	35	0	75	140	57	130	65	30.0	3.00			0	2.2	1,11,41
NGC 5077	12.52	-5	0.11	2.32	0.45	65.2	0	45	0	83	410	38	3750	154	166.7		87	4	0	2.1	8,10,25,41
NGC 5084	11.95	-2	0.73	7.46	1.57	42.4	0	48	0	49	420	42	2300	330	34.0	3.00			84.8		1,11,41
NGC 5102	10.47	-2	0.49	< 3.44		5.6	80	31	170	33	940	35	2430	90	0.9	0.12	0	0.27	72.0		1,10,37,41
NGC 5128	6.62	-2	0.11	398.44	3.85	7.9	23000	460	24700	550	230500	560	492000	1880	124000		6984	210	230.		1,10,29,42
NGC 5195	10.50	-2	0.10	2.32	0.51	14.9	680	20	48330	14	39070	1261	0	454	0	26.7			< 42.4		1,11,42
IC 4296	11.43	-5	0.02	12.86	1.10	78.4	0	27	0	29	140	59	230	73	2060.1		224	45			1,10,30
IC 4329	12.48	-2	0.24	< 12.78		93.8	0	23	0	31	460	61	930	234	0.6	0.1	0.63	0.09			1,11,38
NGC 5322	10.91	-5	0.18	< 3.58		50.8	0	20	0	19	430	38	890	67	42.1		14	1	0	3.0	1,10,12,41
NGC 5318	13.40	-2	0.22	< 2.14		95.7	0	27	0	34	170	29	1240	112	86.3	0.17	60	3	0	1.0	1,10,25,42
NGC 5354	12.19	-2	0.04	< 4.33		63.9	0	47	0	30	420	50	1430	51	33.0	7.00	8.1	0.3	18.9	2.2	1,12,34,42
NGC 5353	12.05	-3	0.30	5.79	0.89	60.8	0	29	0	34	330	54	1290	100	35.0	2.00	34	2.0	17.6		1,11,12,41
NGC 5363	11.06	-2	0.19	4.02	1.31	36.0	190	36	220	50	1700	46	4450	45	95.0	3.00	77	3.0	1.9		1,11,18,41
NGC 5485	12.44	-2	0.08	< 3.59		52.7	0	20	0	19	150	34	850	88	0.9	0.10	0	0.33	0	5.0	1,10,34,41
IC 989	14.00	-5	0.07	< 2.39		157.9	0	38	0	50	120	45	390	79	70.1	0.12			0.54		1,10,42
NGC 5532	12.64	-2	0.00	2.99	0.89	154.6	70	27	0	34	0	38	480	89	1509.7		77		< 1.1		1,10,32,42
NGC 5576	11.76	-5	0.20	< 2.65		42.4	70	34	70	37	90	27	190	247	0	0.33	0	0.17	0	0.4	1,11,34,41
IC 1024	13.90	-2	0.39	< 2.37		40.1	310	24	480	26	4210	33	6930	95	11.0	1.00	11.3	1.0	7.58	0.89	1,13,34,42
NGC 5838	11.72	-2	0.45	1.42	0.27	45.8	120	28	90	41	750	40	1480	82	0	16.7	2.0	0.1	0	1.5	1,11,34,41
NGC 5846	11.13	-2	0.03	51.38	1.52	45.8	0	22	0	22	0	37	0	112	7.8	0.10	5.3	0.3	0	0.2	1,10,34,41
NGC 5866	10.86	-2	0.38	2.02	0.63	24.6	300	16	240	14	5210	21	16610	51	12.9	1.00	7.4	0.3	0	6.0	1,10,34,41
NGC 5982	12.03	-5	0.12	5.12	1.26	69.1	0	20	0	20	0	33	330	31	0	0.33	0	0.17			1,11,34
NGC 6027	14.23	-2	0.28	< 4.45		97.6	0	83	0	100	1030	124	2200	264					3.3		6,42
NGC 6034	14.60	-5	0.11	5.46	1.73	209.5									229.0	0.20	0	91.2			10
NGC 6146	13.50	-2	0.10	< 4.64		183.2	0	33	0	29	0	25	0	143	100.0	0.31	72	4	0	6.0	1,10,25,42
NGC 6876	12.45	-5	0.11	9.29	0.96	73.4	0	24	70	26	90	35	430	92	0	4.01					2,10
NGC 6880	14.00	-1	0.36	< 3.35		75.2	90	22	80	24	970	50	3030	136	0	3.7					1,21
NGC 6963	14.40	-5		< 1.88		89.1									0	16.7					14
NGC 6964	13.12	-5	0.12	< 1.80		79.0	250		254		401		1938		0	13.3					9,14
NGC 7236	14.08	-3	0.00	< 2.57		158.0									336	50			< 0.34		3,17,43
NGC 7237	14.33	-3	0.00	< 3.50		158.3									454	42	14		< 0.34		3,23,43
NGC 7332	11.58	-2	0.56	< 3.15		29.3	110	25	0	32	220	30	360	96	0	20.0			0	1.6	1,11,41
IC 1459	10.96	-5	0.14	8.23	1.16	32.1	160	27	300	41	520	31	1050	91	1066.9		1000		0	5.8	1,10,40,41
NGC 7562	12.28	-5	0.18	< 3.69		72.0	0	29	0	43	0	37	0	268	0	0.30	0	0.30	0.25		1,10,31,46
NGC 7619	12.17	-5	0.04	14.92	1.12	75.0	0	31	0	57	0	38	630	205	6.6		6.6		0	1.1	1,10,31,41
NGC 7626	12.17	-5	0.05	5.67	0.84	68.3	0	46	0	52	0	42	0	113	227.9		30		0	0.7	1,10,31,41

[a] The values listed as upper limits are 3 σ.

TABLE 1B

LUMINOSITY DATA

Name	$\log(L_B)$ erg/sec	$\log(L_X)$ erg/sec	$\log(L_X/L_B)$	$\log(L_{12})$ erg/sec	$\log(L_{100})$ erg/sec	$\log(L_6)$ erg/sec	$\log(L_{6co})$ erg/sec	$\log(M_{HI})$ $M_\odot$
NGC 127	42.84	< 41.52	< −1.33					
NGC 128	43.69	< 41.53	< −2.14	< 43.22	43.10	< 36.91		9.38
NGC 130	42.89	< 41.62	< −1.27					
NGC 205	41.15	< 38.02	< −3.13	39.01	39.26	< 31.47		5.58
NGC 221	41.08	37.73	−3.35	39.65	< 39.35	< 31.47		< 5.69
NGC 315	44.02	42.06	−1.96	< 43.25	42.63	38.80	38.52	< 9.50
NGC 499	43.74	42.45	−1.29	< 43.12	< 42.50	37.45		< 9.33
NGC 507	44.19	43.05	−1.15	< 42.64	< 42.22	< 37.55	< 37.25	< 10.07
NGC 533	43.87	42.64	−1.23	< 43.47	< 42.60	36.92		
NGC 584	43.57	< 40.69	< −2.88	< 42.55	41.95	< 34.93	< 34.92	< 9.33
NGC 596	43.32	< 40.63	< −2.69	< 42.44	< 41.72	< 34.94	< 34.92	
NGC 720	43.47	41.34	−2.13	42.26	< 41.33	< 34.81	< 34.74	< 9.04
NGC 984	42.91	< 41.62	< −1.29	< 43.02	42.04	37.56		10.15
NGC 1044	43.48	< 41.40	< −2.08			38.46	37.18	
NGC 1052	43.20	40.71	−2.49	42.54	42.14	37.79	37.78	9.03
NGC 1167	43.79	< 41.56	< −2.23	< 43.23	43.05	38.74	< 38.64	10.50
NGC 1172	42.64	< 40.22	< −2.42	< 42.11	< 41.35			< 9.04
NGC 1201	43.30	< 40.86	< −2.44	< 42.36	< 41.44	< 35.88		< 9.74
NGC 1316	44.04	41.25	−2.80	42.64	43.10	38.47	35.65	< 8.35
NGC 1332	43.29	40.81	−2.48	42.14	42.19	< 34.68		
NGC 1387	43.04	40.76	−2.28	42.35	42.73	< 35.73		
NGC 1389	42.82	< 40.36	< −2.46	< 42.01	< 41.37	< 34.65	< 34.64	
NGC 1395	43.44	41.14	−2.30	42.41	41.57	35.09	35.10	
NGC 1399	43.46	42.28	−1.18	42.10	41.38	37.01	36.69	< 8.90
NGC 1404	43.35	41.47	−1.88	42.10	41.33	< 34.49	< 34.49	
NGC 1400	41.88	< 39.58	< −2.30	< 41.12	41.35	33.88		< 7.93
NGC 1407	43.61	41.31	−2.30	42.40	41.79	36.50		< 9.19
NGC 1497	43.40	< 41.57	< −1.83		< 43.43	37.55	36.87	9.12
NGC 1510	42.05	< 40.14	< −1.91	< 42.17	42.55	< 35.54		8.02
NGC 1553	43.42	40.90	−2.52	42.18	41.75	< 35.52		< 9.52
NGC 1574	43.12	< 40.59	< −2.53	41.95	41.51	< 35.52		
NGC 1600	44.01	41.95	−2.06	< 42.82	42.22	37.03		< 10.59
NGC 1947	42.78	< 40.30	< −2.48	42.00	42.28	35.61		
NGC 2314	43.63	< 41.41	< −2.22	< 42.99	42.41	38.48	36.54	< 10.05
NGC 2300	43.50	41.51	−1.99	42.63	< 41.86	35.02	35.02	< 9.72
NGC 2444	43.39	< 41.65	< −1.74	< 43.53	43.73	< 37.15		< 10.17
NGC 2562	43.58	< 41.59	< −1.99	< 43.27	42.66	< 36.91		< 9.12
NGC 2563	43.70	42.12	−1.58	< 42.98	< 42.79	< 35.26		< 9.08
NGC 2629	43.40	< 41.24	< −2.17	< 42.89	42.51	37.30	37.25	
NGC 2685	42.99	< 40.46	< −2.53	42.11	42.13	35.13		9.71
NGC 2694	42.98	< 41.69	< −1.29				< 37.92	
NGC 2693	43.86	< 41.64	< −2.22	< 43.25	43.01	36.04	35.96	< 10.60
NGC 2716	43.48	< 40.99	< −2.49	43.16	42.78	< 36.51		
NGC 2832	44.25	42.74	−1.51	43.49	43.51	< 37.60		< 10.45
NGC 2859	43.43	< 40.38	< −3.05	< 42.43	42.22	< 35.00	< 34.71	< 8.75
NGC 2911	43.57	< 41.33	< −2.24	< 42.89	42.51	37.54	37.67	9.70
NGC 2974	43.55	40.92	−2.63	< 42.40	42.63	35.96	36.08	9.47
NGC 3078	43.60	41.17	−2.43			37.46	37.33	< 9.53
NGC 3065	43.18	41.38	−1.80	< 42.58	42.73			9.67
NGC 3115	43.01	< 39.95	< −3.06	41.81	< 40.82	< 33.36		< 7.71
NGC 3222	43.69	< 41.63	< −2.06			< 37.03		< 10.19
NGC 3258	43.47	41.49	−1.99	< 42.66	42.45	37.05	35.91	< 9.18
NGC 3377	42.69	< 39.44	< −3.25	41.51	40.80	< 33.78	< 33.78	< 6.99
NGC 3379	43.00	< 40.13	< −2.87	41.91	< 40.77	34.31	33.91	< 6.91
NGC 3384	42.85	< 39.88	< −2.97	41.76	40.91	< 35.07	< 33.71	< 7.26
NGC 3458	43.00	< 41.02	< −1.98	< 42.43	< 41.81		< 34.84	< 9.34
NGC 3516	43.56	42.16	−1.40	43.46	42.95	36.56	36.56	< 9.78
NGC 3585	43.66	40.37	−3.29	42.40	< 41.53	< 34.94		< 9.89
NGC 3607	43.48	40.88	−2.60			35.38	35.25	< 8.25
NGC 3608	43.30	40.50	−2.80			34.88	< 34.75	< 8.11
NGC 3818	43.00	< 40.98	< −2.03	< 42.62	< 41.70	< 34.99	< 34.81	< 9.59
NGC 3894	43.49	41.52	−1.97	< 42.85	42.46	38.24	38.29	
NGC 3923	43.82	41.35	−2.47	42.60	< 41.87	35.67	< 34.95	< 9.97
NGC 3990	42.53	< 40.43	< −2.11	< 41.99	41.56			
NGC 3998	43.38	41.94	−1.44	42.48	42.17	36.82	36.63	9.26
NGC 4105	43.48	40.91	−2.57	< 42.36	42.23	35.62		9.72
NGC 4168	42.88	40.30	−2.59	< 42.24	41.71	35.24	35.29	
NGC 4203	42.64	40.96	−1.68	< 41.74	41.75	35.33	35.23	9.20
NGC 4215	43.19	< 40.89	< −2.30	< 42.80	< 42.02	< 36.28	< 34.99	< 9.06
NGC 4251	42.64	< 39.55	< −3.09	< 41.65	< 40.85	< 34.24	< 33.87	< 7.50
NGC 4261	43.85	41.70	−2.15	43.01	41.70	39.20	37.78	< 10.03
NGC 4267	43.05	< 40.29	< −2.76	< 42.04	41.95	< 36.16	< 34.35	< 8.22
NGC 4291	43.35	41.34	−2.01	< 42.31	< 41.55	< 34.60	< 34.83	
NGC 4340	42.99	< 40.32	< −2.67	< 42.00	41.46		< 34.35	< 8.09
NGC 4350	43.01	< 40.16	< −2.85	42.29	41.93	< 35.61	< 34.35	< 8.16
NGC 4365	43.53	40.42	−3.11	42.32	41.70	< 34.34	< 34.29	< 7.90
NGC 4386	43.20	< 40.39	< −2.81	< 42.37	< 41.76		< 34.80	< 9.46
NGC 4374	43.67	41.16	−2.51	42.47	41.95	38.10	36.89	< 9.12
NGC 4382	43.73	40.72	−3.01	< 42.22	< 41.26	< 34.64	< 34.35	< 8.27
NGC 4387	42.67	< 40.53	< −2.14	< 42.14	< 41.62	< 34.64	< 34.37	< 7.77
NGC 4406	43.76	42.24	−1.52	42.32	41.40	< 34.42	< 34.37	8.35

TABLE 1B—*Continued*

Name	log(L_B) erg/sec	log(L_X) erg/sec	log(L_X/L_B)	log(L_{12}) erg/sec	log(L_{100}) erg/sec	log(L_6) erg/sec	log(L_{6co}) erg/sec	log(M_{HI}) $M_\odot$
NGC 4417	42.94	< 41.06	< −1.88	< 42.10	< 41.44	< 35.61	< 34.23	< 8.13
NGC 4425	42.65	< 40.25	< −2.40	< 42.14	< 41.58	< 35.59	< 34.35	< 7.98
NGC 4435	43.08	< 40.52	< −2.56	42.22	42.56		34.72	< 8.12
NGC 4458	42.69	40.22	−2.47	42.10	< 41.52	< 34.64	< 34.35	< 7.78
NGC 4459	43.17	< 40.40	< −2.77	42.66	42.57	35.02	34.54	< 8.42
NGC 4467	41.69	< 39.69	< −2.00					
NGC 4472	44.04	42.06	−1.98	42.42	< 41.39	37.04	36.40	< 7.89
NGC 4473	43.34	40.52	−2.82	42.57	< 41.40	< 34.52	< 34.71	< 8.14
NGC 4474	42.69	< 40.24	< −2.45	< 42.19	< 41.32	< 35.58	< 34.35	< 8.22
NGC 4479	42.48	< 40.10	< −2.38	< 42.14	< 41.54		< 34.35	< 8.14
NGC 4526	43.53	40.14	−3.39	42.79	43.26		35.13	< 8.12
NGC 4507	43.50	< 41.72	< −1.78	43.66	43.55			10.14
NGC 4550	42.83	< 40.20	< −2.63	< 41.90	41.28	< 34.52	< 34.35	< 8.37
NGC 4551	42.71	< 40.38	< −2.33	< 42.07	< 41.56	< 34.64	< 34.35	7.35
NGC 4552	43.45	40.92	−2.53	42.22	41.61	36.67	36.67	< 8.10
NGC 4564	43.02	< 40.19	< −2.83	< 42.16	< 41.64	< 34.52	< 34.35	< 7.86
NGC 4578	42.95	< 40.39	< −2.57	< 42.22	< 41.41	< 35.73	< 34.35	< 7.83
NGC 4589	43.55	< 40.66	< −2.89	< 42.62	42.22	36.51	36.47	< 9.71
NGC 4621	43.50	< 40.43	< −3.07	42.49	< 41.34	35.42	< 34.48	< 8.41
NGC 4638	42.95	40.22	−2.73	< 41.94	< 41.24	< 34.64	< 34.35	< 8.18
NGC 4636	43.58	41.99	−1.59	42.43	< 41.61	36.30	36.09	< 8.45
NGC 4649	43.83	41.61	−2.22	42.70	42.30	36.02	35.91	< 8.73
NGC 4645	43.63	< 40.90	< −2.73	< 43.06	43.00	< 36.60		
NGC 4697	44.01	40.97	−3.04	42.86	42.27	< 34.70	< 34.72	< 10.07
NGC 4754	43.20	< 40.13	< −3.07	< 42.04	< 41.43		< 34.35	< 8.27
NGC 4753	43.34	40.08	−3.26	42.58	42.75	< 34.03	< 34.14	< 9.47
NGC 4756	43.48	42.06	−1.42	< 43.13	< 42.58	36.82		
NGC 4762	43.26	40.52	−2.74	42.29	< 41.27	< 34.94	< 34.12	< 8.11
NGC 4782	43.66	41.77	−1.89	< 43.18	< 42.87	39.04	38.80	< 10.97
IC 3896	43.33	< 41.22	< −2.11	< 42.54	< 42.31	< 36.23		
NGC 4880	42.68	< 40.32	< −2.36	< 41.79	< 41.47	< 34.58		< 7.56
NGC 5044	43.75	43.17	−0.58	43.02	41.78	36.85		< 9.57
NGC 5077	43.52	41.07	−2.45	< 43.04	43.28	37.63	37.35	< 9.51
NGC 5084	43.38	41.21	−2.17	< 42.69	42.70	36.56		10.56
NGC 5102	42.21	< 39.11	< −3.10	40.68	40.96	33.23	< 33.18	8.73
NGC 5128	44.05	41.47	−2.58	43.44	43.57	38.67	37.42	9.53
NGC 5195	43.05	39.79	−3.26	42.46	< 41.56	< 36.03		< 9.35
IC 4296	44.12	41.98	−2.14	< 42.98	42.23	38.88	37.92	
IC 4329	43.86	< 42.13	< −1.73	< 43.06	42.99	35.50	35.52	
NGC 5322	43.95	< 41.04	< −2.91	< 42.47	42.44	36.81	36.34	< 9.59
NGC 5318	43.51	< 41.37	< −2.14	< 43.15	43.13	37.68	37.52	< 9.51

Name	log(L_B) erg/sec	log(L_X) erg/sec	log(L_X/L_B)	log(L_{12}) erg/sec	log(L_{100}) erg/sec	log(L_6) erg/sec	log(L_{6co}) erg/sec	log(M_{HI}) $M_\odot$
NGC 5354	43.64	< 41.33	< −2.31	< 43.04	42.85	36.91	36.30	10.26
NGC 5353	43.65	41.41	−2.24	< 42.60	42.76	36.89	36.88	10.19
NGC 5363	43.59	40.80	−2.80	42.67	42.84	36.87	36.78	8.76
NGC 5485	43.37	< 41.08	< −2.29	< 42.50	42.45	35.18	< 35.22	< 9.65
IC 989	43.70	< 41.85	< −1.85	< 43.73	43.07	38.02		9.50
NGC 5532	44.23	41.93	−2.30	43.50	43.14	39.33	38.04	< 9.79
NGC 5576	43.45	< 40.76	< −2.69	42.38	41.61	< 35.03	< 34.74	< 8.39
IC 1024	42.55	< 40.66	< −1.89	42.98	43.13	36.03	36.04	9.46
NGC 5838	43.54	40.55	−2.99	42.68	42.57	< 36.80	35.40	< 9.06
NGC 5846	43.77	42.11	−1.66	< 42.42	< 41.93	35.99	35.82	< 8.27
NGC 5866	43.34	40.17	−3.18	42.54	43.08	35.67	35.43	< 9.06
NGC 5982	43.77	41.47	−2.30	< 42.74	42.28	< 35.46	< 35.16	
NGC 6027	43.19	< 41.71	< −1.49	< 43.66	43.40			9.87
NGC 6034	43.71	42.46	−1.25			38.78	< 38.86	
NGC 6146	44.03	< 42.27	< −1.76	< 43.80	< 43.24	38.30	38.16	< 11.03
NGC 6876	43.66	41.78	−1.88	< 42.87	42.44	< 36.59		
NGC 6880	43.06	< 41.36	< −1.70	42.99	43.31	< 36.58		
NGC 6963	43.04	< 41.25	< −1.79			< 37.38		
NGC 6964	43.45	< 41.13	< −2.32	43.47	43.16	< 37.17		
NGC 7236	43.67	< 41.89	< −1.79			38.70		< 9.30
NGC 7237	43.57	< 42.02	< −1.55			38.83	37.32	< 9.30
NGC 7332	43.21	< 40.51	< −2.70	42.26	41.57	< 36.49		< 8.59
IC 1459	43.53	41.01	−2.52	42.50	42.11	37.82	37.79	< 9.34
NGC 7562	43.71	< 41.36	< −2.35	< 42.75	< 42.70	< 35.45	< 35.45	8.49
NGC 7619	43.79	42.00	−1.79	< 43.00	42.63	36.35	36.35	< 9.44
NGC 7626	43.70	41.50	−2.20	< 43.09	< 42.28	37.80	36.92	< 9.13

TABLE 1C

REFERENCES TO TABLE 1A

IRAS references:

1. Knapp *et al.*, 1989
2. Knapp *et al.*, 1989, blended:
   NGC 2832 with NGC 2831
   NGC 4638 with NGC 4637
   NGC 6876 with NGC 6877
3. Not observed by IRAS - Lonsdale *et al.*, 1985
4. Rice *et al.*, 1988
5. Fullmer and Lonsdale 1989
6. Fullmer and Lonsdale 1989, blended:
   NGC 1510 with NGC 1512
   NGC 2444 with NGC 2445
   NGC 6027 in a Zwicky Group
   NGC 127, NGC 130 and NGC 128
7. Condon *et al.*, 1991
8. Haynes *et al.*, 1990
9. Vereshchagin *et al.*, 1989

Radio continuum references:

10. FGT
11. Roberts *et al.*, 1991
12. Wrobel 1991
13. Wrobel and Heeschen 1988
14. Ekers and Ekers 1973
15. Fabbiano *et al.*, 1987
16. Wright 1974
17. Sulentic 1976
18. Hummel *et al.*, 1984
19. Haynes *et al.*, 1975
20. Disney and Wall 1977
21. Calvani *et al.*, 1989
22. Hummel *et al.*, 1991
23. Condon *et al.*, 1991

Radio core references:

24. Bridle and Fomalont 1978
25. Wrobel and Heeschen 1984
26. Geldzahler and Fomalont 1978
27. Killeen *et al.*, 1988
28. Stanger and Warwick 1986
29. Burns *et al.*, 1983
30. Killeen *et al.*, 1986
31. Birkinshaw and Davies 1985
32. Fabbiano *et al.*, 1984
33. Feretti *et al.*, 1984
34. Wrobel and Heeschen 1991
35. Bridle and Perley 1984
36. Impey and Gregorini, 1993
37. Sadler *et al.*, 1989
38. Wilkinson *et al.*, 1987
39. Neff and Hutchings 1992
40. Ekers *et al.*, 1989

HI references:

41. Roberts *et al.*, 1991
42. Huchtmeier and Richter 1989
43. Huchtmeier and Richter 1989:
    NGC 7236 blended with NGC 7237
44. Eder *et al.*, 1991
45. van Gorkom *et al.*, 1989: HI in absorption
46. Bottinelli *et al.*, 1990

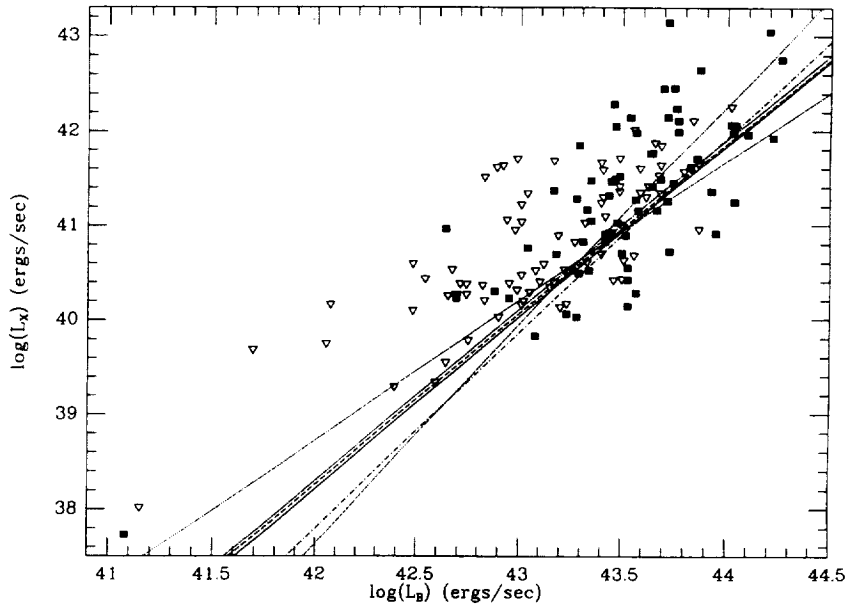

FIG. 1.—L_X vs. L_B for all E and S0 galaxies observed by *Einstein*. Filled squares show X-ray detections; open downward-pointing triangles show 3 σ X-ray upper limits. Fit lines are from the E-M algorithm (*solid line*), the Buckley-James (B-J) algorithm (*dashed line*), Schmitt's binning method (*dotted lines*, showing both fits—L_X on L_B and L_B on L_X—as well as their bisector), and the E-M algorithm applied to the sample with Local Group dE galaxies removed (*dot-dash line*).

TABLE 2A

CORRELATION TESTS ON THE E+S0 SAMPLE

Parameter	L_X		L_B		L_X/L_B	
	N_{tot}[a]	N_{lim}[b]	N_{tot}[a]	N_{lim}[b]	N_{tot}[a]	N_{lim}[b]
L_X[c]	...	...	148	78	148	78
			63.555	$<10^{-4}$	48.283	$<10^{-4}$
			8.656	$<10^{-4}$	7.449	$<10^{-4}$
			0.687	$<10^{-4}$	0.619	$<10^{-4}$
L_X	...	...	146	77	146	77
			76.136	$<10^{-4}$	56.671	$<10^{-4}$
			8.520	$<10^{-4}$	7.283	$<10^{-4}$
			0.695	$<10^{-4}$	0.608	$<10^{-4}$
L_B	...	...	...	...	146	77
					28.642	$<10^{-4}$
					5.358	$<10^{-4}$
					0.446	$<10^{-4}$
L_{12}	132	27, 19, 48	132	75	132	27, 19, 48
	...	...	51.002	$<10^{-4}$	...	...
	4.569	$<10^{-4}$	5.918	$<10^{-4}$	2.499	0.0124
	0.412	$<10^{-4}$	0.486	$<10^{-4}$	0.238	0.0064
L_{12}/L_B	132	27, 19, 48	132	75	132	27, 19, 48
	...	...	2.943	0.0863	...	...
	1.403	0.1605	1.607	0.1080	0.846	0.3977
	−0.091	0.2952	−0.156	0.0736	−0.081	0.3513
L_{100}	133	21, 42, 26	133	47	133	21, 42, 26
	...	...	17.992	$<10^{-4}$	...	...
	1.700	0.0891	4.425	$<10^{-4}$	0.720	0.4715
	0.198	0.0227	0.383	$<10^{-4}$	0.105	0.2277
L_{100}/L_B	133	21, 42, 26	133	47	133	21, 42, 26
	...	...	0.064	0.8004	...	...
	1.665	0.0959	0.202	0.8399	1.263	0.2065
	−0.105	0.2255	−0.014	0.8714	−0.091	0.2949
L_6	131	23, 26, 38	131	61	131	23, 26, 38
	...	...	32.121	$<10^{-4}$	...	...
	5.646	$<10^{-4}$	6.535	$<10^{-4}$	4.472	$<10^{-4}$
	0.492	$<10^{-4}$	0.541	$<10^{-4}$	0.425	$<10^{-4}$
L_6/L_B	131	23, 26, 38	131	61	131	23, 26, 38
	...	...	14.349	0.0002	...	...
	4.778	$<10^{-4}$	4.870	$<10^{-4}$	4.061	$<10^{-4}$
	0.401	$<10^{-4}$	0.393	$<10^{-4}$	0.384	$<10^{-4}$
L_{6cm}	99	17, 17, 30	99	47	99	17, 17, 30
	...	...	31.506	$<10^{-4}$	...	...
	5.398	$<10^{-4}$	5.775	$<10^{-4}$	4.436	$<10^{-4}$
	0.565	$<10^{-4}$	0.585	$<10^{-4}$	0.481	$<10^{-4}$
L_6[d]	99	15, 21, 26	99	41	99	15, 21, 26
	...	...	35.657	$<10^{-4}$	...	...
	5.406	$<10^{-4}$	6.473	$<10^{-4}$	4.171	$<10^{-4}$
	0.534	$<10^{-4}$	0.608	$<10^{-4}$	0.441	$<10^{-4}$
$M_{H\,I}$	115	45, 15, 44	115	89	115	45, 15, 44
	...	...	0.898	0.3434	...	...
	1.097	0.2728	1.049	0.2940	1.226	0.2202
	0.204	0.0294	0.177	0.0582	0.208	0.0265
$M_{H\,I}/L_B$	115	45, 15, 44	115	89	115	45, 15, 44
	...	...	0.894	0.3584	...	...
	0.109	0.9135	1.242	0.2143	0.769	0.4422
	0.018	0.8507	−0.076	0.4199	0.102	0.2778

[a] The values in rows 2–4 of each group in these columns are the test scores for the Cox-Hazard, Kendall's τ, and Spearman rank correlation tests, respectively.

[b] The three values for N_{lim} in the first row of each group in these columns are respectively the number of limit points in the row variable, the number in the column variable, and the number of double limits. The numbers listed in rows 2–4 are probabilities.

[c] This entry shows the analysis for the sample including M32 and NGC 205, as an example of the effects of these two galaxies. They are not included in the remaining analysis in the table.

[d] Correlations with total 6 cm luminosity using only the 6 cm core sample.

TABLE 2B

CORRELATION TESTS ON THE ELLIPTICAL GALAXIES

	L_X		L_B		L_X/L_B	
	N_{tot}	N_{lim}	N_{tot}	N_{lim}	N_{tot}	N_{lim}
L_X	...	...	72	30	72	30
			32.925	$<10^{-4}$	23.027	$<10^{-4}$
			5.973	$<10^{-4}$	5.128	$<10^{-4}$
			0.687	$<10^{-4}$	0.600	$<10^{-4}$
L_B	...	...	...	...	72	30
					12.062	0.0005
					3.754	0.0002
					0.443	0.0002
L_{12}	62	18, 5, 18	62	36	62	18, 5, 18
	...	...	25.291	$<10^{-4}$	...	...
	3.236	0.0012	4.109	$<10^{-4}$	1.816	0.0693
	0.468	0.0003	0.518	0.0001	0.269	0.0359
L_{12}/L_B	62	18, 5, 18	62	36	62	18, 5, 18
	...	...	4.615	0.0317	...	...
	0.826	0.4089	1.778	0.0755	0.176	0.8599
	−0.098	0.4448	−0.230	0.0730	−0.060	0.6393
L_{100}	62	14, 14, 9	62	23	62	14, 14, 9
	...	...	7.782	0.0053	...	...
	1.224	0.2211	3.236	0.0012	0.471	0.6379
	0.196	0.1262	0.430	0.0008	0.109	0.3942
L_{100}/L_B	62	14, 14, 9	62	23	62	14, 14, 9
	...	...	0.675	0.4113	...	...
	1.510	0.1310	0.115	0.9086	1.129	0.2587
	−0.177	0.1669	−0.010	0.9382	−0.133	0.3005
L_6	69	12, 12, 15	69	27	69	12, 12, 15
	...	...	18.327	$<10^{-4}$	...	...
	3.796	0.0001	4.665	$<10^{-4}$	2.951	0.0032
	0.492	0.0001	0.551	$<10^{-4}$	0.380	0.0017
L_6/L_B	69	12, 12, 15	69	27	69	12, 12, 15
	...	...	7.534	0.0061	...	...
	3.264	0.0011	3.322	0.0009	2.836	0.0046
	0.387	0.0014	0.385	0.0015	0.340	0.0051

NOTE.—Table entries as defined in notes to Table 2A.

to be addressed is whether one can identify "dependent" and "independent" variables. We refer readers to the work of Isobe et al. (1990) and Feigelson & Babu (1992a) for general discussions of this and other issues relating to the application of linear regression to various sorts of data. Our use of the survival analysis regression algorithms has led us to conclude that it is best to treat the uncensored variable as the "independent" variable when using the E-M or B-J algorithms on singly censored data sets. These algorithms are explicitly designed to address problems in which there is censoring in the dependent variable. If the censored variable is used as the independent variable, the algorithms will yield zero points that are seriously in error (the slope computations, however, appear quite robust). When using Schmitt's method (on either singly or doubly censored data sets), we do not define an "independent" variable. Instead, we use the bisector of the fits of $(X \mid Y)$ and $(Y \mid X)$ (see Isobe et al. 1990 for background).

There are two objects relatively isolated in the lower left corner of Figure 1. These are the Local Group dwarf galaxies M32 and NGC 205. It is fairly clear that these objects are quite different sorts of galaxies, in terms of their fundamental physical properties, than the more luminous systems that dominate our sample (Kormendy 1985; Bender, Paquet, & Nieto 1991). They are also positioned in the L_X-L_B plane so as to have a large statistical leverage on our analysis. We have therefore repeated our analysis without these systems. The results of the correlation tests (see Table 2A) show somewhat stronger statistical relationships with the Local Group dwarf ellipticals (dE's) removed. The results of the regression analysis are shown in Table 3A, and the E-M line is plotted in Figure 1. While the L_X-L_B slope is steeper if the dwarfs are excluded, the difference is only at the $\sim 1\ \sigma$ level. In general, we find no significant differences in our results with or without the Local Group dwarfs. Since they are fundamentally different sorts of galaxies than the bulk of our sample, we choose to exclude them in the rest of our analysis. Also, for these reasons, we will not use these two objects in comparisons between the E and S0 subsamples below.

Another useful way of presenting the relationship between optical and X-ray emission for our sample is to plot log L_X

TABLE 2C

CORRELATION TESTS ON THE S0 GALAXIES

	L_X		L_B		L_X/L_B	
	N_{tot}	N_{lim}	N_{tot}	N_{lim}	N_{tot}	N_{lim}
L_X	...	...	74	47	74	47
			38.461	$<10^{-4}$	28.350	$<10^{-4}$
			5.016	$<10^{-4}$	4.174	$<10^{-4}$
			0.611	$<10^{-4}$	0.528	$<10^{-4}$
L_B	...	...	...	...	74	47
					10.984	0.0009
					2.652	0.0080
					0.351	0.0027
L_{12}	70	9, 14, 30	70	39	70	9, 14, 30
	...	...	22.851	$<10^{-4}$	...	...
	3.259	0.0011	4.257	$<10^{-4}$	1.424	0.1544
	0.376	0.0018	0.454	0.0002	0.198	0.0994
L_{12}/L_B	70	9, 14, 30	70	39	70	9, 14, 30
	...	...	0.158	0.6907	...	...
	0.385	0.7005	0.089	0.9288	0.225	0.8223
	−0.004	0.9733	−0.025	0.8338	−0.050	0.6774
L_{100}	71	7, 28, 17	71	24	71	7, 28, 17
	...	...	15.590	0.0001	...	...
	2.255	0.0242	4.328	$<10^{-4}$	1.142	0.2533
	0.313	0.0087	0.470	0.0001	0.185	0.1225
L_{100}/L_B	71	7, 28, 17	71	24	71	7, 28, 17
	...	...	1.606	0.2051	...	...
	0.555	0.5791	1.359	0.1743	0.415	0.6784
	0.131	0.2745	0.162	0.1743	0.045	0.7037
L_6	62	11, 14, 23	62	34	62	11, 14, 23
	...	...	12.309	0.0005	...	...
	3.568	0.0004	3.767	0.0002	2.254	0.0242
	0.454	0.0004	0.426	0.0009	0.355	0.0056
L_6/L_B	62	11, 14, 23	62	34	62	11, 14, 23
	...	...	5.241	0.0221	...	...
	3.069	0.0021	2.724	0.0064	1.968	0.0491
	0.393	0.0021	0.303	0.0181	0.337	0.0085

NOTE.—Table entries as defined in notes to Table 2A.

against log (L_X/L_B). There is an obvious trend in such a plot (see Fig. 2) for L_X to increase with increasing L_X/L_B. Our statistical analysis confirms this (see Table 2A). The results of the regressions are given in Table 3A and plotted in Figure 2. We find that the relationship between X-ray and optical emission from early-type systems is steep $[L_X \propto (L_X/L_B)^{\sim 1.8}]$, and is close to the relationship expected from the L_X-L_B relationship $[L_X \propto (L_X/L_B)^2]$. The slopes are steeper than slope 1 by more than 6 σ. The slope 0 case, appropriate for L_X/L_B = constant (i.e., slope 1 in the L_X-L_B plane) is ruled out at more than 13 σ.

We have also tested for a possible relationship between L_B and L_X/L_B. There is statistical evidence for a correlation between these parameters (see Table 2), but it is weaker than that between L_X and L_X/L_B. Furthermore, it appears to be driven by the relatively small range in L_B among the X-ray detections in our sample, and the typically larger values of L_X for the optically brightest galaxies. There appears to be no additional information in this plane that is not more apparent in the L_X-L_B or L_X-L_X/L_B planes.

To investigate this point further, we must move beyond simple bivariate analysis. This study deals with a large, multiparametric data set. Given this, it is important to examine the interrelationships between the various observables for our sample. A number of different multivariate analysis tools have been applied to astrophysical problems in the last five or six years (see Feigelson & Babu 1992b). One, that was applied to a preliminary sample of *Einstein*-selected galaxies (Fabbiano et al. 1988), is the partial Spearman rank analysis (Kendall & Stuart 1976). This analysis builds a matrix of bivariate Spearman rank statistics, and then tests the correlation between subsamples of the parameters in the matrix set while holding all other variables in the matrix set constant. Because our sample contains upper limits for many variables, we generally use the results from the modified Spearman rank analysis to provide inputs for the matrices of bivariate Spearman rank statistics. These matrices are then subject to the partial rank analysis as detailed in Kendall & Stuart (1976).

In this initial case, we tested the triplet of L_X, L_B, and L_X/L_B. The numerical results of the partial rank analysis are shown in

TABLE 3A

REGRESSION ANALYSIS ON E+S0 SAMPLE

X	Y	Slope[a]	σ_S	Intercept	σ_I
L_B[b] ($N = 148$, $N_{ul} = 0$)	L_X ($N_{ul} = 78$)	1.81	0.15	−37.80	6.31
		1.80	0.16	−37.29	...
		1.80	0.11	−37.30	3.87
L_B ($N = 146$, $N_{ul} = 0$)	L_X ($N_{ul} = 77$)	2.01	0.18	−46.68	7.93
		2.00	0.22	−46.17	...
		2.02	0.13	−46.61	4.52
L_X/L_B ($N = 146$, $N_{ul} = 0$)	L_X ($N_{ul} = 77$)	1.79	0.13	+45.08	0.29
		1.84	0.12	+45.11	...
		1.75	0.09	+45.30	0.21
L_B ($N = 132$, $N_{ul} = 0$)	L_{12} ($N_{ul} = 75$)	0.83	0.11	+6.33	4.59
		0.81	0.13	+7.36	...
		1.05	0.10	−3.20	3.46
L_{12} ($N = 132$, $N_{ul} = 75$)	L_X ($N_{ul} = 67$)	...	...	...	...
		...	...	...	...
		1.53	0.12	−23.95	3.89
L_X/L_B ($N = 132$, $N_{ul} = 67$)	L_{12} ($N_{ul} = 75$)	...	...	...	...
		...	...	...	...
		0.82	0.17	+44.27	3.44
L_B ($N = 131$, $N_{ul} = 0$)	L_{12} ($N_{ul} = 75$)	2.79	0.40	−85.68	17.26
		2.87	0.33	−89.20	...
		3.67	0.38	−123.63	12.20
L_X ($N = 131$, $N_{ul} = 64$)	L_6 ($N_{ul} = 61$)	...	...	...	...
		...	...	...	...
		1.61	0.06	−29.72	4.00
L_X/L_B ($N = 131$, $N_{ul} = 64$)	L_6 ($N_{ul} = 61$)	...	...	...	...
		...	...	...	...
		2.32	0.28	+41.63	2.16
L_B ($N = 131$, $N_{ul} = 0$)	L_6/L_B ($N_{ul} = 61$)	1.72	0.39	−82.41	16.82
		1.81	0.33	−86.46	...
		2.73	0.54	−126.31	16.88
L_X ($N = 131$, $N_{ul} = 64$)	L_6/L_B ($N_{ul} = 61$)	...	...	...	...
		...	...	...	...
		1.18	0.18	−55.72	5.51
L_X/L_B ($N = 131$, $N_{ul} = 64$)	L_6/L_B ($N_{ul} = 61$)	...	...	...	...
		...	...	...	...
		2.23	0.38	−2.30	0.79
L_X ($N = 99$, $N_{ul} = 47$)	L_{6co} ($N_{ul} = 47$)	...	...	...	...
		...	...	...	...
		1.53	0.12	−26.86	3.72
L_X/L_B ($N = 99$, $N_{ul} = 47$)	L_{6co} ($N_{ul} = 47$)	...	...	...	...
		...	...	...	...
		2.92	0.33	+42.77	2.49
L_X ($N = 99$, $N_{ul} = 47$)	L_6[c] ($N_{ul} = 41$)	...	...	...	...
		...	...	...	...
		1.57	0.21	−28.11	6.41
L_X/L_B ($N = 99$, $N_{ul} = 47$)	L_6[c] ($N_{ul} = 41$)	...	...	...	...
		...	...	...	...
		2.76	0.43	+40.81	2.46

[a] Numbers in rows 1–3 of each group in the following columns refer to results using the E-M algorithm, the B-J algorithm, and the Schmitt method, respectively.

[b] This entry shows the analysis for the sample including M32 and NGC 205, as an example of the effects of these two galaxies. They are not included in the remaining analysis in the table.

[c] Regressions with total 6 cm luminosity using only the 6 cm core sample.

TABLE 3B

REGRESSION ANALYSIS ON THE ELLIPTICAL GALAXIES

X	Y	Slope	σ_S	Intercept	σ_I
$L_B (N = 72, N_{ul} = 0)$	$L_X (N_{ul} = 30)$	1.95	0.25	−43.94	11.04
		1.93	0.29	−42.99	...
		1.84	0.16	−39.26	5.44
$L_X/L_B (N = 72, N_{ul} = 0)$	$L_X (N_{ul} = 30)$	1.88	0.19	+45.30	0.42
		1.90	0.17	+45.31	...
		1.75	0.19	+45.26	0.37
$L_B (N = 62, N_{ul} = 0)$	$L_{12} (N_{ul} = 36)$	0.84	0.12	+5.87	5.36
		0.84	0.18	+5.97	...
		0.94	0.10	+1.63	3.83
$L_{12} (N = 62, N_{ul} = 36)$	$L_X (N_{ul} = 23)$	...	...	...	...
		...	...	...	...
		1.93	0.21	−40.73	6.87
$L_B (N = 69, N_{ul} = 0)$	$L_6 (N_{ul} = 27)$	3.09	0.60	−98.56	26.30
		3.20	0.53	−103.31	...
		3.62	0.48	−121.31	15.93
$L_X (N = 69, N_{ul} = 27)$	$L_6 (N_{ul} = 27)$	...	...	...	...
		...	...	...	...
		1.75	0.19	−35.75	6.04
$L_X/L_B (N = 69, N_{ul} = 27)$	$L_6 (N_{ul} = 27)$	...	...	...	...
		...	...	...	...
		2.19	0.65	+41.11	3.47
$L_B (N = 69, N_{ul} = 0)$	$L_6/L_B (N_{ul} = 27)$	1.87	0.59	−81.15	25.89
		1.98	0.52	−93.91	...
		2.44	0.60	−113.76	18.98
$L_X (N = 69, N_{ul} = 27)$	$L_6/L_B (N_{ul} = 27)$	...	...	...	...
		...	...	...	...
		1.06	0.24	−50.77	7.19
$L_X/L_B (N = 69, N_{ul} = 27)$	$L_6/L_B (N_{ul} = 27)$	...	...	...	...
		...	...	...	...
		1.64	0.47	−3.50	0.96

NOTE.—Table entries as defined in notes to Table 3A.

Table 4A. In brief, they confirm the results of the bivariate tests that there are strong relationships between L_X and L_B and between L_X and L_X/L_B, but no significant relationship between L_B and L_X/L_B.

3.1.2. *Luminosity Dependence of the Correlations*

The recent study of Kim, Fabbiano, & Trinchieri (1992a,b) shows that high-luminosity early-type galaxies typically have X-ray spectra best fitted by thermal emission from a ~ 1 keV gas. The emission from lower luminosity ellipticals, however, is better fitted by a harder ($\gtrsim 3$ keV) bremsstrahlung spectrum, similar to that seen for spirals (Kim et al. 1992b). The lowest L_X/L_B group also has a very soft (~ 0.2 keV) component (Kim et al. 1992b; Fabbiano, Kim, & Trinchieri 1994), the nature of which is still unclear (see Pellegrini & Fabbiano 1994). A plausible explanation for this is that only the high-luminosity systems are massive enough to retain their hot ISM (Canizares, Fabbiano, & Trinchieri 1987; FGT). The X-ray emission from low-luminosity systems would thus be largely due to stellar X-ray sources. In this case it seems likely that the functional dependence of L_B on L_X will change with increasing luminosity. To test this point, we made subsamples of our data set by imposing limits from both above and below on L_X and L_B, and made fits to the resulting subsamples. The clearest results came from imposing decreasing maxima on L_X. Decreasing the maximum log L_X (in ergs s^{-1}) from 43.2 (the full sample) down to 40.5 results in a decrease in the slope of the L_X-L_B relation from 1.8 ± 0.15 to 1.0 ± 0.2. These values are different at roughly the 3 σ level, arguing strongly that there are at least two distinct physical processes producing the X-ray emission from low-luminosity ($\log L_X \lesssim 40.5$) and high-luminosity ($\log L_X \gtrsim 40.5$) systems (see also FGT). This conclusion is reinforced by the spectral differences found by Kim et al. (1992b) between high- and low-L_X systems. We note that evaluating the L_X-L_B relation for only the more luminous galaxies results in an even steeper slope ($\approx 2.0 \pm 0.2$ for $\log L_B \gtrsim 42$), as expected from the above result. This steepening is statistically marginal ($\sim 1\ \sigma$). It is nonetheless interesting that this slope 2 behavior at high L_B is predicted by the instability-cycle models of Kritsuk (1992). However, a steep L_X-L_B trend is also reproduced for very different physical reasons by the hydrodynami-

TABLE 3C

REGRESSION ANALYSIS ON THE S0 GALAXIES

X	Y	Slope	σ_S	Intercept	σ_I
$L_B (N = 74, N_{ul} = 0)$	$L_X (N_{ul} = 47)$	1.87	0.26	−40.63	11.45
		1.83	0.35	−38.98	...
		1.92	0.20	−42.51	6.91
$L_X/L_B (N = 74, N_{ul} = 0)$	$L_X (N_{ul} = 47)$	2.15	0.39	+46.65	1.22
		2.20	0.60	+46.73	...
		1.83	0.18	+45.64	0.47
$L_B (N = 70, N_{ul} = 0)$	$L_{12} (N_{ul} = 39)$	0.88	0.17	+3.95	7.50
		0.86	0.20	+4.98	...
		1.33	0.19	−15.27	6.30
$L_{12} (N = 70, N_{ul} = 39)$	$L_X (N_{ul} = 44)$	...	...	...	...
		...	...	...	...
		1.17	0.15	−8.86	4.98
$L_{100} (N = 71, N_{ul} = 24)$	$L_X (N_{ul} = 45)$	...	...	...	...
		...	...	...	...
		0.85	0.23	+7.85	6.94
$L_B (N = 62, N_{ul} = 0)$	$L_6 (N_{ul} = 34)$	2.32	0.52	−65.19	22.41
		2.37	0.43	−67.21	...
		3.24	0.72	−104.80	22.86
$L_X (N = 62, N_{ul} = 37)$	$L_6 (N_{ul} = 34)$	...	...	...	...
		...	...	...	...
		1.61	0.28	−29.75	8.58
$L_X/L_B (N = 62, N_{ul} = 37)$	$L_6 (N_{ul} = 34)$	...	...	...	...
		...	...	...	...
		2.52	0.41	+42.16	4.35
$L_B (N = 62, N_{ul} = 0)$	$L_6/L_B (N_{ul} = 34)$	1.38	0.49	−68.02	21.44
		1.42	0.42	−69.75	...
		2.27	0.90	−106.85	27.96
$L_X (N = 62, N_{ul} = 37)$	$L_6/L_B (N_{ul} = 34)$	...	...	...	...
		...	...	...	...
		1.34	0.46	−62.49	13.68
$L_X/L_B (N = 62, N_{ul} = 37)$	$L_6/L_B (N_{ul} = 34)$	...	...	...	...
		...	...	...	...
		1.90	0.62	−2.87	1.27

NOTE.—Table entries as defined in notes to Table 3A.

cal evolution models of Ciotti et al. (1991) for X-ray emission arising from hot gaseous halos around massive early-type galaxies. Both these theories are much more physically developed than the hypothesis presented by Forman et al. (1985) in the first paper to recognize the slope 2 behavior of the L_X-L_B correlation for the most X-ray–luminous early-type galaxies.

We noted above that the relationship between L_X and L_B is shallower for lower maximum L_X values, becoming consistent with slope 1 for galaxies with log $L_X < 40.5$. The simple interpretation of this predicts that the relationship between L_X and L_X/L_B should disappear for a subsample with a maximum L_X of about this value. This is the case: for a sample with log $L_X <$ 40.5, the slope of the regression with log (L_X/L_B) is 1.56 ± 1.38. By evaluating samples of progressively higher minimum L_X, we find that this regression slope converges to unity. This is apparently because the L_B for our sample is more or less constant for the most luminous X-ray galaxies. While systems exist with L_X up to 1.2 dex larger that the cutoff at log $L_X = 42$, the dispersion of log L_B for this sample is only 0.24.

3.1.3. *Comparison with 7S Distances*

Donnelly et al. (1990) suggested that use of the D_n-σ distances derived from the work of Faber et al. (1989, hereafter 7S) caused a decrease in the scatter and increases in both the strength of correlation and the slope of the L_X-L_B relationship. Roughly half of our sample (75 of 148) have 7S velocity distances. In Figure 3 we show a plot of our distances taken from P0, and distances from the 7S velocity distances with $H_0 = 50$ km s^{-1} Mpc^{-1}. The best fit (*solid line*), and both individual fits (*dashed lines*), are consistent with the slope 1, intercept 0 line (*dotted line*). There is thus no evidence for a systematic difference between the two sets of distance estimates.

We derived X-ray and optical luminosities for this subsample, using both our distances and the 7S distances, and then tested both samples for correlation between L_X and L_B. For both samples, all three tests indicate a statistical correlation with $P < 10^{-4}$. In keeping with the findings of Donnelly et al., the scores for the correlation tests are higher for the sample

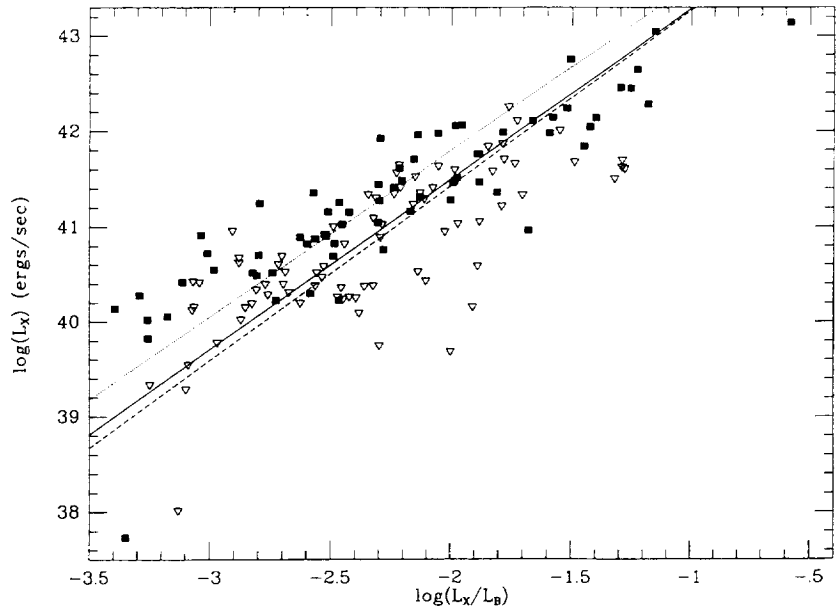

FIG. 2.—L_X vs. L_X/L_B for E and S0 galaxies observed by *Einstein*. Symbols as in Fig. 1. Fit lines are from the E-M algorithm (*solid line*), the B-J algorithm (*dashed line*), and the bisector from Schmitt's method (*dotted line*), all for the sample without the Local Group dwarfs.

with 7S distances. We also computed regression lines for the L_X-L_B relationship using both sets of distances, and both the E-M and B-J algorithms. Figure 4 shows the two scatter plots along with these fits. For distances from P0 we find

$$\log L_X = 2.08(\pm 0.23) \log L_B - 49.45(\pm 10.03), \quad \sigma = 0.61, \quad (1a)$$

$$\log L_X = 2.07(\pm 0.25) \log L_B - 48.96, \quad \sigma = 0.55, \quad (1b)$$

while for distances from 7S we find

$$\log L_X = 2.36(\pm 0.24) \log L_B - 61.62(\pm 10.47), \quad \sigma = 0.58, \quad (2a)$$

$$\log L_X = 2.34(\pm 0.25) \log L_B - 60.92, \quad \sigma = 0.50, \quad (2b)$$

for the two regression algorithms. Again, we confirm the findings of Donnelly et al. that the scatter about the fit line decreases using the 7S distances, and that the slope of the regression line is formally steeper. We note that the increase in slope is not statistically significant for either method ($\Delta_{EM} = 0.28 \pm 0.33$, $\Delta_{BJ} = 0.27 \pm 0.35$). Thus, while the 7S distances do appear to give marginally better results, this is more than offset by their being available for only half of our sample.

TABLE 4A

PARTIAL SPEARMAN RANK ANALYSIS: X-RAY PROPERTIES, E+S0 SAMPLES

Test Pair	Held Parameters	Size	Partial Spearman Rank	Probability
L_B-L_X	L_X/L_B	146	0.596	<0.005
	C_{21}	39	0.469	<0.005
	L_X/L_B, C_{21}	39	0.896	<0.005
L_B-L_X/L_B	L_X	146	0.041	0.314
	C_{21}	39	0.021	>0.400
	L_X, C_{21}	39	−0.864	<0.005
L_X-L_X/L_B	L_B	146	0.463	<0.005
	C_{21}	39	0.309	0.032
	L_B, C_{21}	39	0.965	<0.005
L_B-C_{21}	L_X	39	−0.032	>0.400
	L_X/L_B	39	0.179	0.152
	L_X, L_X/L_B	39	−0.226	0.092
L_X-C_{21}	L_B	39	0.398	0.008
	L_X/L_B	39	0.309	0.032
	L_B, L_X/L_B	39	0.336	0.022
L_X/L_B-C_{21}	L_B	39	0.328	0.023
	L_X	39	−0.098	0.279
	L_B, L_X	39	−0.244	0.077

3.1.4. *Correlations with X-Ray Colors*

Detailed analysis of *Einstein* imaging proportional counter (IPC) data for a number of the brightest early-type galaxies has led to the suggestion that these systems have N_H values in excess of the standard Galactic values (Kim et al. 1992a). Kim et al. (1992b) have defined the index C_{21}, the ratio of the counts in the energy range 0.8–1.36 keV (C_2) to the counts in the energy range 0.16–0.8 keV (C_1). Thus it measures the strength of the low-energy cutoff, and should therefore directly measure N_H in the absence of large ranges in the temperatures or abundances of the X-ray–emitting gas from galaxy to galaxy. However, it would also be sensitive to differences in spectral shape due to abundance variations, or multiple temperature components for a fixed N_H. Recent *ROSAT* results reveal differing spectral shapes for early-type galaxies over a range in

TABLE 4B

PARTIAL SPEARMAN RANK ANALYSIS: X-RAY PROPERTIES, SEPARATE E AND S0 SAMPLES

Test Pair	Held Parameters	Sample	Size	Partial Spearman Rank	Probability
L_B-L_X	L_X/L_B	E	72	0.587	<0.005
	L_X/L_B	S0	74	0.535	<0.005
	C_{21}	E	24	0.486	0.010
	C_{21}	S0	15	0.278	0.181
	L_X/L_B, C_{21}	E	24	0.880	<0.005
	L_X/L_B, C_{21}	S0	15	0.594	0.018
L_B-L_X/L_B	L_X	E	72	0.053	0.332
	L_X	S0	74	0.042	0.362
	C_{21}	E	24	0.127	0.282
	C_{21}	S0	15	−0.095	0.375
	L_X, C_{21}	E	24	−0.842	<0.005
L_X-L_X/L_B	L_B	E	72	0.454	<0.005
	L_B	S0	74	0.423	<0.005
	C_{21}	E	24	0.905	<0.005
	C_{21}	S0	15	0.789	<0.005
	L_B, C_{21}	E	24	0.973	<0.005
L_B-C_{21}	L_X	E	24	−0.240	0.144
	L_X	S0	15	0.249	0.207
	L_X/L_B	E	24	−0.085	0.351
	L_X, L_X/L_B	E	24	−0.242	0.151
	L_X, L_X/L_B	S0	15	0.484	0.048
L_X-C_{21}	L_B	E	24	0.433	0.021
	L_B	S0	15	0.485	0.041
	L_X/L_B	E	24	0.038	>0.400
	L_X/L_B	S0	15	0.457	0.050
	L_B, L_X/L_B	E	24	0.230	0.164
	L_B, L_X/L_B	S0	15	0.613	0.014
L_X/L_B-C_{21}	L_B	E	24	0.397	0.032
	L_X	E	24	0.132	0.275
	L_X	S0	15	−0.119	0.345
	L_B, L_X	E	24	−0.134	0.276
	L_B, L_X	S0	15	0.092	0.384

L_X and L_X/L_B, confirming the "softening" of the spectrum already seen by Kim et al. (1992b) for the lowest luminosity detected X-ray galaxies. Similar effects are seen in some slightly more luminous X-ray galaxies (Fabbiano et al. 1994; Fabbiano and Schweizer 1994). Also, *ROSAT* data do not show excess absorption in the X-ray–luminous galaxies analyzed to date (e.g., Trinchieri et al. 1994; Kim & Fabbiano 1994) despite these data being more sensitive to low X-ray energies than the *Einstein* data.

There are a total of 39 objects in our sample with more than 3 σ detections in both C_1 and C_2. In Table 5 we show the results of bivariate analysis on the C_{21} color, L_B, L_X, and L_X/L_B for this subsample of objects. There is a strong correlation found between L_X and C_{21}, and a somewhat weaker ($\sim$3%) correlation found between L_X/L_B and C_{21}. There is no evidence for correlation between L_B and C_{21}. In Figure 5 we show plots of C_{21} against both L_X and L_X/L_B. The *ROSAT* results noted above would indicate that these trends are the result of differences in the intrinsic spectral shape as a function of L_X, rather than differences in N_H.

We conducted a partial rank analysis of the C_{21} sample, using L_B, L_X, L_X/L_B, and C_{21} as inputs. The results are shown in Table 4A. Briefly, we recover the relationship between L_X and C_{21} found in the bivariate analysis at the $\lesssim$3% level for all combinations including these two variables. The evidence for a relationship between L_X/L_B and C_{21} varies from the $\sim$2% level to nonexistent, depending on the combination examined. Since the worst case is the three-way case including L_X as the frozen variable, we conclude that the relationship between L_X/L_B and C_{21} seen in the bivariate analysis is driven by an underlying relationship between L_X and C_{21}. We find no evidence for a relationship between L_B and C_{21} for any combination.

3.2. *Type Separation*

Our sample is large enough that we can make the crude separation between E ($T \leq -3$) and S0 ($-2 \leq T < 0$) systems and still have statistically interesting numbers of galaxies.

3.2.1. *The Elliptical Galaxies*

There are 72 E galaxies in our sample. Our bivariate statistical analysis shows that L_X is correlated with L_B for this subsample (see Table 2B). The results of the regression analysis are given in Table 3B. The fits, along with the data, are shown in

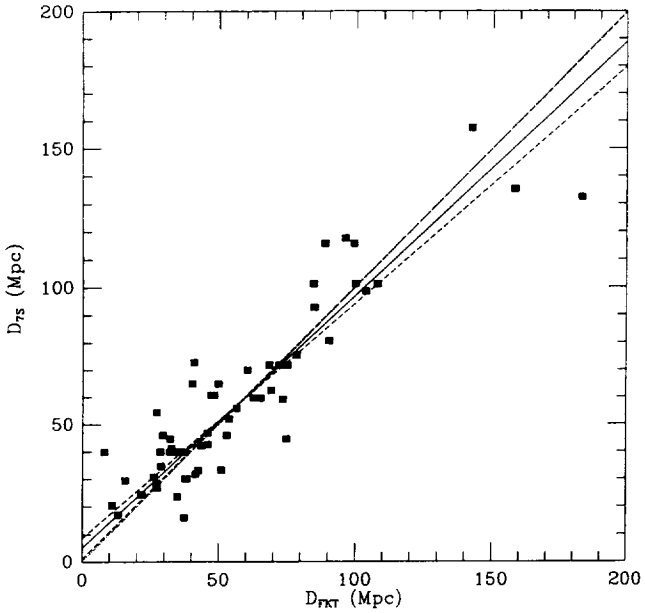

FIG. 3.—Distances from P0 plotted against distances determined from 7S velocity distances. The dotted line has slope 1 and intercept 0. The best fit [linear bisector of $(X \mid Y)$ and $(Y \mid X)$] is shown as a solid line. The fits $(X \mid Y)$ and $(Y \mid X)$ are shown as dashed lines. All the fits are consistent with the dotted line.

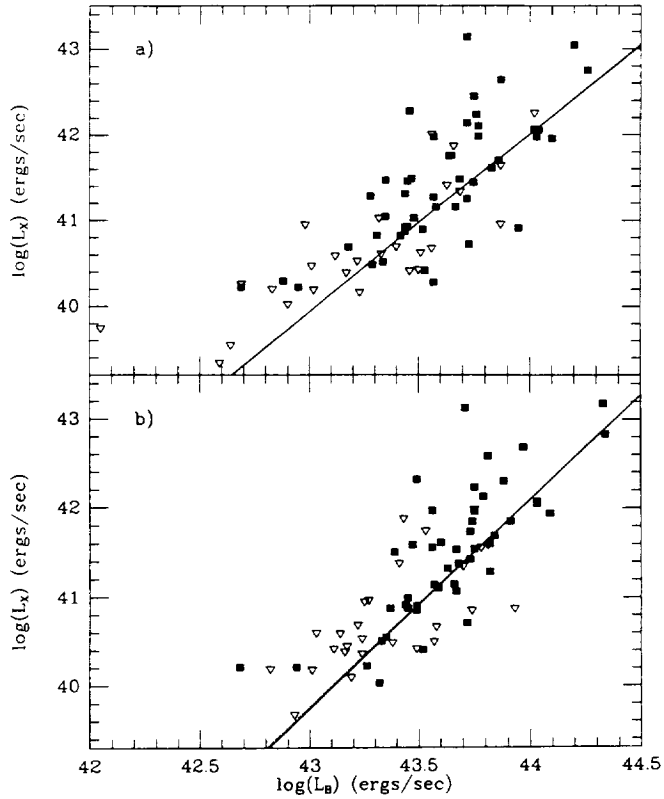

FIG. 4.—L_X vs. L_B for the subset of galaxies with distances from 7S, (*a*) for distances from P0 and (*b*) for distances from 7S. In both cases we show fit lines from the E-M (*solid line*) and B-J (*dotted line*) algorithms.

Figure 6*a*. Although the analysis of just the E galaxies gives slightly shallower regression lines than does the full sample, the differences are not statistically significant. We also find a strong L_X-L_X/L_B relationship for the elliptical galaxies (Table 2B). The results of the regression algorithms (Table 3B) along with the data are shown in Figure 6*b*. The results are consistent with those found for the full sample. The most discrepant slopes (in this case, those from the B-J algorithm and from Schmitt's method) differ by only 0.6 σ. The correlations found between C_{21} and X-ray emission become much weaker if we test only the E galaxies (see Table 5).

The results of a three-way partial rank analysis on L_B, L_X, and L_X/L_B for the elliptical galaxies (see Table 4B) confirm the L_B-L_X, and L_X-L_X/L_B correlations found in the bivariate analysis. For the C_{21} sample of elliptical galaxies, partial rank analysis yields results consistent with the bivariate analysis: the correlations found are the same as for the full sample, but the strengths of the correlations are decreased.

TABLE 5

CORRELATION TESTS ON THE C_{21} SAMPLE

	L_X		L_B		L_X/L_B		L_{12}		L_{100}		$L_{6\,cm}$	
SAMPLE	N_{tot}	N_{lim}	N_{tot}	N_{lim}	N_{tot}	N_{lim}	N_{tot}	N_{lim}	N_{tot}	N_{lim}	N_{tot}	N_{lim}
E+S0	39	0	39	0	39	0	38	13	38	11	39	14
	6.630	0.0100	1.277	0.2585	6.003	0.0143	0.511	0.4749	0.090	0.7637	3.526	0.0604
	2.891	0.0038	1.186	0.2357	2.141	0.0323	0.215	0.8295	0.743	0.4572	1.803	0.0713
	0.434	0.0075	0.191	0.2402	0.334	0.0394	0.075	0.6499	−0.071	0.6653	0.274	0.0911
E	24	0	24	0	24	0	24	8	24	7	24	8
	1.641	0.2002	0.191	0.6620	2.753	0.0971	0.112	0.7374	0.026	0.8709	1.441	0.2300
	1.885	0.0594	0.273	0.7849	1.836	0.0664	1.128	0.2594	0.859	0.3905	1.111	0.2666
	0.373	0.0415	−0.039	0.8527	0.391	0.0365	−0.170	0.4159	−0.141	0.4986	0.223	0.2858
S0	15	0	15	0	15	0	14	5	14	4	15	6
	6.017	0.0142	4.486	0.0342	4.602	0.0319	0.730	0.3929	0.099	0.7535	2.509	0.1132
	2.326	0.0200	1.930	0.0536	1.732	0.0833	0.884	0.3766	0.606	0.5448	1.219	0.2230
	0.596	0.0159	0.457	0.0465	0.443	0.0496	0.313	0.2584	0.137	0.6210	0.348	0.1933

NOTE.—Table entries as defined in notes to Table 2A.

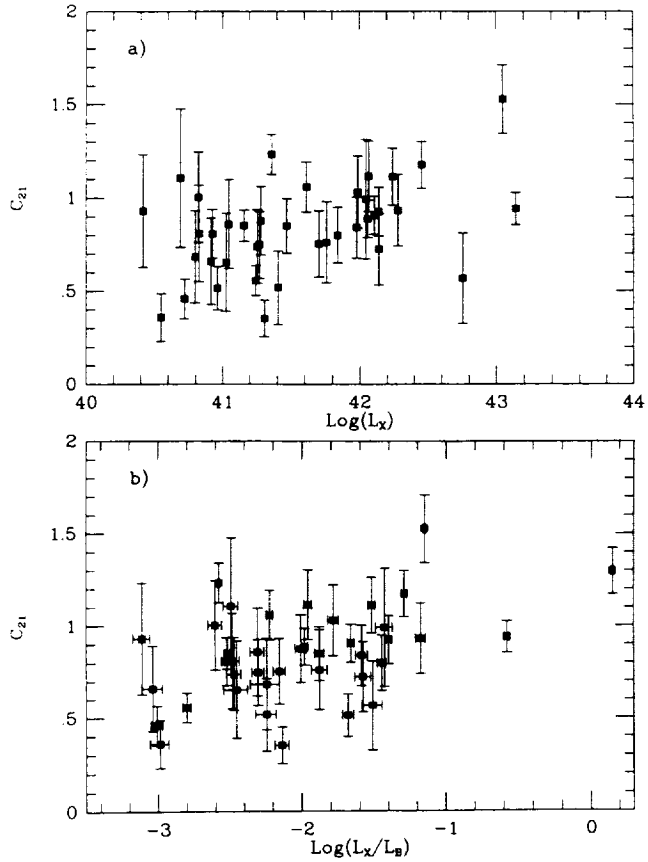

FIG. 5.—C_{21} vs. (*a*) L_X and (*b*) L_X/L_B for the 39 systems with well-determined C_{21} colors. There are weak but statistically significant trends toward higher C_{21} with higher L_X and L_X/L_B.

3.2.2. *The S0 Galaxies*

There are also 74 S0 galaxies in our sample. For these galaxies the results of the correlation tests (Table 2C) indicate that L_X is strongly correlated with L_B. The regression analyses are given in Table 3C. The L_X-L_X/L_B correlation is strongly upheld (Table 2C). The results from the various regression methods are given in Table 3C. The results for both the slopes and the zero points are statistically indistinguishable from those for the elliptical galaxies, although the zero points for the S0 galaxies are consistently smaller than those for the ellipticals. The data, along with the regression lines, are shown in Figure 7. Partial rank analysis of this sample confirms the correlations found in the bivariate analysis and shows no evidence of any L_B-L_X/L_B correlation for the S0 sample (see Table 4B).

As for the E galaxies, the correlation between C_{21} and L_X and L_X/L_B is weaker for the S0 galaxies only than for the full sample (see Table 5). Still, despite a fairly small number of objects (only 15), the correlation with L_X is at the 1%–2% level. It thus appears from this small sample that the relationship between X-ray emission and C_{21} is a function of morphological type, with a stronger correlation found for the S0 than for the E galaxies. The results of the partial rank analysis (see Table 4B) support this conclusion. The sample sizes make this finding tentative at best, but interesting nonetheless. This could be a consequence of S0 galaxies being less X-ray–luminous than E galaxies on average (see § 3.2.3 below). As noted above, recent *ROSAT* results indicate that soft excesses are more significant in less X-ray–luminous galaxies (e.g., Fabbiano et al. 1994).

3.2.3. *Comparison of the E and S0 Samples*

Another way of searching for potential differences between the E and the S0 galaxies is to compare the distribution functions (DFs) of each sample for the various observables. The integral Kaplan-Meier (K-M; see Feigelson & Nelson 1985) DFs of L_B for the E and S0 samples are shown in Figure 8*a*. The mean values are given in Table 6. These values differ by 1.9 σ, the E galaxies being more luminous, on average, than the S0s (consistent with the lower zero points in the fits for the S0s noted above). The results of a variety of two-sample tests (discussed in Feigelson & Nelson 1985 and LaValley et al. 1992), shown in Table 6, indicate that the null hypothesis (that the two samples are drawn from the same distribution) is supported at roughly the 2% level at most. This is consistent with existing studies of field and cluster luminosity function studies of E and S0 galaxies, as reviewed by Binggeli, Sandage, & Tammann (1988).

The difference between the elliptical and the S0 galaxies becomes more clear upon examining the DFs of the X-ray luminosity. The integral K-M DFs of L_X for the E and S0 galaxies

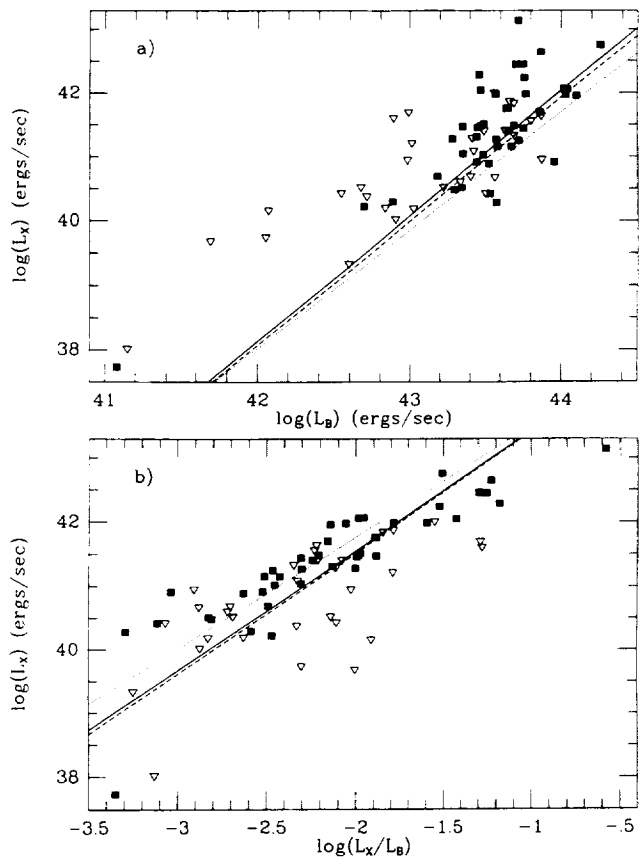

FIG. 6.—L_X vs. (*a*) L_B and (*b*) L_X/L_B for the E galaxies only. Symbols and line coding as in Fig. 2.

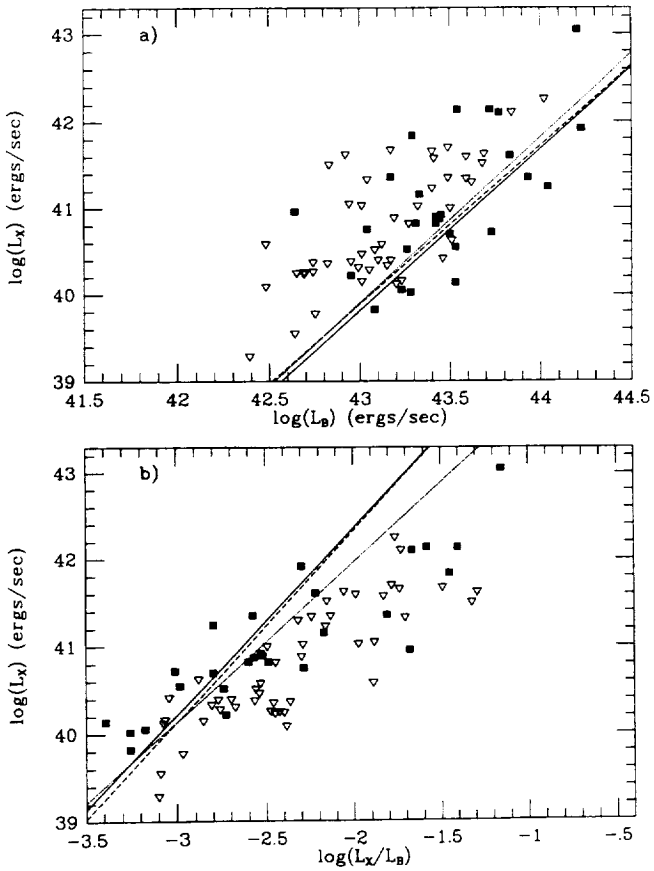

FIG. 7.—L_X vs. (*a*) L_B and (*b*) L_X/L_B for the S0 galaxies only. Symbols and line coding as in Fig. 1.

are shown in Figure 8*b*. The mean values for the two samples are given in Table 6. They differ by 2.8 σ, in the sense that the E galaxies tend to be more X-ray–luminous than the S0s. As the X-ray DFs are substantially more discrepant than the optical DFs, it is unlikely that the difference is wholly the result of a bias in our sample toward optically more luminous elliptical galaxies. As shown in Table 6, the two-sample tests uphold the difference between the samples, with probability $P = 0.0004$–0.0016 that the null hypothesis is upheld. Extending this comparison to the DFs of L_X/L_B argues more strongly that this difference is real. The DFs are shown in Figure 8*c*. The mean values (see Table 6) are distinct at the 3.5 σ level, in the sense that E galaxies tend to have higher X-ray luminosity per unit optical luminosity than do S0 galaxies. This difference is supported by the two-sample tests, which give $P = 0.0005$–0.0012 that the null hypothesis is upheld. Given the results of the regression analysis above, it appears that the slopes of the L_X-L_B relationships are the same for E and S0 galaxies, but that the S0 galaxies are systematically shifted to lower X-ray luminosities than the ellipticals.

Our conclusion that the DF of L_X/L_B is clearly shifted to higher values for the E galaxies compared to the S0s is at odds with the conclusion of Bregman et al. (1992), who found no differences in the X-ray properties of their E and S0 samples. However, they tested for differences in the DFs of R_{ex}, where $R_{ex} = L_X/L_X(\text{best fit})$, and $L_X(\text{best fit}) \propto L_B^{1.75}$. This approach reduces the intrinsic difference between the samples. Moreover, Bregman et al. interpret their results in terms of a cooling flow model with an intrinsic underlying $L_X \propto L_B^{1.7}$ scaling (see also Trinchieri & Fabbiano 1985). However, both the large scatter in this correlation (see Fabbiano 1989) and the luminosity dependence we find for the power-law exponent (see

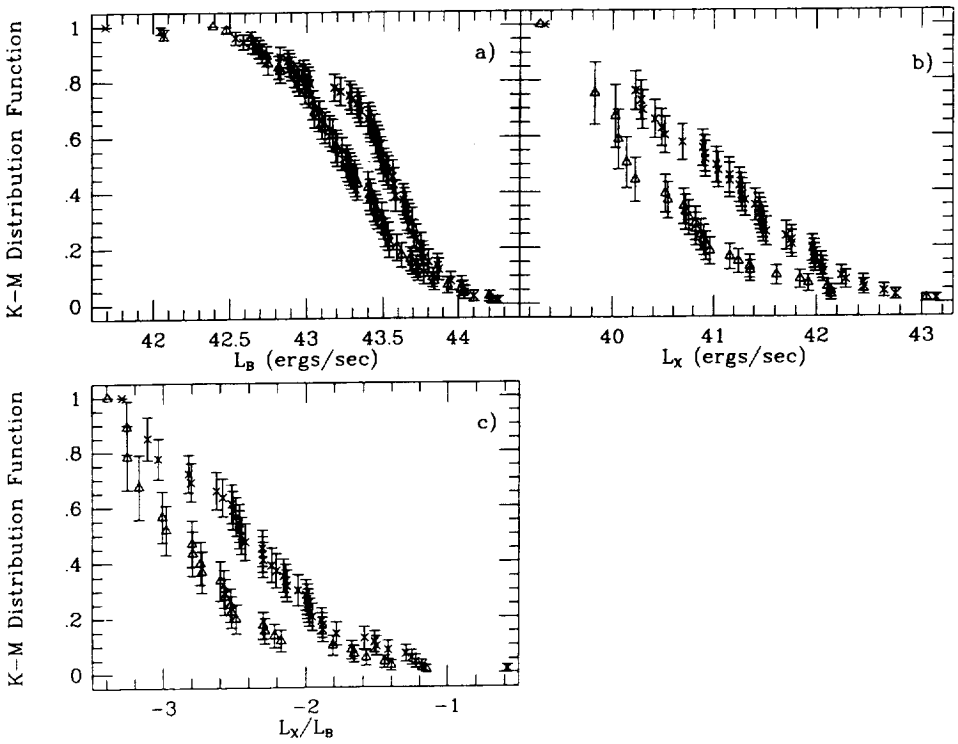

FIG. 8.—Integral K-M DFs for our samples of E and S0 galaxies. The Local Group dE galaxies have not been included. Crosses mark E galaxies; triangles, S0 galaxies. Error bars are 1 σ. (*a*) DFs of L_B. (*b*) DFs of L_X. (*c*) DFs of L_X/L_B.

TABLE 6

COMPARISON BETWEEN E AND S0 SAMPLES

Parameter	Elliptical[a] Sample Size	S0[a] Sample Size	Difference (σ)	Gehan Permutation[b]	Gehan Hypergeometric	logrank	Peto-Peto	Peto-Prentice
L_B	43.403 ± 0.057 (N = 72)	43.262 ± 0.047 (N = 74)	1.9	2.774 (0.0055)	2.794 (0.0052)	2.313 (0.0207)	2.313 (0.0207)	... ...
L_X	40.836 ± 0.138 (N = 72)	40.303 ± 0.130 (N = 74)	2.8	3.525 (0.0004)	3.546 (0.0004)	3.155 (0.0016)	3.469 (0.0005)	3.493 (0.0005)
L_X/L_B	−2.425 ± 0.082 (N = 72)	−2.813 ± 0.076 (N = 74)	3.5	3.349 (0.0008)	3.361 (0.0008)	3.239 (0.0012)	3.443 (0.0006)	3.463 (0.0005)
L_{12}	42.164 ± 0.091 (N = 62)	42.018 ± 0.129 (N = 70)	0.9	0.123 (0.9018)	0.124 (0.9015)	0.726 (0.4676)	0.475 (0.6349)	0.456 (0.6481)
L_{12}/L_B	−1.140 ± 0.046 (N = 62)	−1.025 ± 0.060 (N = 70)	1.5	2.109 (0.0349)	2.103 (0.0354)	1.142 (0.2535)	1.801 (0.0717)	1.810 (0.0702)
L_{100}	41.832 ± 0.105 (N = 62)	42.006 ± 0.111 (N = 71)	1.1	1.638 (0.1015)	1.633 (0.1026)	0.853 (0.3938)	1.446 (0.1481)	1.442 (0.1493)
L_{100}/L_B	−1.604 ± 0.094 (N = 62)	−1.254 ± 0.102 (N = 71)	2.5	2.939 (0.0033)	2.940 (0.0033)	2.295 (0.0217)	2.817 (0.0048)	2.846 (0.0044)
L_6	35.964 ± 0.228 (N = 69)	35.123 ± 0.238 (N = 62)	2.6	2.264 (0.0236)	2.262 (0.0237)	1.786 (0.0742)	2.146 (0.0319)	2.137 (0.0326)
L_6/L_B	−7.454 ± 0.199 (N = 69)	−8.038 ± 0.206 (N = 62)	2.0	1.916 (0.0553)	1.913 (0.0557)	1.361 (0.1735)	1.774 (0.0761)	1.775 (0.0759)

[a] The first row of each pair of values in these columns gives the mean value of the DF for either the E or the S0 sample. The second gives the number of objects in the sample.

[b] The first row of each pair of values in these columns gives the test score for the comparison of the E and S0 samples. The second row gives the probability (in parentheses) that the two samples are drawn from the same parent distribution.

§ 3.1.2 above) suggest that more complex explanations (e.g., Ciotti et al. 1991) of the L_X-L_B diagram are required.

We suggest that the likely cause for this is the influence of the disk in S0 galaxies. The initial mechanism for the heating of gas from photospheric to coronal temperatures in early-type galaxies is simple virial heating, due to the velocity dispersion of the stars in the galaxy. Because a large fraction of the internal energy in S0 galaxies is due to ordered rotation, this heating mechanism will be significantly suppressed. Furthermore, again due to the influence of the disk, the shape of the central potential well is significantly shallower for an S0 galaxy of a given mass than for an elliptical of comparable mass (Binney & Tremaine 1987, §§ 2.1 and 2.6).

4. THE RELATIONSHIP OF L_X WITH OTHER ISM TRACERS

As noted in § 1, the classic problem of what has become of the ISM in early-type galaxies has, in general, been answered by the discovery of X-ray luminous halos of material associated with, at least, the most luminous early-type galaxies. The physical details controlling whether a galaxy can retain its ISM as an X-ray halo are a matter of current vigorous theoretical debate (e.g., Ciotti et al. 1991; David, Forman, & Jones 1991; Bertin, Pignatelli, & Saglia 1993). Our sample is large enough that we can address the issue of relationships between various phases of the ISM in early-type galaxies. The largest and most homogeneous comparison sample is drawn from the *IRAS* data. Large but more heterogeneous samples can be constructed with radio continuum and H I data from the literature.

This analysis is similar in scope to that presented by Roberts et al. (1991) and Bregman et al. (1992), but uses an explicitly X-ray–selected sample, and differs substantially in analytic approach. We thus believe the two studies complement each other very usefully.

4.1. L_X *versus* 12 μm *Data*

4.1.1. *The Full Sample*

The available *IRAS* 12 μm data for the *Einstein* sample are presented in Table 1. They are taken mainly from the work of Knapp et al. (1989), supplemented by a number of other sources. There are data for a total of 134 of the 148 galaxies in the *Einstein* sample. The 12 μm flux from early-type galaxies has typically been ascribed to either photospheric emission or emission from dust created in outer atmospheres of red giants (e.g., Jura et al. 1987; Knapp, Gunn, & Wynn-Williams 1992). Given the ostensibly simple stellar populations of early-type galaxies, one would thus expect $\log(L_{12})$ to show a strong, linear, slope 1 correlation with $\log(L_B)$. This expectation is, in fact, confirmed by our analysis (see Tables 2A and 3A). The fit lines are displayed with the data in Figure 9*a*.

Naively, one would thus expect the relationship between L_X and L_{12} to be similar to that found above between L_X and L_B. The results of the experiment are, however, ambiguous. The two applicable correlation tests for doubly censored samples both indicate that L_X is strongly correlated with L_{12} (see Table 2A). The Schmitt's regression is given in Table 3A. The data and the fit line are shown in Figure 9*b*. If the slope of the L_B-L_{12} relationship is exactly unity, then L_X should scale the same with both L_B and L_{12}. An examination of Table 3A shows this to be ruled out at the 2.7 σ level ($\Delta_{m,2} = 0.49 \pm 0.18$). If one

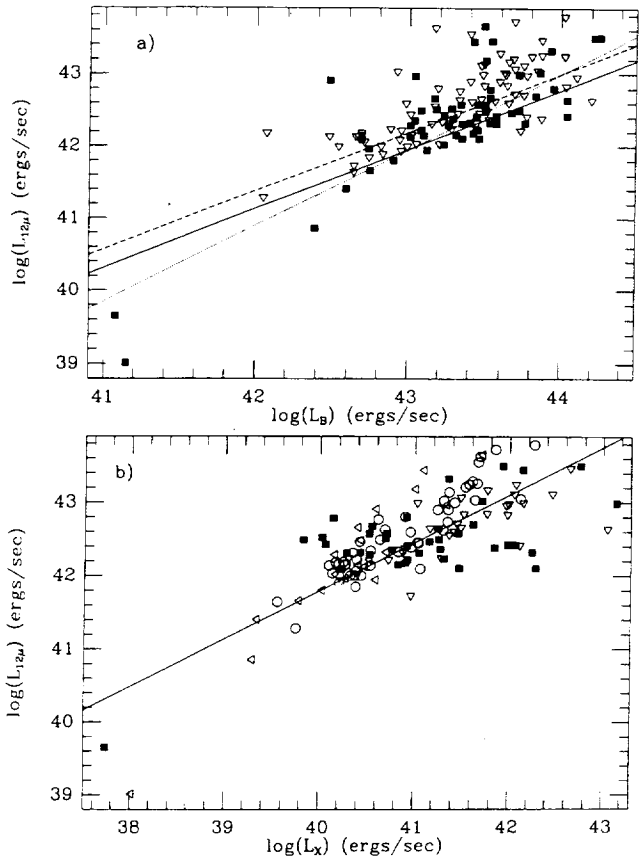

FIG. 9.—L_{12} vs. (*a*) L_B and (*b*) L_X for our sample with 12 μm *IRAS* data. Symbols and line coding as in Fig. 2. Additionally, open left-pointing triangles are 3 σ X-ray upper limits and 12 μm detections, and open circles are 3 σ upper limits in both X-rays and 12 μm. The fit displayed in (*b*) is from Schmitt's method for the sample without the Local Group dE galaxies (*solid line*).

takes the slopes from Schmitt's regression of L_B against L_{12} at face value, then the expected slope for the relationship between L_X and L_{12} would be 1.92 ± 0.16. These differ from the actual values determined at the 2.0 σ level ($\Delta_{m,A} = 0.39 \pm 0.20$). To explore this problem further, we have searched for trends between L_{12}/L_B and L_B, L_X, and L_X/L_B. In no case do we find any evidence for such trends (see Table 2A).

This discrepancy may be no more than a statistical fluke. It may also be driven by a systematic effect, such as the use of unmatched apertures for the various flux measurements, as discussed in Jura et al. (1987) and Knapp et al. (1992). However, we argue that it is likely to be real, based on evidence (see § 4.1.2 below) that the discrepancy is driven by a difference in the 12 μm properties of the E and S0 galaxies in our sample. The results of the partial rank analysis on L_B-L_X-L_X/L_B-L_{12} are presented in Table 7A. For all combinations of variables that include L_B, we find strong correlation between L_B and L_{12}. The only case in which we find evidence for correlation between L_X and L_{12} is the three-way sample not including L_B. It appears that the bivariate L_X-L_{12} correlation is driven mainly by the mutual dependence of both these parameters on L_B.

There is no evidence for correlation between L_{12} and C_{21} for the 38 galaxies with well-determined C_{21} values and *IRAS* measurements (see Table 5). This conclusion is fully supported by a partial rank analysis including these variables (see Table 7A).

4.1.2. *Type Separation*

We have analyzed the data for E and S0 galaxies separately to search for possible systematic differences between the galaxy types. Knapp et al. (1989) found significant differences in the *IRAS* 60 and 100 μm (FIR) properties for E and S0 galaxies, although there was no significant difference between the two classes in the *IRAS* 12 and 25 μm (mid-IR[MIR]) data. We have a sample of 62 elliptical galaxies. Our analysis for this sample is given in Tables 2B and 3B. We find no compelling evidence for any correlations with L_{12}/L_B. The L_B-L_{12} and L_X-L_{12} results are shown in Figures 10*a* and 11*a*. A partial rank analysis on L_B-L_X-L_X/L_B-L_{12} for the E sample gives results fully consistent with those for the full sample (see Table 7B). A partial rank analysis on L_B-L_X-L_X/L_B-L_{12}-C_{21} on the E subsamples reveals no trends not found for the full sample.

There are 70 S0 galaxies in the 12 μm sample. Our bivariate analysis for this sample is given in Tables 2C and 3C. There is no evidence for correlations between L_{12} and L_X/L_B, or between L_{12}/L_B and any tested quantity for the S0 sample. The fits and data for the L_{12}-L_B relationships for the S0 galaxies are shown in Figure 10*b*. Those for the L_{12}-L_X relation are displayed in Figure 11*b*. The integral K-M DFs for the 12 μm luminosities and the 12 μm to *B* ratio are shown in Figure 12. The mean values, along with the results of the two-sample tests, are given in Table 6. In agreement with earlier work by Knapp et al. (1989), we find no statistically significant difference in the 12 μm properties of E and S0 galaxies in our sample. We do, however, find the S0s to have marginally higher (at the 1.5 σ level) L_{12}/L_B than do the Es. A partial rank analysis on L_B-L_X-L_X/L_B-L_{12} for the S0 sample yields qualitatively similar results to those for the E sample: The weight of evidence is for an underlying L_B-L_{12} relation driving the bivariate correlation between L_{12} and L_X (see Table 7B). Having only 14 objects for a L_B-L_X-L_X/L_B-L_{12}-C_{21} partial rank analysis, we have not conducted this test.

We note that the ~ 2 σ discrepancy between the expected and derived slopes of the L_X-L_{12} relationship for the full sample, discussed in § 4.1.1 above, appears to be entirely driven by the S0 galaxies (see Tables 3B, 3C, and 6). There is growing evidence that S0 galaxies are more able to retain significant quantities of "spiral-like" ISM than are ellipticals (e.g., Thronson et al. 1989; Knapp et al. 1989). Many S0 galaxies are also known to be undergoing current massive star formation (Pogge & Eskridge 1987, 1993). We thus speculate that a possible cause for the discrepancy in the slope of the L_X-L_{12} relationship for the S0 galaxies is due to a significant contribution from dust heated in star-forming regions. While our results are consistent with this interpretation, we caution the reader that we find no difference between the two samples at greater than the 2 σ level. However, additional support for this hypothesis is found in our analysis of optical-IR colors for our sample (§ 4.3 below).

4.2. L_X *versus* 100 μm *Data*

The *IRAS* 100 μm data for 135 of the galaxies in the *Einstein* sample are also given in Table 1, again mainly taken from Knapp et al. (1989) with some additional sources. There are

TABLE 7A

PARTIAL SPEARMAN RANK ANALYSIS: *IRAS* 12 MICRON PROPERTIES, E+S0 SAMPLES

Test Pair	Held Parameters	Size	Partial Spearman Rank	Probability
L_B-L_X	L_{12}	132	0.625	<0.005
	L_X/L_B, L_{12}	132	0.531	<0.005
	L_{12}, C_{21}	38	0.430	<0.005
	L_X/L_B, L_{12}, C_{21}	38	0.855	<0.005
L_B-L_X/L_B	L_{12}	132	0.392	<0.005
	L_X, L_{12}	132	0.043	0.316
	L_{12}, C_{21}	38	0.026	>0.400
	L_X, L_{12}, C_{21}	38	−0.818	<0.005
L_B-L_{12}	L_X	132	0.304	<0.005
	L_X/L_B	132	0.437	<0.005
	L_X, L_X/L_B	132	0.305	<0.005
	C_{21}	38	0.515	<0.005
	L_X, C_{21}	38	0.495	<0.005
	L_X/L_B, C_{21}	38	0.515	<0.005
	L_X, L_X/L_B, C_{21}	38	0.208	0.120
L_B-C_{21}	L_{12}	38	0.197	0.129
	L_X, L_{12}	38	−0.017	>0.400
	L_X/L_B, L_{12}	38	0.173	0.168
	L_X, L_X/L_B, L_{12}	38	−0.108	0.268
L_X-L_X/L_B	L_{12}	132	0.583	<0.005
	L_B, L_{12}	132	0.471	<0.005
	L_{12}, C_{21}	38	0.879	<0.005
	L_B, L_{12}, C_{21}	38	0.962	<0.005
L_X-L_{12}	L_B	132	0.116	0.095
	L_X/L_B	132	0.347	<0.005
	L_B, L_X/L_B	132	0.118	0.093
	C_{21}	38	0.179	0.156
	L_B, C_{21}	38	−0.072	0.340
	L_X/L_B, C_{21}	38	0.485	<0.005
	L_B, L_X/L_B, C_{21}	38	0.068	0.351
L_X-C_{21}	L_{12}	38	0.453	<0.005
	L_B, L_{12}	38	0.417	0.006
	L_X/L_B, L_{12}	38	0.264	0.063
	L_B, L_X/L_B, L_{12}	38	0.229	0.095
L_X/L_B-L_{12}	L_B	132	0.026	0.384
	L_X	132	−0.021	>0.400
	L_B, L_X	132	−0.033	0.357
	C_{21}	38	−0.095	0.289
	L_B, C_{21}	38	−0.094	0.292
	L_X, C_{21}	38	−0.466	<0.005
	L_B, L_X, C_{21}	38	−0.091	0.301
L_X/L_B-C_{21}	L_{12}	38	0.385	0.010
	L_B, L_{12}	38	0.375	0.014
	L_X, L_{12}	38	−0.056	0.376
	L_B, L_X, L_{12}	38	−0.120	0.246
L_{12}-C_{21}	L_B	38	−0.039	>0.400
	L_X	38	−0.015	>0.400
	L_X/L_B	38	0.105	0.268
	L_B, L_X	38	−0.005	>0.400
	L_B, L_X/L_B	38	0.000	>0.400
	L_X, L_X/L_B	38	−0.039	>0.400
	L_B, L_X, L_X/L_B	38	−0.016	>0.400

two main sources of 100 μm emission recognized in normal spiral galaxies: emission from cirrus, and emission from dust heated by nearby regions of massive star formation (e.g., Soifer et al. 1989). In either case, the dominant source of 100 μm emission from late-type galaxies clearly appears to be interstellar dust. The relative amount of dust per unit stellar mass is ostensibly much smaller in early-type galaxies than it is in late-type galaxies. To the extent that this dust is traced by FIR emission, the work of Knapp et al. (1989) demonstrates this quite well. They report detections at 100 μm for only ~45% of ellip-

TABLE 7B

PARTIAL SPEARMAN RANK ANALYSIS: *IRAS* 12 MICRON PROPERTIES, SEPARATE E AND S0 SAMPLES

Test Pair	Held Parameters	Sample	Size	Partial Spearman Rank	Probability
L_B-L_X	L_{12}	E	62	0.543	<0.005
	L_{12}	S0	70	0.553	<0.005
	L_X/L_B, L_{12}	E	62	0.471	<0.005
	L_X/L_B, L_{12}	S0	70	0.475	<0.005
L_B-L_X/L_B	L_{12}	E	62	0.308	0.008
	L_{12}	S0	70	0.326	<0.005
	L_X, L_{12}	E	62	0.018	>0.400
	L_X, L_{12}	S0	70	0.064	0.305
L_X-L_{12}	L_X	E	62	0.317	0.007
	L_X	S0	70	0.302	0.006
	L_X/L_B	E	62	0.466	<0.005
	L_X/L_B	S0	70	0.418	<0.005
	L_X, L_X/L_B	E	62	0.318	0.007
	L_X, L_X/L_B	S0	70	0.303	0.007
L_X-L_X/L_B	L_{12}	E	62	0.543	<0.005
	L_{12}	S0	70	0.508	<0.005
	L_B, L_{12}	E	62	0.470	<0.005
	L_B, L_{12}	S0	70	0.416	<0.005
L_X-L_{12}	L_B	E	62	0.200	0.064
	L_B	S0	70	0.132	0.152
	L_X/L_B	E	62	0.398	<0.005
	L_X/L_B	S0	70	0.326	<0.005
	L_B, L_X/L_B	E	62	0.183	0.084
	L_B, L_X/L_B	S0	70	0.129	0.158
L_X/L_B-L_{12}	L_B	E	62	0.083	0.263
	L_B	S0	70	0.034	0.391
	L_X	E	62	−0.009	>0.400
	L_X	S0	70	−0.005	>0.400
	L_B, L_X	E	62	−0.014	>0.400
	L_B, L_X	S0	70	−0.024	>0.400

tical galaxies. The percentage for S0 galaxies is higher, but still only 68%. For comparison, Bothun, Lonsdale, & Rice (1989) find that more than 90% of UGC spirals with $m_B \leq 13.5$ are detected by *IRAS* in the FIR. One currently favored hypothesis is that the material responsible for FIR emission in early-type galaxies is accreted material (e.g., Forbes 1991). If this is the case, and the X-ray emission is due to a gravitationally bound thermal plasma, there should not necessarily be any relationship between L_X and L_{100}, the 100 μm luminosity. Alternatively, the dust could be intrinsic to the host galaxy, but interaction with the X-ray plasma and interstellar radiation field (ISRF) could then evaporate the grains (e.g., Boulanger et al. 1988; Knapp et al. 1992). How this would manifest itself in terms of global luminosity correlations would depend on the balance between the grain formation (or accretion) and evaporation timescales. The correlation tests uphold the null hypothesis at the $\approx$5% level (Table 2A). Also, we find no correlation between L_{100} and either L_X/L_B (Table 2A) or C_{21} (Table 5), and no correlations of L_{100}/L_B with any tested parameter (Table 2A).

The results of a partial rank analysis on L_B-L_X-L_X/L_B-L_{100} confirm that there is no significant correlation between L_X and L_{100} for our sample. They do reveal a correlation between L_B and L_{100} (see Table 8A). We also tested the combination L_B-L_X-L_X/L_B-L_{100}-C_{21}. No new trends were uncovered by this analysis.

We now consider the L_X-L_{100} relations for the E and S0 subsamples. There are 62 elliptical galaxies in the subsample. The data are shown in Figure 13. As for the full sample, there is no significant correlation between L_{100} and either L_X or L_X/L_B, and none between L_{100}/L_B and L_B, L_X, or L_X/L_B (Table 2B). A four-component partial rank analysis on L_B-L_X-L_X/L_B-L_{100} for the E galaxies is similar to that for the full sample. The one significant difference is that the (*weak*) evidence for an L_X-L_{100} trend in the full sample disappears completely when only the E galaxies are considered. Adding L_{12} to the partial rank analysis, we note that there is no evidence for a correlation between L_{12} and L_{100} for the E galaxies (such a trend *does* appear for the full sample). Thus, for the E galaxies alone, the sources of 12 and 100 μm radiation are apparently uncoupled. These results are shown in Table 8B.

Turning to the S0 sample (N = 71), we find somewhat different results (see Table 2C). Taking the more pessimistic of the correlation test results, there is evidence for a correlation between L_X and L_{100} for the S0 sample at the $\approx$2.3 σ level (although there is no evidence for a correlation between L_{100} and L_X/L_B). Accepting the relationship between L_{100} and L_X as real, we derive a regression line from Schmitt's method

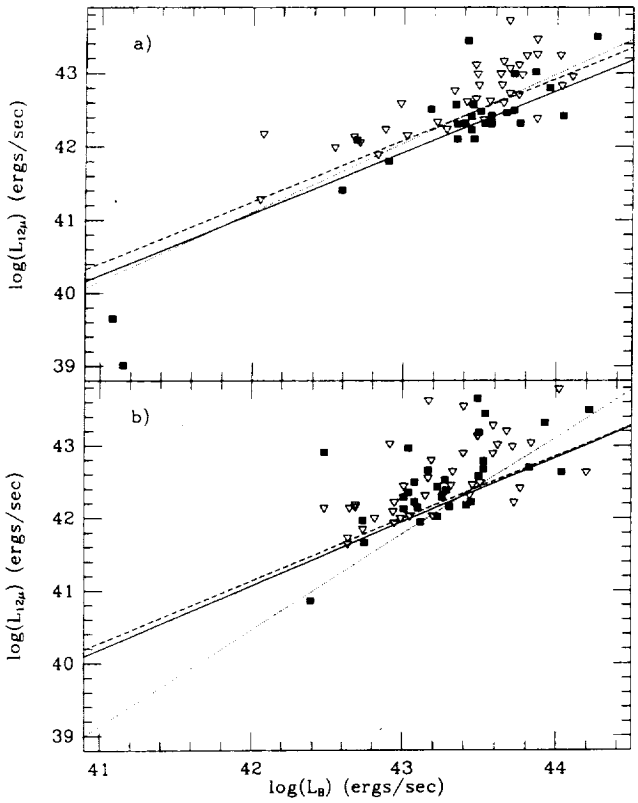

FIG. 10.—L_{12} vs. L_B for (*a*) E and (*b*) S0 galaxies in our sample with 12 μm *IRAS* data. Symbols and line coding as in Fig. 2.

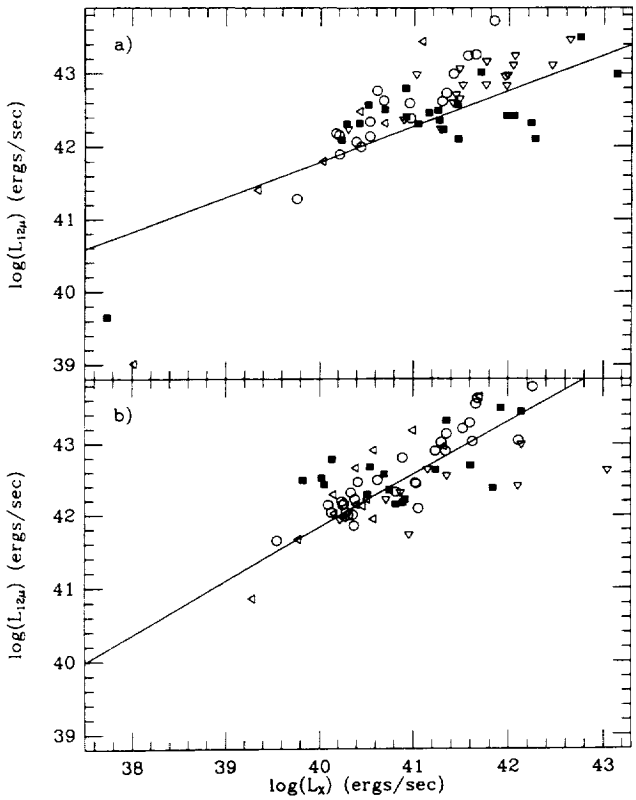

FIG. 11.—L_{12} vs. L_X for (*a*) E and (*b*) S0 galaxies in our sample with 12 μm *IRAS* data. Symbols and line coding as in Fig. 9.

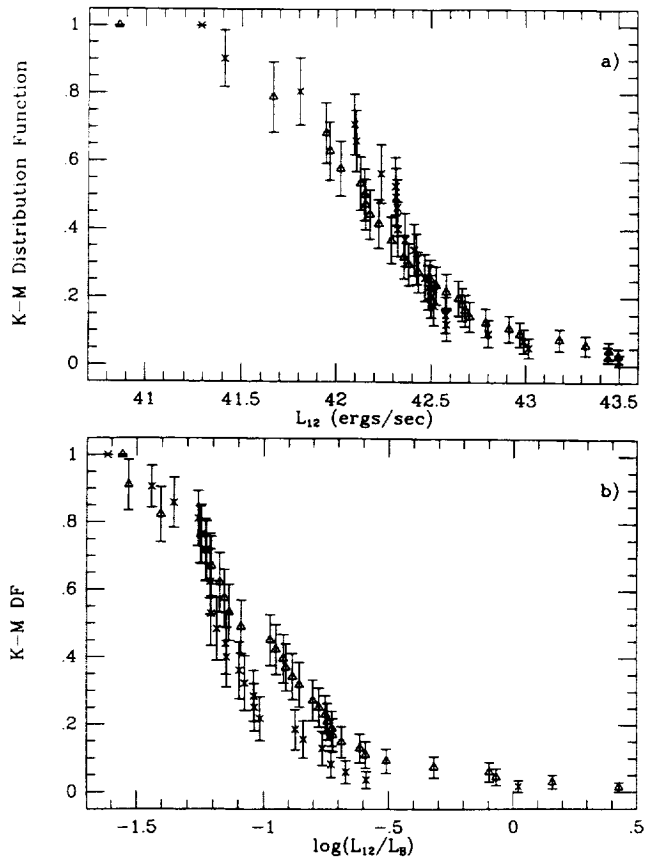

FIG. 12.—Integral K-M DFs of (*a*) L_{12} and (*b*) L_{12}/L_B for our samples of E and S0 galaxies. Symbols and error bars as in Fig. 8.

(Table 3C and Figure 13). The slope of this relationship (0.85 ± 0.23) does not differ significantly from unity. Thus, if the effect is real, it is an example of a "bright things are bright" relationship and does not necessarily indicate any direct connection between the X-ray– and FIR-emitting materials. We find no evidence of any trend with L_{100}/L_B (Table 2C). A partial rank analysis of L_B-L_X-L_X/L_B-L_{100} on just the S0 galaxies (Table 8B) suggests that the bivariate L_X-L_{100} relationship is driven by the mutual dependence of both these parameters on L_B. Including L_{12} in the partial rank analysis, we find that the L_{12}-L_{100} correlation found for the full sample (Table 8A) is driven entirely by the S0 galaxies. Indeed, there is a *stronger* correlation between L_{12} and L_{100} for the S0 sample than between L_B and L_{100}. Thus, in distinction to the E galaxies, the 12 μm and 100 μm emission from S0 galaxies do appear coupled for our sample.

A comparison of the 100 μm properties of the two subsamples reveals that the L_{100} DFs for the E and S0 galaxies are not significantly different, while the S0 galaxies tend to have larger L_{100}/L_B than the E galaxies at the 2.5 σ level. This is quite in keeping with earlier results (e.g., Knapp et al. 1989) showing S0 galaxies to have relatively more FIR emission than E galaxies. These results are given in Table 6 and displayed in Figure 14.

A number of physical factors may be involved in causing the differences between the E and S0 samples. First, it appears that

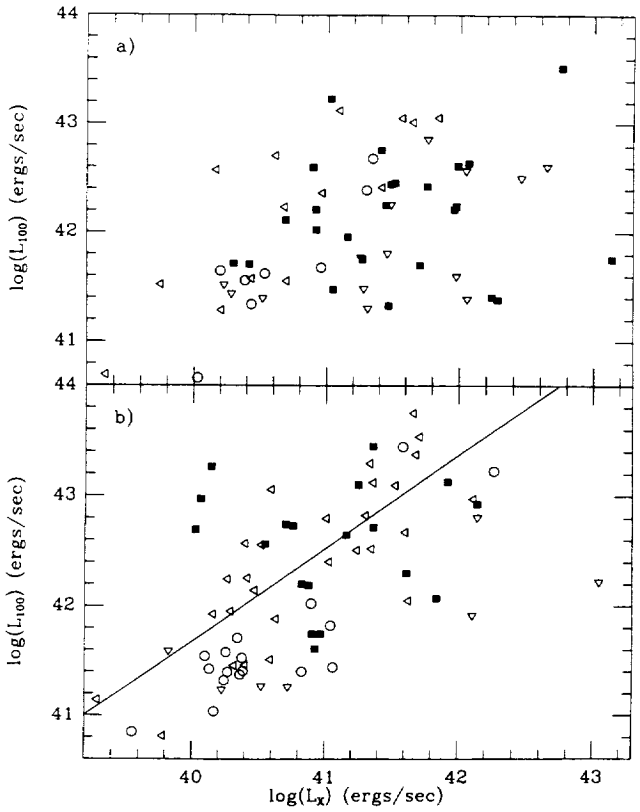

FIG. 13.—L_{100} vs. L_X for (*a*) E and (*b*) S0 galaxies in our sample with *IRAS* 100 μm data. Symbols and line coding as in Fig. 9.

a larger fraction of the X-ray emission from S0 galaxies is due to the same sort of stellar X-ray sources that provide the X-ray emission from spiral galaxies (Kim et al. 1992b), for which there is known to be a strong correlation between X-ray and 100 μm emission (Fabbiano et al. 1988). Second, while the FIR emission from elliptical galaxies may be due to accreted material (although the L_B-L_{100} correlation for the E galaxies shown in Table 8B argues against this), the evidence that the cool ISM in S0 galaxies is accreted is far less convincing (e.g., Jura 1986; Thronson & Bally 1987; Bertola et al. 1988; Marston 1988; Véron-Cetty & Véron 1988; Kim 1989; Knapp et al. 1989; Eskridge & Pogge 1991; Goudfrooij 1991; Shields 1991). Instead, it appears that a significant fraction of the FIR emission from S0 galaxies is due to radiation from dust intrinsic to the disk.

4.3. *L_X versus IRAS Colors*

We have examined our data to see whether there are any significant trends between X-ray emission and *IRAS* colors. A number of the possible FIR colors have been used by previous authors (e.g., Helou 1986; Soifer et al. 1987; Soifer et al. 1989; Rowan-Robinson & Crawford 1989; Helou, Ryter, & Soifer 1991) to generate diagnostic diagrams for separating AGNs, starbursts, and ISM heated by an ambient ISRF. Figure 15 shows histograms of the same flux ratios for our sample as are used by Soifer et al. (1989, their Fig. 2) for the *IRAS* Bright Galaxy Sample (IBGS). This sample is dominated by late-type

TABLE 8A

PARTIAL SPEARMAN RANK ANALYSIS: *IRAS* 100 MICRON PROPERTIES, E+S0 SAMPLES

Test Pair	Held Parameters	Size	Partial Spearman Rank	Probability
L_B-L_X	L_{100}	133	0.686	<0.005
	L_X/L_B, L_{100}	133	0.585	<0.005
	L_{12}, L_{100}	132	0.636	<0.005
	L_X/L_B, L_{12}, L_{100}	132	0.541	<0.005
L_B-L_X/L_B	L_{100}	133	0.444	<0.005
	L_X, L_{100}	133	0.046	0.304
	L_{12}, L_{100}	132	0.401	<0.005
	L_X, L_{12}, L_{100}	132	0.048	0.295
L_B-L_{12}	L_{100}	132	0.374	<0.005
	L_X, L_{100}	132	0.180	0.021
	L_X/L_B, L_{100}	132	0.318	<0.005
	L_X, L_X/L_B, L_{100}	132	0.181	0.021
L_B-L_{100}	L_X	133	0.345	<0.005
	L_X/L_B	133	0.378	<0.005
	L_{12}	132	0.198	0.013
	L_X, L_X/L_B	133	0.346	<0.005
	L_X, L_{12}	132	0.248	<0.005
	L_X/L_B, L_{12}	132	0.219	0.007
	L_X, L_X/L_B, L_{12}	132	0.249	<0.005
L_X-L_X/L_B	L_{100}	133	0.609	<0.005
	L_B, L_{100}	133	0.466	<0.005
	L_{12}, L_{100}	132	0.583	<0.005
	L_B, L_{12}, L_{100}	132	0.464	<0.005
L_X-L_{12}	L_{100}	132	0.367	<0.005
	L_B, L_{100}	132	0.164	0.033
	L_X/L_B, L_{100}	132	0.305	<0.005
	L_B, L_X/L_B, L_{100}	132	0.154	0.042
L_X-L_{100}	L_B	133	−0.099	0.139
	L_X/L_B	133	0.175	0.023
	L_{12}	132	0.007	>0.400
	L_B, L_X/L_B	133	−0.069	0.224
	L_B, L_{12}	132	−0.153	0.043
	L_X/L_B, L_{12}	132	0.015	>0.400
	L_B, L_X/L_B, L_{12}	132	−0.123	0.086
L_X/L_B-L_{12}	L_{100}	132	0.215	0.007
	L_B, L_{100}	132	0.059	0.254
	L_X, L_{100}	132	−0.012	>0.400
	L_B, L_X, L_{100}	132	−0.020	>0.400
L_X/L_B-L_{100}	L_B	133	−0.081	0.190
	L_X	133	−0.025	0.389
	L_{12}	132	−0.009	>0.400
	L_B, L_X	133	−0.039	0.331
	L_B, L_{12}	132	−0.096	0.148
	L_X, L_{12}	132	−0.016	>0.400
	L_B, L_X, L_{12}	132	−0.028	0.377
L_{12}-L_{100}	L_B	132	0.358	<0.005
	L_X	132	0.439	<0.005
	L_X/L_B	132	0.466	<0.005
	L_B, L_X	132	0.374	<0.005
	L_B, L_X/L_B	132	0.361	<0.005
	L_X, L_X/L_B	132	0.439	<0.005
	L_B, L_X, L_X/L_B	132	0.373	<0.005

TABLE 8B

PARTIAL SPEARMAN RANK ANALYSIS: *IRAS* 100 MICRON PROPERTIES, SEPARATE E AND S0 SAMPLES

Test Pair	Held Parameters	Sample	Size	Partial Spearman Rank	Probability
L_B-L_X	L_{100}	E	62	0.642	<0.005
	L_{100}	S0	71	0.570	<0.005
	L_X/L_B, L_{100}	E	62	0.557	<0.005
	L_X/L_B, L_{100}	S0	71	0.495	<0.005
	L_{12}, L_{100}	E	62	0.547	<0.005
	L_{12}, L_{100}	S0	70	0.542	<0.005
	L_X/L_B, L_{12}, L_{100}	E	62	0.473	<0.005
	L_X/L_B, L_{12}, L_{100}	S0	70	0.464	<0.005
L_B-L_X/L_B	L_{100}	E	62	0.386	<0.005
	L_{100}	S0	71	0.329	<0.005
	L_X, L_{100}	E	62	0.020	>0.400
	L_X, L_{100}	S0	71	0.054	0.333
	L_{12}, L_{100}	E	62	0.312	0.008
	L_{12}, L_{100}	S0	70	0.322	<0.005
	L_X, L_{12}, L_{100}	E	62	0.023	>0.400
	L_X, L_{12}, L_{100}	S0	70	0.066	0.298
L_B-L_{12}	L_{100}	E	62	0.477	<0.005
	L_{100}	S0	70	0.175	0.080
	L_X, L_{100}	E	62	0.280	0.017
	L_X, L_{100}	S0	70	0.079	0.261
	L_X/L_B, L_{100}	E	62	0.425	<0.005
	L_X/L_B, L_{100}	S0	70	0.151	0.114
	L_X, L_X/L_B, L_{100}	E	62	0.280	0.018
	L_X, L_X/L_B, L_{100}	S0	70	0.080	0.262
L_B-L_{100}	L_X	E	62	0.407	<0.005
	L_X	S0	71	0.370	<0.005
	L_X/L_B	E	62	0.424	<0.005
	L_X/L_B	S0	71	0.440	<0.005
	L_{12}	E	62	0.373	<0.005
	L_{12}	S0	70	0.286	0.009
	L_X, L_X/L_B	E	62	0.407	<0.005
	L_X, L_X/L_B	S0	71	0.369	<0.005
	L_X, L_{12}	E	62	0.380	<0.005
	L_X, L_{12}	S0	70	0.256	0.019
	L_X/L_B, L_{12}	E	62	0.377	<0.005
	L_X/L_B, L_{12}	S0	70	0.280	0.011
	L_X, L_X/L_B, L_{12}	E	62	0.380	<0.005
	L_X, L_X/L_B, L_{12}	S0	70	0.257	0.020
L_X-L_X/L_B	L_{100}	E	62	0.581	<0.005
	L_{100}	S0	71	0.510	<0.005
	L_B, L_{100}	E	62	0.472	<0.005
	L_B, L_{100}	S0	71	0.416	<0.005
	L_{12}, L_{100}	E	62	0.541	<0.005
	L_{12}, L_{100}	S0	70	0.505	<0.005
	L_B, L_{12}, L_{100}	E	62	0.466	<0.005
	L_B, L_{12}, L_{100}	S0	70	0.416	<0.005
L_X-L_{12}	L_{100}	E	62	0.443	<0.005
	L_{100}	S0	70	0.198	0.054
	L_B, L_{100}	E	62	0.203	0.063
	L_B, L_{100}	S0	70	0.123	0.171
	L_X/L_B, L_{100}	E	62	0.377	<0.005
	L_X/L_B, L_{100}	S0	70	0.172	0.085
	L_B, L_X/L_B, L_{100}	E	62	0.186	0.083
	L_B, L_X/L_B, L_{100}	S0	70	0.115	0.189

TABLE 8B—*Continued*

Test Pair	Held Parameters	Sample	Size	Partial Spearman Rank	Probability
L_X-L_{100}	L_B	E	62	−0.124	0.182
	L_B	S0	71	0.028	>0.400
	L_X/L_B	E	62	0.164	0.105
	L_X/L_B	S0	71	0.258	0.018
	L_{12}	E	62	0.103	0.223
	L_{12}	S0	70	0.134	0.146
	L_B, L_X/L_B	E	62	−0.102	0.225
	L_B, L_X/L_B	S0	71	0.025	>0.400
	L_B, L_{12}	E	62	−0.128	0.176
	L_B, L_{12}	S0	70	−0.030	>0.400
	L_X/L_B, L_{12}	E	62	0.090	0.248
	L_X/L_B, L_{12}	S0	70	0.117	0.183
	L_B, L_X/L_B, L_{12}	E	62	−0.107	0.218
	L_B, L_X/L_B, L_{12}	S0	70	−0.019	>0.400
L_X/L_B-L_{12}	L_{100}	E	62	0.252	0.026
	L_{100}	S0	70	0.100	0.216
	L_B, L_{100}	E	62	0.084	0.262
	L_B, L_{100}	S0	70	0.045	0.359
	L_X, L_{100}	E	62	−0.007	>0.400
	L_X, L_{100}	S0	70	−0.002	>0.400
	L_B, L_X, L_{100}	E	62	−0.014	>0.400
	L_B, L_X, L_{100}	S0	70	−0.007	>0.400
L_X/L_B-L_{100}	L_B	E	62	−0.072	0.291
	L_B	S0	71	0.012	>0.400
	L_X	E	62	−0.008	>0.400
	L_X	S0	71	0.022	>0.400
	L_{12}	E	62	0.050	0.351
	L_{12}	S0	70	0.066	0.295
	L_B, L_X	E	62	−0.015	>0.400
	L_B, L_X	S0	71	0.001	>0.400
	L_B, L_{12}	E	62	−0.073	0.290
	L_B, L_{12}	S0	70	−0.030	>0.400
	L_X, L_{12}	E	62	−0.007	>0.400
	L_X, L_{12}	S0	70	−0.002	>0.400
	L_B, L_X, L_{12}	E	62	−0.015	>0.400
	L_B, L_X, L_{12}	S0	70	−0.019	>0.400
L_{12}-L_{100}	L_B	E	62	0.009	>0.400
	L_B	S0	70	0.603	<0.005
	L_X	E	62	0.160	0.114
	L_X	S0	70	0.646	<0.005
	L_X/L_B	E	62	0.210	0.054
	L_X/L_B	S0	70	0.680	<0.005
	L_B, L_X	E	62	0.035	0.393
	L_B, L_X	S0	70	0.602	<0.005
	L_B, L_X/L_B	E	62	0.016	>0.400
	L_B, L_X/L_B	S0	70	0.603	<0.005
	L_X, L_X/L_B	E	62	0.160	0.117
	L_X, L_X/L_B	S0	70	0.646	<0.005
	L_B, L_X, L_X/L_B	E	62	0.035	0.395
	L_B, L_X, L_X/L_B	S0	70	0.602	<0.005

galaxies, many of which are starbursts, are interacting, or have prominent active nuclei. The dotted histograms in Figure 15 are for the IBGS, scaled to our sample size. The distribution of the 60 μm/100 μm ratios peaks at lower values for our sample than for the IBGS. This would appear to indicate overall lower dust temperature in our sample relative to the IBGS, possibly because the dust in our sample is more like Galactic cirrus than like dust heated by H II regions. This is in keeping with the differences in morphology between the two samples. The distributions of the 12 μm/25 μm, 12 μm/60 μm, and 25 μm/60 μm ratios are shifted to larger values for our sample than for the IBGS. This makes sense if the relative contribution of photospheric emission to dust emission in the MIR is greater for our sample than for the IBGS.

Helou et al. (1991) have introduced the Γ parameter [$\Gamma = \nu f_\nu(12)/\mathrm{FIR}$] to be used in conjunction with Θ (the ratio of the 60 μm and 100 μm fluxes) as a diagnostic of the contribution as a function of grain size to the overall *IRAS* flux of a source. They give distributions in this "Γ-Θ" plane for regions associated with Galactic disk stars, Virgo spirals, and the IBGS, and for a sample of "cold" galaxies in their Figure 1. We show the distribution of our sample in the Γ-Θ plane in Figure 16, along

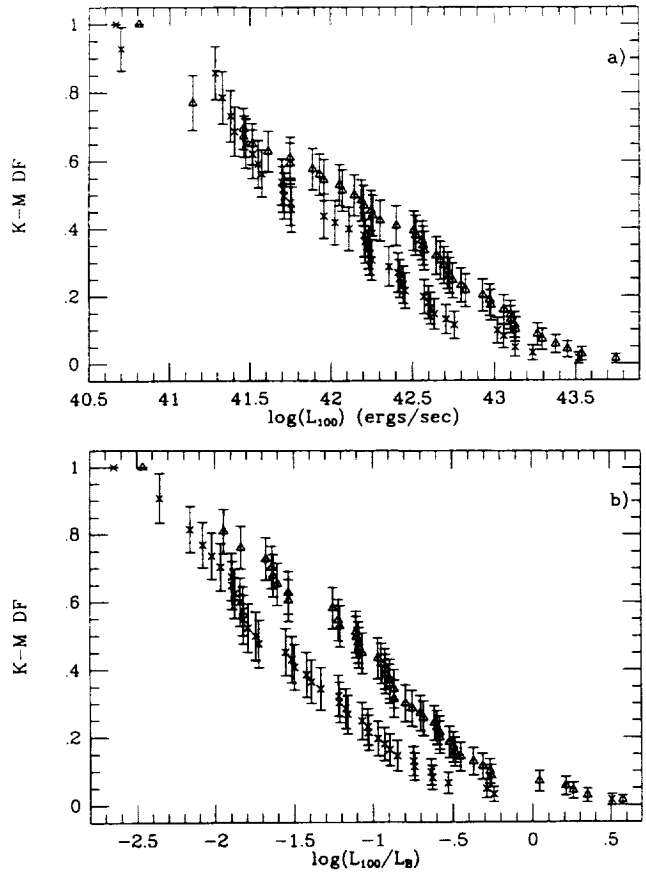

FIG. 14.—Integral K-M DFs of (*a*) L_{100} and (*b*) L_{100}/L_B for our samples of E and S0 galaxies. Symbols and error bars as in Fig. 8.

with outlines of the regions occupied by the various samples from Helou et al. (1991) as labeled in the figure caption. An examination of Figure 16 points out two particularly interesting features. First, the distribution of our sample in Γ goes to far higher values than are found for any of the Helou et al. late-type galaxy or stellar samples. Virtually all the E galaxies are high-Γ objects. Second, while our sample has no objects with Θ as large as the largest values found either in the IBGS or in regions near Galactic stars, it has many objects with Θ-values larger than those found for the cold galaxy sample. The first of these distinctions is reasonably explained by assuming that a significant fraction of the 12 μm flux from our sample comes from stars or AGNs, and by noting that the FIR is typically much lower for early-type galaxies than for spirals (Knapp et al. 1989). It could also be due to a grain-size spectrum strongly skewed to small grains due to efficient sputtering by the harder ISRF of early-type galaxies. The second distinction indicates that, while the overall FIR flux from E/S0 galaxies is not due to emission from dust as warm as that associated with major starbursts, the dust in early-type galaxies is heated as effectively as that in normal spirals.

Returning to the morphological segregation in Figure 16, we note that nearly all the objects that fall into the region occupied by the Virgo spiral sample and the circumstellar ISM are S0 galaxies. There is no evidence for any significant difference in the typical Θ values of the E and S0 galaxies: the separation is entirely due to the S0 galaxies having typically lower Γ-values than the E galaxies. Recalling that we find no compelling evidence for a difference in the 12 μm DFs of the E and S0 galaxies (§ 4.1.2 above), the separation in Γ seems driven by the larger relative amount of FIR radiation from S0s than from Es—a result fully in keeping with the study of Knapp et al. (1989),

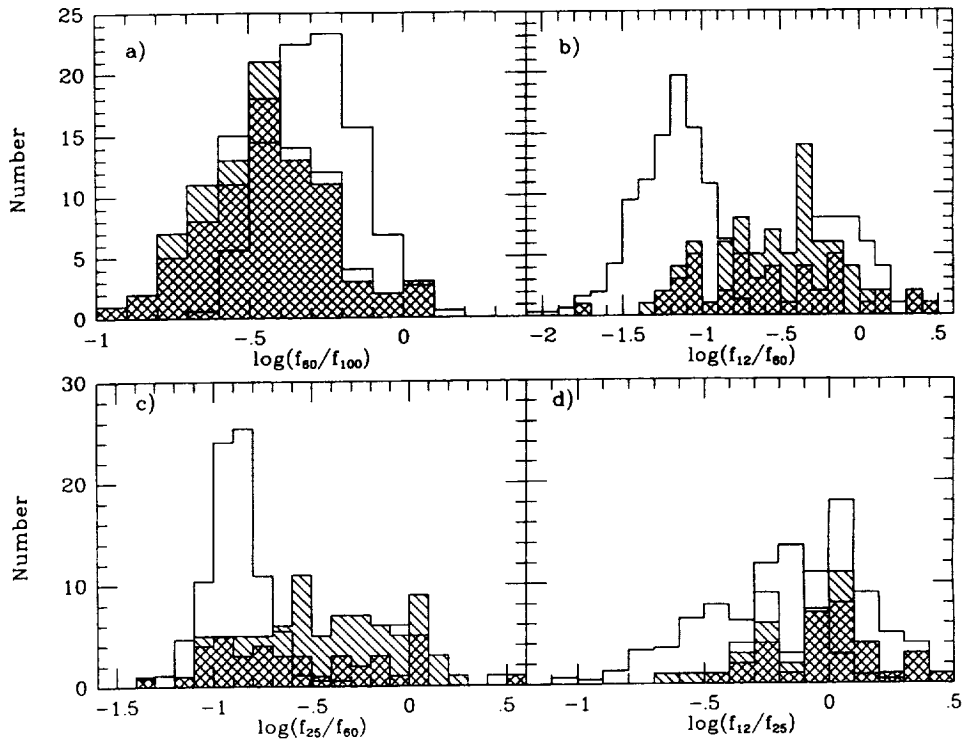

FIG. 15.—Histograms of various infrared colors for our sample, following Soifer et al. (1989). Cross-hatched areas show detections; hatched areas include upper limits; and open areas also include lower limits. Dotted histograms are for the IBGS (Soifer et al. 1989) scaled to our sample size.

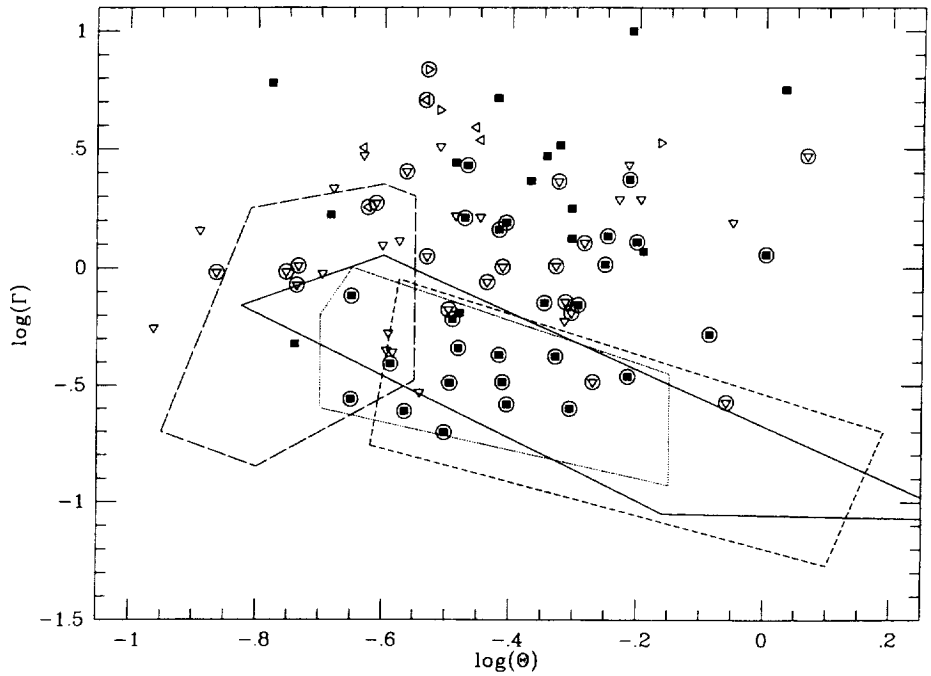

FIG. 16.—"Γ-Θ" plot for our sample, following Helou et al. (1991), showing a significant number of objects with much larger Γ-values than are found for spiral samples. Symbols as in Fig. 9. Circled objects are S0 galaxies. Outlined regions are the areas occupied by the various samples of Helou et al. (1991): *Solid outline:* ISM near Galactic disk stars. *Dotted outline:* Virgo spirals. *Dashed outline:* IBGS. *Long-dashed outline:* "Cold" galaxies and diffuse Galactic ISM.

and consistent with the higher values of L_{100}/L_B that we found for the S0 sample compared with the E sample in § 4.1.2.

Plots of the *IRAS* colors against L_X and L_X/L_B do not define any clear correlations. There is a vague tendency for the systems with the largest L_X/L_B to have the highest Θ-values, but no trend is apparent at all over the lowest 2 dex in L_X/L_B. There also appears to be a trend of increasing Θ with increasing L_X. However, given the scarcity of points with log $L_X < 40$ in our sample, this could easily be a selection effect. Plots of these two distributions are shown in Figure 17. We note that these are the *best* trends we find between X-ray emission and *IRAS* colors. Given the existence of both lower and upper limits in the FIR colors, there are no statistical tests of correlation that can be applied to these samples.

Finally, we have examined two *IRAS*-optical color-color plots to search for evidence of extinction in our sample. In Figure 18 we plot L_{12}/L_{100} against L_B/L_{100}. The circled points are the S0 galaxies. If the 12 μm flux is due to photospheric emission, and there is no substantial optical extinction, the data should scatter about a line of slope 1. Such a line is drawn (with an arbitrary zero point) in the figure. The bulk of the points are consistent with such a relationship. If there is a significant amount of dust extinction, then the B flux will be decreased more than the 12 μm flux, and there will be an increase in the 100 μm emission. These effects will cause dusty systems to lie substantially to the left of the slope 1 line (due to both the decrease in B and the increase in 100 μm), and to lie in the lower part of the plot (mainly due to the 100 μm enhancement). A number of objects do lie in this region. They are labeled in the figure. Note that virtually all these anomalous objects are S0 galaxies. The one E galaxy that is highly deviant is the dwarf elliptical NGC 1510 ($M_B \sim -18$). Recent work (e.g., Bender et al. 1991) indicates that such galaxies do not fall along a simple extension of the properties of giant ellipticals. Additionally, NGC 1510 is known to have an H II region–like nuclear spectrum (Phillips, Charles, & Baldwin 1983). We also note that most of the deviant S0 galaxies are known to be not entirely "normal" S0s. NGC 2444 is the early-type component of Arp 143, and is paired with a highly distorted ring galaxy (Arp 1966). NGC 6964 is also in an interacting pair with the starburst system NGC 6962 (Bernlohr 1993). NGC 6027 is the brightest member of Seyfert's Quintet (Hickson group 79; Hickson 1982). NGC 4507 has a weak Seyfert 2 nucleus (Phillips et al. 1983). Finally, NGC 6880 has optical dust lanes (Corwin, de Vaucouleurs, & de Vaucouleurs 1985).

In Figure 19 we plot L_{12}/L_{100} against L_{12}/L_B. In this case, the standard assumptions that the 12 μm flux is due to photospheric emission, and that there is no substantial optical extinction, would result in the points scattering about some constant value of L_{12}/L_B. Objects with significant extinction will tend to populate the lower right area of the plot. Once again, a number of points lie in this regime. They are the same objects as in Figure 18. Three of these galaxies are in the "spiral" region of Figure 16 (NGC 2444, NGC 6880, and IC 1024). Note that the one object in the elliptical sample that lies at the lower left in the plot is the Local Group nucleated dwarf elliptical NGC 205. This object is clearly very different from normal giant ellipticals in its structural properties (e.g., Kormendy 1985; Bender et al. 1991), its stellar populations (e.g., Wilcots et al. 1990; Davidge 1992), and its ISM (e.g., Johnson & Gottesman 1983; Fich & Hodge 1991). The above findings reinforce the results of §§ 4.1.2 and 4.2 that the S0 galaxies are the objects driving the discrepancy between our results for the L_{12}-L_B correlation and our expectations, that S0 galaxies have a

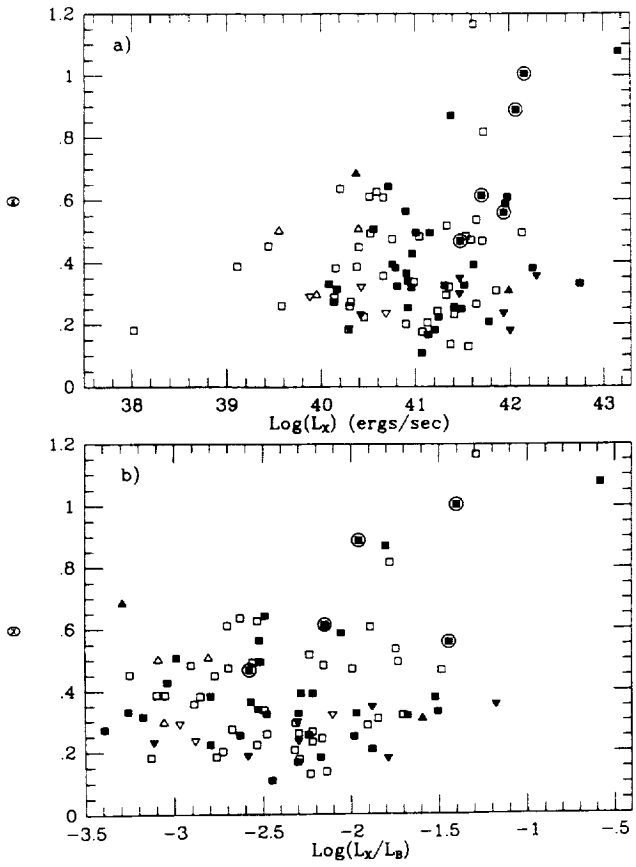

FIG. 17.—Θ-parameter for objects in our sample plotted against (*a*) L_X and (*b*) L_X/L_B. Filled symbols are X-ray detections; open symbols are X-ray upper limits. Squares are 60 and 100 μm detections, upward-pointing triangles are Θ lower limits, and downward-pointing triangles are Θ upper limits. Circled points are known AGNs.

significantly larger nonphotospheric contribution to their 12 μm flux than do E galaxies, and that S0 galaxies have larger FIR-to-optical and FIR-to-MIR ratios than do E galaxies. We note that an actual enhancement of the 12 μm flux from S0 galaxies (rather than just a decrease in the *B*-band flux due to extinction) would cause the observed difference in slope between the L_{12}-L_X relationships for the E and S0 galaxies determined in § 4.1.2.

4.4. *L_X versus Radio Emission*

There are published integrated 6 cm radio continuum measurements for 133 of our sample (see Table 1). Unfortunately, these data are very heterogeneous, having been collected by a large number of workers with many telescope/receiver combinations over the last ~20 years. The relationship between radio power and X-ray emission from early-type galaxies has been studied previously with smaller samples (e.g., FGT). The standard hypothesis (see Fabbiano 1989 and references therein) is that the X-ray gas acts as a confining medium for outflowing material from an active nuclear source. There also could be a connection in the opposite sense: the central source could be fueled by cooling flow gas (FGT). We have analyzed both the relationship between X-ray and total radio emission and, where the data are available, that between X-ray and core radio emission.

4.4.1. *Total Radio Emission*

There are strong statistical correlations between the 6 cm radio luminosity (L_6) and L_X, L_B, and L_X/L_B for our sample (see Table 2A). Strong correlations also exist between the radio-to-optical ratio (L_6/L_B) and the X-ray and optical data. We derive L_6 by summing the radio power over a ~1% bandwidth of 50 MHz. The regressions are given in Table 3A. The

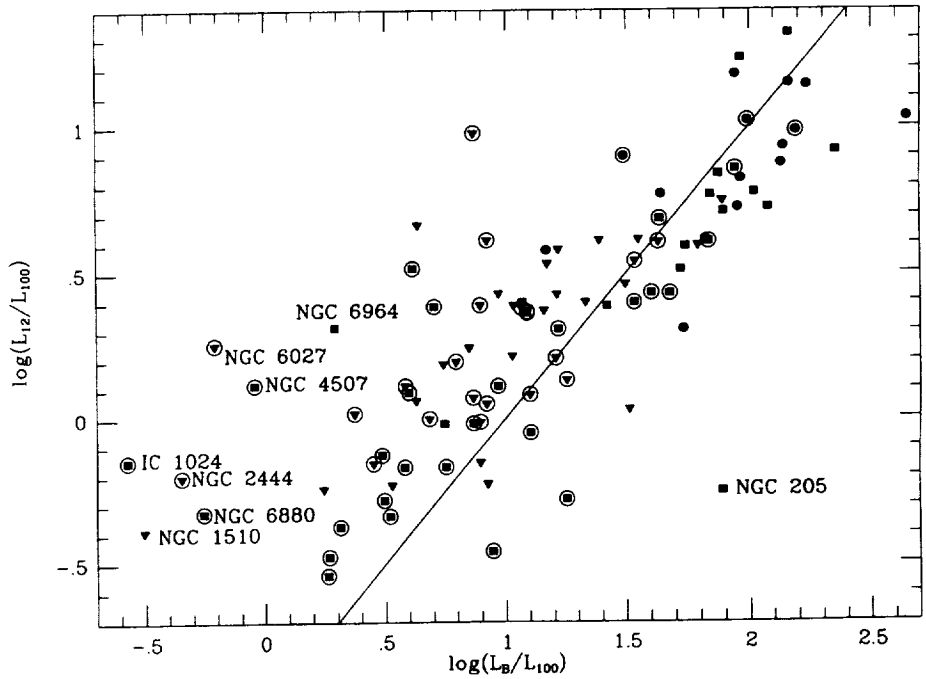

FIG. 18.—L_{12}/L_{100} vs. L_B/L_{100} for our sample. The squares are objects detected in both 12 and 100 μm. Downward-pointing triangles are objects with 12 μm upper limits. Filled circles are objects with 100 μm upper limits (and are thus double lower limits in this plot). Circled points are S0 galaxies. The line has slope 1 with an arbitrary zero point. Objects that deviate from this trend are labeled.

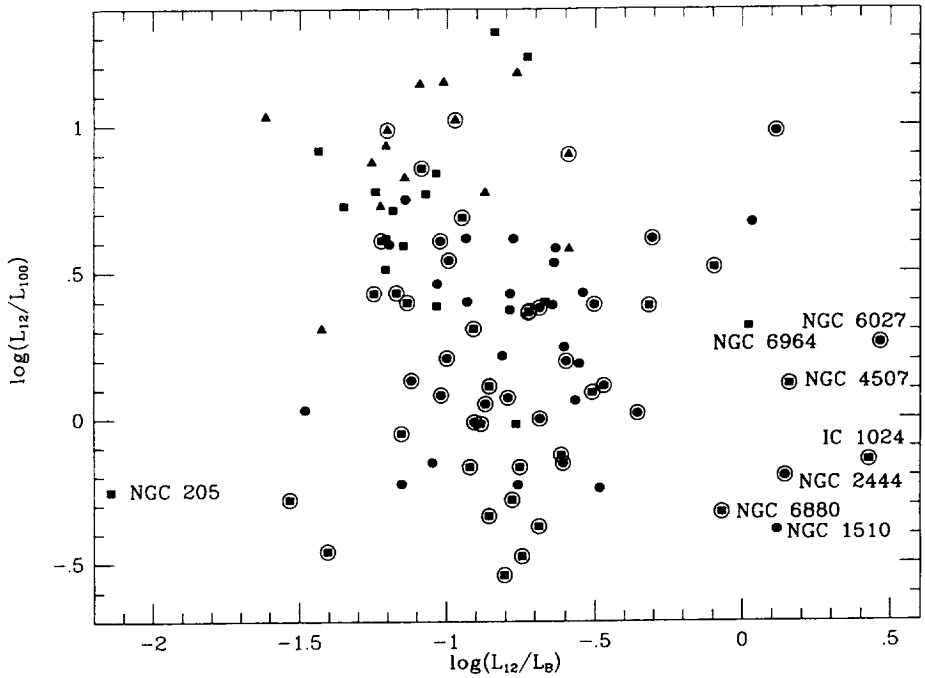

FIG. 19.—L_{12}/L_{100} vs. L_{12}/L_B for our sample. Filled squares are objects detected in both 12 and 100 μm. Upward-pointing triangles are objects with 100 μm upper limits (lower limits in this plot). Filled circles are objects with 12 μm upper limits (double upper limits in this plot). Circled points are S0 galaxies. Objects that deviate from the typical L_{12}/L_B are labeled.

fits for L_B, L_X and L_X/L_B are shown along with the data in Figures 20 (for L_6) and 21 (for L_6/L_B). We note that the regressions on the current sample yield slopes that are consistent in all cases with those given by FGT. It is clear that there is a relationship between the X-ray and radio emission in our sample that cannot be explained as a "bright-things-are-bright" correlation: The L_6-L_X relationship is steeper than slope 1 at nearly the 8 σ level, while the relationship between L_X and L_6/L_B is almost exactly slope 1. Given this, and the slopes of the L_B-L_6 and L_X-L_6 regressions (Table 3A), one might argue that the relationship we derive between L_X and L_6 is a statistical fluke, entirely driven by the (statistically stronger; see Table 2A) relationships between L_B and both L_X and L_6. However, we also derive strong statistical relationships between L_6 and L_X/L_B, L_6/L_B and L_X, and L_6/L_B and L_X/L_B. Thus for a given L_B, those objects with higher X-ray luminosities also tend to have higher radio luminosities. Furthermore, the X-ray luminosity scales linearly with the radio-to-optical ratio.

A partial rank analysis on L_B-L_X-L_X/L_B-L_6 shows the L_B-L_6 relationship to be the dominant statistical relationship. It *does* appear to drive the bivariate correlation between L_X and L_6 (see Table 9A). However, there is also a strong correlation between L_X/L_B and L_6, even accounting for the L_B-L_6 correlation. Thus there appears to be an underlying physical relationship between the total radio power and the X-ray–to–optical ratio for our sample. Including L_{12} in the partial rank analysis does not change any of these results. We also tested the combination L_B-L_X-L_X/L_B-L_{100}-L_6. This revealed a strong correlation between L_{100} and L_6 (see Table 9A). Among the six luminosity pairs in the test, it is second only to L_B-L_X in strength (stronger than any L_X- or L_X/L_B-L_6 trend): the presence of FIR emission appears strongly coupled to the ability of early-type galaxies to generate nonthermal radio emission. This point is investigated further in § 4.4.2 below.

Because of the known differences in radio emission from E and S0 galaxies (Walsh et al. 1989; Wrobel & Heeschen 1991), we have examined the results for our morphological subsamples. There are 69 elliptical galaxies in our 6 cm sample. Our bivariate analyses of these samples are given in Tables 2B and 3B. The regression lines against L_B, L_X, and L_X/L_B are statistically identical to the fits for the full sample and to those given in FGT. The fits are shown with the data in Figures 22 (for L_6) and 23 (for L_6/L_B).

A partial rank analysis on the variables L_B-L_X-L_X/L_B-L_6 for the E galaxies only gives substantially weaker results for correlations between L_6 and both L_X and L_X/L_B than were obtained for the full sample (see Table 9B). The inclusion of L_{12} in the analysis reveals no new trends. Including L_{100}, we find, as for the full sample, that a strong correlation exists between L_{100} and L_6 for the E galaxies. This is in keeping with the result of Walsh et al. (1989) that powerful radio galaxies tend to also have significant FIR emission.

There are 62 S0 galaxies in our 6 cm sample. The bivariate analysis is given in Tables 2C and 3C. Although the statistical case for correlation is a bit less strong than for the E galaxies, it is still quite good. The fits and the generating data are shown in Figures 24 (for L_6) and 25 (for L_6/L_B). Once again, these results are consistent with those of FGT. There is no evidence from the fits for a statistically significant difference between the E and S0 galaxies in their radio to X-ray properties.

A partial rank analysis on the variables L_B-L_X-L_X/L_B-L_6 for the S0 galaxies shows a weaker relation between L_B and L_6 than

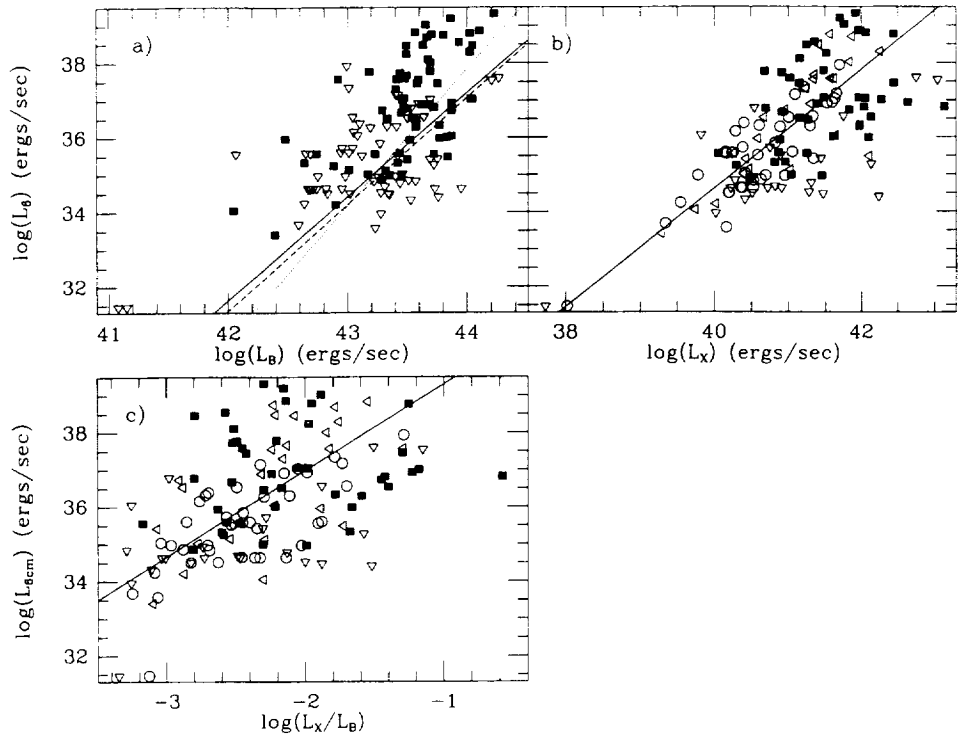

FIG. 20.—Radio luminosity at 6 cm for the full sample plotted against (*a*) L_B, (*b*) L_X, and (*c*) L_X/L_B. Symbols and line coding as in Fig. 9.

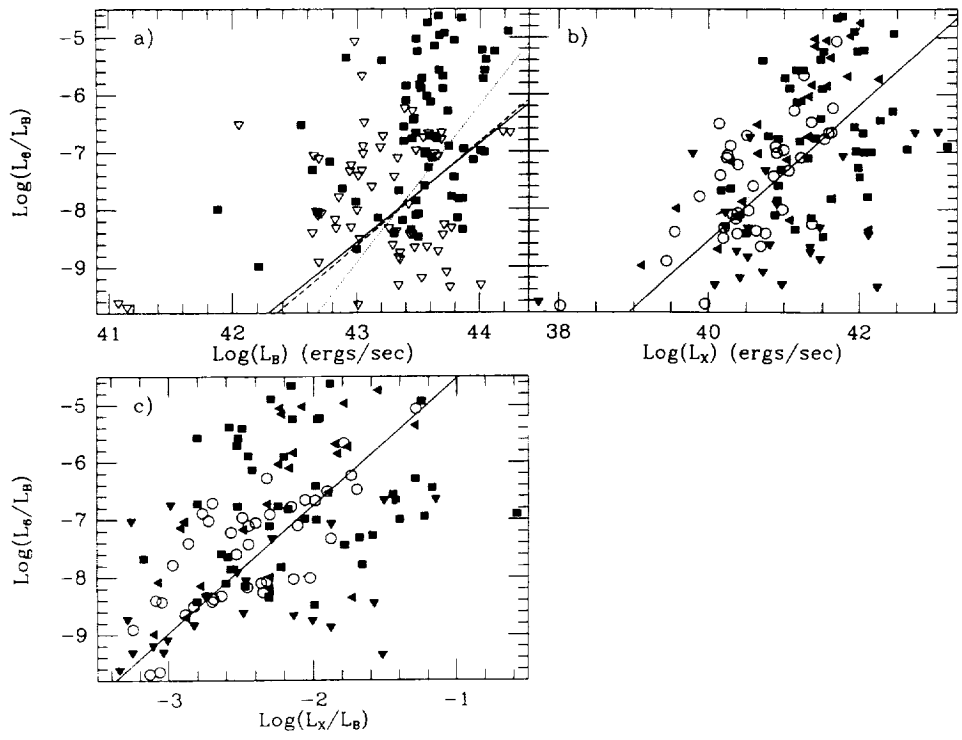

FIG. 21.—L_6/L_B vs. (*a*) L_B, (*b*) L_X, and (*c*) L_X/L_B for the full sample. Symbols and line coding as in Fig. 9.

TABLE 9A

PARTIAL SPEARMAN RANK ANALYSIS: 6 CENTIMETER PROPERTIES, E+S0 SAMPLES

Test Pair	Held Parameters	Size	Partial Spearman Rank	Probability
L_B-L_X	L_6	131	0.583	<0.005
	L_X/L_B, L_6	131	0.532	<0.005
	L_{12}, L_6	120	0.533	<0.005
	L_{100}, L_6	121	0.611	<0.005
	L_X/L_B, L_{12}, L_6	120	0.483	<0.005
	L_X/L_B, L_{100}, L_6	121	0.551	<0.005
L_B-L_X/L_B	L_6	131	0.281	<0.005
	L_X, L_6	131	−0.023	0.397
	L_{12}, L_6	120	0.258	<0.005
	L_{100}, L_6	121	0.316	<0.005
	L_X, L_{12}, L_6	120	−0.029	0.378
	L_X, L_{100}, L_6	121	−0.014	>0.400
L_B-L_{12}	L_6	120	0.362	<0.005
	L_X, L_6	120	0.242	<0.005
	L_X/L_B, L_6	120	0.349	<0.005
	L_X, L_X/L_B, L_6	120	0.239	<0.005
L_B-L_{100}	L_6	121	0.189	0.020
	L_X, L_6	121	0.280	<0.005
	L_X/L_B, L_6	121	0.238	<0.005
	L_X, L_X/L_B, L_6	121	0.277	<0.005
L_B-L_6	L_X	131	0.319	<0.005
	L_X/L_B	131	0.434	<0.005
	L_{12}	120	0.474	<0.005
	L_{100}	121	0.443	<0.005
	L_X, L_X/L_B	131	0.318	<0.005
	L_X, L_{12}	120	0.289	<0.005
	L_X, L_{100}	121	0.178	0.027
	L_X/L_B, L_{12}	120	0.379	<0.005
	L_X/L_B, L_{100}	121	0.309	<0.005
	L_X, L_X/L_B, L_{12}	120	0.289	<0.005
	L_X, L_X/L_B, L_{100}	121	0.178	0.028
L_X-L_X/L_B	L_6	131	0.510	<0.005
	L_B, L_6	131	0.444	<0.005
	L_{12}, L_6	120	0.524	<0.005
	L_{100}, L_6	121	0.532	<0.005
	L_B, L_{12}, L_6	120	0.472	<0.005
	L_B, L_{100}, L_6	121	0.451	<0.005
L_X-L_{12}	L_6	120	0.299	<0.005
	L_B, L_6	120	0.117	0.106
	L_X/L_B, L_6	120	0.290	<0.005
	L_B, L_X/L_B, L_6	120	0.131	0.083
L_X-L_{100}	L_6	121	−0.063	0.249
	L_B, L_6	121	−0.219	0.009
	L_X/L_B, L_6	121	0.008	>0.400
	L_B, L_X/L_B, L_6	121	−0.146	0.059
L_X-L_6	L_B	131	0.193	0.015
	L_X/L_B	131	0.324	<0.005
	L_{12}	120	0.431	<0.005
	L_{100}	121	0.476	<0.005
	L_B, L_X/L_B	131	0.091	0.164
	L_B, L_{12}	120	0.195	0.019
	L_B, L_{100}	121	0.262	<0.005
	L_X/L_B, L_{12}	120	0.269	<0.005
	L_X/L_B, L_{100}	121	0.291	<0.005
	L_B, L_X/L_B, L_{12}	120	0.085	0.191
	L_B, L_X/L_B, L_{100}	121	0.141	0.067
L_X/L_B-L_{12}	L_6	120	0.103	0.143
	L_B, L_6	120	0.003	>0.400
	L_X, L_6	120	−0.068	0.236
	L_B, L_X, L_6	120	−0.059	0.264
L_X/L_B-L_{100}	L_6	121	−0.130	0.082
	L_B, L_6	121	−0.195	0.018
	L_X, L_6	121	−0.114	0.112
	L_B, L_X, L_6	121	−0.106	0.135
L_X/L_B-L_6	L_B	131	0.245	<0.005
	L_X	131	0.180	0.021
	L_{12}	120	0.387	<0.005
	L_{100}	121	0.433	<0.005
	L_B, L_X	131	0.178	0.023
	L_B, L_{12}	120	0.248	<0.005
	L_B, L_{100}	121	0.293	<0.005
	L_X, L_{12}	120	0.177	0.029
	L_X, L_{100}	121	0.196	0.018
	L_B, L_X, L_{12}	120	0.178	0.029
	L_B, L_X, L_{100}	121	0.195	0.018
L_{12}-L_6	L_B	120	0.105	0.135
	L_X	120	0.161	0.042
	L_X/L_B	120	0.269	<0.005
	L_B, L_X	120	0.080	0.205
	L_B, L_X/L_B	120	0.101	0.147
	L_X, L_X/L_B	120	0.170	0.034
	L_B, L_X, L_X/L_B	120	0.089	0.182
L_{100}-L_6	L_B	121	0.333	<0.005
	L_X	121	0.445	<0.005
	L_X/L_B	121	0.479	<0.005
	L_B, L_X	121	0.371	<0.005
	L_B, L_X/L_B	121	0.369	<0.005
	L_X, L_X/L_B	121	0.456	<0.005
	L_B, L_X, L_X/L_B	121	0.382	<0.005

for either the full sample or the E galaxies. However, the evidence for a relation between L_X and L_6 is somewhat stronger for the S0 than for the E galaxies (see Tables 9B and 9C). Including L_{12} in the analysis weakens most trends with L_6, and shows a strong trend between L_{12} and L_6 not seen for either the full sample or the E galaxies (see Table 9C). This is another indication that the 12 μm emission in S0 galaxies is not due only to photospheric and circumstellar dust emission. Including L_{100}, we find evidence for an L_{100}-L_6 correlation as for the E galaxies.

The Kaplan-Meier DFs of L_6 and L_6/L_B of the two morphological subsamples do suggest a difference. These are plotted in integral form in Figure 26. The means of the distributions are given in Table 6. The mean luminosities differ at the 2.6 σ level, while the mean radio-to-optical ratios differ at the 2.0 σ level. In both cases, the S0 galaxies are more radio-weak than the Es. The results of the two-sample tests, also shown in Table 6, maintain evidence for differences at about this level of significance. As was found for the L_X-L_B relationship, the slope of the relation between L_X and L_6 is the same for both E and S0

TABLE 9B

PARTIAL SPEARMAN RANK ANALYSIS: 6 CENTIMETER PROPERTIES, SEPARATE E AND S0 SAMPLES

Test Pair	Held Parameters	Sample	Size	Partial Spearman Rank	Probability
L_B-L_X	L_6	E	69	0.522	<0.005
	L_6	S0	62	0.561	<0.005
	L_X/L_B, L_6	E	69	0.474	<0.005
	L_X/L_B, L_6	S0	62	0.502	<0.005
	L_{12}, L_6	E	61	0.428	<0.005
	L_{12}, L_6	S0	59	0.527	<0.005
	L_{100}, L_6	E	61	0.547	<0.005
	L_{100}, L_6	S0	60	0.563	<0.005
	L_X/L_B, L_{12}, L_6	E	61	0.396	<0.005
	L_X/L_B, L_{12}, L_6	S0	59	0.467	<0.005
	L_X/L_B, L_{100}, L_6	E	61	0.498	<0.005
	L_X/L_B, L_{100}, L_6	S0	60	0.493	<0.005
L_B-L_X/L_B	L_6	E	69	0.247	0.023
	L_6	S0	62	0.293	0.012
	L_X, L_6	E	69	−0.014	>0.400
	L_X, L_6	S0	62	0.034	0.296
	L_{12}, L_6	E	61	0.177	0.092
	L_{12}, L_6	S0	59	0.278	0.020
	L_{100}, L_6	E	61	0.262	0.024
	L_{100}, L_6	S0	60	0.317	0.008
	L_X, L_{12}, L_6	E	61	−0.013	>0.400
	L_X, L_{12}, L_6	S0	59	0.037	0.393
	L_X, L_{100}, L_6	E	61	0.042	>0.400
	L_X, L_{100}, L_6	S0	60	0.057	0.339
L_B-L_{12}	L_6	E	61	0.410	<0.005
	L_6	S0	59	0.280	0.018
	L_X, L_6	E	61	0.290	0.014
	L_X, L_6	S0	59	0.184	0.089
	L_X/L_B, L_6	E	61	0.392	<0.005
	L_X/L_B, L_6	S0	59	0.266	0.023
	L_X, L_X/L_B, L_6	E	61	0.290	0.015
	L_X, L_X/L_B, L_6	S0	59	0.185	0.089
L_B-L_{100}	L_6	E	61	0.277	0.018
	L_6	S0	60	0.299	0.011
	L_X, L_6	E	61	0.359	<0.005
	L_X, L_6	S0	60	0.311	0.009
	L_X/L_B, L_6	E	61	0.311	0.009
	L_X/L_B, L_6	S0	60	0.320	0.008
	L_X, L_X/L_B, L_6	E	61	0.358	<0.005
	L_X, L_X/L_B, L_6	S0	60	0.314	0.009
L_B-L_6	L_X	E	69	0.349	<0.005
	L_X	S0	62	0.195	0.070
	L_X/L_B	E	69	0.471	<0.005
	L_X/L_B	S0	62	0.332	<0.005
	L_{12}	E	61	0.452	<0.005
	L_{12}	S0	59	0.341	<0.005
	L_{100}	E	61	0.400	<0.005
	L_{100}	S0	60	0.253	0.028
	L_X, L_X/L_B	E	69	0.348	<0.005
	L_X, L_X/L_B	S0	62	0.189	0.078
	L_X, L_{12}	E	61	0.282	0.017
	L_X, L_{12}	S0	59	0.172	0.101
	L_X, L_{100}	E	61	0.131	0.173
	L_X, L_{100}	S0	60	0.060	0.328
	L_X/L_B, L_{12}	E	61	0.386	<0.005
	L_X/L_B, L_{12}	S0	59	0.264	0.024
	L_X/L_B, L_{100}	E	61	0.290	0.014
	L_X/L_B, L_{100}	S0	60	0.161	0.120
	L_X, L_X/L_B, L_{12}	E	61	0.281	0.018
	L_X, L_X/L_B, L_{12}	S0	59	0.166	0.116
	L_X, L_X/L_B, L_{100}	E	61	0.128	0.180
	L_X, L_X/L_B, L_{100}	S0	60	0.052	0.352

TABLE 9B—*Continued*

Test Pair	Held Parameters	Sample	Size	Partial Spearman Rank	Probability
L_X-L_X/L_B	L_6	E	69	0.493	<0.005
	L_6	S0	62	0.478	<0.005
	L_B, L_6	E	69	0.441	<0.005
	L_B, L_6	S0	62	0.396	<0.005
	L_{12}, L_6	E	61	0.439	<0.005
	L_{12}, L_6	S0	59	0.476	<0.005
	L_{100}, L_6	E	61	0.471	<0.005
	L_{100}, L_6	S0	60	0.491	<0.005
	L_B, L_{12}, L_6	E	61	0.408	<0.005
	L_B, L_{12}, L_6	S0	59	0.404	<0.005
	L_B, L_{100}, L_6	E	61	0.406	<0.005
	L_B, L_{100}, L_6	S0	60	0.398	<0.005
L_X-L_{12}	L_6	E	61	0.344	<0.005
	L_6	S0	59	0.236	0.040
	L_B, L_6	E	61	0.173	0.096
	L_B, L_6	S0	59	0.100	0.234
	L_X/L_B, L_6	E	61	0.317	0.008
	L_X/L_B, L_6	S0	59	0.221	0.050
	L_B, L_X/L_B, L_6	E	61	0.163	0.115
	L_B, L_X/L_B, L_6	S0	59	0.106	0.225
L_X-L_{100}	L_6	E	61	−0.062	0.320
	L_6	S0	60	0.076	0.286
	L_B, L_6	E	61	−0.245	0.033
	L_B, L_6	S0	60	−0.115	0.204
	L_X/L_B, L_6	E	61	0.010	>0.400
	L_X/L_B, L_6	S0	60	0.099	0.234
	L_B, L_X/L_B, L_6	E	61	−0.187	0.084
	L_B, L_X/L_B, L_6	S0	60	−0.073	0.296
L_X-L_6	L_B	E	69	0.211	0.044
	L_B	S0	62	0.259	0.023
	L_X/L_B	E	69	0.360	<0.005
	L_X/L_B	S0	62	0.330	<0.005
	L_{12}	E	61	0.440	<0.005
	L_{12}	S0	59	0.361	<0.005
	L_{100}	E	61	0.491	<0.005
	L_{100}	S0	60	0.347	<0.005
	L_B, L_X/L_B	E	69	0.132	0.155
	L_B, L_X/L_B	S0	62	0.185	0.082
	L_B, L_{12}	E	61	0.261	0.024
	L_B, L_{12}	S0	59	0.212	0.060
	L_B, L_{100}	E	61	0.336	<0.005
	L_B, L_{100}	S0	60	0.252	0.029
	L_X/L_B, L_{12}	E	61	0.322	0.007
	L_X/L_B, L_{12}	S0	59	0.249	0.033
	L_X/L_B, L_{100}	E	61	0.345	<0.005
	L_X/L_B, L_{100}	S0	60	0.230	0.043
	L_B, L_X/L_B, L_{12}	E	61	0.173	0.098
	L_B, L_X/L_B, L_{12}	S0	59	0.139	0.164
	L_B, L_X/L_B, L_{100}	E	61	0.233	0.041
	L_B, L_X/L_B, L_{100}	S0	60	0.174	0.099
L_X/L_B-L_{12}	L_6	E	61	0.144	0.147
	L_6	S0	59	0.089	0.255
	L_B, L_6	E	61	0.061	0.326
	L_B, L_6	S0	59	0.008	>0.400
	L_X, L_6	E	61	−0.017	>0.400
	L_X, L_6	S0	59	−0.029	>0.400
	L_B, L_X, L_6	E	61	−0.012	>0.400
	L_B, L_X, L_6	S0	59	−0.036	0.396
L_X/L_B-L_{100}	L_6	E	61	−0.112	0.206
	L_6	S0	60	−0.022	>0.400
	L_B, L_6	E	61	−0.185	0.084
	L_B, L_6	S0	60	−0.121	0.193
	L_X, L_6	E	61	−0.094	0.241
	L_X, L_6	S0	60	−0.068	0.308
	L_B, L_X, L_6	E	61	−0.090	0.251
	L_B, L_X, L_6	S0	60	−0.082	0.273

TABLE 9B—*Continued*

Test Pair	Held Parameters	Sample	Size	Partial Spearman Rank	Probability
L_X/L_B-L_6	L_B	E	69	0.209	0.046
	L_B	S0	62	0.223	0.044
	L_X	E	69	0.131	0.155
	L_X	S0	62	0.137	0.158
	L_{12}	E	61	0.350	<0.005
	L_{12}	S0	59	0.301	0.011
	L_{100}	E	61	0.406	<0.005
	L_{100}	S0	60	0.300	0.011
	L_B, L_X	E	69	0.128	0.163
	L_B, L_X	S0	62	0.128	0.177
	L_B, L_{12}	E	61	0.249	0.030
	L_B, L_{12}	S0	59	0.205	0.066
	L_B, L_{100}	E	61	0.299	0.011
	L_B, L_{100}	S0	60	0.230	0.043
	L_X, L_{12}	E	61	0.156	0.126
	L_X, L_{12}	S0	59	0.138	0.165
	L_X, L_{100}	E	61	0.174	0.196
	L_X, L_{100}	S0	60	0.142	0.155
	L_B, L_X, L_{12}	E	61	0.153	0.133
	L_B, L_X, L_{12}	S0	59	0.130	0.182
	L_B, L_X, L_{100}	E	61	0.171	0.100
	L_B, L_X, L_{100}	S0	60	0.138	0.164
L_{12}-L_6	L_B	E	61	0.087	0.255
	L_B	S0	59	0.286	0.016
	L_X	E	61	0.130	0.173
	L_X	S0	59	0.298	0.012
	L_X/L_B	E	61	0.259	0.024
	L_X/L_B	S0	59	0.375	<0.005
	L_B, L_X	E	61	0.037	0.388
	L_B, L_X	S0	59	0.257	0.028
	L_B, L_X/L_B	E	61	0.069	0.303
	L_B, L_X/L_B	S0	59	0.279	0.020
	L_X, L_X/L_B	E	61	0.131	0.173
	L_X, L_X/L_B	S0	59	0.299	0.013
	L_B, L_X, L_X/L_B	E	61	0.039	0.386
	L_B, L_X, L_X/L_B	S0	59	0.259	0.028
L_{100}-L_6	L_B	E	61	0.319	0.007
	L_B	S0	60	0.455	<0.005
	L_X	E	61	0.455	<0.005
	L_X	S0	60	0.512	<0.005
	L_X/L_B	E	61	0.489	<0.005
	L_X/L_B	S0	60	0.555	<0.005
	L_B, L_X	E	61	0.374	<0.005
	L_B, L_X	S0	60	0.467	<0.005
	L_B, L_X/L_B	E	61	0.354	<0.005
	L_B, L_X/L_B	S0	60	0.468	<0.005
	L_X, L_X/L_B	E	61	0.462	<0.005
	L_X, L_X/L_B	S0	60	0.515	<0.005
	L_B, L_X, L_X/L_B	E	61	0.382	<0.005
	L_B, L_X, L_X/L_B	S0	60	0.472	<0.005

galaxies, but the S0s are shifted to lower radio luminosity. This is consistent with the findings of Wrobel & Heeschen (1991) based on radio observations of a purely optically selected sample of E and S0 galaxies. Since both the size and significance of the offsets in L_X and L_6 for the E and S0 galaxies are comparable, we have also investigated the DF of the quantity L_X/L_6. There are upper limits in both quantities. No statistical methods are available that can robustly determine a distribution function with upper and lower limits (and many limit ratios!), so we have simply tested the sample of objects detected both in X-rays and at 6 cm. For these galaxies there is no evidence that the DFs of L_X/L_6 of the E and S0 galaxies differ: the mean values differ by 0.096 ± 0.370; the two-sample tests all support the null hypothesis at higher than 75%. Whatever governs the relationship between radio continuum and X-ray emission does not appear to differ between E and S0 galaxies from these data.

4.4.2. *X-Ray–FIR–Radio Correlation*

A previous analysis of a smaller sample of early-type galaxies led to the suggestion of a relationship between the distribution

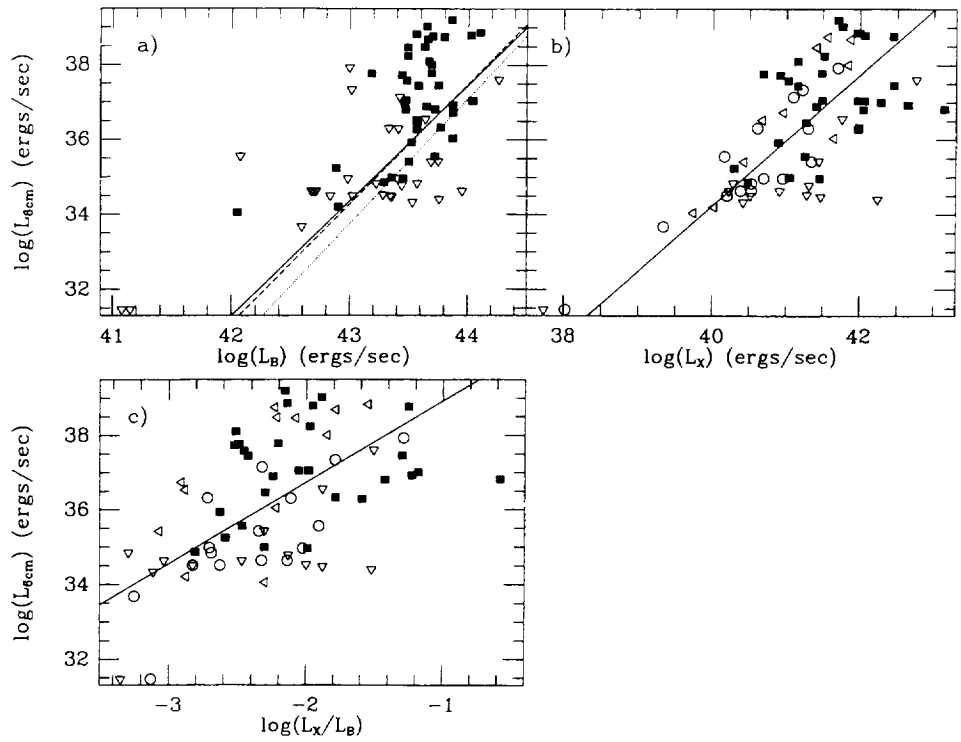

FIG. 22.—L_6 vs. (a) L_B, (b) L_X, and (c) L_X/L_B, for elliptical galaxies only. Symbols and line coding as in Fig. 9.

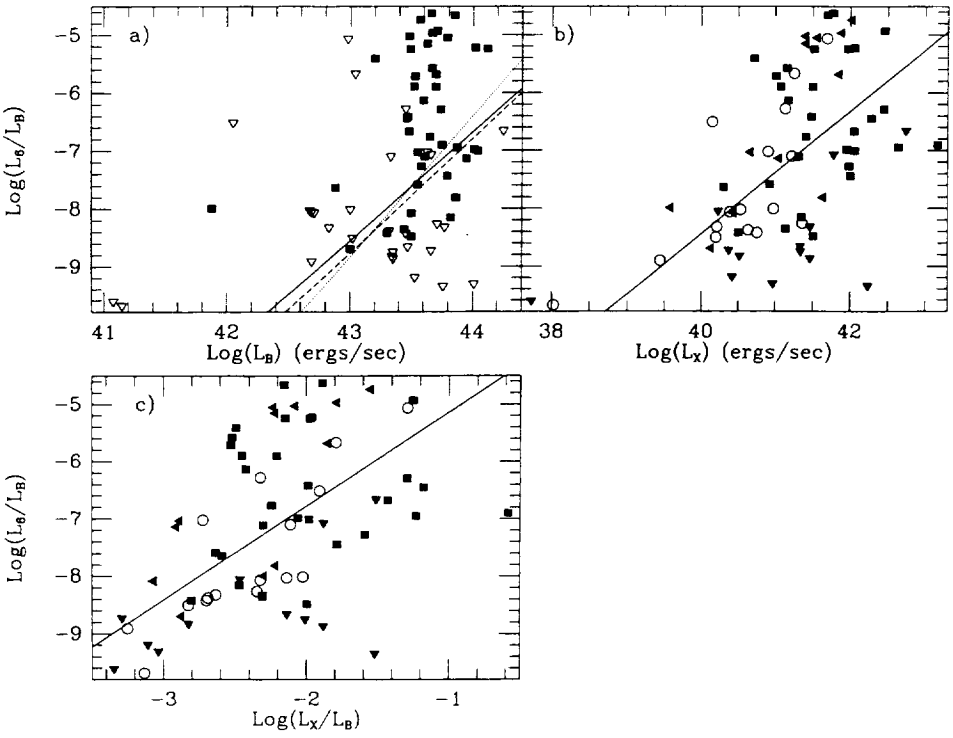

FIG. 23.—L_6/L_B vs. (a) L_B, (b) L_X, and (c) L_X/L_B, for elliptical galaxies only. Symbols and line coding as in Fig. 9.

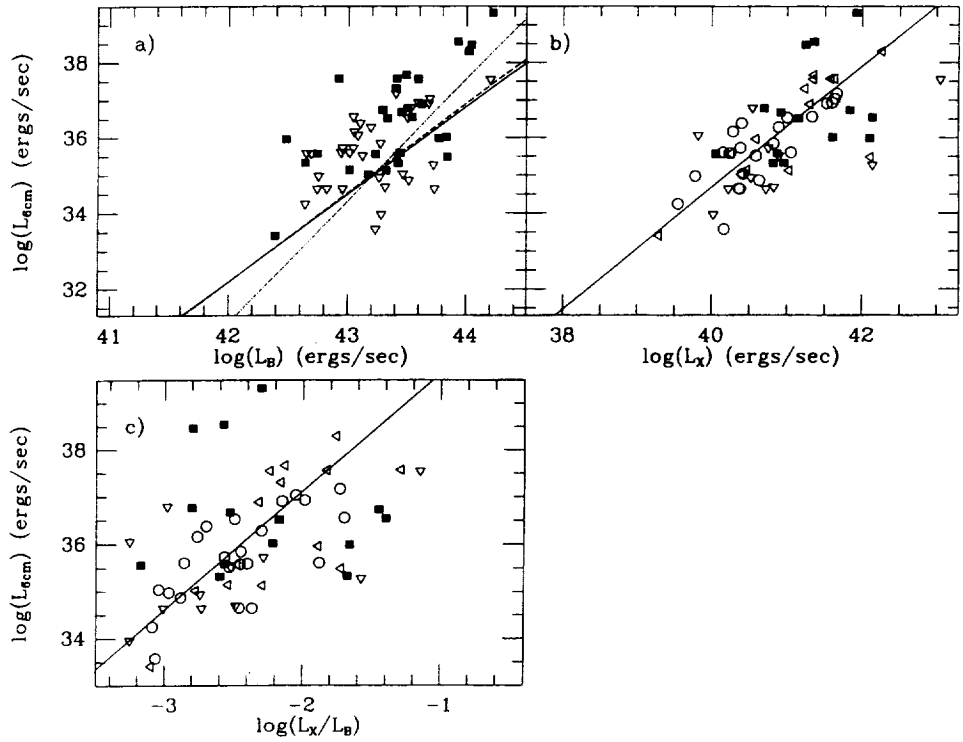

FIG. 24.—L_6 vs. (*a*) L_B, (*b*) L_X, and (*c*) L_X/L_B, for S0 galaxies only. Symbols and line coding as in Fig. 9.

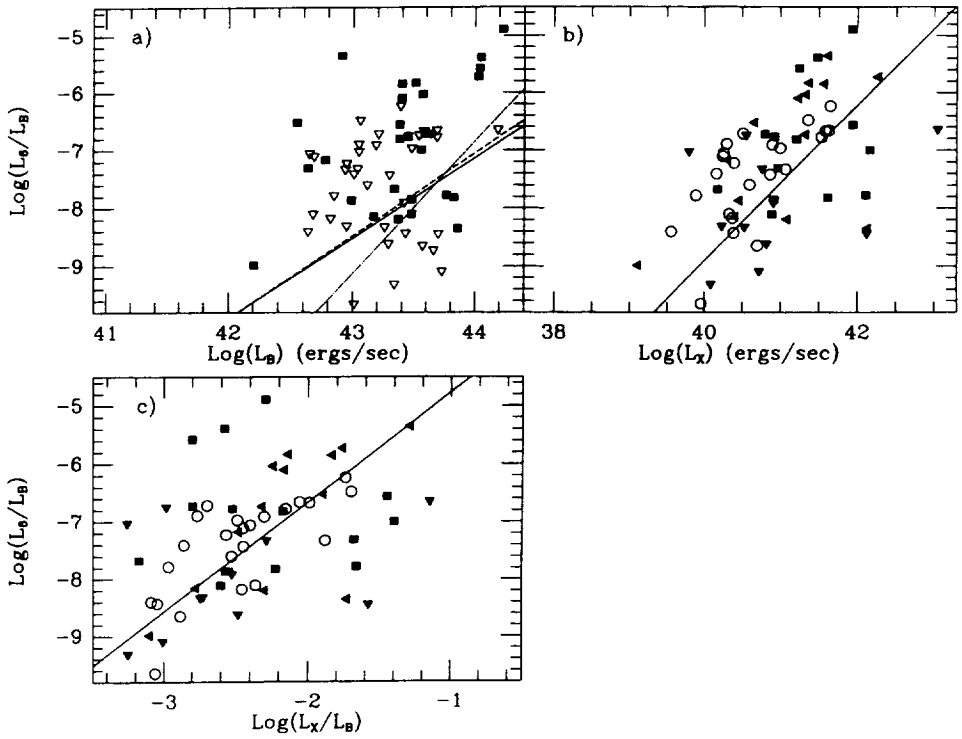

FIG. 25.—L_6/L_B vs. (*a*) L_B, (*b*) L_X, and (*c*) L_X/L_B, for S0 galaxies only. Symbols and line coding as in Fig. 9.

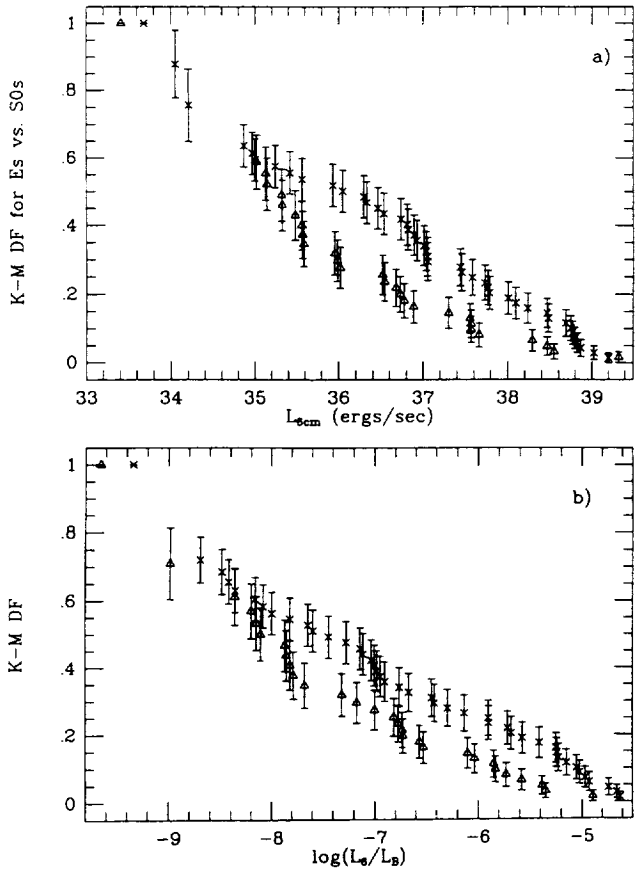

FIG. 26.—Integral K-M DFs of (*a*) L_6 and (*b*) L_6/L_B for our samples of E and S0 galaxies. Symbols as in Fig. 8.

of points in the L_6-L_{100} plane and the range of L_X/L_B for the objects considered (Kim & Fabbiano 1990). Specifically, the systems with the highest L_X/L_B tend to have larger ratio and FIR luminosities than the systems with the lowest L_X/L_B. Furthermore, in the region where the L_{100}'s of the two samples overlap, the high L_X/L_B galaxies are shifted to higher radio luminosities than the low L_X/L_B galaxies. We have repeated this analysis with our current sample. The data are shown for systems with log $(L_X/L_B) > -2.4$ in Figure 27*a* and those with log $(L_X/L_B) < -2.7$ in Figure 27*b*. These ranges correspond to systems with log $(L_X/L_B) > 30.3$ ergs s^{-1} $L_\odot^{-1}$ and log $(L_X/L_B) < 30.0$ ergs s^{-1} $L_\odot^{-1}$ in the units of Kim & Fabbiano (1990). The general pattern discerned by Kim & Fabbiano (1990) remains: systems with high L_X/L_B have generally higher radio and FIR luminosities than those with low L_X/L_B. Furthermore, compared to the rough locus in the L_6-L_{100} plane defined by the low L_X/L_B systems, those with the highest values of L_X/L_B tend to have radio excesses for their FIR luminosities. In agreement with the partial rank analysis presented in § 4.4.1, this result indicates that the presence of a hot ISM in early-type galaxies is a key factor in their ability to generate both radio continuum and FIR emission, and thus argues against the interpretation that radio and FIR emission in early-type galaxies are fueled by external accretion (e.g., Walsh et al. 1989; Forbes 1991). Rather, it is in keeping with the suggestion (FGT) that the hot ISM fuels the central engine responsible for the radio emission.

4.4.3. *Core Radio Emission*

The relationship between X-ray emission and radio-core luminosity was examined by FGT for a sample of 29 objects. Since that study, a large number of arcsecond-scale resolution 6 cm core observations have been published, mainly by Wrobel & Heeschen (1991). Combined with older data on objects not included in the FGT X-ray sample, we now have 6 cm core data for 99 of our sample of 148 galaxies (see Table 1). In Figure 28 we plot L_6 against L_{6co} (the 6 cm radio-core luminosity) for the objects in our sample. The dotted line shows $L_6 \equiv L_{6co}$. The scatter of points below this line can be due either to systematic and statistical errors or to intrinsic source variability.

We have tested for bivariate correlation between the radio core luminosity and the X-ray and optical luminosities as described above. The results of these tests are given in Table 2A. Also shown in Table 2A are the results of correlation analyses performed on the total radio luminosity of the sample for which we have core radio data. In comparing these results, we are thus comparing results drawn from the same sample. The

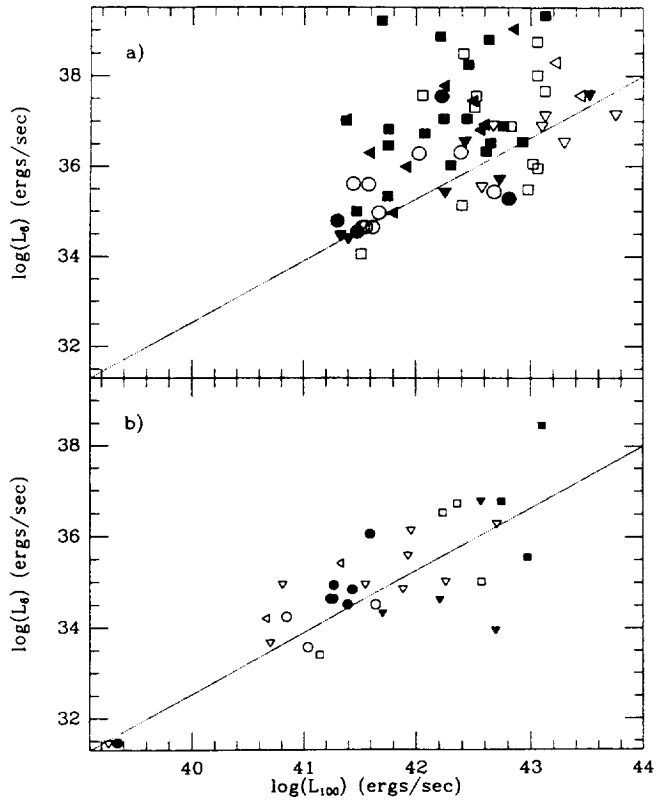

FIG. 27.—L_6 vs. L_{100} for (*a*) galaxies with log $(L_X/L_B) > -2.4$, and (*b*) log $(L_X/L_B) < -2.7$. Symbols are coded as follows: Filled symbols indicate X-ray detections. Open symbols show X-ray upper limits. Squares indicate both 6 cm and 100 μm detections. Circles indicate both 6 cm and 100 μm upper limits. Downward-pointing triangles indicate 100 μm detections and 6 cm upper limits. Left-pointing triangles indicate 6 cm detections and 100 μm upper limits. We also add the same fiducial line (it is *not* a fit line) to both (*a*) and (*b*).

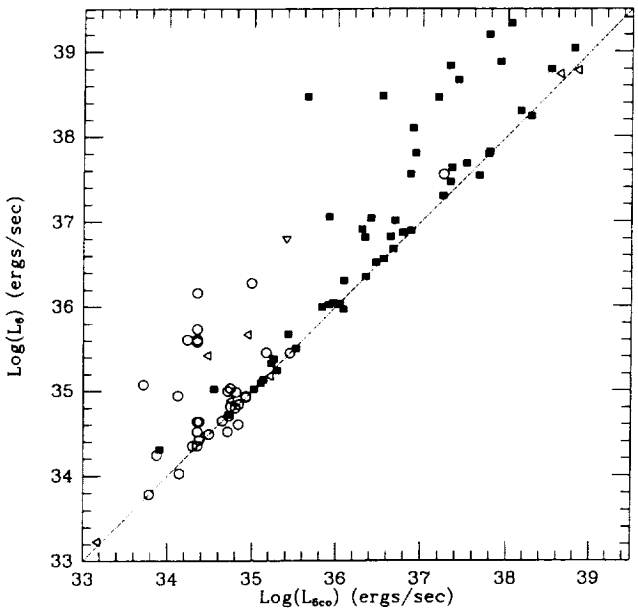

FIG. 28.—L_6 vs. L_{6co}. Symbols as in Fig. 9. The dotted line is $L_6 \equiv L_{6co}$.

tests of L_{6co} with L_X, L_B, and L_X/L_B all show strong statistical correlation, comparable to the results for L_6 for the core sample. We show the results of our regression analysis in Table 3A and Figure 29.

Using the core sample, we find no difference in the slopes of the regressions with X-ray emission for core and total radio power. This may simply be a reflection of our sample being largely core-dominated. We note, also, that there is no significant difference between the fits to the total 6 cm emission for the core sample and those for the full sample (see Table 3A). We find the slope of the relationship between core radio and X-ray luminosities for our sample to be 1.53 ± 0.12—greater than slope 1 at the 4.4 σ level. The relationship between core radio luminosity and the X-ray–to–optical ratio also shows a steep slope (2.92 ± 0.33, inconsistent with slope 1 at the 5.8 σ level). Our slope is consistent with that found by FGT to less than 1 σ (they find a slope of 2.45 ± 0.44). Our results therefore support the notion discussed by FGT that systems with more extensive X-ray halos are able to fuel compact nuclear sources at substantially higher rates than less X-ray–luminous systems.

A partial rank analysis on L_B-L_X-L_X/L_B-L_{6co} shows somewhat stronger trends between L_{6co} and both L_X and L_X/L_B than were found for L_6 in § 4.4.1 above. This is confirmed by a partial rank test including both L_6 and L_{6co}: Both L_X and L_X/L_B are more correlated with *core* radio luminosity than with *total* radio luminosity. However, L_B is clearly more correlated with L_6 than with L_{6co} (see Table 10). This argues that radio cores are fueled by a hot ISM (as suggested by FGT) but that total radio power is more dependent on total luminosity (or mass) and is not intrinsically linked to the presence of a hot ISM. This last finding may have implications for the rate of formation of massive nuclear black holes in early-type galaxies. If the total radio power is a function of the mass of a nuclear black hole, then our result would imply that more massive black holes form in more massive galaxies.

Curiously, when we add L_{12} to the partial rank analysis, and compare the results with those determined for the L_B-L_X-L_X/L_B-L_{12}-L_6 analysis from § 4.4.1 above, we find stronger

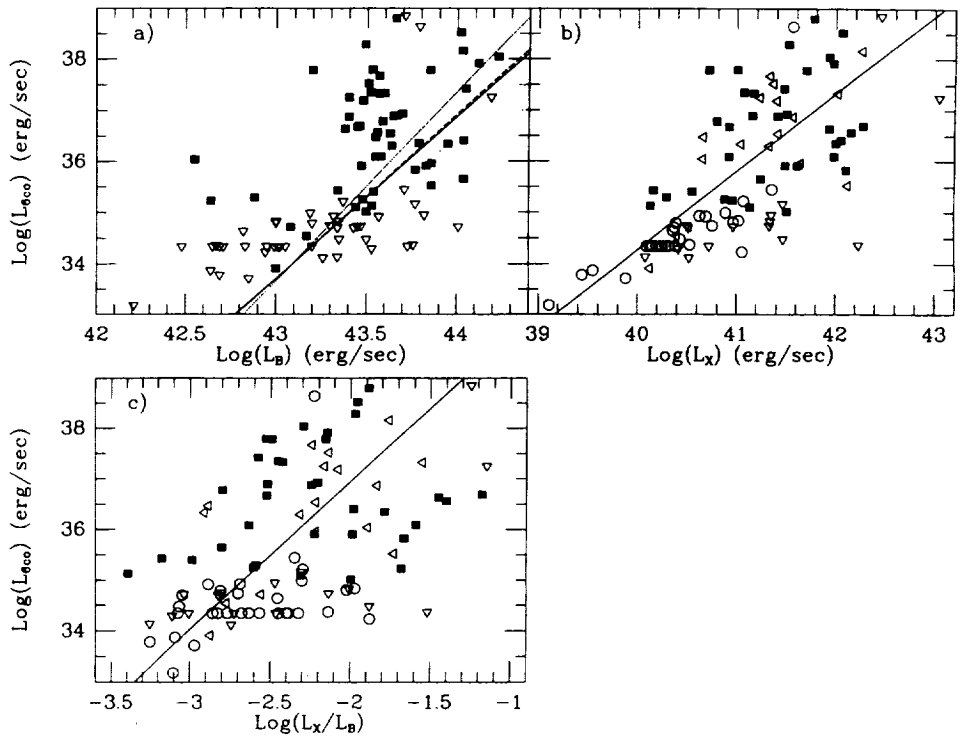

FIG. 29.—L_{6co} vs. (*a*) L_B, (*b*) L_X, and (*c*) L_X/L_B. Symbols and line coding as in Fig. 9.

TABLE 10

PARTIAL SPEARMAN RANK ANALYSIS: 6 CENTIMETER CORE SAMPLE

Test Pair	Held Parameters	Size	Partial Spearman Rank	Probability
L_B-L_X	L_{6co}	99	0.527	<0.005
	L_6	99	0.535	<0.005
	L_X/L_B, L_{6co}	99	0.496	<0.005
	L_X/L_B, L_6	99	0.499	<0.005
	L_{12}, L_{6co}	92	0.459	<0.005
	L_{100}, L_{6co}	93	0.565	<0.005
	L_X/L_B, L_{12}, L_{6co}	92	0.434	<0.005
	L_X/L_B, L_{100}, L_{6co}	93	0.520	<0.005
L_B-L_X/L_B	L_{6co}	99	0.208	0.022
	L_6	99	0.226	0.015
	L_X, L_{6co}	99	−0.034	0.373
	L_X, L_6	99	−0.035	0.369
	L_{12}, L_{6co}	92	0.168	0.060
	L_{100}, L_{6co}	93	0.265	0.007
	L_X, L_{12}, L_{6co}	92	−0.029	0.394
	L_X, L_{100}, L_{6co}	93	0.058	0.296
L_B-L_{12}	L_{6co}	92	0.334	<0.005
	L_X, L_{6co}	92	0.241	0.013
	L_X/L_B, L_{6co}	92	0.331	<0.005
	L_X, L_X/L_B, L_{6co}	92	0.238	0.014
L_B-L_{100}	L_{6co}	93	0.192	0.037
	L_X, L_{6co}	93	0.334	<0.005
	L_X/L_B, L_{6co}	93	0.270	0.006
	L_X, L_X/L_B, L_{6co}	93	0.336	<0.005
L_B-L_{6co}	L_X	99	0.328	<0.005
	L_X/L_B	99	0.478	<0.005
	L_{12}	92	0.476	<0.005
	L_{100}	93	0.416	<0.005
	L_X, L_X/L_B	99	0.327	<0.005
	L_X, L_{12}	92	0.264	0.007
	L_X, L_{100}	93	0.066	0.267
	L_X/L_B, L_{12}	92	0.383	<0.005
	L_X/L_B, L_{100}	93	0.229	0.017
	L_X, L_X/L_B, L_{12}	92	0.262	0.008
	L_X, L_X/L_B, L_{100}	93	0.042	0.348
L_B-L_6	L_X	99	0.394	<0.005
	L_X/L_B	99	0.517	<0.005
	L_X, L_X/L_B	99	0.393	<0.005
L_X-L_X/L_B	L_{6co}	99	0.442	<0.005
	L_6	99	0.470	<0.005
	L_B, L_{6co}	99	0.400	<0.005
	L_B, L_6	99	0.424	<0.005
	L_{12}, L_{6co}	92	0.417	<0.005
	L_{100}, L_{6co}	93	0.391	<0.005
	L_B, L_{12}, L_{6co}	92	0.388	<0.005
	L_B, L_{100}, L_{6co}	93	0.303	<0.005
L_X-L_{12}	L_{6co}	92	0.264	0.007
	L_B, L_{6co}	92	0.117	0.147
	L_X/L_B, L_{6co}	92	0.269	0.006
	L_B, L_X/L_B, L_{6co}	92	0.132	0.115
L_X-L_{100}	L_{6co}	93	−0.177	0.048
	L_B, L_{6co}	93	−0.326	<0.005
	L_X/L_B, L_{6co}	93	−0.047	0.332
	L_B, L_X/L_B, L_{6co}	93	−0.212	0.024
L_X-L_{6co}	L_B	99	0.282	<0.005
	L_X/L_B	99	0.399	<0.005
	L_{12}	92	0.495	<0.005
	L_{100}	93	0.568	<0.005
	L_B, L_X/L_B	99	0.165	0.056
	L_B, L_{12}	92	0.303	<0.005
	L_B, L_{100}	93	0.430	<0.005
	L_X/L_B, L_{12}	92	0.335	<0.005
	L_X/L_B, L_{100}	93	0.353	<0.005
	L_B, L_X/L_B, L_{12}	92	0.177	0.051
	L_B, L_X/L_B, L_{100}	93	0.280	<0.005
L_X-L_6	L_B	99	0.204	0.024
	L_X/L_B	99	0.377	<0.005
	L_B, L_X/L_B	99	0.104	0.167
L_X/L_B-L_{12}	L_{6co}	92	0.047	0.331
	L_B, L_{6co}	92	−0.012	>0.400
	L_X, L_{6co}	92	−0.071	0.254
	L_B, L_X, L_{6co}	92	−0.062	0.283
L_X/L_B-L_{100}	L_{6co}	93	−0.325	<0.005
	L_B, L_{6co}	93	−0.373	<0.005
	L_X, L_{6co}	93	−0.280	<0.005
	L_B, L_X, L_{6co}	93	−0.283	<0.005
L_X/L_B-L_{6co}	L_B	99	0.314	<0.005
	L_X	99	0.219	0.018
	L_{12}	92	0.449	<0.005
	L_{100}	93	0.566	<0.005
	L_B, L_X	99	0.218	0.019
	L_B, L_{12}	92	0.344	<0.005
	L_B, L_{100}	93	0.471	<0.005
	L_X, L_{12}	92	0.245	0.011
	L_X, L_{100}	93	0.350	<0.005
	L_B, L_X, L_{12}	92	0.244	0.012
	L_B, L_X, L_{100}	93	0.346	<0.005
L_X/L_B-L_6	L_B	99	0.251	0.007
	L_X	99	0.183	0.039
	L_B, L_X	99	0.182	0.041
L_{12}-L_{6co}	L_B	92	0.211	0.024
	L_X	92	0.243	0.011
	L_X/L_B	92	0.377	<0.005
	L_B, L_X	92	0.164	0.066
	L_B, L_X/L_B	92	0.202	0.031
	L_X, L_X/L_B	92	0.252	0.009
	L_B, L_X, L_X/L_B	92	0.174	0.054
L_{100}-L_{6co}	L_B	93	0.477	<0.005
	L_X	93	0.606	<0.005
	L_X/L_B	93	0.670	<0.005
	L_B, L_X	93	0.548	<0.005
	L_B, L_X/L_B	93	0.566	<0.005
	L_X, L_X/L_B	93	0.643	<0.005
	L_B, L_X, L_X/L_B	93	0.591	<0.005

evidence for an L_{12}-L_{6cm} correlation than for an L_{12}-L_6 correlation (see Table 10). Our analysis on the variables L_B-L_X-L_X/L_B-L_{100}-L_{6cm} demonstrates a significantly stronger relationship between L_{100} and L_{6cm} than was found for L_{100} and L_6 in § 4.4.1. This indicates that the presence of FIR emission in early-type galaxies is strongly coupled to the ability of these galaxies to generate core radio power, rather than to some global property.

4.5. L_X *versus* H I 21 cm *Emission*

We have compiled the available data on H I 21 cm line emission for the galaxies in our sample. These data are largely obtained from the compilations of Roberts et al. (1991) and Huchtmeier & Richter (1989), supplemented with a few newer references (see notes to Table 1). The H I fluxes ($\Sigma_{H\,I}$) expressed in Jy km s^{-1} have been converted to $M_{H\,I}$ in solar masses, using our distances (D in Mpc) and the standard formula (see Roberts 1975):

$$M_{H\,I}(M_\odot) = 2.36 \times 10^5 D^2 \Sigma_{H\,I}\,. \quad (3)$$

For those objects with only upper limits ($\sigma_{H\,I}$), expressed in janskys (or millijanskys) per channel, we derived H I mass limits from the following relation:

$$M_{H\,I}(M_\odot) \leq 2.36 \times 10^5 D^2 3\sigma_{H\,I}\Delta v\,. \quad (4a)$$

The velocity width, Δv, was estimated following Knapp et al. (1985) and Wardle & Knapp (1986):

$$\Delta v = 0.25(L_B/L_\odot)^{1/3}\,. \quad (4b)$$

Figure 30 shows the H I mass data plotted against L_B, L_X, and L_X/L_B. The plots show no compelling evidence for any correlation, and this is borne out by the results of our bivariate analysis (see Table 2A). Note that we have also tested for correlations with $M_{H\,I}/L_B$, and found nothing. This is in keeping with the results of Knapp et al. (1985). A partial rank analysis on L_B-L_X-L_X/L_B-$M_{H\,I}$ shows no evidence for any trends of $M_{H\,I}$ with either the optical or the X-ray properties of our sample (see Table 11).

5. SUMMARY AND SUGGESTIONS FOR FUTURE RESEARCH

We have analyzed the relationships between optical luminosity and ISM parameters for the *Einstein* sample of early-type galaxies (P0). This sample is the largest currently available sample of early-type galaxies with X-ray observations. The principal results of this study are as follows:

1. We confirm earlier results (e.g., Forman et al. 1985; Trinchieri et al. 1986; Donnelly et al. 1990) showing a strong, steep correlation between L_B and L_X in early-type galaxies. This correlation holds for all statistical tests applied to the data. It is maintained whether or not we include the Local Group dwarf galaxies NGC 205 and M32 in the analysis. When we fit the data with a power law, we find a slope of 1.8 ± 0.1 for the full sample. Considering only the brighter galaxies, the slope becomes 2.0 ± 0.2. The use of 7S distances does not significantly alter these results. Not surprisingly, we also find strong correlations between L_X and L_X/L_B that are much steeper than slope 1, in the sense that the most X-ray–luminous galaxies have the highest L_X/L_B. Partial rank analysis confirms these trends.

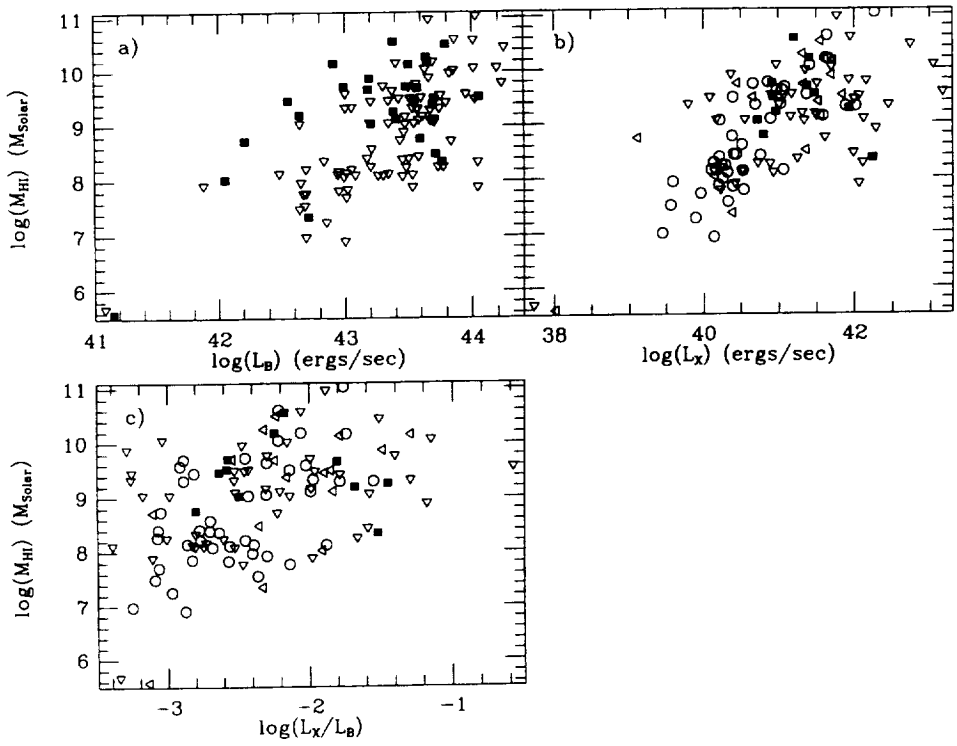

FIG. 30.—$M_{H\,I}$ vs. (*a*) L_B, (*b*) L_X, and (*c*) L_X/L_B. Symbols as in Fig. 9.

TABLE 11

PARTIAL SPEARMAN RANK ANALYSIS: H I SAMPLE

Test Pair	Held Parameters	Size	Partial Spearman Rank	Probability
L_B-L_X	M_{H_I}	115	0.693	<0.005
	L_X/L_B, M_{H_I}	115	0.600	<0.005
L_B-L_X/L_B	M_{H_I}	115	0.435	<0.005
	L_X, M_{H_I}	115	0.031	0.371
L_B-M_{H_I}	L_X	115	0.048	0.308
	L_X/L_B	115	0.094	0.171
	L_X, L_X/L_B	115	0.044	0.322
L_X-L_X/L_B	M_{H_I}	115	0.602	<0.005
	L_B, M_{H_I}	115	0.463	<0.005
L_X-M_{H_I}	L_B	115	0.114	0.120
	L_X/L_B	115	0.098	0.161
	L_B, L_X/L_B	115	0.052	0.295
L_X/L_B-M_{H_I}	L_B	115	0.145	0.064
	L_X	115	0.106	0.139
	L_B, L_X	115	0.105	0.144

2. We find a significant difference in the slope of the L_X-L_B correlation between low-L_X galaxies ($\log L_X \leq 40.5$) and high-L_X galaxies. In the former, $L_X \propto L_B^{\sim 1}$, confirming the analysis of FGT, who suggested that there is a significant difference between the emission mechanisms of low- and high-L_X early-type galaxies based on their loci in the L_X-L_B diagram. This result is also in agreement with the differences in the average X-ray spectra of low- and high-L_X/L_B found by Kim et al. (1992b).

3. We find a significant correlation between L_X and C_{21} in the sense that galaxies with higher L_X have more pronounced low-energy cutoffs. Partial rank analysis indicates that the bivariate L_X/L_B-C_{21} correlation is actually driven by the dependence of both these variables on L_X. These results are in keeping with recent *ROSAT* observations showing intrinsically softer X-ray spectra for lower L_X and L_X/L_B galaxies.

4. Analyses of separate samples of E and S0 galaxies each yield strong correlations between L_B-L_X and L_X-L_X/L_B. The regression slopes for these morphological subsamples are consistent with each other, and with the above results for the full sample. Comparison of the Kaplan-Meier distribution functions for the two morphological subsamples indicates that the S0 galaxies have lower mean L_X (at the 2.8 σ level) and L_X/L_B (at the 3.5 σ level) than do the E galaxies, but that their L_B DFs are not significantly different (the mean L_B of the E galaxies is brighter than that of the S0 galaxies, but only at the 1.8 σ level). Thus S0 galaxies of a given optical luminosity are less able to maintain a significant halo of coronal gas than are E galaxies. We speculate that this is due to the increased fraction of rotational energy and shallower total potential of S0 compared to E galaxies due to the presence of disks.

5. We find a strong correlation between L_B and L_{12} for our full sample. The power-law slope of this correlation is 1.0 ± 0.1, in keeping with the expectation (e.g., Knapp et al. 1989; Knapp et al. 1992) that 12 μm emission from early-type galaxies should come mainly from circumstellar dust and cool stellar photospheres. If this is the case, then we would expect the slope of the L_X-L_{12} to be the same as that of the L_X-L_B correlation. Instead, we find them to differ by ~ 2.5 σ. Partial rank analysis indicates that the dominant underlying L_X-L_B and L_B-L_{12} relationships are what drive the bivariate L_X-L_{12} correlation. Considering the E and S0 galaxies separately, we find that the discrepancy between the observed and expected L_X-L_{12} behavior for our sample is due to the S0 galaxies having excess 12 μm emission for their optical luminosity, compared to the E galaxies. We speculate that this may be due to a contribution to the 12 μm flux from dust heated in star-forming regions in S0 disks.

6. We find no compelling evidence for a trend of L_{100} with L_X for the full sample from our either our bivariate or partial rank analysis. This may indicate that the dusty ISM in early-type galaxies is accreted. Alternatively, grains created in early-type galaxies may be destroyed relatively quickly by the hot ISM and ISFR in these galaxies. There is evidence for significant L_B-L_{100} and L_{12}-L_{100} correlations. These suggest that the second interpretation is more likely correct.

7. The lack of correlation between L_X and L_{100} is more pronounced for the E galaxies than for the full sample. There is evidence for such a trend for the S0 galaxies from the bivariate analysis, but it is not confirmed by the partial rank analysis. The L_{12}-L_{100} trend found for the full sample appears to be entirely driven by the S0 galaxies, as no evidence for such a trend exists among the E galaxies. This L_{12}-L_{100} correlation for the S0 galaxies is much stronger than any L_B-L_{12} relationship, arguing that much of the 12 μm emission from the S0 galaxies is interstellar, rather than photospheric in origin.

8. Differences between *IRAS* colors of our sample and the IBGS are consistent with lower dust temperatures and with higher average contribution of stellar (or circumstellar) emission to the MIR for the early-type sample than for the IBGS. The distribution of our sample in the Γ-Θ plane defined by Helou et al. (1991) is consistent with this interpretation. The distributions of the E and S0 galaxies in this plane further argues for a significant spiral-like interstellar dust contribution to the ISM of S0 galaxies. Optical-*IRAS* color-color plots provide further evidence that extinction is significant for some of the galaxies in our sample, and essentially all of these galaxies are S0s (see also points 5 and 7 above).

9. We find strong bivariate correlations between L_6 (and L_6/L_B) and L_B, L_X, and L_X/L_B. Partial rank analysis shows the L_B-L_6 trend to be the strongest of these, but all three are statistically significant. In particular, we cannot account for the L_X/L_B-L_6 relationship as being driven by underlying trends of these variables with L_B. Thus we find evidence for an underlying physical relationship between total radio power and X-ray–to–optical ratio. Regression analysis yields slopes much steeper than unity for the trends of L_6 with both L_X and L_X/L_B, arguing that this is *not* an example of a "bright-things-are-bright" correlation.

10. The strongest trend we find with L_6 from our partial rank analysis is that with L_{100}: the presence of an FIR-emitting ISM appears strongly coupled to the ability of early-type galaxies to generate nonthermal radio emission. We have confirmed the suggestion of Kim & Fabbiano (1990) that there is a relationship between L_X/L_B and the distribution of points in the L_6-L_{100} plane. Specifically, the systems with high L_X/L_B tend

to have higher L_6 and L_{100} than those with low L_X/L_B. Further, for a given L_{100}, the X-ray–bright galaxies are shifted to higher L_6 compared to the X-ray–faint galaxies. It appears from this that a hot ISM is a key factor for the generation of radio continuum emission in early-type galaxies. This mutual dependence between X-ray, radio, and FIR properties is in keeping with the idea that cooling flows may be responsible for fueling the active nucleus (FGT), and that the FIR from early-type galaxies with nonthermal radio sources is due to emission from dust heated by the nuclear engine rather than from externally accreted material (e.g., Walsh et al. 1989; Knapp et al. 1992).

11. There is no evidence for any difference between the E and the S0 galaxies in their radio to X-ray properties. We do find an L_{12}-L_6 trend for the S0 galaxies that is not present for the E galaxies. This further argues that there is a substantial nonphotospheric component to the 12 μm emission of S0 galaxies. In keeping with earlier studies (e.g., Wrobel & Heeschen 1991), we find that the E galaxies tend to have higher radio luminosities than the S0 galaxies at the $\sim 2.5\ \sigma$ level.

12. When we analyze radio core data for our sample, we find bivariate correlations with L_X and L_X/L_B comparable to those found for total radio emission. The regression slopes are consistent with those computed for total radio emission also. These results are in agreement with those from the smaller sample of FGT. Partial rank analysis shows stronger correlations between L_{6cm} and X-ray properties than those found for L_6. Thus the hot ISM in early-type galaxies does appear to be linked to core rather than total nonthermal radio activity. L_B, however, is more strongly coupled to L_6 than to L_{6cm}. It thus appears that radio cores are fueled by a hot ISM (as suggested by FGT) but that total radio power is related to total mass (assuming the mass of an early-type galaxy to scale with its optical luminosity) rather than to the presence of a hot ISM. This last point suggests that if massive black holes are the nuclear engines, the mass of the black hole is larger in more massive galaxies.

13. We find stronger correlations of L_{12} and L_{100} with L_{6cm} than with L_6. This reinforces the conclusion that substantial FIR emission is related to nuclear processes in early-type galaxies. It also supports the idea that there is a significant (nuclear) interstellar contribution to the MIR emission.

14. We find no evidence for a correlation of $M_{H\,I}$ with X-ray properties. This is in keeping with the results of Knapp et al. (1985), and is consistent with the hypothesis that the H I in E galaxies is accreted material.

There are a number of avenues that suggest themselves for further research based on the results of this study. One is the extension of the current work to consideration of observables related to the structure and stellar populations of the galaxies in our sample. We are undertaking this project and will report on our results in subsequent papers of this series. A second possibility that we are considering is to expand the current sample by constructing a similar X-ray database from the *ROSAT* observations of normal early-type galaxies. A subsequent analysis of such a combined *Einstein-ROSAT* X-ray database could also make use of the growing and now substantial collection of Hα data on early-type galaxies (Pogge & Eskridge 1987, 1993; Kim 1989; Shields 1991; Trinchieri and di Serego Alighieri 1991; Buson et al. 1993; Goudfrooij et al. 1994). Finally, we have conducted an ensemble study of the global properties of galaxies. While such a study is useful in identifying overall correlations between various global properties, only detailed, high-resolution studies of a substantial sample of early-type galaxies, in wavelengths ranging from X-rays through radio emission, will reveal the details of the physics underlying the feedback between the overall structure and the ISM in early-type galaxies.

We would like to thank Jay Gallagher, Glen Mackie, and Ginevra Trinchieri for their comments on this study as it has progressed. We would also like to thank Eric Feigelson and Michael LaValley for providing us with the latest versions of the ASURV software package. G. F. would like to thank the Aspen Summer School for the opportunity to focus on this project. P. B. E. would like to thank the organizers and participants of the Third Teton Summer School, where early results of this project were discussed. This research has made use of the NASA/IPAC Extragalactic Database (NED), which is operated by the Jet Propulsion Laboratory, Caltech, under contract with the National Aeronautics and Space Administration. D. W. K. acknowledges support by KOSEF grant 923-0200-007-2. We are grateful to the National Aeronautics and Space Administration for support of this research under LTSA grant NAGW2681 and contract NAS8-39073 (AXAF Science Center).

REFERENCES

Arp, H. 1966, ApJS, 14, 1
Bender, R., Paquet, A., & Nieto, J.-L. 1991, A&A, 246, 349
Bernlohr, K. 1993, A&A, 268, 25
Bertin, G., Pignatelli, E., & Saglia, R. P. 1993, A&A, 271, 381
Bertola, F., Galletta, G., Kotanyi, C., & Zeilinger, W. W. 1988, MNRAS, 234, 733
Binggeli, B., Sandage, A., & Tammann, G. A. 1988, ARA&A, 26, 509
Binney, J., & Tremaine, S. 1987, Galactic Dynamics (Princeton: Princeton Univ. Press)
Birkinshaw, M., & Davies, R. L. 1985, ApJ, 291, 32
Bothun, G. D., Lonsdale, C. J., & Rice, W. 1989, ApJ, 341, 129
Bottinelli, L., & Gouguenheim, L., 1977, A&A, 54, 641
Bottinelli, L., Gouguenheim, L., Fouqué, & Paturel, G. 1990, A&AS, 82, 391
Boulanger, F., Beichman, C., Désert, F. X., Helou, G., Pérault, M., & Ryter, C. 1988, ApJ, 332, 328
Bregman, J. N., Hogg, D. E., & Roberts, M. S. 1992, ApJ, 387, 484
Bridle, A. H., & Fomalont, E. B. 1978, AJ, 83, 704
Bridle, A. H., & Perley, R. A. 1984, ARA&A, 22, 319
Burns, J. O., Feigelson, E. D., & Schreier, E. J. 1983, ApJ, 273, 128
Buson, L. M., et al. 1993, A&A, 280, 409
Calvani, M., Fasano, G., & Franceschini, A. 1989, AJ, 97, 1319
Canizares, C. R., Fabbiano, G., & Trinchieri, G. 1987, ApJ, 312, 503
Ciotti, L., D'Ercole, A., Pellegrini, S., & Renzini, A. 1991, ApJ, 376, 380
Condon, J. J., Frayer, D. T., & Broderick, J. J. 1991, AJ, 101, 362
Corwin, H. G., Jr., de Vaucouleurs, A., & de Vaucouleurs, G. 1985, Southern Galaxy Catalogue (Austin: Univ. Texas Press)
David, L. P., Forman, W., & Jones, C. 1991, ApJ, 380, 39
Davidge, T. J. 1992, ApJ, 397, 457
de Vaucouleurs, G., de Vaucouleurs, A., Corwin, H. G., Jr., Buta, R. J., Paturel, G., & Fouqué, P. 1991, Third Reference Catalogue of Bright Galaxies (New York: Springer-Verlag) (RC3)

Disney, M. J., & Wall, J. V. 1977, MNRAS, 179, 235
Donnelly, R. H., Faber, S. M., & O'Connell, R. M. 1990, ApJ, 354, 52
Eder, J. A., Giovanelli, R., & Haynes, M. P. 1991, AJ, 102, 572
Ekers, R. D., & Ekers, J. A. 1973, A&A, 24, 247
Ekers, R. D., et al. 1989, MNRAS, 236, 737
Eskridge, P. B., & Pogge, R. W. 1991, AJ, 101, 2056
Fabbiano, G. 1989, ARA&A, 27, 87
Fabbiano, G., Gioia, I. M., & Trinchieri, G. 1988, ApJ, 324, 749
———. 1989, ApJ, 347, 127 (FGT)
Fabbiano, G., Kim, D.-W., & Trinchieri, G. 1992, ApJS, 80, 531 (P0)
———. 1994, ApJ, 429, 94
Fabbiano, G., Klein, U., Trinchieri, G., & Wielebinski, R. 1987, ApJ, 312, 111
Fabbiano, G., Miller, L., Trinchieri, G., Longair, M., & Elvis, M. 1984, ApJ, 277, 115
Fabbiano, G., & Schweizer, F. 1994, ApJ, submitted
Faber, S. M., & Gallagher, J. S. 1976, ApJ, 204, 365
Faber, S. M., Wegner, G., Burstein, D., Davies, R. L., Dressler, A., Lynden-Bell, D., & Terlevich, R. J. 1989, ApJS, 69, 763 (7S)
Feigelson, E. D., & Babu, G. J. 1992a, ApJ, 397, 55
———. 1992b, Statistical Challenges in Modern Astronomy (New York: Springer-Verlag)
Feigelson, E. D., & Nelson, P. I. 1985, ApJ, 293, 192
Feretti, L., Giovannini, G., Gregorini, L., Parma, P., & Zamorani, G. 1984, A&A, 139, 55
Fich, M., & Hodge, P. W. 1991, ApJ, 374, L17
Forbes, D. A. 1991, MNRAS, 249, 779
Forman, W., Jones, C., & Tucker, W. 1985, ApJ, 293, 102
Forman, W., Schwarz, J., Jones, C., Liller, W., & Fabian, A. C. 1979, ApJ, 234, L27
Fosbury, R. A. E., Mebold, U., Goss, H. M., & Dopita, M. A. 1978, MNRAS, 183, 549
Frank, J., & Gisler, G. 1976, MNRAS, 176, 533
Fullmer, L., & Lonsdale, C. 1989, Catalogued Galaxies and Quasars Observed in the *IRAS* Survey, Version 2 (Pasadena: JPL)
Gallagher, J. S., Knapp, G. R., Faber, S. M., & Balick, B. 1977, ApJ, 215, 463
Geldzahler, B. J., & Fomalont, E. B. 1978, AJ, 83, 1047
Giacconi, R., et al. 1979, ApJ, 230, 540
Gisler, G. 1976, A&A, 51, 137
Goudfrooij, P. 1991, Messenger, 63, 42
Goudfrooij, P., Hansen, L., Jørgensen, H. E., & Nørgaard-Nielsen, H.-U. 1994, A&AS, 105, 341
Gunn, J. E., & Gott, J. R. 1972, ApJ, 176, 1
Haynes, R. F., Herter, T., Barton, A. S., & Benensohn, J. S. 1990, AJ, 99, 1740
Haynes, R. F., Huchtmeier, W. K. H., Siegman, B. C., & Wright, A. E. 1975, A Compendium of Radio Measurements of Bright Galaxies (Melbourne: CSIRO)
Helou, G. 1986, ApJ, 311, L33
Helou, G., Ryter, C., & Soifer, B. T. 1991, ApJ, 376, 505
Hickson, P. 1982, ApJ, 255, 382
Hoyle, F. 1960, MNRAS, 120, 338
Huchtmeier, W. K., & Richter, O.-G. 1989, A General Catalog of H I Observations of Galaxies (New York: Springer-Verlag)
Humason, M. L., Mayall, N. U., & Sandage, A. R. 1956, AJ, 61, 97
Hummel, E., Beck, R., & Dettmar, R.-J. 1991, A&AS, 87, 309
Hummel, E., van der Hulst, J. M., & Dickey, J. M. 1984, A&A, 134, 207
Impey, C., & Gregorini, L. 1993, AJ, 105, 853
Isobe, T., Feigelson, E. D., Akritas, M. G., & Babu, G. J. 1990, ApJ, 364, 104
Isobe, T., Feigelson, E. D., & Nelson, P. I. 1986, ApJ, 306, 490
Johnson, D. W., & Gottesman, S. T. 1983, ApJ, 275, 549
Johnson, H. E., & Axford, W. I. 1971, ApJ, 165, 381
Jura, M. 1986, ApJ, 306, 483
Jura, M., Kim, D.-W., Knapp, G. R., & Guhathakurta, P. 1987, ApJ, 312, L11
Kendall, M., & Stuart, A. 1976, The Advanced Theory of Statistics, Vol. 2 (New York: Macmillan)
Killeen, N. E. B., Bicknell, G. V., & Ekers, R. D. 1986, ApJ, 302, 306
———. 1988, ApJ, 325, 180
Kim, D.-W. 1989, ApJ, 346, 653
Kim, D.-W., & Fabbiano, G. 1990, in Ap&SS Conf. Proc. 160, Windows on Galaxies, ed. G. Fabbiano, J. S. Gallagher, & A. Renzini (Dordrecht: Kluwer), 293
———. 1994, ApJ, in press
Kim, D.-W., Fabbiano, G., & Trinchieri, G. 1992a, ApJS, 80, 645
———. 1992b, ApJ, 393, 134
Knapp, G. R., Gallagher, J. S., & Faber, S. M. 1978, AJ, 83, 139
Knapp, G. R., Guhathakurta, P., Kim, D.-W., & Jura, M. 1989, ApJS, 70, 329
Knapp, G. R., Gunn, J. E., & Wynn-Williams, C. G. 1992, ApJ, 399, 76
Knapp, G. R., Turner, E. L., & Cunniffe, P. E. 1985, AJ, 90, 454
Kormendy, J. 1985, ApJ, 295, 73
Kritsuk, A. G. 1992, A&A, 261, 78
LaValley, M. P., Isobe, T., & Feigelson, E. D. 1992, BAAS, 24, 839
Lonsdale, C. J., Helou, G., Good, J. C., & Rice, W. 1985, Catalogued Galaxies and Quasars in the *IRAS* Survey (Pasadena: JPL)
Maltby, P., & Moffet, A. T. 1962, ApJS, 7, 141
Marston, A. P. 1988, MNRAS, 231, 333
Mathews, W. G., & Baker, J. C. 1971, ApJ, 170, 241
Mayall, N. U. 1939, PASP, 51, 282
Neff, S. G., & Hutchings, J. B. 1992, AJ, 103, 1746
Pellegrini, S., & Fabbiano, G. 1994, ApJ, 429, 105
Phillips, M. M., Charles, P. A., & Baldwin, J. A. 1983, ApJ, 266, 485
Pogge, R. W., & Eskridge, P. B. 1987, AJ, 93, 291
———. 1993, AJ, 106, 1405
Rice, W., Lonsdale, C. J., Soifer, B. T., Neugebauer, G., Kopan, E. L., Lloyd, L. A., deJong, T., & Habing, H. J. 1988, ApJS, 68, 91
Roberts, M. S. 1975, in Stars and Stellar Systems, Vol. 9, Galaxies and the Universe, ed. A. Sandage, M. Sandage, & J. Kristian (Chicago: Univ. Chicago Press), 309
Roberts, M. S., Hogg, D. E., Bregman, J. N., Forman, W. R., & Jones, C. 1991, ApJS, 75, 751
Rowan-Robinson, M., & Crawford, J. 1989, MNRAS, 238, 523
Sadler, E. M., Jenkins, C. R., & Kotanyi, C. G. 1989, MNRAS, 240, 591
Sage, L. J., & Wrobel, J. M. 1989, ApJ, 344, 204
Sandage, A. 1961, A Hubble Atlas of Galaxies (Washington, DC: Carnegie Institution of Washington)
Schmitt, J. H. M. M. 1985, ApJ, 293, 178
Shields, J. C. 1991, AJ, 102, 1314
Soifer, B. T., Boehmer, L., Neugebauer, G., & Sanders, D. B. 1989, AJ, 98, 766
Soifer, B. T., Sanders, D. B., Madore, B. F., Neugebauer, G., Danielson, G. E., Elias, J. H., Lonsdale, C. J., & Rice, W. L. 1987, ApJ, 320, 238
Stanger, V. J., & Warwick, R. S. 1986, MNRAS, 220, 363
Sulentic, J. W. 1976, ApJS, 32, 171
Thronson, H. A., Jr., & Bally, J. 1987, ApJ, 319, L63
Thronson, H. A., Jr., Tacconi, L., Kenney, J., Greenhouse, M. A., Margulis, M., Tacconi-Garman, L., & Young, J. S. 1989, ApJ, 344, 747
Trinchieri, G., & di Serego Alighieri, S. 1991, AJ, 101, 1647
Trinchieri, G., & Fabbiano, G. 1985, ApJ, 296, 447
Trinchieri, G., Fabbiano, G., & Canizares, C. R. 1986, ApJ, 310, 637
Trinchieri, G., Kim, D.-W., Fabbiano, G., & Canizares, C. 1994, ApJ, 428, 555
van Gorkom, J. H., Knapp, G. R., Ekers, R. D., Ekers, D. D., Laing, R. A., & Polk, K. S. 1989, AJ, 97, 708
Vereshchagin, S. V., Smirnov, M. A., & Tutukov, A. V. 1989, Soviet Astron.—AJ, 33, 269
Véron-Cetty, M.-P., & Véron, P. 1988, A&A, 204, 28
Walsh, D. E. P., Knapp, G. R., Wrobel, J. M., & Kim, D.-W. 1989, ApJ, 337, 209
Wardle, M., & Knapp, G. R. 1986, AJ, 91, 23
Whiteoak, J. B., & Gardner, F. F. 1977, Australian J. Phys., 30, 187
Wilcots, E. M., Hodge, P. W., Eskridge, P. B., Bertola, F., & Buson, L. 1990, ApJ, 364, 87
Wilkinson, A., Browne, I. W. A., Kotanyi, C., Christiansen, W. A., Williams, R., & Sparks, W. B. 1987, MNRAS, 224, 895
Wright, A. E. 1974, MNRAS, 167, 273
Wrobel, J. M. 1991, AJ, 101, 127
Wrobel, J. M., & Heeschen, D. S. 1984, ApJ, 287, 41
———. 1988, ApJ, 335, 677
———. 1991, AJ, 101, 148

THE ASTROPHYSICAL JOURNAL, 442:523–537, 1995 April 1

A MULTIPARAMETRIC ANALYSIS OF THE *EINSTEIN* SAMPLE OF EARLY-TYPE GALAXIES. II. GALAXY FORMATION HISTORY AND PROPERTIES OF THE INTERSTELLAR MEDIUM

PAUL B. ESKRIDGE[1,2] AND GIUSEPPINA FABBIANO[3]
Harvard-Smithsonian Center for Astrophysics, 60 Garden Street, Cambridge, MA 02138
AND
DONG-WOO KIM[4]
Harvard-Smithsonian Center for Astrophysics; and Department of Astronomy and Space Science, Chungnam National University, Taejon, 305-764, South Korea
Received 1994 July 22; accepted 1994 October 12

ABSTRACT

We have conducted bivariate and multivariate statistical analysis of data measuring the integrated luminosity, shape, and potential depth of the *Einstein* sample of early-type galaxies (presented by Fabbiano et al. 1992). We find significant correlations between the X-ray properties and the axial ratios (a/b) of our sample, such that the roundest systems tend to have the highest L_X and L_X/L_B. The most radio-loud objects are also the roundest. We confirm the assertion of Bender et al. (1989) that galaxies with high L_X are boxy (have negative a_4). Both a/b and a_4 are correlated with L_B, but not with *IRAS* 12 μm and 100 μm luminosities. There are strong correlations between L_X, Mg_2, and σ_v in the sense that those systems with the deepest potential wells have the highest L_X and Mg_2. Thus the depth of the potential well appears to govern both the ability to retain an ISM at the present epoch and to retain the enriched ejecta of early star formation bursts. Both L_X/L_B and L_6 (the 6 cm radio luminosity) show threshold effects with σ_v, exhibiting sharp increases at $\log(\sigma_v) \approx 2.2$. Finally, there is clearly an interrelationship between the various stellar and structural parameters: The scatter in the bivariate relationships between the shape parameters (a/b and a_4) and the depth parameter (σ_v) is a function of abundance in the sense that, for a given a_4 or a/b, the systems with the highest σ_v also have the highest Mg_2. Furthermore, for a constant σ_v, disky galaxies tend to have higher Mg_2 than boxy ones. Alternatively, for a given abundance, boxy ellipticals tend to be more massive than disky ellipticals. One possibility is that early-type galaxies of a given mass, originating from mergers (boxy ellipticals), have *lower* abundances than "primordial" (disky) early-type galaxies. Another is that disky inner isophotes are due not to primordial dissipational collapse, but to either the self-gravitating inner disks of captured spirals or the dissipational collapse of new disk structures from the premerger ISM. The high measured nuclear Mg_2 values would thus be due to enrichment from secondary bursts of star formation triggered by the merging event.

Subject headings: galaxies: elliptical and lenticular, cD — galaxies: ISM — galaxies: structure — X-rays: galaxies

1. INTRODUCTION

The connection between the structural and stellar properties of galaxies and the nature of their interstellar medium (ISM) was first discussed by Spitzer (1954). The basic situation, as it was understood ~35 years ago, was laid out by Sandage (1961). Our ability to observe, and thus our understanding of, the ISM has increased enormously since then. Current observational techniques allow us to collect data on the solid phase of the ISM (dust grains), as well as gas phases ranging from cold molecular cloud cores ($T \sim 10$ K, $n \sim 10^6$ cm^{-3}) to X-ray–emitting gas ($T \sim 10^{6-7}$ K, $n \gtrsim 0.1$ cm^{-3}). Our understanding of the relationships between ISM properties and the structural and stellar properties of galaxies is thus undergoing a concomitant rapid development.

Early-type (E and S0) galaxies, once considered devoid of intestellar gas, are now known to possess rich and complex ISM. Although many early-type galaxies exhibit the ISM tracers more traditionally associated with late-type galaxies (e.g., Huchtmeier & Richter 1989 and Eder, Giovanelli, & Haynes 1991 for H I; Sage & Wrobel 1989 and Thronson et al., 1989 for CO; Goudfrooij et al. 1994 for Hα; Knapp et al. 1989 for FIR), X-ray observations, beginning with the *Einstein Observatory* (Giacconi et al. 1979) have demonstrated that the ISM in luminous early-type galaxies is typically dominated by a hot ISM (see Fabbiano 1989 and references therein).

In the previous paper of this series (Eskridge, Fabbiano, & Kim 1995, hereafter P1), we presented an analysis of the ISM properties of the *Einstein* sample of early-type galaxies (Fabbiano, Kim, & Trinchieri 1992, hereafter P0). The major results of P1 are as follows: In agreement with previous studies (see Fabbiano 1989 and references therein), we find a strong correlation between L_B and L_X, with a power-law slope of 1.8 ± 0.1. However, this is actually a combination of a slope 1 relation for the fainter galaxies [$\log(L_X) \leq 40.5$] and a slope 2 relation for the more luminous galaxies. This result is consistent with previous work indicating that X-ray–faint early-type galaxies do not retain any significant quantities of hot ISM (Trinchieri & Fabbiano 1985; Fabbiano, Gioia, & Trinchieri 1989, hereafter FGT). In this case, their X-ray emission should be dominated by the integrated output of discrete sources similar to those found in the bulge of M31 (van Speybroeck et al. 1979). The X-ray emission from more distant spiral bulges is

[1] Current address: Department of Physics and Astronomy, University of Alabama, Tuscaloosa, AL 35487.
[2] paul@hera.astr.ua.edu.
[3] pepi@cfa.harvard.edu.
[4] kim@cfa.harvard.edu.

well modeled by a composite of such sources (Fabbiano, Gioia, & Trinchieri 1988). These results are also supported by differences found between the X-ray spectra of X-ray–bright and X-ray–faint E and S0 galaxies, suggesting the presence of stellar emission in the X-ray–faint objects (Kim, Fabbiano, & Trinchieri 1992b; Fabbiano, Kim, & Trinchieri 1994; Fabbiano 1994).

The mean values of the distribution functions of both L_X and L_X/L_B for the S0's are lower than those for the E's at the 2.8 σ and 3.5 σ levels, respectively. Thus, for a given stellar luminosity, the potential wells of S0's may be shallower than those of E's. The rotation of the S0 disks may be an important factor (see also Pellegrini 1994). The other differences found between E and S0 galaxies may be related to differences in their star formation histories: Our S0 sample has excess 12 μm emission compared to the E sample, when scaled by their optical luminosities. This may be due to emission from dust heated in star-forming regions in S0 disks. This interpretation is supported by the existence of a strong L_{12}-L_{100} correlation for our S0 sample that is not found for the Es and by an analysis of optical-IR colors.

We also find strong indications of a connection between galaxy ISM and nuclear activity. There are steep power-law slopes between radio luminosity and optical, X-ray properties, and FIR properties. This last point argues that the presence of a FIR-emitting ISM in early-type galaxies is coupled to their ability to generate nonthermal radio continuum, as previously argued by, e.g., Walsh et al. (1989). However, we also find that for a given L_{100}, galaxies with larger L_X/L_B tend to be stronger nonthermal radio sources, as originally suggested by Kim & Fabbiano (1990). We note that while L_B is most strongly correlated with L_6, the *total* radio luminosity (summed over a $\sim 1\%$ bandwidth around 6 cm—see P1), both L_X and L_X/L_B are more strongly correlated with L_{6co}, the *core* radio luminosity. These points support the argument (proposed by FGT) that radio cores in early-type galaxies are fueled by the accretion of cooling flow gas from the hot ISM.

The picture that emerges from P1 connects the properties of the ISM in E and S0 galaxies to their star formation history and nuclear activity. We confirm the differences between X-ray–bright and X-ray–faint galaxies and link these differences to the relative ability to retain a hot ISM. This ability is potentially connected to galaxy morphology, but this is not a complete explanation, as both Es and S0's can be found over a very large range of L_X/L_B. However, the results of P1 suggest a link between the characteristics of the galaxy potential and the retention of a hot ISM. This is not a tautology, as other mechanisms such as ram-pressure stripping, interactions with close neighbors (e.g., White & Sarazin 1991), variation in the SN Ia rate, and overall evolutionary state of the ISM (e.g., Ciotti et al., 1991; Pellegrini & Fabbiano 1994) could also effect the L_X/L_B for galaxies of a given luminosity.

To further explore the role of the shape and depth of the galaxy potential in determining the state of the ISM in early-type galaxies and how this relates to galaxy formation mechanisms, we extend the study of P1 with a consideration of available data on the structure and stellar populations of the *Einstein* sample. The data collected in P1 (see Table 1 of P1) will be used in this paper to compare with the information relating to the structural and stellar properties of the sample. In § 2, we describe how we have built our data set for this project and review the required statistical methods. We present our analysis of the axial ratio data in § 3. The Mg_2 results are given in § 4, those for σ_v in § 5, and those for a_4 in § 6. We summarize our results and conclusions and discuss possible strategies for future research in § 7. The Appendix contains details of our statistical analysis.

2. SAMPLE CONSTRUCTION AND STATISTICAL METHODS

We have gathered information from the literature regarding the structural and chemical properties of the galaxies in our sample. Axial ratios have been taken from de Vaucouleurs et al. (1991, hereafter RC3). These are listed, for the entire sample, in Table 1 of P1. We discovered a zero-point offset between the a/b values from de Vaucouleurs, de Vaucouleurs, & Corwin (1976) and those of Faber et al. (1989, hereafter 7S). Such an offset does not exist for the RC3 values compared to the 7S values. We have therefore adopted the more extensive set of values from the RC3. The a_4 parameter, defined in Bender et al. (1989), is a measure of the amplitude of the cos (4θ) Fourier component of the deviation from ellipticity of the isophotes of early-type systems. Values of a_4 for 47 galaxies in our sample have been published by Bender et al. (1989) and Peletier et al. (1990). We have taken values of log (σ_v) (for 74 galaxies) and Mg_2 (for 73 galaxies)from 7S. All these available data are given in Table 1.

Many of our data in the X-ray, FIR, and radio are upper limits. Therefore, the use of standard statistical techniques is manifestly invalid for our project. Instead we use techniques from the field of survival analysis for both evaluating the existence of bivariate correlations amongst our data and for determining best-fit regression coefficients. These methods explicitly account for the existence of upper limits in the samples being tested, subject to regularity conditions that may or may not apply in the case of any given data sample. This last point is, of course, the standard problem in all astronomical statistical analysis. In an effort to minimize it, we use a number of different statistical tests, each with their own assumptions about the nature of the data and distribution of the upper limits, in the hopes that gross violations of the normality assumptions by our data will manifest themselves in highly discrepant results for the various statistical tests. Basic references in the astronomical literature for these methods are Feigelson & Nelson (1985), Schmitt (1985), Isobe, Feigelson, & Nelson (1986), LaValley, Isobe & Feigelson (1992), and Fiegelson & Babu (1992). Details of our particular procedures are given in P1.

As we are dealing with a multiparametric data set, it is important to investigate possible interrelationships between the various observables in our sample. A technique used in previous studies (Fabbiano et al. 1988; P1) is the partial Spearman rank method (Kendall & Stuart 1976). In brief, to apply this method, one builds a matrix of modified Spearman rank coefficients for the parameters to be tested, and then tests the correlation between subsamples of the parameters in the matrix set while holding all other variables in the matrix set constant. The major results of the partial-rank analysis are presented in the text below. The full details of our results are tabulated in Appendix A. As we do not have terribly large samples for some combinations of observables, there is some reason for concern that we may obtain correlations (or noncorrelations) from our partial-rank analysis that would not stand up if we had a truly large sample. In order to examine this possibility, we drew a number of random subsamples from our L_B-L_X-a/b and L_B-L_X-a/b-Mg_2 samples (discussed in §§ 3 and 4, below) and subjected them to partial-rank analysis. In no case did correlations appear for the subsamples that were

TABLE 1

STRUCTURAL DATA

Name	Type	log(a/b) 7S	log(a/b) RC3	Mg_2 mags	logσ_v km/sec	$a_4/a\times100$
NGC 205	-3	0.26	0.30			
NGC 221	-6	0.06	0.13	0.185	1.892	
NGC 315	-3	0.14	0.20	0.283	2.546	−0.46
NGC 499	-3	0.19	0.10	0.334	2.374	
NGC 507	-2	0.02	0.00	0.302	2.563	
NGC 533	-5	0.10	0.21	0.316	2.504	0.00
NGC 584	-2	0.22	0.26	0.283	2.337	1.50
NGC 596	-5	0.06	0.19	0.249	2.179	1.30
NGC 720	-5	0.22	0.29	0.330	2.392	−0.30
NGC 1052	-3	0.17	0.16	0.316	2.313	0.00
NGC 1172	-2	0.04	0.11	0.246	2.083	
NGC 1316	-2	0.12	0.15			
NGC 1395	-5	0.11	0.12	0.313	2.412	
NGC 1399	-5	0.07	0.03	0.334	2.491	
NGC 1404	-5	0.08	0.05	0.317	2.353	
NGC 1400	-3	0.04	0.06	0.309	2.398	0.00
NGC 1407	-5	0.02	0.03	0.327	2.455	−0.30
NGC 1553	-2		0.20			
NGC 1600	-5	0.19	0.17	0.324	2.506	−1.10
NGC 2314	-5	0.11	0.09	0.327	2.463	
NGC 2300	-5	0.11	0.14	0.319	2.430	1.10
NGC 2563	-2	0.16	0.14	0.330	2.416	
NGC 2629	-2	0.15	0.07	0.308	2.380	
NGC 2694	-5		0.01			
NGC 2693	-5	0.18	0.16	0.328	2.445	1.00
NGC 2832	-5	0.14	0.10	0.340	2.557	−0.40
NGC 2974	-5	0.16	0.23	0.300	2.346	0.50
NGC 3078	-5	0.19	0.08	0.334	2.376	
NGC 3115	-2	0.41	0.47	0.309	2.425	
NGC 3258	-5	0.04	0.07	0.342	2.435	0.00
NGC 3377	-5	0.27	0.24	0.270	2.116	1.55
NGC 3379	-5	0.07	0.05	0.308	2.303	0.25
NGC 3585	-3	0.24	0.26	0.308	2.343	
NGC 3607	-2	0.09	0.30	0.303	2.394	
NGC 3608	-5	0.13	0.09	0.312	2.310	−0.20
NGC 3818	-5	0.20	0.22	0.315	2.314	2.30
NGC 3894	-5	0.27	0.21	0.322	2.422	−0.70
NGC 3923	-3	0.23	0.18	0.306	2.335	−0.40
NGC 4105	-2	0.10	0.13	0.299	2.384	
NGC 4168	-5	0.04	0.08	0.260	2.259	0.80
NGC 4251	-2		0.39			2.80
NGC 4261	-5	0.09	0.05	0.330	2.468	−1.60
NGC 4291	-5	0.13	0.08	0.308	2.413	−0.40
NGC 4365	-5	0.14	0.14	0.321	2.394	−1.10
NGC 4374	-5	0.08	0.06	0.305	2.458	−0.50
NGC 4382	-2		0.11			0.80
NGC 4387	-5	0.24	0.21	0.240	1.922	−1.00
NGC 4406	-3	0.13	0.19	0.311	2.398	−0.85
NGC 4458	-5	0.10	0.04	0.227	2.027	
NGC 4467	-5	0.12	0.10	0.262	1.917	
NGC 4472	-3	0.12	0.09	0.306	2.458	−0.35
NGC 4473	-5	0.29	0.25	0.304	2.250	0.90
NGC 4550	-3		0.55			1.67
NGC 4551	-5	0.15	0.10	0.264	1.999	−0.90
NGC 4552	-2	0.02	0.04	0.324	2.417	
NGC 4564	-5	0.40	0.38	0.321	2.185	2.20
NGC 4589	-5	0.09	0.09	0.320	2.332	
NGC 4621	-5	0.19	0.16	0.328	2.381	1.50
NGC 4636	-3	0.09	0.11	0.311	2.281	−0.15
NGC 4649	-2	0.10	0.09	0.338	2.533	−0.50
NGC 4645	-5	0.24	0.21	0.273	2.233	
NGC 4697	-5	0.23	0.19	0.297	2.218	2.00
NGC 4782	-5	0.08	0.02	0.333	2.522	
IC 3896	-5	0.04	0.12		2.346	
NGC 5044	-5	0.00	0.00	0.324	2.370	
NGC 5077	-5	0.17	0.11	0.295	2.439	−0.90
NGC 5102	-2	0.24	0.49	0.005		
IC 4296	-5	0.06	0.02	0.323	2.509	
IC 4329	-2	0.15	0.24	0.336	2.447	0.80
NGC 5322	-5	0.17	0.18	0.276	2.350	−0.90
NGC 5485	-2	0.04	0.08	0.291	2.190	
NGC 5532	-2		0.00			−0.70
NGC 5576	-5	0.14	0.20	0.253	2.272	−0.50
NGC 5846	-2	0.04	0.03	0.321	2.444	
NGC 5982	-5	0.14	0.12	0.296	2.425	−0.80
NGC 6146	-2	0.16	0.10	0.289	2.435	
NGC 6876	-5	0.11	0.11	0.284	2.364	0.60
NGC 7236	-3	0.13	0.00	0.309	2.226	
NGC 7237	-3	0.03	0.00	0.327	2.234	
NGC 7332	-2		0.56			
IC 1459	-5	0.15	0.14	0.321	2.488	
NGC 7562	-5	0.18	0.18	0.291	2.385	
NGC 7619	-5	0.12	0.04	0.336	2.528	0.30
NGC 7626	-5	0.06	0.05	0.336	2.369	0.40

not also present for the full sample. A number of correlations that are present for the full sample disappeared for some of the subsamples. However, this was typically due to the decrease in the number of objects in the sample, rather than a decrease in the correlation statistic. We conclude that the strong correlations and clear noncorrelations we find are robust. It is, however, quite possible that our more marginal results would be reversed if tested with a larger sample. We urge the reader to keep this caveat in mind.

3. COMPARISONS WITH AXIAL RATIOS

3.1. *X-Ray and Optical Trends*

In Figure 1*a* we show a scatter plot of L_B against a/b. There is some evidence for a relationship in that the most luminous objects are also the roundest. Table 2 shows the results of the bivariate correlation tests on this sample: there does appear to be a statistically significant effect. If we break the sample into E and S0 subsets, we find similar distributions for both types, with the distinction that the range in axial ratio for the S0's is inevitably larger than that of the ellipticals. However, the statistical analysis of the two subsets shows no compelling evidence for correlation between L_B and a/b (see Table 2). The correlation for the full sample is only at the $\sim 1\%$ level: halving the sample size by testing the Es and S0's independently may simply reduce the sample size to the point that the correlation vanishes. Also, any intrinsic relationship between axial ratio and luminosity will be partially masked by the projection of the three-dimensional galaxies onto two dimensions. We note, however, that the most optically luminous galaxies in both subsamples are also the roundest.

The comparison of L_X with a/b is shown in Figure 1*b*. The trend with a/b noted above for L_B appears much more pronounced for L_X. Indeed, the results of the bivariate analysis (Table 2) show the effect to be much stronger than for L_B. We note that the correlation we see is not a strict linear one. It is more of a wedge: Galaxies with small a/b span the full range of L_X. Galaxies with large a/b all have $L_X \lesssim 10^{41}$ ergs s^{-1}. One might expect that this effect would be a strong function of morphology, but separation by type shows that, as well as it can be defined (given the inevitably small number of ellipticals with large a/b), the trend holds up for both ellipticals and S0's. The statistical correlation does not, however, (Table 2). It breaks down particularly for the ellipticals. We note that the only two objects with log $(a/b) \gtrsim 0.3$ (i.e., roughly E5) have fairly low X-ray upper limits. These could, however, be misclassified S0's. The trend for the S0's is weaker than for the full sample but is still significant in two of the three tests. The relationship defined by L_X/L_B is stronger than that defined by L_X (see Table 2 and Fig. 1*c*), and once again, the trend holds for both morphological subsets. More importantly, with the exception of the Cox-Hazard test for the Es, the statistical correlation holds for both subsets: For either Es or S0's alone, there is a positive correlation such that those systems with the largest L_X/L_B are the roundest objects. It is very hard to imagine how projection effects could create such a correlation, although they could easily destroy it, as apparently round galaxies could be *intrinsically* flattened, but viewed face on.

A partial-rank analysis on L_B-L_X-L_X/L_B-a/b for the full sample confirms that the underlying trend is that between L_X/L_B and a/b, in the sense that the roundest galaxies have the largest L_X/L_B (see Table A1a; see Appendix for details on this table). The bivariate trends of a/b with both L_B and L_X appear to be driven by this underlying relationship. We obtain the same results if we remove the Local Group dwarfs from the

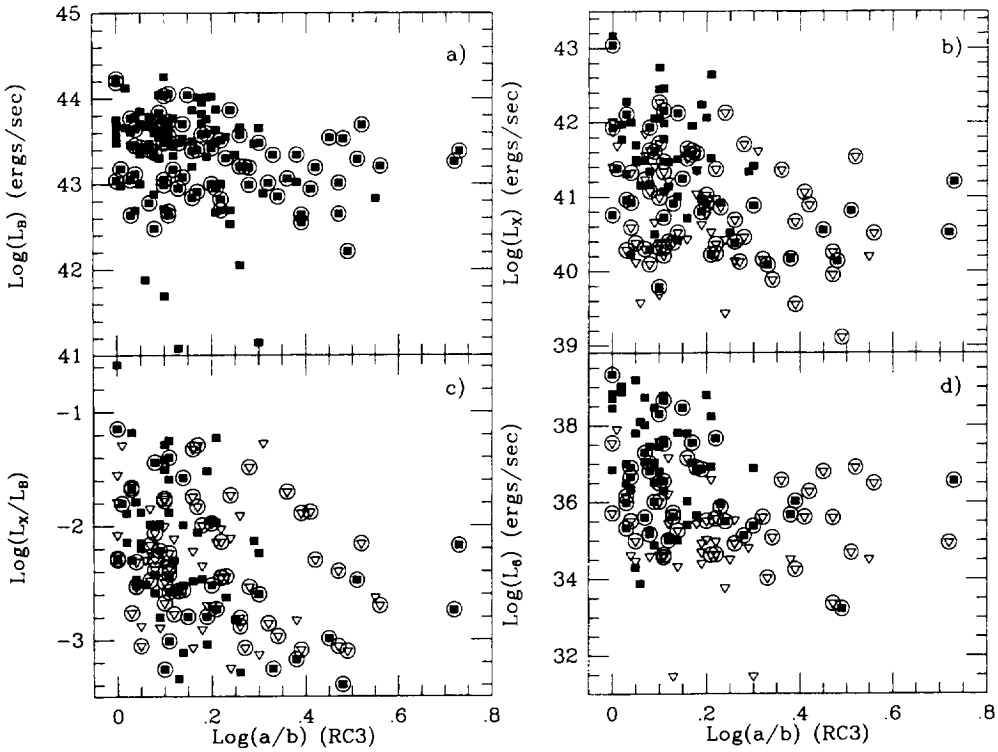

FIG. 1.—Plot of log (a/b) against (a) L_B, (b) L_X, (c) L_X/L_B, and (d) L_6 for the full sample. Solid squares represent detections. Down-pointing open triangles represent upper limits. Circled points represent the S0's.

TABLE 2

BIVARIATE CORRELATION TESTS WITH THE LUMINOSITY DATA

	L_X		L_B		L_X/L_B		L_{12}		L_{100}		L_6	
	N_{tot}	N_{lim}[b]	N_{tot}	N_{lim}	N_{tot}	N_{lim}	N_{tot}	N_{lim}	N_{tot}	N_{lim}	N_{tot}	N_{lim}
	Cox-Hazard[a]	prob		prob		prob		prob		prob		prob
	Kendall's τ	prob		prob		prob		prob		prob		prob
	Spearman rank	prob		prob		prob		prob		prob		prob
a/b	147	77	147	0	147	77	134	75	135	48	133	63
	9.727	0.0018	6.671	0.0098	14.343	0.0002	0.549	0.4587	1.724	0.1892	2.876	0.0899
	4.337	$< 10^{-4}$	3.260	0.0011	4.735	$< 10^{-4}$	1.013	0.3112	0.594	0.5522	4.960	$< 10^{-4}$
	−0.346	$< 10^{-4}$	−0.270	0.0011	−0.389	$< 10^{-4}$	−0.080	0.3544	−0.077	0.3756	−0.435	$< 10^{-4}$
Mg_2	73	26	73	0	73	26	69	39	69	28	72	26
	17.442	$< 10^{-4}$	20.965	$< 10^{-4}$	13.450	0.0002	8.786	0.0030	4.549	0.0329	12.823	0.0003
	4.395	$< 10^{-4}$	3.212	0.0013	3.962	0.0001	2.991	0.0028	1.366	0.1720	3.472	0.0005
	0.514	$< 10^{-4}$	0.361	0.0022	0.479	$< 10^{-4}$	0.372	0.0022	0.185	0.1261	0.426	0.0003
σ_v	74	27	74	0	74	27	68	39	68	29	72	27
	29.165	$< 10^{-4}$	50.449	$< 10-4$	21.787	$< 10^{-4}$	8.909	0.0028	11.516	0.0007	16.694	$< 10^{-4}$
	6.091	$< 10^{-4}$	5.984	$< 10-4$	5.072	$< 10^{-4}$	2.523	0.0116	3.166	0.0015	4.259	$< 10^{-4}$
	0.670	$< 10^{-4}$	0.634	$< 10-4$	0.586	$< 10^{-4}$	0.312	0.0105	0.398	0.0011	0.494	$< 10^{-4}$
a_4	47	16	47	0	47	16	46	26	46	18	47	20
	9.648	0.0019	6.287	0.0122	10.010	0.0016	2.813	0.0935	4.331	0.0374	7.338	0.0068
	2.684	0.0073	2.351	0.0187	2.397	0.0165	1.371	0.1704	1.679	0.0932	2.889	0.0039
	−0.424	0.0040	−0.324	0.0280	−0.374	0.0111	−0.218	0.1438	−0.300	0.0439	−0.381	0.0097
a_4	44	13	44	0	44	13	43	23	43	16	44	18
no dEs	15.540	0.0001	12.601	0.0004	11.426	0.0007	6.704	0.0096	5.602	0.0179	10.758	0.0010
	3.333	0.0009	3.261	0.0011	2.795	0.0052	1.878	0.0603	2.076	0.0379	3.526	0.0004
	−0.537	0.0004	−0.473	0.0019	−0.439	0.0040	−0.307	0.0466	−0.378	0.0144	−0.498	0.0011
a/b	73	31	73	0	73	31	64	36	64	24	70	29
Es only	1.017	0.3132	3.749	0.0528	0.877	0.3490	3.475	0.0623	1.572	0.2099	1.147	0.2842
	2.620	0.0088	1.411	0.1582	2.835	0.0046	1.392	0.1640	0.627	0.5307	4.117	$< 10^{-4}$
	−0.295	0.0119	−0.169	0.1484	−0.323	0.0058	−0.181	0.1500	−0.106	0.4011	−0.479	0.0001
a/b	74	47	74	0	74	47	70	39	71	24	62	34
S0s only	2.708	0.0998	2.699	0.1004	3.953	0.0468	0.066	0.7970	1.184	0.2764	6.513	0.0107
	2.978	0.0029	1.845	0.0650	3.259	0.0011	0.236	0.8134	0.474	0.6354	2.481	0.0131
	−0.329	0.0049	−0.215	0.0665	−0.343	0.0034	0.004	0.9729	−0.092	0.4400	−0.328	0.0104

[a] The values in rows (2)–(4) of these columns are the test scores for the three correlation tests.

[b] The N_{lim} are the number of limit points.

sample. Recalling that projection effects will *clearly* weaken a trend between L_X/L_B and a/b, *we find compelling evidence for a physical correlation between the presence of X-ray gas and the shape of the gravitational potential in early-type galaxies.* The trends of a/b with both L_X and L_X/L_B are significantly weakened with a_4 held constant (see Table A1a). This may be an effect of the reduction in sample size (less than a third of our full sample has a_4 measurements), or it may be due to underlying trends of both the X-ray properties and a/b with a_4. This matter is discussed further in §§ 6.1 and 6.3. An L_B-a/b trend *does* appear when pairs or triplets including the X-ray properties and either or both of Mg_2 and σ_v are held constant (see Table A1a). This trend is in the sense that more optically luminous galaxies are *flatter* for constant Mg_2 or σ_v. This is in keeping with the observation that systems with more predominant disk components (i.e., spirals) tend to have lower abundances than do ellipticals for a given luminosity.

Considering the Es only, the partial-rank analysis gives trends that are substantially weaker (see Table A1b). However, we still find evidence for trends between a/b and both L_X and L_X/L_B, with the L_X/L_B-a/b relation being the stronger. Removal of the Local Group dwarfs does not change these results. For the S0's, the trends are significantly stronger than for the Es (although weaker than for the full sample), with the L_X/L_B-a/b trend again being the dominant one (see Table A1b). This is particularly interesting, as the presence of significant disks in the S0's should make the L_X/L_B-a/b correlation more susceptible to projection than the Es. This therefore supports the conclusion that there is an underlying physical effect operating to enhance L_X/L_B is those galaxies with the roundest potentials.

3.2. *Trends with Other ISM Tracers*

The same sort of trend appears to exist between L_6 and a/b (see Fig. 1*d*), although the Cox-Hazard test is discrepant for the full sample and the Es (see Table 2). Partial-rank analysis confirms that there is a good correlation between radio power and axial ratio, independent of trends between these parameters and optical or X-ray properties (see Table A1a). This trend is in keeping with the result of Disney, Sparks, & Wall (1984) that radio-loud ellipticals tend to be significantly rounder than radio-silent ellipticals. Smith & Heckman (1989) do not confirm this result. However, they concentrate specifically on the most powerful radio galaxies, whereas both the Disney et al. sample and our own examine galaxies over a much larger range of radio power.

Knapp, Gunn, & Wynn-Williams (1992) argue quite convincingly that the bulk of the midinfrared emission from early-type galaxies is due to stellar and circumstellar radiation and thus should scale with optical luminosity (see, however the recent work of Sauvage & Thuan 1994). In P1, we found a difference at the 2 σ level between the slopes of the relationships of L_B and L_{12} with L_X that appears to be driven entirely by the S0's. Having derived a reasonably strong correlation between L_B and a/b, we have thus tested for a correlation between L_{12} and a/b. We find no evidence for such a correlation for our full sample (see Table 2). We also find no compelling evidence for correlation for either the Es or S0's tested separately, but the S0's form an essentially random sample, while the Es show at least *some* weak trend (see Table 2). If there is an underlying (if weak) relationship between the stellar luminosity (L_*) and *intrinsic* axial ratio of ellipticals/bulges, this relationship will appear weaker due to projection effects. Such a trend is suggested by the result of Kim (1988) that the *IRAS* 12 μm detection rate is significantly higher for round ellipticals than for flattened ones. For S0's, in addition to the bulge there is some contribution from the disk. If S0 disks do, in fact, have significant amounts of cool ISM (as argued in P1), then the total emission at 12 μm will be a composite of both stellar emission and diffuse emission from warm grains. The presence of a disk will make the system intrinsically flatter. Furthermore, the more prominent the disk, the more its diffuse ISM will contribute to L_{12}, and the larger its intrinsic a/b. This will work in the sense of destroying any correlation between L_{12} and a/b seen for "pure" bulge populations as a manifestation of an intrinsic L_*-a/b correlation.

We have tested our sample for a possible correlation of L_{100} with a/b and have found no evidence for any such correlation (see Table 2).

4. COMPARISONS WITH Mg_2

Mg_2 values are given for 73 of the galaxies in our sample by 7S. Figure 2*a* shows these data plotted against L_B. The point for NGC 5102 is far off-scale at (0.005, 42.2). However, as this system has an A-type spectrum (Bica & Alloin 1987), it is unlikely that the Mg_2 index measures the same physical variable as it is argued to do in typical early-type galaxies. Faber (1973) pointed out that there is a positive correlation between Mg absorption-line strength and L_B in early-type galaxies (although her original Mg_0 differs slightly from Mg_2—see Faber, Burstein, & Dressler 1977). Mg_2 is taken to be a variable of metallicity for systems in which the dominant stellar population is old (Terlevich et al. 1981; Buzzoni, Gariboldi, & Mantegazza 1992; Worthey 1994). The conversion between Mg_2 and [Fe/H] used by Terlevich et al. is taken directly from theoretical (Mould 1978) and observational (Burstein 1979) work on K giants and applied without comment to composite galaxy spectra. That of Buzzoni et al. is computed using both observations of Galactic stars, and population synthesis models covering a range of abundances and IMFs. Worthey's (1994) models indicate that the slope and zero point of such a relationship are both functions of the age of the stellar population even without variations in the IMF. Figure 3 shows the loci of the Terlevich et al. and Buzzoni et al. (with a Salpeter IMF) calibrations, and points for Worthey's (1994) models for ages from 1.5 Gyr to 17 Gyr. The agreement between the Terlevich et al. and Buzzoni et al. calibrations becomes quite poor at the lowest metallicities. However, we have only one object with $Mg_2 < 0.22$, so that is not a severe problem in our case. The Buzzoni et al. models are computed for a range of IMFs. Changing the IMF mainly affects the zero point of their Mg_2-[Fe/H] relation, such that a better agreement over our plotted range in Mg_2 is shown by assuming a shallower IMF. Also, the Worthey (1994) models for ages from 8 to 17 Gyr mainly fall between the Terlevich et al. and Buzzoni et al. calibrations.

The Mg_2 index depends on stellar surface gravity and temperature as well as both luminosity and abundance (e.g., Faber et al. 1985). Faber et al. (1985) also point out that high-resolution spectral studies often conclude that the metallicities of strong-lined stars are significantly lower than do medium- and low-resolution studies. Also, recent work (Efstathiou & Gorgas 1985; Worthey, Faber, & Gonzalez 1992; Carollo, Danziger, & Buson 1993) indicates that [Mg/Fe] is not constant among samples of elliptical galaxies. Theoretical work (Stiavelli & Matteucci 1991), and observations of the Galactic bulge (Matteucci & Brocato 1990) and of line-strength gra-

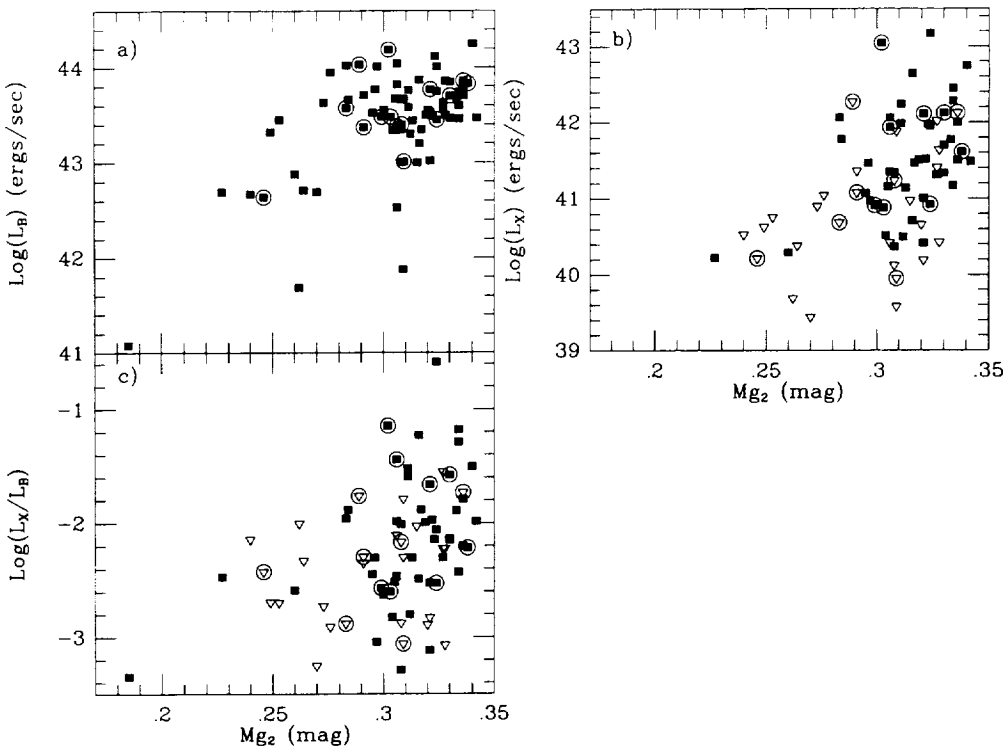

FIG. 2.—Mg_2 vs. (*a*) L_B, (*b*) L_X, and (*c*) L_X/L_B for our sample. Symbols as in Fig. 1.

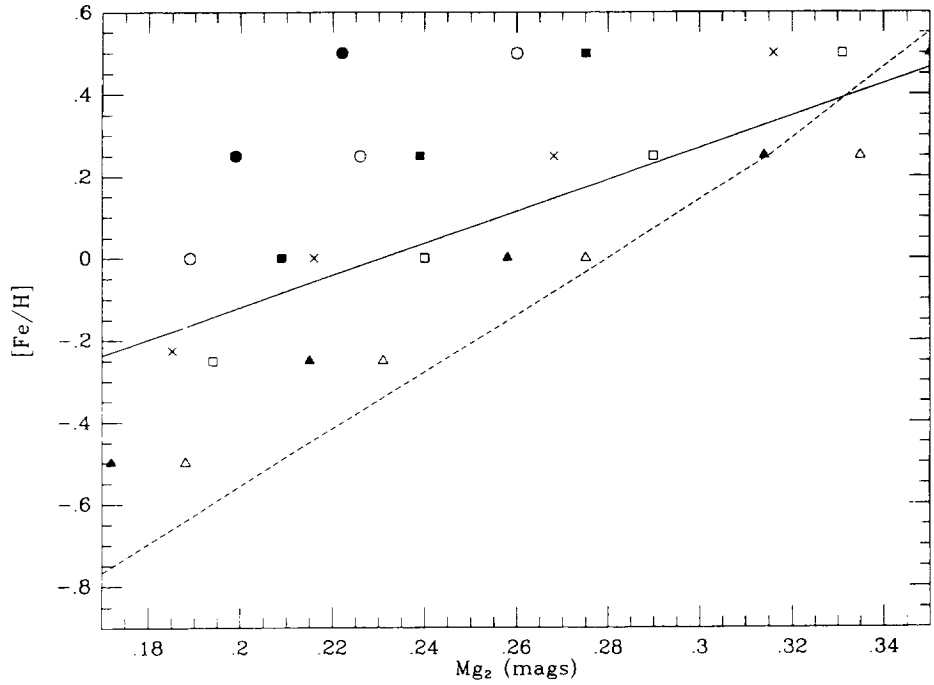

FIG. 3.—Mg_2-[Fe/H] calibrations from Terlevich et al. (1981), shown as a solid line, and Buzzoni et al. (1992) for a Salpeter IMF, shown as a dashed line. Also shown are points from the models of Worthey (1994) for a Salpeter IMF and ages of 1.5 Gyr (*solid circles*), 2 Gyr (*open circles*), 3 Gyr (*solid squares*), 5 Gyr (*crosses*), 8 Gyr (*open squares*), 12 Gyr (*solid triangles*), and 17 Gyr (*open triangles*).

dients in ellipticals (Davies, Sadler, & Petetier 1993; Carollo et al. 1993) point to Mg and Fe having very different evolutionary enrichment paths. The principal source for Mg appears to be Type II SNs (Woosley & Weaver 1986), while Type Ia and Ib SNs appear to be the source for the majority of the Fe (Nomoto, Thielemann, & Yokoi 1984; Iben et al. 1987). Furthermore, Worthey et al. (1992) and Worthey (1993) both note that their models (based on fits to field and cluster GK stars, and fits to theoretical isochrones) predict variations in [Mg/Fe] as a function of the age of a stellar population, such that older metal-rich populations will have higher [Mg/Fe] than younger ones of similar [Fe/H] (see Fig. 3). This suggests that some of the scatter in the Mg-Fe trend is due to scatter in the mixture of ages in the stellar populations of early-type galaxies. Finally, Schweizer et al. (1990) note that the magnitude and direction of the scatter about their Mg_2-M_B relationship have a negative correlation with the Σ-parameters (defined by Schweizer et al. 1990 to quantify fine structure in early-type galaxies), and Bender & Surma (1992) find evidence in four galaxies that Mg_2 increases discontinously at the same radii as the onset of kinematically decoupled cores in these galaxies. Both of these findings argue that the dynamical history of an early-type galaxy will have a significant effect on its Mg_2 strength.

As the Buzzoni et al. and Worthey (1994) models include at least some of these considerations, it is hoped that they would give a systematically more robust calibration than that of Terlevich et al. However, over the range in Mg_2 populated by our sample, the calibrations for old stellar populations differs by no more than $\lesssim 0.15$ dex in [Fe/H], or less than a factor of 2. It appears from this that the use of the Mg_2 index as indicative of trends in abundance in elliptical galaxies is quite reasonable, although the results discussed above indicate that an accurate conversion of Mg_2 measurements to values of [Fe/H] is likely to be unobtainable.

4.1. *X-Ray and Optical Trends*

Accepting the above cautionary note, we conclude that our data show a correlation of higher luminosity with higher metallicity. The results of the correlation tests between Mg_2 and L_X, L_B, and L_X/L_B are given in Table 2 (NGC 5102 excluded). They all support the impression from the plots in Figure 2. The brightest systems, as well as those systems with the highest L_X/L_B, are the most metal-rich. This is generally in keeping with current notions of galaxy formation and evolution (e.g., Ferrini & Poggianti 1993 and references therein). We note that the statistically strongest correlation is that between Mg_2 and L_X. This is borne out by a partial-rank analysis on L_B-L_X-L_X/L_B-Mg_2 (see Table A2; see Appendix for details on this table). The analysis of this parameter space shows no evidence for any underlying relationship between L_B and Mg_2! The bivariate trend shown in Table 2 is entirely driven by the mutual correlations of both Mg_2 and L_B on L_X. This is a *very* curious result. It may be due to the strong nonlinear relationship between L_B and L_X ($L_X \propto L_B^{\sim 2}$—see P1). The rapid increase in X-ray flux among the most luminous galaxies could be driving the statistical outcome. Even so, this result indicates that the retention of metals produced in the initial burst of star formation and of a gravitationally bound hot ISM are physically coupled to one another. Both the existence of an X-ray halo and the retention of metals may be tied to the depth and shape of the gravitational potential. In keeping with this interpretation, we note that an L_B-Mg_2 trend *does* appear for constant a/b (see Table A2), and that the L_X-Mg_2 and L_X/L_B-Mg_2 trends tend to break down when tested for constant σ_v or a_4 (see Table A2). This matter is discussed further in §§ 5.3 and 6.3 below.

In P1 we demonstrated a correlation between L_X and the X-ray spectral shape parameter C_{21}. This parameter is defined as the ratio of counts in the 0.8–1.36 keV band to that in the 0.16–0.8 keV band (Kim et al. 1992a). The trend is in the sense that more luminous galaxies tend to have more pronounced low-energy cutoffs in their X-ray spectra. As discussed in P1, recent *ROSAT* results (e.g., Fabbiano et al. 1994; Trinchieri et al. 1994; Fabbiano & Schweizer 1994; Kim & Fabbiano 1995) suggest that this is due to a change in the intrinsic source spectrum as a function of L_X rather than to an increase in intrinsic absorption in high L_X galaxies. Another possible explanation is that galaxies with higher L_X tend also to have higher gas-phase abundances. In fact, Trinchieri, Fabbiano, & Canizares (1986) find that some of the brightest X-ray ellipticals would require gas Fe abundances substantially larger than the stellar abundances derived from Mg_2 measurements in order to reduce the derived N_H to the Galactic foreground value. It is quite possible that the two abundance scales are systematically offset. However, recent papers generally claim significantly lower abundances in the hot ISM than those determined for the stellar populations: Recent *Ginga* measurements of the 6.5 keV Fe line from NGC 1399 and NGC 4472 suggest Fe abundances between solar and 0.3 solar (Awaki et al. 1991; Ikebe et al. 1992). Results from *ROSAT* (Forman et al. 1993) are in agreement. Results for these same galaxies from BBXRT also suggest subsolar gas abundances (Serlemitsos et al. 1993). These results have, however, been questioned by Renzini et al. (1993). To explore this point further, we tested for a correlation between Mg_2 and C_{21}. The results are shown in Table 3: There is no significant bivariate correlation between these two quantities for our sample. This result is reinforced by a partial-rank analysis on L_B-L_X-L_X/L_B-Mg_2-C_{21}: again, we find no evidence for any correlation between Mg_2 and C_{21} (see Table A2). *This suggests that stronger low-energy cutoffs in X-ray–luminous early-type galaxies cannot be related solely to higher metal abundances in the X-ray–emitting gas, unless the metallicity of the ISM is totally unrelated to that of the stars.* This result has clear implications for our understanding of the X-ray spectra of early-type galaxies. In particular, it supports modelling of *ROSAT* data of X-ray–faint galaxies with multicomponent spectra, rather than with very low abundance, single-temperature models (Fabbiano et al. 1994).

4.2. *Trends with Other ISM Parameters*

The same general trend of higher luminosity with higher metallicity is also seen in all other plots of luminosity against Mg_2 (see Fig. 4). Our bivariate analysis (see Table 2) shows that, of these, the strongest relationship is between Mg_2 and L_6. This correlation is, however, weaker than that with L_X. There is some evidence that Mg_2 is correlated with L_{12}, but no significant evidence for a correlation with L_{100}. This supports the notion that the 12 μm luminosity is related to the stellar emission (e.g., Jura et al. 1987; Knapp et al. 1992). The 100 μm emission may be due to some component that is not intrinsic to the host galaxy (e.g., Forbes 1991). Alternatively, the grains radiating at 100 μm may be evaporated by the hot ISM and harsh ISRF characteristic of early-type galaxies (e.g., Boulanger et al. 1988; Knapp et al. 1992). Given that essentially all the objects with Mg_2 values from 7S in our sample are ellipticals, this is in keeping with the lack of correlation between L_X and L_{100} found in P1.

TABLE 3

BIVARIATE CORRELATION TESTS ON THE C_{21} SAMPLE

Sample	a/b N_{tot} Cox-Hazard Kendall's τ Spearman rank	N_{lim} prob prob prob	Mg_2 N_{tot}	N_{lim} prob prob prob	σ_v N_{tot}	N_{lim} prob prob prob	a_4 N_{tot}	N_{lim} prob prob prob
E+S0	39	0	28	0	28	0	19	0
	2.103	0.1470	0.646	0.4217	2.494	0.1143	1.624	0.2026
	0.984	0.3253	0.158	0.8742	1.225	0.2204	1.053	0.2922
	−0.178	0.2734	−0.030	0.8744	0.200	0.2991	−0.259	0.2710
E	24	0	22	0	22	0	17	0
	1.758	0.1849	0.122	0.7271	0.008	0.9294	0.263	0.6083
	0.722	0.4705	0.537	0.5915	0.677	0.4984	0.414	0.6792
	−0.197	0.3448	0.073	0.7382	0.106	0.6265	−0.102	0.6832
S0	15	0	6	0	6	0	2	0
	1.069	0.3011	1.305	0.2533	3.110	0.0778		
	0.698	0.4854	1.315	0.1885	1.691	0.0909		
	−0.178	0.5060	−0.429	0.3379	0.657	0.1417		

NOTE.—Table entries as defined in notes to Table 2.

4.3. *The Trend with a/b*

We see no relationship in the scatter plot of Mg_2 against a/b, and both the bivariate correlation tests (see Table 4) and partial-rank analysis (see Table A2) confirm this.

5. COMPARISONS WITH σ_v

5.1. *X-Ray and Optical Trends*

There are central velocity dispersion measurements [log (σ_v)] from 7S for 74 galaxies in our sample. Under the reasonable assumption that σ_v measures the depth of the gravitational potential well of a galaxy, and the perhaps somewhat less reasonable assumption that L_B traces the mass of the galaxy, we would expect a strong positive correlation between L_B and σ_v in our sample. This is, in fact what we find (see Fig. 5*a* and Table 2). The plots against L_X and L_X/L_B (Figs. 5*b* and 5*c*) show the same sort of relationship. The bivariate correlation analyses given in Table 2 confirm that the relationship is quite strong for L_X and L_X/L_B. Given that the sense of the correlation is maintained when we scale the X-ray luminosities by the *B*-band luminosities in our sample, we conclude that the existence of a deep potential well appears to be crucial for large L_X/L_B in early-type galaxies (see also FGT). A partial-rank analysis on L_B-L_X-L_X/L_B-σ_v reveals the trends of σ_v with L_B and L_X to be of roughly comparable strength, and stronger than that between σ_v and L_x/L_B (see Table A3; see Appendix for details on this table). These trends indicate that total luminous mass and hot ISM content are both linked to the depth of

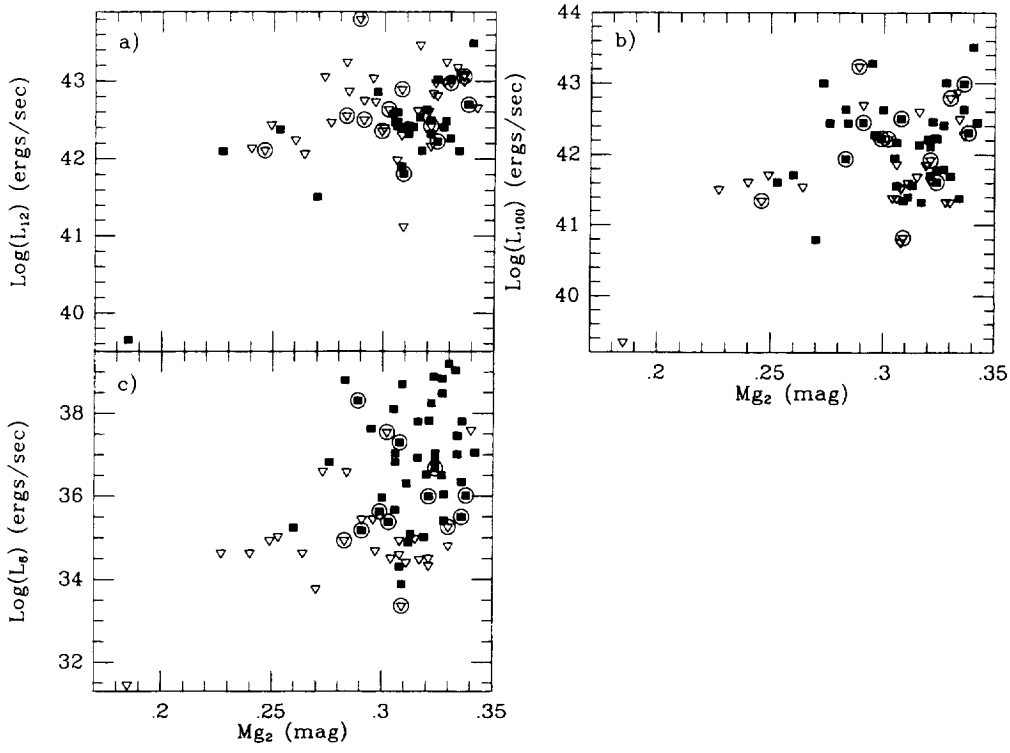

FIG. 4.—Mg_2 vs. (*a*) L_{12}, (*b*) L_{100}, and (*c*) L_6 for our sample. Symbols as in Fig. 1.

TABLE 4

BIVARIATE CORRELATION TESTS ON THE STRUCTURAL DATA

	a/b		Mg_2		σ_v	
	N_{tot}	N_{lim}	N_{tot}	N_{lim}	N_{tot}	N_{lim}
	Cox-Hazard	prob		prob		prob
	Kendall's τ	prob		prob		prob
	Spearman rank	prob		prob		prob
Mg_2	73	0				
	1.356	0.2442				
	0.940	0.3472				
	−0.101	0.3908				
σ_v	74	0	74	0		
	1.383	0.2396	46.057	$< 10^{-4}$		
	2.150	0.0316	5.284	$< 10^{-4}$		
	−0.249	0.0331	0.576	$< 10^{-4}$		
a_4	47	0	43	0	43	0
	11.247	0.0008	0.135	0.7138	8.150	0.0043
	2.510	0.0121	0.252	0.8013	2.369	0.0179
	0.374	0.0112	0.027	0.8630	−0.342	0.0265
a_4 no dEs	44	0	40	0	40	0
	11.472	0.0007	0.577	0.4477	11.649	0.0006
	2.829	0.0047	0.420	0.6743	3.278	0.0010
	0.421	0.0058	−0.079	0.6201	−0.515	0.0013

NOTE.—Table entries as defined in notes to Table 2.

the potential well; a satisfying, if not terribly surprising result. The L_X-σ_v and L_X/L_B-σ_v trends do tend to weaken somewhat when tested for constant a_4, but this appears to be due mainly to the decrease in sample size (from 73 to 40 objects) when a_4 is considered.

5.2. *Trends with Other ISM Parameters*

For the 6 cm data, the distribution looks more like a threshold relation than a linear correlation (see Fig. 6). For log $(\sigma_v) \lesssim 2.2$ (measured in km s^{-1}) there are no detected 6 cm radio sources with luminosities greater than 10^{35} ergs s^{-1}. Above this threshold, there are immediately systems with 6 cm luminosities of $\approx 10^{39}$ ergs s^{-1}. The *IRAS* data at both 12 μm and 100 μm (also shown in Fig. 6) suggest positive correlations also, but do not appear as strong as those with either L_X or L_6. This impression is confimed by the bivariate analysis in Table 2: The correlations with the *IRAS* luminosities are significant at the 0.1%–1% level. The optical, radio, and X-ray corre-

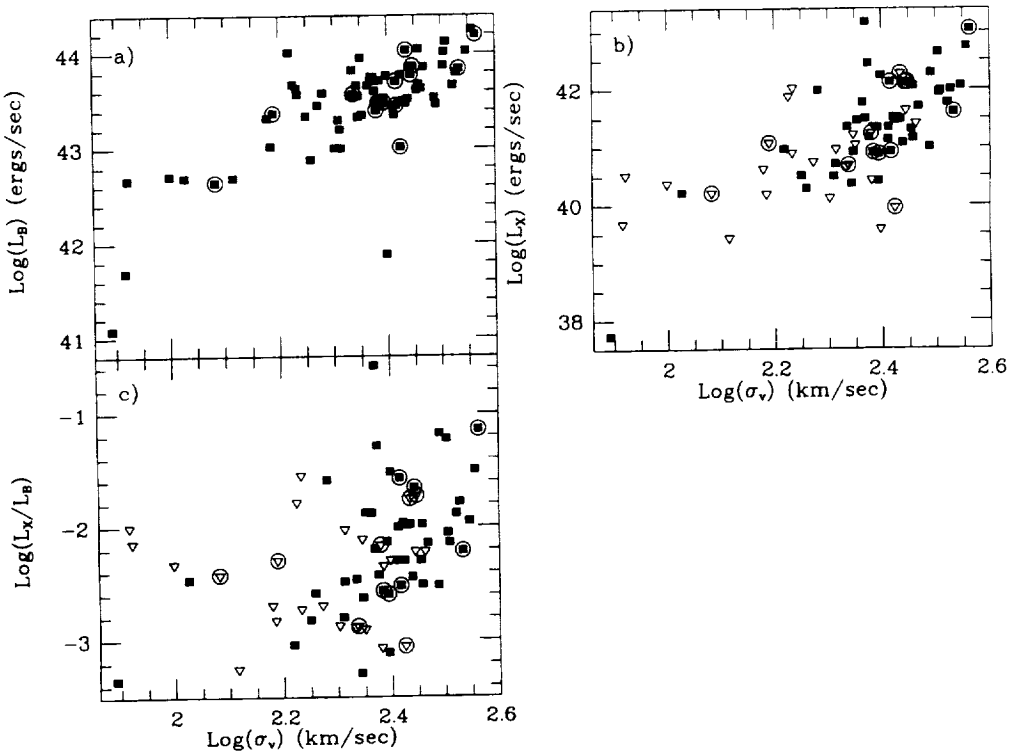

FIG. 5.—σ_v vs. (*a*) L_B, (*b*) L_X, and (*c*) L_X/L_B for our sample. Symbols as in Fig. 1.

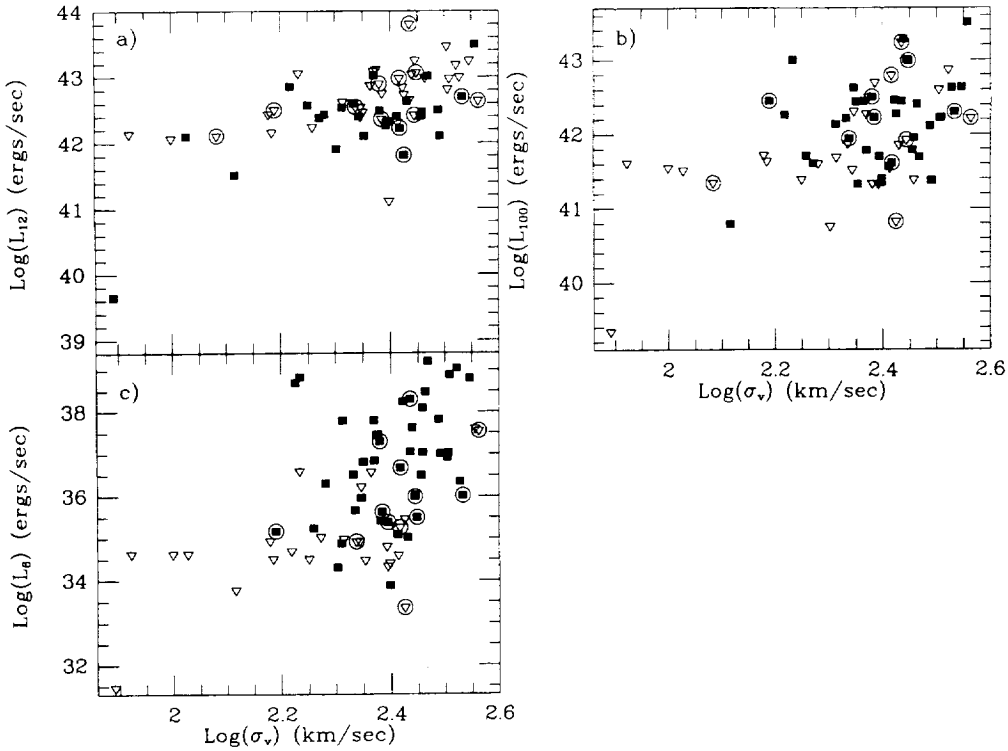

FIG. 6.—σ_v vs. (*a*) L_{12}, (*b*) L_{100}, and (*c*) L_6 for our sample. Symbols as in Fig. 1.

lations are all significant at levels of $<0.01\%$. This suggests a picture in which the fuel source (cooling X-ray gas) and feeding rate (which determines the radio power) of the central engine are both directly coupled to the central potential depth, in keeping with the notions of FGT.

5.3. *Trends with Other Structural Parameters*

It is not surprising that we should find a good correlation between Mg_2 and σ_v for our sample, given that these data are drawn from 7S, who find such a correlation for their full sample (also see Bender 1992). The results for our objects are shown in Figure 7*b* and Table 4. It is somewhat surprising that the correlation between a/b and σ_v is so weak, however (see Fig. 7*a* and Table 4). While there is a general trend for the galaxies with the largest values of σ_v to be the roundest, the data are not at all compelling. Partial-rank analysis shows that the only example of a significant a/b-σ_v trend occurs for constant L_B, in the sense that galaxies with deeper potential wells tend to be rounder than those with shallow potential wells. This could be because there is more internal support from rotation in the flatter systems at a given luminosity. There is a very strong correlaton between Mg_2 and σ_v for all tested combinations (see Table A3); see Appendix for details on this table).

6. COMPARISONS WITH a_4

6.1. *X-Ray and Optical Trends*

We have taken measurements of the amplitude of the cos (4 θ) Fourier term of the isophotal deviations from ellipticity for 47 galaxies in our sample from the papers of Bender et al. (1989) and Peletier et al. (1990). These data are given in Table 1. These a_4 values are measured from isophotes at $\lesssim 2r_e$ (typically $\sim 0.5r_e$ for the Peletier et al. sample), and thus describe the morphology of the inner parts of these galaxies. In Figure 8*a* we show that our sample is representative of the full samples of these earlier studies in that more luminous ellipticals tend to be boxy (have negative a_4 terms), while the less luminous tend to be disky (positive a_4). The exceptions to this are three boxy dwarf ellipticals, marked in the figure. Recent work (e.g., Bender & Nieto 1990; Carter & Sadler 1990; Held, Mould & de Zeeuw 1990; Bender, Paquet, & Nieto 1991) indicates that these galaxies do not fall along a simple extension of the properties of giant ellipticals. This deviation is therefore neither surprising nor (for the work discussed here!) terribly significant.

Bender et al. (1989) comment that they see a relationship between L_X and a_4 for their sample. They do not test for such a relationship, possibly due to the very small number of objects for which they had X-ray data. Our sample is substantially larger (see Figs. 8*b* and 8*c*). The results of the bivariate correlation analysis of a_4 with L_B, L_X, and L_X/L_B are given in Table 2. This analysis confirms the assertion of Bender et al. (1989) that X-ray–luminous galaxies tend to be boxier than X-ray–faint galaxies at the $\sim 0.1\%$ level if the dE's are not included. The strength of the bivariate correlation with L_B is marginally worse than that with L_X. The trend with L_X/L_B, again in the sense that the galaxies with the highest L_X/L_B tend to be boxy, is statistically the weakest of the three, but the correlation is *still* significant at a level of $\lesssim 0.5\%$ for all three tests. Partial-rank analysis on L_B-L_X-L_X/L_B-a_4 reveals that the trend of L_X with a_4 is the strongest of the three and appears to drive the other two (see Table A4; see Appendix for details on this table). The L_X-a_4 trend breaks down when tested for constant σ_v. We noted in § 5.1 that there is a strong L_X-σ_v trend. This trend is maintained for constant a_4 (see Table A3), arguing that an underlying trend between a_4 and σ_v is driving the L_X-a_4 correlation. We explore this result further in § 6.3 below.

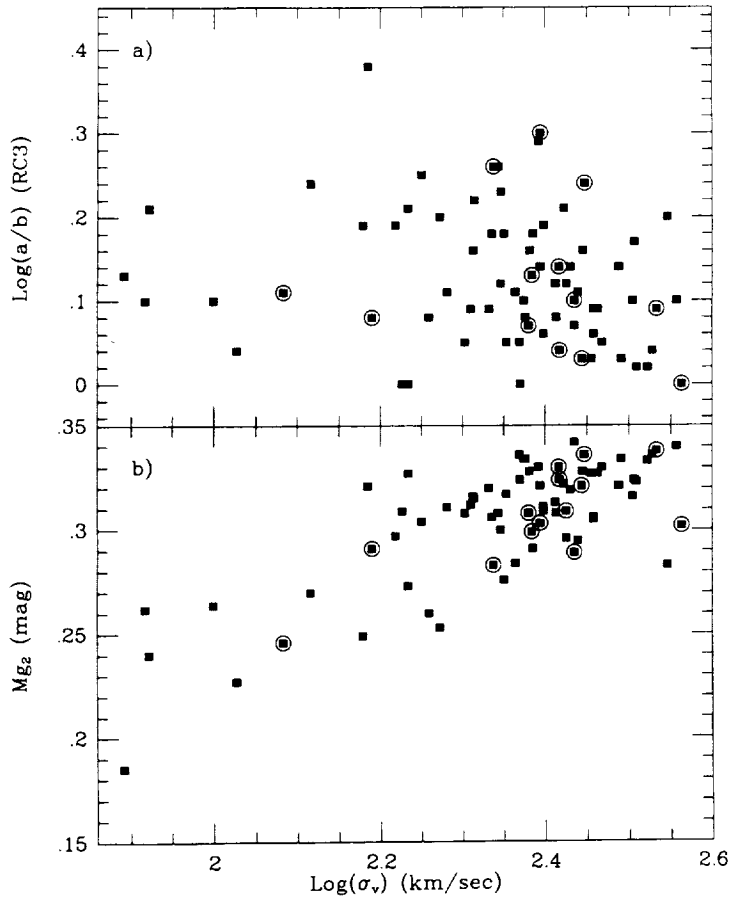

FIG. 7.—σ_v vs. (*a*) a/b, and (*b*) Mg_2 for our sample. Symbols as in Fig. 1.

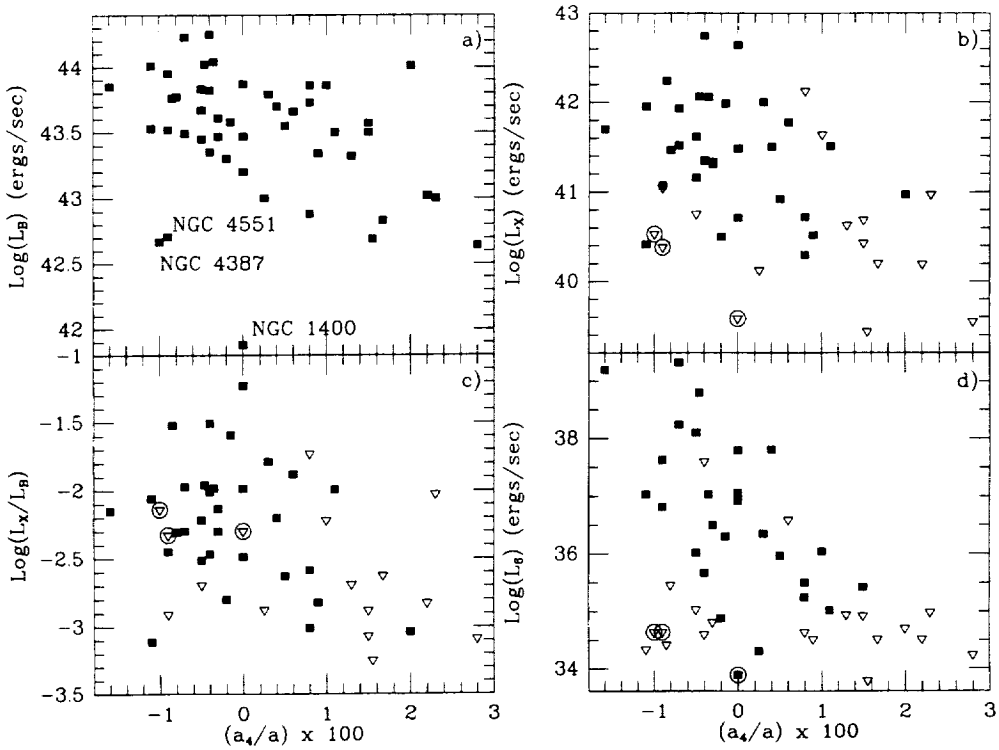

FIG. 8.—a_4 vs. (*a*) L_B, (*b*) L_X, (*c*) L_X/L_B, and (*d*) L_6 for our sample. The dwarf ellipticals are identified in (*a*), and circled in (*b*), (*c*), and (*d*). All other symbols as in Fig. 1.

6.2. *Trends with Other ISM Parameters*

There are trends of marginal statistical significance between a_4 and both L_{12} and L_{100}, at the $\lesssim 6\%$ and $\lesssim 4\%$ confidence levels respectively (see Table 2). A strong trend is apparent between a_4 and L_6 in Figure 8*d*. This correlation is confirmed at roughly the 0.1% level (Table 2). There are *no* high-luminosity 6 cm sources in our sample that are disky galaxies. This is in keeping with previous findings that central radio sources are more prevalent in ellipticals without disk features (Peletier et al. 1990). A partial-rank analysis including L_6 indicates that the relationship between L_6 and a_4 is stronger than that between L_B and a_4 (see Table A4), although weaker than the L_X-a_4 correlation: Boxy galaxies generate more radio power than disky galaxies of the same optical and X-ray luminosities.

The picture that emerges from our consideration of the relationship of structural parameters to the luminosities in our various wavebands is that L_B, L_X, L_X/L_B, and L_6 *are correlated with both the depth of the potential (as measured by* σ_v *and* Mg_2*) and the shape of the potential (as measured by* a/b *and* a_4*).*

6.3. *Trends with Other Parameters*

We find a correlation at the $\sim 0.5\%$ level (see Table 4) between a_4 and a/b in the sense that rounder galaxies tend to be boxy, and flatter galaxies tend to be disky. This is not a tautology: recall that a/b simply measures the ratio of the projected major and minor axes of a system; a_4 measures the extent and sense of deviation of the isophotes of a system from pure elliptical symmetry. It is entirely possible, from a mathematical point of view, for a system with high ellipticity to have boxy isophotes, or one with very low ellipticity to have disky isophotes. The data are shown in Figure 9*a*. A partial-rank analysis on L_B-L_X-L_X/L_B-a/b-a_4 supports this picture (see Tables A1 and A4) but suggests that the a/b-a_4 trend may be largely driven by underlying relationships of both a_4 and a/b with the luminosity parameters.

Much to our surprise, the data show no indication for a correlation between a_4 and Mg_2 (see Fig. 9*b* and Table 4). One might expect there to be a relationship between these such that boxy galaxies would tend to have higher Mg_2 than disky galaxies. Indeed, Sil'chenko (1994) finds some evidence for just such a result. However, if anything, the data we have show an opposite trend: the lowest values of Mg_2 tend to be from boxy galaxies. Overall, though, there is no indication from this sample for any significant trend. A partial-rank analysis on L_B-L_X-L_X/L_B-a/b-a_4-Mg_2 confirms this result (see Table A4).

With the exception of two dwarf galaxies, we see a steep correlation between a_4 and σ_v for our sample (see Fig. 9*c*), in the sense that boxy galaxies tend to have large velocity dispersions. For the full sample this correlation is significant at the $\sim 2.7\%$ level (see Table 4). Removing the dwarfs galaxies improves this to a $\sim 0.1\%$ correlation. A partial-rank analysis on L_B-L_X-L_X/L_B-a/b-a_4-σ_v suggests that this correlation may be the underlying cause of the observed relation between a_4 and a/b (see Table A4). Testing L_B-L_X-L_X/L_B-a/b-a_4-Mg_2-σ_v, we find statistical evidence for a positive correlation between a_4 and Mg_2 at the $\sim 4\%$–5% level. We note that this correlation appears *only* when we test for a constant σ_v. This therefore implies that, *for a given potential depth*, disky galaxies have *higher* metallicity *or* older stellar populations than boxy galaxies. We also note that the strongest σ_v-a_4 correlations all result when tested with constant Mg_2 (see Table A4). The effect of Mg_2 can be seen in Figure 9*c* where the points enclosed in

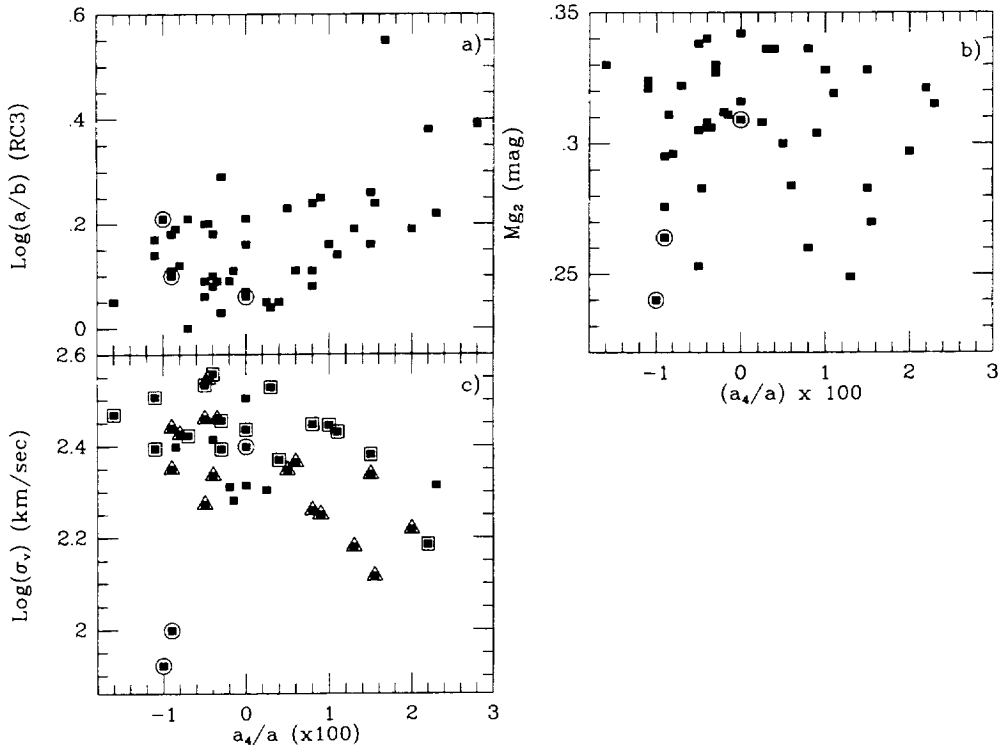

FIG. 9.—a_4 vs. (*a*) a/b, (*b*) Mg_2, and (*c*) σ_v for our sample. Symbols as in Fig. 8. In (*c*) the points enclosed in squares are the systems with the highest 40% of Mg_2 values; those enclosed in triangles are the lowest 40%.

squares are the 40% of the sample with the largest Mg_2 values, and those enclosed in triangles are the 40% with the smallest Mg_2 values. For a given a_4 value, the high-Mg_2 objects have systematically higher σ_v than the low-Mg_2 objects.

One possible interpretation of these results is suggested by the hypothesis that boxy ellipticals are the product of mergers of smaller systems, while disky ellipticals are "primordial" in the sense that the overall morphology of the system is a reflection of its state at the epoch of galaxy formation (e.g., Nieto & Bender 1989; Kormendy & Djorgovski 1989; Barnes & Hernquist 1992). At the present epoch, there appears to be a mass-abundance relationship amongst galaxies of a given morphology (e.g., Faber 1973; Wyse & Silk 1985; Dekel & Silk 1986; DeYoung & Gallagher 1990; Franx & Illingworth 1990) such that less massive systems are less metal-rich. If such a relationship has always held, then the formation of a boxy E of some mass M from two smaller objects would result in a *lower* abundance galaxy than a disky E of the same mass M if the bulk of the stars in the boxy galaxy had already formed *before* the merger. Furthermore, boxy galaxies that formed from the merging of lower mass progenitors will result in objects with lower current stellar abundances compared to those formed from the merging of higher mass progenitors, because a larger fraction of the enriched ejecta from the initial merger induced burst of star formation will escape from their shallower potential wells.

A second possibility is that disky systems are the products of mergers involving at least one disk galaxy, in which either the self-gravitating part of the disk survives the accretion event (as may be the case in Cen A), or the ISM undergoes dissipational collapse to form a new central disk system (e.g., Hernquist & Barnes 1991). This is the most reasonable explanation for galaxies with kinematically decoupled cores (e.g., Bender 1990; Bertola 1992) and may hold for disky galaxies in general. This is because both the studies of Bender et al. (1989) and Peletier et al. (1990) determine the a_4 parameter at fairly small radii. Bender et al. (1989) state that all their a_4 values are computed from isophotes within $2r_e$. Peletier et al. (1990) publish the radii at which they determined a_4. The mean is $\sim 0.5r_e$, with a few as low as $0.1r_e$, and only three of 35 galaxies $\geq 1r_e$. Thus "disky" systems are so labeled because their inner isophotes have disk features. Several of the systems with negative a_4 from the Bender et al. (1989) sample have very boxy isophotes at large radii (F. Schweizer 1994, private communication) and thus appear to be merger remnants on that criterion. Bender & Surma (1992) observed four ellipticals with kinematically decoupled cores and found a sharp increase in the Mg_2 line strengths at the same radii at which the peculiar kinematics appear. As the Mg_2 values from 7S are all nuclear values, the trend of higher Mg_2 line strengths in disky systems at a given σ_v may be due to higher abundances in the captured or secondary nuclear disks of merger remnants with disky central isophotes.

7. SUMMARY AND SUGGESTIONS FOR FUTURE RESEARCH

1. Rounder galaxies tend to have larger L_X, L_X/L_B, and L_6. Partial-rank analysis shows the L_X/L_B-a/b trend to be the strongest of the three. This suggests a connection between the shape of the potential and the ability to retain substantial halos of hot ISM. These in turn could be responsible for both feeding the nuclear sources through cooling flows and confining radio lobes (see also FGT). The same general trends hold for correlations with a_4, but the strongest trend here is that between a_4 and L_X (confirming the observation of Bender et al. 1989).

2. Axial ratio (a/b) and boxiness (a_4) are correlated in the sense that flatter galaxies tend to have diskier isophotes. Partial-rank analysis suggests that the trends between a_4 and a/b may be driven by underlying relationships of both axial ratio and a_4 with the luminosity parameters.

3. Both a/b and a_4 are correlated with L_B but are not strongly correlated with either L_{12} or L_{100}. The lack of any strong trend with L_{12}, and the results of P1, indicate that there may be some significant contribution to the 12 μm emission from hot dust in early-type galaxies that is not directly related to the stellar component. For the S0's, there may be a contribution from dust associated with disk star formation regions. The lack of trends with L_{100} is consistent with the notion that the FIR-emitting material is accreted (e.g., Forbes 1991), or that it is evaporated by the hot ISM and hard ISRF on fairly short timescales (e.g., Knapp et al. 1992).

4. There are strong correlations between Mg_2, σ_v, and L_X. Partial-rank analysis shows that the depth of the potential well is the crucial parameter. From a physical standpoint, the deeper the potential well, the better a galaxy is able to retain its hot ISM at the current epoch (the L_X-σ_v correlation), and the better it was able to retain the enriched ejecta from its initial phase of strong star formation, and reprocess this ejecta into new stars (the Mg_2-σ_v correlation).

5. There is no significant correlation between the X-ray spectral parameter C_{21} and Mg_2. C_{21} is defined by Kim et al. (1992a) as the ratio of emission in the 0.8–1.36 keV band to that in the 0.16–0.8 keV band and thus measures the shape of the X-ray spectrum in this region. The lack of correlation between C_{21} and Mg_2 suggests that the relative absence of low-energy cutoffs in X-ray–faint early-type galaxies (see Kim, Fabbiano, & Trinchieri 1992b) is not related to lower abundances in the X-ray–emitting gas, unless the metallicity of the ISM is unrelated to that of the stars. This supports the conclusion of Fabbiano et al. (1994) that X-ray–faint ellipticals have complex X-ray spectra.

6. Many of the trends we find are "wedgelike" or "threshold-like" rather than being a simple power law. One of the most impressive of these is the L_6-σ_v trend discussed in § 5.2. We find a threshold of $\log(\sigma_v) \approx 2.2$ above which the maximum radio luminosities in our sample jump abruptly by more than an order of magnitude. Below this value of σ_v, it appears that the potential well is too shallow to efficiently transport material to the nuclear engine. It does not seem coincidental that, at this same value of σ_v, we see a jump in the maximum detected L_X/L_B of more than one order of magnitude.

7. X-ray, radio, and optical luminosities are all correlated with both shape (a/b, a_4), and depth (Mg_2, σ_v) parameters. There are also strong relationships among the shape and the depth parameters. However, trends between the shape parameters (a/b, a_4) and one of the depth parameters (Mg_2 or σ_v) are modulated by the other parameter. That is, for instance, at a given a_4 value, the spread in σ_v appears directly related to the spread in Mg_2 such that the higher σ_v objects also have higher Mg_2. Alternatively, for a given σ_v, boxy galaxies tend to have *lower* Mg_2 values (and thus, we surmise, lower stellar abundances) than disky galaxies. This suggests that the presence of a hot ISM is dependent on both the shape (a/b, a_4) and the depth (Mg_2, σ_v) of the potential, but that these two families of parameters are not related in a simple way.

The nature of the coupling between the shape and depth parameters is clearly an important input for understanding the formation and evolution of early-type systems. A galaxy may have a deep potential either because of initial conditions (the result of a large primordial fluctuation) or because it is the product of mergers of a number of less massive objects. We observe that Es with disky inner isophotes have larger nuclear Mg_2 strengths than galaxies with boxy inner isophotes at a given σ_v. If disky isophotes signal "primordial" ellipticals (ones that have not experienced significant merging since the epoch of galaxy formation) and boxy isophotes signal systems that have been built up by mergers, two possible explanations of this result suggest themselves. First, if the presently observed mass-abundance relationship for galaxies is a relic of a fundamental constraint of the galaxy formation process, then a disky elliptical of a given mass could have a higher average central stellar abundance than a merger product (a boxy elliptical) of the same mass that was formed from lower mass (and thus lower abundance) precursors. Second, boxy ellipticals could have lower Mg_2 values for a given [Fe/H] due to an overall younger stellar population resulting from merger-induced star formation bursts. Alternatively, if disky isophotes signal merger systems that have either formed secondary nuclear disks (see Hernquist & Barnes 1991), or captured self-gravitating spiral disks, then the enhancement of nuclear Mg_2 strengths at a given σ_v may be due to high abundances in those disks (see Bender & Surma 1992).

Various avenues present themselves for further study of these possibilities. One that we are pursuing is the comparison of the database from this work and P1 with the dynamically motivated κ-parameters defined by Bender, Burstein, & Faber (1992). It would also be very interesting to study the radial gradients of Mg_2 and σ_v for early-type galaxies with a range in X-ray properties and to look for other signs of fine structure (as discussed by, e.g., Schweizer & Seitzer 1992) as a function of X-ray properties. Such studies ought to make great contributions to our understanding of the formation histories and physical evolution of early-type galaxies.

We would like to thank Glen Mackie and Ginevra Trinchieri for their comments on this study as it has progressed, and François Schweizer for stimulating comments and a critical reading of the manuscript. We would also like to thank Eric Feigelson and Michael LaValley for providing us with the latest versions of the ASURV software package. G. F. would like to thank the Aspen Summer School for the opportunity to focus on this project. P. B. E. would like to thank the organizers and participants of the Third Teton Summer School, where easly results of this project were discussed. This research has made use of the NASA/IPAC Extragalactic Database (NED) which is operated by the Jet Propulsion Laboratory, Caltech, under contract with the National Aeronautics and Space Administration. We are grateful to the National Aeronautics and Space Administration for suport of this research under the LTSA grant NAGW 2681 and contract NAS 8-39073 (AXAF Science Center).

TABLE A1a

PARTIAL SPEARMAN RANK ANALYSIS: TRENDS WITH log (a/b), E + S0 SAMPLE

Test Pair	Held parameters	Size	Paritial Spearman rank	Probability
L_B–a/b	L_X	147	−0.047	0.287
	L_X/L_B	147	−0.108	0.099
	Mg_2	73	0.066	0.292
	σ_v	74	0.176	0.072
	a_4	44	−0.138	0.199
	L_X,L_X/L_B	147	−0.030	0.361
	L_X,Mg_2	73	0.254	0.019
	L_X,σ_v	74	0.277	0.010
	L_X,a_4	44	0.024	> 0.400
	L_X/L_B,Mg_2	73	0.197	0.051
	L_X/L_B,σ_v	74	0.231	0.026
	L_X/L_B,a_4	44	−0.063	0.349
	L_6,a_4	44	−0.004	> 0.400
	Mg_2,σ_v	73	0.164	0.090
	Mg_2,a_4	40	0.057	0.368
	σ_v,a_4	40	0.197	0.125
	L_X,L_X/L_B,Mg_2	73	0.278	0.010
	L_X,L_X/L_B,σ_v	74	0.282	0.009
	L_X,L_X/L_B,a_4	44	0.015	> 0.400
	L_X,L_6,a_4	44	0.076	0.319
	L_X,Mg_2,σ_v	73	0.274	0.012
	L_X,Mg_2,a_4	40	0.120	0.241
	L_X,σ_v,a_4	40	0.211	0.108
	L_X/L_B,L_6,a_4	44	0.026	> 0.400
	L_X/L_B,Mg_2,σ_v	73	0.223	0.035
	L_X/L_B,Mg_2,a_4	40	0.098	0.283
	L_X/L_B,σ_v,a_4	40	0.200	0.125
	Mg_2,σ_v,a_4	40	0.170	0.169
	L_X,L_X/L_B,L_6,a_4	44	0.070	0.336
	L_X,L_X/L_B,Mg_2,σ_v	73	0.283	0.010
	L_X,L_X/L_B,Mg_2,a_4	40	0.116	0.249
	L_X,L_X/L_B,σ_v,a_4	40	0.201	0.127
	L_X,Mg_2,σ_v,a_4	40	0.182	0.155
	L_X/L_B,Mg_2,σ_v,a_4	40	0.173	0.168
	L_X,L_X/L_B,Mg_2,σ_v,a_4	40	0.173	0.171

APPENDIX

Tables A1–A4 contain the detailed results of the partial Spearman rank statistical analysis. Table A1 shows the analysis of L_B-a/b, L_X-a/b, L_X/L_B-a/b, and L_6-a/b. Table A2 shows L_B-Mg_2, L_X-Mg_2, L_X/L_B-Mg_2, C_{21}-Mg_2, and a/b-Mg_2. Table A3 shows L_B-σ_v, L_X-σ_v, L_X/L_B-σ_v, a/b-σ_v, and Mg_2-σ_v. Table A4 shows L_B-a_4, L_X-a_4, L_X/L_B-a_4, L_6-a_4, a/b-a_4, Mg_2-a_4, and σ_v-a_4. The tables are organized into sections, with each section showing correlation probabilities for a given pair of inputs (for instance, L_B-a/b in Table A1). Within each section, column (1) identifies the test pair, column (2) identifies the quantities to be held constant in the test, column (3) gives the number of objects in the sample, column (4) gives the partial Spearman rank statistic, and column (5) gives the probability that the test pair show a correlelation for that set of parameters.

Tables A1–A4 are published in their entirety in computer-readable form in the AAS CD-ROM Series, Volume 4. A portion of Table A1a appears on the preceding page.

REFERENCES

Awaki, H., Koyama, K., Kunieda, H., Takano, S., Tawara, Y., & Ohashi, T. 1991, ApJ, 336, 88
Barnes, J. E., & Hernquist, L. 1992, ARA&A, 30, 705
Bender, R. 1990, in Dynamics and Interactions of Galaxies, ed. E. R. Weilen (Heidelberg: Springer), 249
———. 1992, in IAU Symp. 149. The Steller Populations of Galaxies, ed. B. Barbuy & A. Renzini (Dordrecht: Kluwer), 267
Bender, R., Burstein, D., & Faber, S. M. 1992, ApJ, 399, 462
Bender, R., & Nieto, J.-L. 1990, A&A, 239, 97
Bender, R., Paquet, A., & Nieto, J.-L. 1991, A&A, 246, 349
Bender, R., & Surma, P. 1992, A&A, 258, 250
Bender, R., Surma, P., Döbereiner, S., Möllenhoff, C., & Madejesky, R. 1989, A&A, 217, 35
Bertola, F. 1992, in Morphology and Physical Classification of Galaxies, ed. G. Longo, M. Capaccioli, & G. Busarello (Dordrecht: Kluwer), 115
Bica, E., & Alloin, D. 1987, A&AS, 70, 281
Boulanger, F., Beichman, C., Désert, F. X., Helou, G., Pérault, M., & Ryter, C. 1988, ApJ, 332, 328
Burstein, D. 1979, ApJ, 232, 74
Buzzoni, A., Gariboldi, G., & Mantegazza, L. 1992, AJ, 103, 1814
Carollo, C. M., Danziger, I. J., & Buson, L. 1993, MNRAS, 265, 553
Carter, D., & Sadler, E. M. 1990, MNRAS, 245, 12P
Ciotti, L., D'Ercole, A., Pellegrini, S., & Renzini, A. 1991, ApJ, 376, 380
Davies, R. L., Sadler, E. M., & Peletier, R. F. 1993, MNRAS, 262, 650
Dekel, A., & Silk, J. 1986, ApJ, 303, 39
de Vaucouleurs, G., de Vaucouleurs, A., & Corwin, H. G. 1976, Second Reference Catalogue of Bright Galaxies (Austin: University of Texas Press)
de Vaucouleurs, G., de Vaucouleurs, A., Corwin, H. G., Jr., Buta, R. J., Paturel, G., & Fouqué, P. 1991, Third Reference Catalogue of Bright Galaxies (New York: Springer (RC3)
DeYoung, D., & Gallagher, J. 1990, ApJ, 356, L15
Disney, M. J., Sparks, W. B., & Wall, J. V. 1984, MNRAS, 206, 899
Eder, J. A., Giovanelli, R., & Haynes, M. P. 1991, AJ, 102, 572
Efstathiou, G., & Gorgas, J. 1985, MNRAS, 215, 37P
Eskridge, P. B., Fabbiano, G., & Kim, D.-W. 1995, ApJS, in press (P1)
Fabbiano, G. 1989, ARA&A, 27, 87
———. 1994, in New Horizons of X-Ray Astronomy: First Results from *ASCA*, ed. F. Makino & T. Ohashi (Tokyo: Universal Academy), 159
Fabbiano, G., Gioia, I. M., & Trinchieri, G. 1988, ApJ, 324, 749
———. 1989, ApJ, 347, 127 (FGT)
Fabbiano, G., Kim, D.-W., & Trinchieri, G. 1992, ApJS, 80, 531 (P0)
———. 1994, ApJ, 429, 94
Fabbiano, G., & Schweizer, F. 1995, ApJ, submitted
Faber, S. M. 1973, ApJ, 179, 731
Faber, S. M., Burstein, D., & Dressler, A. 1977, AJ, 82, 941
Faber, S. M., Friel, E. D., Burstein, D., & Gaskell, C. M. 1985, ApJS, 57, 711
Faber, S. M., Wegner, G., Burstein, D., Davies, R. L., Dressler, A., Lynden-Bell, D., & Terlevich, R. J. 1989, ApJS, 69, 763 (7S)
Feigelson, E. D., & Babu, G. J. 1992, Statistical Challenges in Modern Astronomy (New York: Springer)
Feigelson, E. D., & Nelson, P. I. 1985, ApJ, 293, 192
Ferrini, F., & Poggianti, B. M. 1993, ApJ, 410, 44
Forbes, D. A. 1991, MNRAS, 249, 779
Forman, W., Jones, C., David, L., Franx, M., Makishima, K., & Ohashi, T. 1993, ApJ, 418, L55
Franx, M., & Illingworth, G. 1990, ApJ, 359, L41
Giacconi, R., et al. 1979, ApJ, 230, 540
Goudfrooij, P., Hansen, L., Jørgensen, H. E., & Nørgaard-Nielsen, H.-U. 1994, A&AS, 105, 341
Held, E. V., Mould, J. R., & de Zeeuw, P. T. 1990, AJ, 100, 415
Hernquist, L., & Barnes, J. E. 1991, Nature, 354, 210
Huchtmeier, W. K., & Richter, O.-G. 1989, A General Catalog of H I Observations of Galaxies (New York: Springer)
Iben, I., Jr., Nomoto, K., Tornambè, A., & Tutukov, A. 1987, ApJ, 317, 717
Ikebe, Y., et al. 1992, ApJ, 384, L5
Isobe, T., Feigelson, E. D., & Nelson, P. I. 1986, ApJ, 306, 490
Jura, M., Kim, D.-W., Knapp, G. R., & Guhathkurta, P. 1987, ApJ, 312, L11
Kendall, M., & Stuart, A. 1976, The Advanced Theory of Statistics, Vol. 2 (New York: Macmillan)
Kim, D.-W. 1988, Ph.D. thesis, Univ. California, Los Angeles
Kim, D.-W., & Fabbiano, G. 1990, in Windows on Galaxies, ed. G. Fabbiano, J. S. Gallagher, & A Renzini (Dordrecht: Kluwer), 293
———. 1995, ApJ, 441, 182
Kim, D.-W., Fabbiano, G., & Trinchieri, G. 1992a, ApJS, 80, 645
———. 1992b, ApJ, 393, 134
Knapp, G. R., Guhathakurta, P., Kim, D.-W., & Jura, M. 1989, ApJS, 70, 329
Knapp, G. R., Gunn, J. E., & Wynn-Williams, C. G. 1992, ApJ, 399, 76
Kormendy, J., & Djorgovski, S. 1989, ARA&A, 27, 235
LaValley, M. P., Isobe, T., & Feigelson, E. D. 1992, BAAS, 24, 839
Matteucci, F., & Brocato, E. 1990, ApJ, 365, 539
Mould, J. R. 1978, ApJ, 220, 434
Nieto, J.-L., & Bender, R. 1989, A&A,, 215, 266
Nomoto, K., Thielemann, F. K., & Yokoi, K. 1984, ApJ, 286, 644
Peletier, R. F., Davies, R. L., Illingworth, G. D., Davis, L. E., & Cawson, M. 1990, AJ, 100, 1091
Pellegrini, S. 1994, A&A, in press
Pellegrini, S., & Fabbiano, G. 1994, ApJ, 429, 105
Renzini, A., Ciotti, L., D'Ercole, A., & Pellegrini, S. 1993, ApJ, 419, 52
Sage, L. J., & Wrobel, J. M. 1989, ApJ, 344, 204
Sandage, A. 1961, A Hubble Atlas of Galaxies (Washington: Carnegie Institute of Washington)
Sauvage, M., & Thuan, T. X. 1994, ApJ,, 429, 153
Schmitt, J. H. M. M. 1985, ApJ, 293, 178
Schweizer, F., & Seitzer, P. 1992, AJ, 104, 1039
Schweizer, F., Seitzer, P., Faber, S. M., Burstein, D., Dalle, Ore, C. M., & Gonzalez, J. J. 1990, ApJ, 364, L33
Serlemitsos, P. J., Loewenstein, M., Mushotzky, R. F., Marshall, F. E., & Petre, R. 1993, ApJ, 413, 518
Sil'chenko, O. K. 1994, Astron. Rept., 38, 3
Smith, E. P., & Heckman, T. M. 1989, ApJ, 341, 658
Spitzer, L., Jr. 1954, ApJ, 120, 1
Stiavelli, M., & Matteucci, F. 1991, ApJ, 377, L79
Terlevich, R., Davies, R. L., Faber, S. M., & Burstein, D. 1981, MNRAS, 196, 381
Thronson, H. A., Jr., Tacconi, L., Kenney, J., Greenhouse, M. A., Margulis, M., Tacconi-Garman, L., & Young, J. S. 1989, ApJ, 344, 747
Trinchieri, G., & Fabbiano, G. 1985, ApJ, 296, 447
Trinchieri, G., Fabbiano, G., & Canizares, C. R. 1986, ApJ, 310, 637
Trinchieri, G., Kim, D.-W., Fabbiano, G., & Canizares, C. 1994, ApJ, 428, 555
van Speybroeck, L., Epstein, A., Forman, W., Giacconi, R., & Jones, C. 1979, ApJ, 234, L45
Walsh, D. E. P., Knapp, G. R., Wrobel, J. M., & Kim, D.-W. 1989, ApJ, 337, 209
White, R. E., III, & Sarazin, C. L. 1991, ApJ, 367, 476
Woosley, S. E., & Weaver, T. A. 1986, in IAU Colloq. 89, Radiation Hydrodynamics in Stars and Compact Objects, ed. D. Mihalas & K. H. Winkler (Berlin: Springer), 91
Worthey, G. 1993, ApJ, 409, 530
———. 1994, ApJS, 95, 107
Worthey, G., Faber, S. M., & Gonzalez, J. J. 1992, ApJ, 398, 69
Wyse, R., & Silk, J. 1985, ApJ, 296, L1

Harvard-Smithsonian Center for Astrophysics

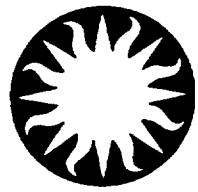

Preprint Series

No. 4031
(Received February 7, 1995)

A MULTIPARAMETRIC ANALYSIS OF THE *EINSTEIN* SAMPLE OF EARLY-TYPE GALAXIES III: COMPARISONS WITH THE κ-PARAMETERS

Paul B. Eskridge
Harvard-Smithsonian Center for Astrophysics
and
Department of Physics and Astronomy, University of Alabama

Giuseppina Fabbiano
Harvard-Smithsonian Center for Astrophysics

and

Dong-Woo Kim
Harvard-Smithsonian Center for Astrophysics
and
Department of Astronomy and Space Science, Chungnam National University

To appear in
The Astrophysical Journal
July 20, 1995

Center for Astrophysics
Preprint Series No. 4031

A MULTIPARAMETRIC ANALYSIS OF THE EINSTEIN SAMPLE OF EARLY-TYPE GALAXIES

III: COMPARISONS WITH THE κ-PARAMETERS

Paul B. Eskridge[1],

Harvard-Smithsonian Center for Astrophysics
60 Garden Street
Cambridge, MA 02138
and
Department of Physics and Astronomy[2]
University of Alabama
Tuscaloosa, AL 35487

Giuseppina Fabbiano[1],

Harvard-Smithsonian Center for Astrophysics

and Dong-Woo Kim[1]

Harvard-Smithsonian Center for Astrophysics
and
Department of Astronomy and Space Science
Chungnam National University
Taejon, 305-764, S. Korea

Accepted for publication in the 20 July 1995
issue of **The Astrophysical Journal**

1: Internet addresses:
paul@hera.astr.ua.edu
pepi@cfa.harvard.edu
kim@cfa.harvard.edu
2: Current address

Abstract

We have extended our bivariate and multivariate statistical analysis of the *Einstein* sample of early-type galaxies (Fabbiano *et al.*, 1992; Eskridge *et al.*, 1995a,b) to include a consideration of the κ parameters defined by Bender *et al.* (1992). The κ parameters are defined such that κ_1 scales with virial mass, κ_3 scales with inner M/L ratio, and κ_2 is perpendicular to both κ_1 and κ_3. The κ_1–κ_3 plane is essentially edge-on to the Bender *et al.* (1992) formulation of the fundamental plane, and the parameter $\delta\kappa_3$ describes the scatter about that plane. We find that L_B, L_X, and L_6 are all strongly correlated with κ_1. Partial Spearman rank analysis shows these trends to be independent of the correlations between the luminosities. There are also significant bivariate trends of both L_X and L_6 with κ_3. Partial Spearman rank analysis indicates that the L_X–κ_3 is the dominant one, thus arguing for a connection between the prominence of x-ray coronae and the inner M/L. This suggests that galaxies with central excesses of dark matter also have more massive extended dark matter halos, providing a mechanism for retaining larger amounts of hot ISM. We find evidence for a correlation between Mg_2 and $\delta\kappa_3$ that is independent of correlations of these two parameters with σ_v, and is enhanced when tested for constant a_4. The strengthening of the Mg_2–$\delta\kappa_3$ correlation when tested for constant a_4 indicates an underlying connection between the scatter about the fundamental plane, and the type II SN enrichment history of the central regions of elliptical galaxies that is independent of the details of the central structure of individual galaxies. This suggests that the Mg_2–$\delta\kappa_3$ trend is not related to the Mg_2 enhancements associated with kinematically decoupled cores seen in some disky elliptical galaxies (e.g., Bender & Surma 1992). It may be that systems with higher inner M/L_e (at a given mass) were more able to retain the metals generated in early epochs of star formation. Alternatively, systems experiencing more active or prolonged star formation may have produced an excess of baryonic dark matter from stellar remnants that is reflected in their higher M/L_e.

Subject Headings: galaxies: elliptical and lenticular, cD — galaxies: evolution — galaxies: general — galaxies: ISM — galaxies: structure – x-rays: galaxies

1. Introduction

The *Einstein* sample of early-type galaxies (Fabbiano *et al.*, 1992, hereafter P0) is the largest currently available sample of E and S0 galaxies observed in x-rays. There are *Einstein* observations of 148 normal or nearly normal early-type galaxies in the sample. We have been using this sample to explore the relationships of x-ray properties of E/S0 galaxies to other tracers of the ISM (Eskridge *et al.*, 1995a, hereafter P1) and to observables related to the structure and stellar populations of the sample (Eskridge *et al.*, 1995b,

hereafter P2). X-ray emission from luminous early-type galaxies is largely due to halos of gravitationally bound, hot ($T \sim 10^{6-7}$K) gas (Forman *et al.*, 1979; 1985; Trinchieri & Fabbiano 1985). Such gas is often the dominant mass-phase of the ISM in early-type galaxies (e.g., Fabbiano 1989 and references therein). Thus the *Einstein* sample offers us the opportunity to explore the physical relationships that govern the ISM, and to search for inter-relationships between the ISM and other global properties of early-type galaxies.

In P1 we presented an analysis of the ISM properties of the *Einstein* sample. The major results of P1 are as follows: We confirm the results of earlier studies (see Fabbiano 1989 and references therein), finding a strong correlation between L_B and L_X, with a power-law slope of 1.8±0.1. However, this is actually a combination of a slope-1 relation for the fainter galaxies ($log(L_X) \leq 40.5$) and a slope-2 relation for the more luminous galaxies. This is consistent with other work indicating that x-ray luminous early-type galaxies are so due to extensive halos of coronal gas, while x-ray faint early-type galaxies owe their emission to unresolved stellar x-ray sources (e.g., Trinchieri & Fabbiano 1985; Fabbiano *et al.*, 1989, hereafter FGT; Kim *et al.*, 1992; Fabbiano *et al.*, 1994). The mean values of the distribution functions of both L_X and L_X/L_B for the S0s are lower than those for the Es, thus, for a given stellar luminosity, the potential wells of S0s may be shallower than those of Es. Our S0 sample has excess 12μm emission compared to the Es. This may be due to emission from dust heated in star-forming regions in S0 disks. This interpretation is supported by the existence of a strong L_{12}–L_{100} correlation for our S0 sample that is not found for the Es, and by an analysis of optical–IR colors. We also find strong indications of a connection between galaxy ISM and nuclear activity. There are steep power-law slopes between radio luminosity and optical, x-ray properties, and FIR properties. We note that, while L_B is most strongly correlated with L_6, the *total* radio luminosity (summed over a ~1% bandwidth around 6cm – see P1), both L_X and L_X/L_B are more strongly correlated with L_{6co}, the *core* radio luminosity. These points support the argument (proposed by FGT) that radio cores in early-type galaxies are fueled by the accretion of cooling flow gas from the hot ISM.

The picture that emerges from P1 connects the properties of the ISM in E and S0 galaxies to their star formation history and nuclear activity. In P2, we examined the structural and chemical properties of the sample, and how these relate to the hot ISM. The major results of P2 are as follows: Rounder and boxier galaxies tend to have larger L_X, L_X/L_B, and L_6 (the L_X–a_4 trend has been noted previously from smaller samples by Bender *et al.*, 1989 and Djorgovski & de Carvalho 1990b). This suggests a connection between the shape of the potential and the ability to retain substantial halos of coronal gas. These in turn could be responsible for both feeding the nuclear sources through cooling flows and confining radio lobes (see also FGT). Both a/b and a_4 (the amplitude of the $cos(4\theta)$ term of the Fourier decomposition of the shape of a galaxy's isophotes, following Bender *et al.*, 1989) are correlated with L_B, but are not strongly correlated with either L_{12} or L_{100}. The lack of a trend with L_{12}, and the results of P1, indicate that there may be some significant contribution to the 12μm emission from hot dust in early-type galaxies that is not directly related to the stellar component. For the S0s, there may be a contribution from dust associated with disk star-formation regions.

There are strong correlations between Mg_2, σ_v, and L_X. Partial-rank analysis (see P1 and §2 below) shows that the depth of the gravitational potential well (as measured by

σ_v) is the crucial parameter. From a physical standpoint, the deeper the potential well, the better a galaxy is able to retain its hot ISM at the current epoch, and the better it was able to retain the enriched ejecta from its initial phase of strong star formation, and reprocess this ejecta into new stars. We find a threshold of $\log(\sigma_v) \approx 2.2$ above which the maximum radio luminosities in our sample jump abruptly by more than an order of magnitude. Below this value of σ_v, it appears that the potential well is too shallow to efficiently transport material to the nuclear engine. It does not seem coincidental that, at this same value of σ_v, we see a jump in the maximum detected L_X/L_B of more than one order of magnitude.

Finally, X-ray, radio, and optical luminosities are all correlated with both shape (a/b, a_4), and depth (Mg_2, σ_v) parameters. There are also strong relationships amongst the shape and the depth parameters. However, trends between the shape parameters (a/b, a_4) and one of the depth parameters (Mg_2 or σ_v) are modulated by the other parameter. That is, for instance, at a given a_4 value, the spread in σ_v appears directly related to the spread in Mg_2 such that the higher σ_v objects also have higher Mg_2. Alternatively, for a given σ_v, boxy galaxies tend to have *lower* Mg_2 values (and thus, we surmise, lower stellar abundances) than disky galaxies. This suggests that the presence of a hot ISM is dependent on both the shape (a/b, a_4) and the depth (Mg_2, σ_v) of the potential, but that these two families of parameters are not related in a simple way. These results, and the recent papers of Bender *et al.* (1992, 1993) prompted us to search for relationships between the observables in our database and the κ-parameters defined by Bender *et al.* (1992).

The recent work of Bender *et al.* (1992, 1993) introduced a set of parameters (the κ parameters) that provide an orthogonal coordinate system claimed to be a nearly perfect means of describing the so-called "fundamental plane" of elliptical galaxies. This is a roughly planar, two-dimensional structure in the parameter space defined by central velocity dispersion, effective radius, and effective surface brightness, about which the properties of elliptical galaxies are seen to scatter. The existence of the fundamental plane was first pointed out by Dressler *et al.* (1987) and Djorgovski & Davis (1987; see Djorgovski & DeCarvalho 1990a for a review). Bender *et al.* (1992) define the κ parameters as follows:

$$\kappa_1 \equiv (\log {\sigma_v}^2 + \log r_e)/\sqrt{2}; \tag{1a}$$

$$\kappa_2 \equiv (\log {\sigma_v}^2 + 2\log I_e - \log r_e)/\sqrt{6}; \tag{1b}$$

$$\kappa_3 \equiv (\log {\sigma_v}^2 - \log I_e - \log r_e)/\sqrt{3}. \tag{1c}$$

They also define the auxiliary parameter

$$\delta\kappa_3 \equiv \kappa_3 - 0.15\kappa_1 - 0.36. \tag{1d}$$

Here, r_e is the effective radius, σ_v the central velocity dispersion, and I_e a measure of the effective surface brightness (see Bender *et al.*, 1992 for details). Accepting the arguments of Bender *et al.* (1992), these definitions result in $\kappa_1 \propto \log M$, $\kappa_2 \propto \log({I_e}^3 M/L_e)$, and $\kappa_3 \propto \log(M/L_e)$. Where M/L_e is mass-to-light ratio defined by a hybrid of central and effective radius properties, and thus pertains to the inner part of the galaxy. The relationship $\kappa_3 - 0.15\kappa_1 - 0.36 = 0$ is their solution for the fundamental plane, thus the κ_1–κ_2 plane gives close to a face-on view of the fundamental plane, the κ_1–κ_3 plane gives an edge-on

view, and $\delta\kappa_3$ measures the scatter about the fundamental plane. A comparison of x-ray data with the κ parameters gives us another way to probe the link between emission properties (and thus the state of the ISM in early-type galaxies) and fundamental physical properties such as total mass, and dark matter content.

The rest of the paper is organized as follows: In §2 we discuss the nature and construction of our sample, and briefly review our statistical methods. The results are given in §3; trends with L_B in §3.1, those with L_X in §3.2, those with the 6cm radio-continuum properties in §3.3, and those with IRAS 12μm and 100μm luminosities in §3.4. Trends with structural and stellar properties of the sample are presented in §§3.5 and 3.6. In §4 we review our results, and suggest stratagies for future research. Some of the detailed statistical results are presented in the Appendix.

2. Sample Construction and Analysis Techniques

There are 46 galaxies in common between the *Einstein* and Bender *et al.* (1992) samples. Table 1 gives the κ-parameter data for these objects. Other data used below can be found in Table 1 of P1 (axial ratio, and optical, x-ray, IRAS, and radio flux data) and Table 1 of P2 (Mg_2, σ_v, and a_4 measurements). In Figure 1 we show the κ_1–κ_2 and κ_1–κ_3 distributions of these galaxies, using the symbol conventions of Bender *et al.* (1992). We also include arrows in Figure 1a that indicate the directions that various physical processes will move galaxies in the κ_1–κ_2 plane following Bender *et al.* (1992). Our sub-sample of the Bender *et al.* (1992) galaxies is still large enough to outline the loci in the κ planes, and thus appears to be a fair sample. We note that the diffuse dwarfs NGC 205 and NGC 4467 are included in our sample. As these objects are structurally distinct from classical ellipticals (Kormendy 1985) we shall not include them in our analysis below. They shall, however, be included in the figures.

Many of our data in the x-ray, FIR, and radio are upper-limits. Therefore, the use of standard statistical techniques is manifestly invalid for our project. Instead we use techniques from the field of survival analysis for evaluating the existence of bivariate correlations amongst our data. These methods explicitly account for the existence of upper limits in the samples being tested, subject to regularity conditions that may or may not apply in the case of any given data sample. This last point is, of course, the standard problem in all astronomical statistical analysis. In an effort to minimize it, we use a number of different statistical tests, each with their own assumptions about the nature of the data and distribution of the upper limits, in the hopes that gross violations of the normality assumptions by our data will manifest themselves in highly discrepant results for the various statistical tests. Basic references in the astronomical literature for these methods are Feigelson & Nelson (1985), Schmitt (1985), Isobe *et al.* (1986), LaValley *et al.* (1992), and Feigelson & Babu (1992). Details of our particular procedures are given in P1.

As we are dealing with a multiparametric data set, it is important to investigate possible inter-relationships between the various observables in our sample. A technique used in previous studies (Fabbiano *et al.*, 1988; P1; P2) is the partial Spearman rank method (Kendall & Stuart 1976). In brief, to apply this method, one builds a matrix of modified Spearman rank coefficients for the parameters to be tested, and then tests the correlation between subsamples of the parameters in the matrix-set while holding all other variables

in the matrix-set constant. The major results of the partial-rank analysis are presented in the text below. The full details of our results are tabulated in the Appendix.

3. Results

3.1 Trends with L_B

In Figure 2, we show plots of the κ parameters against L_B. Table 2 shows the results of the bivariate correlation tests on these data. The strongest correlation is that between L_B and κ_1 ($P < 10^{-4}$; fig. 2a). Weaker correlations are present between L_B and κ_2 (a negative trend at the $\lesssim$0.2% level), and with κ_3 (at the $\lesssim$0.7% level). Much of the scatter in the L_B–κ_2 and L_B–κ_3 plots (figs. 2b and 2c respectively) is caused by the few systems that are not "normal" ellipticals (the compact elliptical M32, and the bulges of S0 galaxies). We thus repeated the correlation analysis on sub-sets of the complete sample (see Table 2).

The negative correlation between L_B and κ_2 is significant for all tested samples. Recall that $\kappa_2 \propto I_e{}^3(M/L)$. Giant elliptical galaxies are known to show an anticorrelation between luminosity and surface brightness (L—Σ, e.g., Kormendy 1985). This result appears to reflect that trend, and argues that the $I_e{}^3$ proportionality dominates that with M/L in κ_2 for giant ellipticals. The removal of the compact dE (M32) and the S0 bulges weakens the trend. This is in keeping with Kormendy's (1985) result that compact dEs and bulges are both known to follow the L—Σ relationship defined by giant ellipticals. The analysis shows almost perfect random scatter in the plot of L_B against $\delta\kappa_3$.

The L_B–κ_3 trend disappears if M32 is removed. Thus, we find no evidence for a relationship between optical luminosity and M/L_e for normal ellipticals. Given the range in L_B of our sample, this is completely in keeping with the results of Lauer (1985). We note that L_B and κ_3 both correlate with κ_1, but that the κ_1–κ_3 trend (the equation of the fundametal plane from Bender *et al.*, 1992) has a very shallow slope (0.15). If there is such a shallow relation between L_B and κ_3 it could easily be masked by the scatter in our sample.

In Figure 3, we again show the distribution of our points in the κ-planes, but using different symbols for quartiles in L_B. We note that the most optically luminous galaxies tend to cluster in the "merging corner" of Bender *et al.* (1992), and that the distribution of points is generally as expected from the definitions of the κ parameters.

3.2 Trends with L_X

Plots of the κ-parameters against L_X are shown in Figure 4. Results of the bivariate correlation tests are given in Table 2. As for L_B, there is an obvious trend between κ_1 and L_X. The strength of this trend is essentially unaffected by removing M32 and the S0 bulges. Partial rank analysis shows that the L_X–κ_1 relationship is weaker than that between L_B and κ_1, but is still significant when taken for constant L_B (see Table A1). Therefore there is a direct link between mass and the presence of a hot ISM. This agrees with previous results (FGT; P1; P2) and with model predictions (e.g. Ciotti *et al.* 1991). We also find a statistically significant negative bivariate correlation between κ_2 and L_X. However, partial rank analysis shows the L_X–κ_2 trend to be driven by mutual correlations with L_B.

A stronger correlation (at the <0.4% level in all tests) exists between κ_3 with L_X. This correlation is confirmed by partial-rank analysis at the ~1.5% level, while no trend is found between L_B and κ_3 (see Table A3). This result can also be seen by an examination of the κ-planes using quartiles in L_X (Figure 5): the highest L_X galaxies are much more tightly clustered in the upper-right corner of the κ_1–κ_3 plane than are the highest L_B galaxies (see fig. 3). The difference between figures 3 and 5 appears entirely due to the correlation of κ_3 with L_X. More x-ray luminous galaxies tend to have higher M/L_e. The same is not true for optically luminous galaxies. Figure 5 also shows that high-L_X galaxies are not especially more concentrated in the "merging corner" of the κ_1–κ_2 plane, (while figure 3 does show such a concentration for the high L_B galaxies), so merging is not necessarily a key factor in producing high L_X galaxies. This is contrary to the early conclusions of Bender *et al.* (1989; see also Djorgovski & deCarvalho 1990a).

The L_X–κ_3 correlation points to a relationship between a global property of elliptical galaxies (the amount of hot ISM they are able to retain) and a property of the cores of elliptical galaxies (their inner M/L ratios). If the depth of the gravitational potential is a major factor in the ability of galaxies to retain their hot ISM (see e.g. Ciotti *et al.* 1991), the L_X–κ_3 relationship we find suggests that galaxies with relatively larger amounts of dark matter in their inner regions tend to have more massive dark matter halos.

As a number of parameters considered in earlier parts of this study (see P1 and P2) correlate more strongly with L_X/L_B than with either L_B or L_X, we examined the relationship of the κ parameters against L_X/L_B. No interesting correlations were found. The results of the statistical analysis are shown in Table 2.

3.3. Trends with the 6 cm Radio Luminosity

We find a very strong correlation between κ_1 and L_6 (nearly as strong as that with L_X) for all the samples we test (see Figure 6 and Table 2). Inspection of Figure 6a shows a threshold, as for other trends with L_6 discussed in P2: All systems detected at 6cm have $\kappa_1 \geq 3.5$. There is a significant negative trend between κ_2 and L_6 for all tested samples. There is also a significant trend between κ_3 and L_6 for all tested samples, in the sense that those systems with the largest M/L_e ratios have the strongest nonthermal radio emission. In keeping with this, we find that, as for L_X, the most radio luminous galaxies in our sample are tightly clustered in the upper-right corner of the κ_1–κ_3 plane (see Figure 7).

Partial-rank analysis, including L_6 along with L_B, L_X and the κ parameters, shows that the bivariate trends of L_6 with κ_2 and κ_3 are likely to be driven by underlying relationships of L_6, κ_2, and κ_3 with both L_B and L_X. However, the strong bivariate L_6–κ_1 trend is maintained when L_B and L_X dependancies are considered. Thus we find a strong relationship between the virial mass of early-type galaxies and their ability to generate non-thermal radio power. This relationship is *independent* of trends with either optical or x-ray luminosity.

3.4. Trends with mid and far IR Luminosities

Table 2 shows that the only significant correlation including L_{12} is that with κ_1. It is, however, much weaker than the correlations between κ_1 and L_B, L_X, or L_6. Also, when one consideres only giant and intermediate ellipticals (see Table 2c), the correlation is marginal at best. There are no significant trends with any of the other κ parameters.

The correlation between κ_1 and L_{100} is stronger that that betweeen κ_1 and L_{12}, and is significant for all of the samples tested. There is also a significant negative correlation (at the 1–2% level) between κ_2 and L_{100}. However, a partial-rank analysis on L_B, L_{100}, L_6, and the κ parameters indicates that the L_{100} trends found here are driven by the L_{100}–L_6 and L_B–L_{100} relationships found in P1, and the L_6–κ trends discussed in §3.3 above.

3.5. Trends with the Shape Parameters a/b and a_4

Table 3 shows some evidence for trends between κ_1, κ_3, and a/b, in the sense that larger κ_1 or κ_3 tend to imply rounder isophotes. This is reminiscent of the results presented in P2. Partial rank analysis indicates that these trends are driven by the underlying trend of a/b with σ_v (see P2 and Table A3). There is no compelling evidence for trends of a/b with either κ_2 or $\delta\kappa_3$. Similarly, we find no significant correlations of a_4 with any of the κ parameters. Our results are in agreement with previous conclusions pointing to a lack of correlation between axial ratio and the fundamental properties of early-type galaxies (e.g. Vader 1986).

3.6. Trends with Mg_2 and σ_v

Given the definition of κ_1 and κ_3, strong bivariate correlations are expected (and found) with σ_v irrespective of sample. Bivariate correlations are also found between Mg_2 and both κ_1 and κ_3 (see Table 3 and Figure 8). However, partial rank analysis shows that these are driven by the underlying strong Mg_2–σ_v trend (see Tables A1 and A3; see also Bender *et al.*, 1993, and P2). We find no evidence for any trend between κ_2 and either σ_v or Mg_2.

We find evidence for a positive trend between σ_v and $\delta\kappa_3$ for samples with the dwarf galaxies removed from our bivariate analysis (see Table 3b,c and Figure 9). A stronger bivariate correlation exists between Mg_2 and $\delta\kappa_3$ once we remove M32 from the sample (see Table 3b,c and Figure 8). The results of the partial-rank analysis indicate that the Mg_2–$\delta\kappa_3$ and Mg_2–σ_v trends are what drives the bivariate σ_v–$\delta\kappa_3$ correlation (see Table A4). This is important, as one could otherwise argue for a weak residual dependance of $\delta\kappa_3$ on σ_v on the basis of dimensional analysis. The inclusion of a_4 in the partial-rank analysis yields a *much* stronger correlations of Mg_2 with $\delta\kappa_3$, for a_4 constant. Analogous behaviour is seen with a/b (the most interesting results are shown in Tables A1–A4).

As the Mg_2–$\delta\kappa_3$ trend is not due to underlying relationships of both these parameters with σ_v, we are forced to consider possible reasons for a $\delta\kappa_3$–Mg_2 correlation. The evolutionary pathway for enrichment of Mg (e.g., Woosley & Weaver 1986) indicates that the scatter about the fundamental plane may be associated with variation in the SNII rate from system to system, and thus with the differences in early epochs of star formation in different systems. It may be that the high-Mg_2 systems are merger products in which secondary central disks have formed, and undergone (now intermediate age) bursts of star formation (Bender & Surma 1992; P2), although the strengthening of the Mg_2–$\delta\kappa_3$ trend for constant a_4 argues against this. Such a situation would cause a weakening of the Mg_2–$\delta\kappa_3$ correlation when tested for constant a_4, the opposite of what is observed.

The sense of the correlation indicates that systems with anomalously high M/L_e for their mass also tend to have enhanced Mg_2 values. These enhanced Mg_2 values may be due to an overall enhancement in metallicity in the cores of the affected galaxies. Thus it may simply be that those systems with higher M/L_e (at a given mass) were more able to retain

the metals generated in early epochs of star formation (due to less effective galactic winds – see e.g., Ciotti *et al.*, 1991). Another possibility is that large (central) Mg_2 values reflect enhanced abundances of elements primarily produced in Type II SN. Galaxies with such enhancements may have experienced enhanced central star formation at some point, and are thus also systems that have a significant fraction of baryonic dark matter in the form of stellar remnants. Our data do not allow us to distinguish amongst these alternatives, although a number of recent and ongoing studies are shedding further light on this area (e.g., Buzzoni *et al.*, 1992; Worthey *et al.*, 1992; Carollo *et al.*, 1993; Davies *et al.*, 1993; Worthey 1993).

4. Summary and Suggestions for Future Research

The main results of this study are as follows:

1). There are strong bivariate correlations of κ_1 with L_B, L_X, and L_6, all of which are upheld in a partial-rank analysis. Of these, the strongest is that between κ_1 and L_B. However, the correlations between κ_1 and both L_X and L_6 are still significant for constant L_B. These correlations point to galaxy mass as a key factor in x-ray and radio emission. This agrees with previous results pointing to the galaxy potential as a key factor in the retention of a hot ISM (e.g. FGT; Ciotti *et al.* 1991; P1; P2), and linking nuclear accretion of the latter, through cooling flows, to nuclear activity (FGT).

2). There are strong bivariate correlations between κ_3 and both L_X and L_6. Also, the distribution of points in the κ_1–κ_3 plane shows a much tighter grouping amongst the x-ray- or radio-brightest galaxies than amongst the optically brightest galaxies. Partial-rank analysis demonstrates that the L_X–κ_3 relationship is the dominant one, and that this trend holds up at the $\sim$1.5% confidence level when tested for constant L_B. This argues for a connection between a global property of galaxies (the amount of material in their x-ray coronae) and a core property (the inner M/L). The current finding may thus fit into the general framework of the fueling of central sources by cooling x-ray gas as suggested by FGT. It also suggests that variations in dark matter content (at a given optical luminosity) amongst elliptical galaxies may be a crucial factor in determining whether or not they can retain halos of coronal x-ray gas, and that the relative excess of dark matter in the core is an index of the presence of larger dark matter halos. A similar connection was made in P1 between L_X and the core radio luminosity.

3). While high L_B galaxies tend to concentrate in the 'merging corner' of the κ_1–κ_2 diagram (see Bender *et al.* 1992), the same is not true for high-L_X galaxies. Merging may, therefore, not be a key factor for the presence of a hot ISM.

4). We find evidence for bivariate trends between $\delta\kappa_3$ and both Mg_2 and σ_v. Partial-rank analysis indicates that the Mg_2–$\delta\kappa_3$ trend is the fundamental one. This result does not appear to be caused by a residual definitional dependence of $\delta\kappa_3$ on σ_v. The sense of the trend is that systems that have high M/L_e for their mass also tend to have enhanced central Mg_2 values. This may be due to the enhanced ability of such galaxies to maintain on-going or episodic central star formation for extended periods, or to retain the enriched ejecta of early epochs of star formation, or both. The Mg_2–$\delta\kappa_3$ trend becomes stronger when tested for constant a_4. This suggests that the Mg_2–$\delta\kappa_3$ correlation cannot be entirely driven by the existence of metal-rich nuclear disks (such as those discovered by Bender &

Surma 1992) in systems that scatter above the fundamental plane. Were this so, the trend would become weaker, rather than stronger, when evaluated for constant a_4, as it would be due to an Mg_2 enhancement that is linked to the presence of disky isophotes.

These findings suggest a number of areas for future study. The connection between global properties and the inner M/L ratio may be due to an underlying similarity in the overall potential structures of early-type galaxies. In this case, those systems with the highest inner M/L ratio would also tend to have the highest global M/L ratios. Current work on ROSAT data of early-type galaxies may help to resolve this puzzle. The relationship of the metal abundance parameter Mg_2 with the scatter about the Bender *et al.* (1992) realization of the fundamental plane is also a finding that begs for future research. In particular, it is important to see if such a trend is upheld for the Fe-lines as well as Mg_2. It would also be very interesting to see if there were any effects with either Mg_2 or Fe-line radial gradients. Given current efforts (many referred to above) in optical spectroscopy of elliptical galaxies, both of these projects could be accomplished in the next few years.

Acknowledgments

We would like to thank David Burstein for suggesting that we consider the κ-parameters as part of our study, and George Djorgovski for refereeing the paper. We also thank Glen Mackie and Ginevra Trinchieri for their comments on this study as it has progressed. We also thank Eric Feigelson and Michael LaValley for providing us with the latest versions of the ASURV software package. GF would like to thank the Aspen Summer School for the opportunity to focus on this project. This research has made use of the NASA/IPAC Extragalactic Database (NED) which is operated by the Jet Propulsion Laboratory, Caltech, under contract with the National Aeronautics and Space Administration. We are grateful to the National Aeronautics and Space Administration for support of this research under the LTSA grant NAGW2681 and contract NAS8-39073 (AXAF Science Center).

Appendix

Tables A1—A4 contain the detailed results of the partial Spearman Rank statistical analysis for those trends that are strong enough to warrant notice. Table A1 shows the analysis of trends with κ_1 (L_B, L_X, L_6, and Mg_2 are shown). Table A2 shows the analysis of trends with κ_2 (only L_B is shown). Table A3 shows the analysis of trends with κ_3 (L_B, L_X, a/b, and Mg_2 are shown). Table A4 shows the analysis of trends with $\delta\kappa_3$ (a/b, Mg_2, and σ_v are shown). Within each section, column 1 identifies the test pair, column 2 identifies the quantities to be held constant in the test, column 3 gives the sample under consideration ("Full" means all available non-dEs are included, "no cEs" means that the compact dwarf M32 has been excluded, and "no S0s" means that the S0 bulges have *also* been excluded). Column 4 gives the number of objects in the sample. Column 5 gives the partial Spearman rank statistic. Column 6 gives the probability that the test pair show a correlation for that set of parameters.

REFERENCES

Bender, R., Surma, P., Döbereiner, S., Möllenhoff, C., & Madejesky, R., 1989, AAp, 217, 35.

Bender, R., Burstein, D., & Faber, S.M., 1992, ApJ, 399, 462.

Bender, R., & Surma, P., 1992, AAp, 258, 250.

Bender, R., Burstein, D., & Faber, S.M., 1993, ApJ, 411, 153.

Buzzoni, A., Gariboldi, G., & Mantegazza, L., 1992, AJ, 103, 1814.

Carollo, C.M., Danziger, I.J., & Buson, L., 1993, MNRAS, 265, 553.

Ciotti, L., D'Ercole, A., Pellegrini, S., & Renzini, A., 1991, ApJ, 376, 380.

Davies, R.L., Sadler, E.M., & Peletier, R.F., 1993, MNRAS, 262, 650.

Djorgovski, S., & Davis, M., 1987, ApJ, 313, 59.

Djorgovski, S. & de Carvalho, R., 1990a, in "Windows on Galaxies," Astrophysics and Space Sciences Conference Proceedings Vol. 160, eds. G. Fabbiano, J.S. Gallagher, & A. Renzini (Dordrecht: Kluwer) pg. 9

Djorgovski, S. & de Carvalho, R., 1990b, in "Windows on Galaxies," Astrophysics and Space Sciences Conference Proceedings Vol. 160, eds. G. Fabbiano, J.S. Gallagher, & A. Renzini (Dordrecht: Kluwer) pg. 307.

Dressler, A., Lynden-Bell, D., Burstein, D., Davies, R.L., Faber, S.M., Terlevich, R.J., & Wegner, G., 1987, ApJ, 313, 42.

Eskridge, P.B., Fabbiano, G., & Kim, D.-W., 1995a, ApJS, In press. (P1)

Eskridge, P.B., Fabbiano, G., & Kim, D.-W., 1995b, ApJ, In press. (P2)

Fabbiano, G., Gioia, I.M., & Trinchieri, G., 1988, ApJ, 324, 749.

Fabbiano, G., 1989, ARA&A, 27, 87.

Fabbiano, G., Gioia, I.M., & Trinchieri, G., 1989, ApJ, 347, 127 (FGT).

Fabbiano, G., Kim, D.-W., & Trinchieri, G., 1992, ApJS, 80, 531 (P0).

Fabbiano, G., Kim, D.-W., & Trinchieri, G., 1994, ApJ, 429, 94.

Feigelson, E.D., & Nelson, P.I., 1985, ApJ, 293, 192.

Feigelson, E.D., & Babu, G.J., 1992, "Statistical Challenges in Modern Astronomy," (New York: Springer-Verlag).

Forman, W., Schwarz, J., Jones, C., Liller, W., & Fabian, A.C., 1979, ApJLet, 234, L27.

Forman, W., Jones, C., & Tucker, W., 1985, ApJ, 293, 102.

Isobe, T., Feigelson, E.D., & Nelson, P.I., 1986, ApJ, 306, 490.

Kendall, M., & Stuart, A., 1976, The Advanced Theory of Statistics, Vol. II (New York: Macmillan).

Kim, D.-W., Fabbiano, G., & Trinchieri, G., 1992, ApJ, 393, 134.

Kormendy, J., 1985, ApJ, 295, 73.

Lauer, T.R., 1985, ApJ, 292, 104.

LaValley, M.P., Isobe, T., & Feigelson, E.D., 1992, BAAS, 24, 839.

Schmitt, J.H.M.M., 1985, ApJ, 293, 178.

Trinchieri, G., & Fabbiano, G., 1985, ApJ, 296, 447.

Vader, J.P., 1986, ApJ, 306, 390.

Woosley, S.E., & Weaver, T.A., 1986, in "IAU Colloquium 89, Radiation Hydrodynamics in Stars & Compact Objects" eds. D. Mihalas & K.H. Winkler (Berlin: Springer) pg. 91.

Worthey, G., Faber, S.M., & Gonzalez, J.J., 1992, ApJ, 398, 69.

Worthey, G., 1993, ApJ, 409, 530.

TABLE 1 - κ-Parameter Data

Name	Type	κ_1	κ_2	κ_3	$\delta\kappa_3$
NGC 205	-3	2.219	2.898	0.856	0.163
NGC 221	-6	2.022	4.773	0.742	0.079
NGC 315	-3	4.652	2.988	1.010	−0.047
NGC 584	-2	3.818	3.756	0.766	−0.167
NGC 720	-5	3.977	3.525	0.924	−0.033
NGC 1052	-3	3.783	3.518	0.893	−0.034
NGC 1395	-5	4.003	3.517	0.968	0.007
NGC 1399	-5	4.045	3.798	0.991	0.025
NGC 1404	-5	3.708	3.982	0.795	−0.121
NGC 1407	-5	4.209	3.262	1.044	0.053
NGC 1553	-2	3.400	4.214	0.582	−0.288
NGC 1600	-5	4.506	3.069	0.993	−0.043
NGC 2300	-5	4.077	3.408	1.016	0.014
NGC 2694	-5	3.156	4.117	0.763	−0.070
NGC 2974	-5	3.880	3.460	0.929	−0.013
NGC 3115	-2	3.446	4.204	0.921	0.044
NGC 3377	-5	3.234	3.627	0.805	−0.040
NGC 3379	-5	3.509	3.970	0.874	−0.012
NGC 3607	-2	3.963	3.383	1.048	0.064
NGC 3608	-5	3.654	3.489	1.061	0.152
NGC 3818	-5	3.575	3.613	1.084	0.187
NGC 4168	-5	3.893	3.000	0.937	−0.007
NGC 4261	-5	4.120	3.531	1.009	0.031
NGC 4291	-5	3.710	4.004	0.985	0.068
NGC 4365	-5	3.918	3.471	1.042	0.094
NGC 4374	-5	4.002	3.726	0.980	0.019
NGC 4387	-5	2.855	3.516	0.676	−0.112
NGC 4406	-3	4.066	3.316	0.983	0.013
NGC 4467	-5	2.571	3.216	0.903	0.157
NGC 4472	-3	4.194	3.423	0.960	−0.029
NGC 4473	-5	3.469	3.897	0.792	−0.089
NGC 4551	-5	3.006	3.506	0.765	−0.046
NGC 4564	-5	3.332	3.722	0.857	−0.003
NGC 4589	-5	3.914	3.290	0.960	0.013
NGC 4621	-5	3.844	3.636	0.971	0.034
NGC 4636	-3	3.931	3.014	0.957	0.008
NGC 4649	-2	4.200	3.639	1.058	0.038
NGC 4697	-5	3.757	3.280	0.764	−0.159
IC 4296	-5	4.458	3.134	1.016	−0.013
NGC 5322	-5	3.933	3.586	0.789	−0.161
NGC 5576	-5	3.537	3.896	0.784	−0.107
NGC 5846	-2	4.242	3.094	1.084	0.058
NGC 7332	-2	3.020	4.577	0.445	0.368
IC 1459	-5	4.082	3.729	0.984	0.012
NGC 7619	-5	4.330	3.416	1.040	0.030
NGC 7626	-5	4.155	3.146	0.894	−0.089

TABLE 2a - Bivariate Correlation Tests with the Luminosity Parameters

	κ_1		κ_2		κ_3		$\delta\kappa_3$	
	N_{tot}	N_{lim}	N_{tot}	N_{lim}	N_{tot}	N_{lim}	N_{tot}	N_{lim}
	Cox-Hazard[a)]	prob		prob		prob		prob
	Kendall's τ	prob		prob		prob		prob
	Spearman rank	prob		prob		prob		prob
$_B$	44	0	44	0	44	0	44	0
	63.213	$< 10^{-4}$	10.002	0.0016	7.309	0.0069	1.403	0.2363
	6.313	$< 10^{-4}$	3.845	0.0001	2.945	0.0032	0.395	0.6931
	0.843	$< 10^{-4}$	−0.540	0.0004	0.445	0.0035	−0.075	0.6245
$_X$	44	14	44	14	44	14	44	14
	23.415	$< 10^{-4}$	9.294	0.0023	9.941	0.0016	0.178	0.6732
	5.528	$< 10^{-4}$	2.990	0.0028	3.496	0.0005	0.376	0.7066
	0.798	$< 10^{-4}$	−0.452	0.0030	0.529	0.0005	0.057	0.7061
$_X/L_B$	44	14	44	14	44	14	44	14
	16.870	$< 10^{-4}$	8.860	0.0029	8.957	0.0028	0.057	0.8109
	4.597	$< 10^{-4}$	2.767	0.0057	3.203	0.0014	0.257	0.7974
	0.679	$< 10^{-4}$	−0.411	0.0070	0.483	0.0015	0.054	0.7218
$_{12}$	41	16	41	16	41	16	41	16
	11.426	0.0007	2.788	0.0950	3.075	0.0795	0.021	0.8859
	3.002	0.0027	1.309	0.1904	1.948	0.0514	0.287	0.7738
	0.445	0.0049	−0.170	0.2835	0.312	0.0483	0.033	0.8345
$_{100}$	41	16	41	16	41	16	41	16
	10.501	0.0012	5.622	0.0177	0.714	0.3980	1.122	0.2894
	3.254	0.0011	2.478	0.0132	1.477	0.1396	1.277	0.2016
	0.520	0.0010	−0.398	0.0118	0.247	0.1189	−0.199	0.2084
$_6$	44	19	44	19	44	19	44	19
	20.435	$< 10^{-4}$	11.511	0.0007	10.582	0.0011	0.243	0.6220
	5.127	$< 10^{-4}$	2.974	0.0029	2.852	0.0043	0.100	0.9204
	0.749	$< 10^{-4}$	−0.459	0.0026	0.450	0.0031	0.030	0.8455

a). The values in rows 2-4 of these columns are the test scores for the three correlation tests.

The diffuse dEs NGC 205 and NGC 4467 are not included.

TABLE 2b - Bivariate Correlation Tests with the Luminosity Parameters

	κ_1		κ_2		κ_3		$\delta\kappa_3$	
	N_{tot}	N_{lim}	N_{tot}	N_{lim}	N_{tot}	N_{lim}	N_{tot}	N_{lim}
	Cox-Hazard	prob		prob		prob		prob
	Kendall's τ	prob		prob		prob		prob
	Spearman rank	prob		prob		prob		prob
L_B	43	0	43	0	43	0	43	0
	47.562	$< 10^{-4}$	8.478	0.0036	3.413	0.0647	0.556	0.4559
	6.082	$< 10^{-4}$	3.528	0.0004	2.660	0.0078	0.042	0.9666
	0.831	$< 10^{-4}$	−0.507	0.0010	0.409	0.0080	−0.017	0.9139
L_X	43	14	43	14	43	14	43	14
	29.475	$< 10^{-4}$	7.841	0.0051	8.479	0.0036	0.059	0.8080
	5.383	$< 10^{-4}$	2.764	0.0057	3.308	0.0009	0.666	0.5054
	0.793	$< 10^{-4}$	−0.432	0.0051	0.504	0.0011	0.086	0.5783
L_X/L_B	43	14	43	14	43	14	43	14
	20.307	$< 10^{-4}$	7.090	0.0078	7.218	0.0072	0.001	0.9794
	4.416	$< 10^{-4}$	2.525	0.0116	2.998	0.0027	0.553	0.5799
	0.649	$< 10^{-4}$	−0.369	0.0167	0.442	0.0042	0.088	0.5702
L_{12}	40	16	40	16	40	16	40	16
	9.881	0.0017	0.519	0.4711	1.937	0.1639	0.078	0.7805
	2.726	0.0064	0.964	0.3350	1.696	0.0899	0.632	0.5276
	0.415	0.0096	−0.122	0.4447	0.274	0.0870	0.101	0.5265
L_{100}	40	15	40	15	40	15	40	15
	10.500	0.0012	3.721	0.0537	0.298	0.5853	0.616	0.4326
	3.042	0.0023	2.239	0.0251	1.256	0.2092	1.049	0.2943
	0.488	0.0023	−0.360	0.0246	0.204	0.2017	−0.145	0.3642
L_6	43	18	43	18	43	18	43	18
	25.775	$< 10^{-4}$	11.062	0.0009	9.209	0.0024	0.463	0.4962
	5.001	$< 10^{-4}$	2.781	0.0054	2.656	0.0079	0.366	0.7141
	0.731	$< 10^{-4}$	−0.419	0.0067	0.417	0.0069	0.090	0.5583

Table entries as defined in notes to Table 2a.

The compact dE M32 has been removed.

TABLE 2c - Bivariate Correlation Tests with the Luminosity Parameters

	κ_1		κ_2		κ_3		$\delta\kappa_3$	
	N_{tot}	N_{lim}	N_{tot}	N_{lim}	N_{tot}	N_{lim}	N_{tot}	N_{lim}
	Cox-Hazard	prob		prob		prob		prob
	Kendall's τ	prob		prob		prob		prob
	Spearman rank	prob		prob		prob		prob
$_B$	40	0	40	0	40	0	40	0
	45.665	$< 10^{-4}$	7.080	0.0078	2.619	0.1056	0.124	0.7243
	5.828	$< 10^{-4}$	3.217	0.0013	2.343	0.0191	0.245	0.8066
	0.818	$< 10^{-4}$	−0.477	0.0029	0.365	0.0227	0.022	0.8905
$_X$	40	12	40	12	40	12	40	12
	26.219	$< 10^{-4}$	6.045	0.0139	10.280	0.0013	0.759	0.3835
	5.128	$< 10^{-4}$	2.324	0.0201	3.050	0.0023	1.181	0.2377
	0.789	$< 10^{-4}$	−0.372	0.0201	0.487	0.0024	0.190	0.2343
$_X/L_B$	40	12	40	12	40	12	40	12
	17.951	$< 10^{-4}$	5.818	0.0159	8.852	0.0029	1.379	0.2402
	4.148	$< 10^{-4}$	2.100	0.0358	2.753	0.0059	1.114	0.2653
	0.628	0.0001	−0.306	0.0557	0.418	0.0090	0.193	0.2282
$_{12}$	37	16	37	16	37	16	37	16
	8.401	0.0038	0.230	0.6312	3.992	0.0457	0.247	0.6188
	2.179	0.0293	0.436	0.6630	1.459	0.1444	0.967	0.3337
	0.354	0.0338	−0.034	0.8401	0.241	0.1477	0.145	0.3834
$_{100}$	37	14	37	14	37	14	37	14
	11.896	0.0006	5.332	0.0209	1.785	0.1815	0.534	0.4650
	2.951	0.0032	2.195	0.0282	1.265	0.2059	0.712	0.4762
	0.501	0.0027	−0.370	0.0265	0.225	0.1767	−0.082	0.6207
$_6$	40	15	40	15	40	15	40	15
	22.746	$< 10^{-4}$	8.676	0.0032	8.852	0.0029	0.915	0.3389
	4.730	$< 10^{-4}$	2.322	0.0203	2.285	0.0223	0.546	0.5848
	0.721	$< 10^{-4}$	−0.359	0.0250	0.389	0.0150	0.140	0.3828

Table entries as defined in notes to Table 2a.

M32 and the S0 bulges (NGC 1553, NGC 3115, and NGC 7332) removed.

TABLE 3a - Bivariate Correlations with the Structural and Stellar Parameters

	κ_1		κ_2		κ_3		$\delta\kappa_3$	
	N_{tot}	N_{lim}	N_{tot}	N_{lim}	N_{tot}	N_{lim}	N_{tot}	N_{lim}
	Cox-Hazard	prob		prob		prob		prob
	Kendall's τ	prob		prob		prob		prob
	Spearman rank	prob		prob		prob		prob
a/b	44	0	44	0	44	0	44	0
	8.399	0.0038	2.425	0.1194	4.482	0.0343	1.516	0.2183
	2.796	0.0052	1.398	0.1621	2.270	0.0232	0.942	0.3460
	−0.401	0.0085	0.198	0.1937	−0.341	0.0255	−0.140	0.3575
Mg_2	41	0	41	0	41	0	41	0
	13.324	0.0003	3.088	0.0789	24.464	$< 10^{-4}$	0.354	0.5517
	3.946	0.0001	0.753	0.4513	3.868	0.0001	2.204	0.0275
	0.581	0.0002	−0.136	0.3910	0.582	0.0002	0.355	0.0248
σ_v	41	0	41	0	41	0	41	0
	73.744	$< 10^{-4}$	2.486	0.1149	23.918	$< 10^{-4}$	0.224	0.6363
	6.493	$< 10^{-4}$	1.236	0.2166	5.000	$< 10^{-4}$	1.719	0.0856
	0.861	$< 10^{-4}$	−0.202	0.2010	0.704	$< 10^{-4}$	0.290	0.0671
a_4	31	0	31	0	31	0	31	0
	5.822	0.0158	0.353	0.5526	$< 10^{-3}$	0.9968	0.129	0.7199
	1.838	0.0661	0.374	0.7082	0.953	0.3407	0.017	0.9864
	−0.309	0.0902	0.099	0.5866	−0.135	0.4597	−0.012	0.9498

Table entries as defined in notes to Table 2a.

The diffuse dEs are not included.

TABLE 3b - Bivariate Correlations with the Structural and Stellar Parameters

	κ_1		κ_2		κ_3		$\delta\kappa_3$	
	N_{tot}	N_{lim}	N_{tot}	N_{lim}	N_{tot}	N_{lim}	N_{tot}	N_{lim}
	Cox-Hazard	prob		prob		prob		prob
	Kendall's τ	prob		prob		prob		prob
	Spearman rank	prob		prob		prob		prob
a/b	43	0	43	0	43	0	43	0
	9.115	0.0025	4.465	0.0346	4.691	0.0303	1.493	0.2218
	2.925	0.0034	1.478	0.1394	2.317	0.0205	0.986	0.3243
	−0.424	0.0060	0.211	0.1708	−0.352	0.0224	−0.142	0.3568
Mg_2	40	0	40	0	40	0	40	0
	7.361	0.0067	0.022	0.8830	16.020	0.0001	11.951	0.0005
	3.627	0.0003	0.315	0.7529	3.569	0.0004	2.683	0.0073
	0.548	0.0006	−0.069	0.6661	0.550	0.0006	0.446	0.0053
σ_v	40	0	40	0	40	0	40	0
	64.654	$< 10^{-4}$	0.012	0.9120	17.875	$< 10^{-4}$	4.765	0.0290
	6.269	$< 10^{-4}$	0.816	0.4147	4.744	$< 10^{-4}$	2.179	0.0293
	0.850	$< 10^{-4}$	−0.141	0.3792	0.681	$< 10^{-4}$	0.380	0.0176

Table entries as defined in notes to Table 2a.

The compact dE M32 has been removed.

TABLE 3c - Bivariate Correlations with the Structural and Stellar Parameters

	κ_1		κ_2		κ_3		$\delta\kappa_3$	
	N_{tot}	N_{lim}	N_{tot}	N_{lim}	N_{tot}	N_{lim}	N_{tot}	N_{lim}
	Cox-Hazard	prob		prob		prob		prob
	Kendall's τ	prob		prob		prob		prob
	Spearman rank	prob		prob		prob		prob
a/b	40	0	40	0	40	0	40	0
	3.304	0.0691	0.417	0.5184	1.483	0.2232	0.552	0.4574
	2.218	0.0266	0.467	0.6405	1.728	0.0840	1.670	0.0950
	−0.337	0.0352	0.054	0.7376	−0.274	0.0875	−0.266	0.0970
Mg_2	39	0	39	0	39	0	39	0
	7.466	0.0063	0.035	0.8513	15.892	0.0001	12.347	0.0004
	3.633	0.0003	0.242	0.8086	3.500	0.0005	2.798	0.0051
	0.554	0.0006	−0.053	0.7445	0.548	0.0007	0.468	0.0039
σ_v	39	0	39	0	39	0	39	0
	67.934	$< 10^{-4}$	0.152	0.6962	17.908	$< 10^{-4}$	4.631	0.0314
	6.570	$< 10^{-4}$	1.004	0.3153	4.768	$< 10^{-4}$	2.178	0.0294
	0.891	$< 10^{-4}$	−0.169	0.2965	0.691	$< 10^{-4}$	0.380	0.0192

Table entries as defined in notes to Table 2a.

M32 and the S0 bulges (NGC 1553, NGC 3115, and NGC 7332) have been removed.

TABLE A1 - Partial Spearman Rank Analysis: Trends with κ_1

Test Pair†	Held parameters	Sample	Size	Partial Spearman rank	Probability
L_B–κ_1	L_X	Full	44	0.673	< 0.005
	L_X	no cEs	43	0.643	< 0.005
	L_X	no S0s	40	0.640	< 0.005
	L_6	Full	44	0.708	< 0.005
	L_6	no cEs	43	0.702	< 0.005
	L_6	no S0s	40	0.692	< 0.005
	L_X,L_6	Full	44	0.562	< 0.005
	L_X,L_6	no cEs	43	0.544	< 0.005
	L_X,L_6	no S0s	40	0.536	< 0.005
L_X–κ_1	L_B	Full	44	0.560	< 0.005
	L_B	no cEs	43	0.544	< 0.005
	L_B	no S0s	40	0.572	< 0.005
	L_6	Full	44	0.701	< 0.005
	L_6	no cEs	43	0.690	< 0.005
	L_6	no S0s	40	0.710	< 0.005
	L_B,L_6	Full	44	0.550	< 0.005
	L_B,L_6	no cEs	43	0.523	< 0.005
	L_B,L_6	no S0s	40	0.567	< 0.005
L_6–κ_1	L_B	Full	44	0.493	< 0.005
	L_B	no cEs	43	0.487	< 0.005
	L_B	no S0s	40	0.494	< 0.005
	L_X	Full	44	0.621	< 0.005
	L_X	no cEs	43	0.586	< 0.005
	L_X	no S0s	40	0.607	< 0.005
	L_B,L_X	Full	44	0.481	< 0.005
	L_B,L_X	no cEs	43	0.461	< 0.005
	L_B,L_X	no S0s	40	0.487	< 0.005

TABLE A1 - continued

Test Pair†	Held parameters	Sample	Size	Partial Spearman rank	Probability
Mg_2–κ_1	a/b	Full	41	0.488	< 0.005
	a/b	no cEs	40	0.434	< 0.005
	a/b	no S0s	39	0.449	< 0.005
	σ_v	Full	41	0.148	0.192
	σ_v	no cEs	40	0.142	0.205
	σ_v	no S0s	39	0.080	0.319
	a_4	Full	31	0.560	< 0.005
	a/b,σ_v	Full	41	0.096	0.282
	a/b,σ_v	no cEs	40	0.079	0.321
	a/b,σ_v	no S0s	39	0.060	0.365
	a/b,a_4	Full	31	0.492	< 0.005
	σ_v,a_4	Full	31	0.044	> 0.400
	a/b,σ_v,a_4	Full	31	0.016	> 0.400

† The following combinations show no correlations: a/b–κ_1, a_4–κ_1

TABLE A2 - Partial Spearman Rank Analysis: Trends with κ_2

Test Pair†	Held parameters	Sample	Size	Partial Spearman rank	Probability
L_B–κ_2	L_X	Full	44	−0.354	0.011
	L_X	no cEs	43	−0.320	0.022
	L_X	no S0s	40	−0.331	0.022
	L_6	Full	44	−0.358	0.010
	L_6	no cEs	43	−0.346	0.015
	L_6	no S0s	40	−0.350	0.017
	L_X,L_6	Full	44	−0.264	0.048
	L_X,L_6	no cEs	43	−0.249	0.062
	L_X,L_6	no S0s	40	−0.273	0.050

† The following test pairs show no correlation: L_X–κ_2, L_6–κ_2, a/b–κ_2, Mg_2–κ_2, a_4–κ_2

TABLE A3 - Partial Spearman Rank Analysis: Trends with κ_3

Test Pair†	Held parameters	Sample	Size	Partial Spearman rank	Probability
L_B–κ_3	L_X	Full	44	0.132	0.208
	L_X	no cEs	43	0.097	0.271
	L_X	no S0s	40	0.064	0.352
	L_6	Full	44	0.225	0.078
	L_6	no cEs	43	0.209	0.095
	L_6	no S0s	40	0.177	0.152
	L_X,L_6	Full	44	0.035	> 0.400
	L_X,L_6	no cEs	43	0.018	> 0.400
	L_X,L_6	no S0s	40	−0.017	> 0.400
L_X–κ_3	L_B	Full	44	0.343	0.014
	L_B	no cEs	43	0.336	0.017
	L_B	no S0s	40	0.351	0.016
	L_6	Full	44	0.379	0.007
	L_6	no cEs	43	0.363	0.010
	L_6	no S0s	40	0.365	0.013
	L_B,L_6	Full	44	0.314	0.023
	L_B,L_6	no cEs	43	0.304	0.028
	L_B,L_6	no S0s	40	0.325	0.024

TABLE A3 - continued

Test Pair†	Held parameters	Sample	Size	Partial Spearman rank	Probability
a/b–κ_3	Mg_2	Full	41	−0.156	0.181
	Mg_2	no cEs	40	−0.178	0.150
	Mg_2	no S0s	39	−0.164	0.175
	σ_v	Full	41	−0.133	0.215
	σ_v	no cEs	40	−0.147	0.196
	σ_v	no S0s	39	−0.091	0.293
	a_4	Full	31	−0.418	0.011
	Mg_2,σ_v	Full	41	−0.069	0.341
	Mg_2,σ_v	no cEs	40	−0.080	0.318
	Mg_2,σ_v	no S0s	39	−0.033	> 0.400
	Mg_2,a_4	Full	31	−0.259	0.089
	σ_v,a_4	Full	31	−0.260	0.088
	Mg_2,σ_v,a_4	Full	31	−0.207	0.156
Mg_2–κ_3	a/b	Full	41	0.512	< 0.005
	a/b	no cEs	40	0.464	< 0.005
	a/b	no S0s	39	0.462	< 0.005
	σ_v	Full	41	0.278	0.044
	σ_v	no cEs	40	0.267	0.052
	σ_v	no S0s	39	0.241	0.077
	a_4	Full	31	0.627	< 0.005
	a/b,σ_v	Full	41	0.255	0.062
	a/b,σ_v	no cEs	40	0.238	0.079
	a/b,σ_v	no S0s	39	0.227	0.092
	a/b,a_4	Full	31	0.560	< 0.005
	σ_v,a_4	Full	31	0.332	0.041
	a/b,σ_v,a_4	Full	31	0.294	0.068

† The following test pairs show no correlation: L_6–κ_3, a_4–κ_3

TABLE A4 - Partial Spearman Rank Analysis: Trends with $\delta\kappa_3$

Test Pair†	Held parameters	Sample	Size	Partial Spearman rank	Probability
a/b–$\delta\kappa_3$	Mg_2	Full	41	−0.121	0.233
	Mg_2	no cEs	40	−0.075	0.327
	Mg_2	no S0s	39	−0.145	0.202
	σ_v	Full	41	−0.157	0.178
	σ_v	no cEs	40	−0.120	0.236
	σ_v	no S0s	39	−0.186	0.141
	a_4	Full	31	−0.467	< 0.005
	Mg_2,σ_v	Full	41	−0.105	0.263
	Mg_2,σ_v	no cEs	40	−0.041	> 0.400
	Mg_2,σ_v	no S0s	39	−0.114	0.250
	Mg_2,a_4	Full	31	−0.339	0.038
	σ_v,a_4	Full	31	−0.378	0.022
	Mg_2,σ_v,a_4	Full	31	−0.327	0.046
Mg_2–$\delta\kappa_3$	a/b	Full	41	0.285	0.040
	a/b	no cEs	40	0.385	0.009
	a/b	no S0s	39	0.383	0.010
	σ_v	Full	41	0.236	0.076
	σ_v	no cEs	40	0.302	0.033
	σ_v	no S0s	39	0.327	0.024
	a_4	Full	31	0.566	< 0.005
	a/b,σ_v	Full	41	0.205	0.108
	a/b,σ_v	no cEs	40	0.282	0.045
	a/b,σ_v	no S0s	39	0.294	0.041
	a/b,a_4	Full	31	0.480	< 0.005
	σ_v,a_4	Full	31	0.429	0.010
	a/b,σ_v,a_4	Full	31	0.387	0.022

TABLE A4 - continued

Test Pair†	Held parameters	Sample	Size	Partial Spearman rank	Probability
σ_v–$\delta\kappa_3$	a/b	Full	41	0.217	0.092
	a/b	no cEs	40	0.312	0.028
	a/b	no S0s	39	0.279	0.047
	Mg_2	Full	41	0.101	0.268
	Mg_2	no cEs	40	0.168	0.164
	Mg_2	no S0s	39	0.146	0.201
	a_4	Full	31	0.421	0.010
	a/b,Mg_2	Full	41	0.081	0.313
	a/b,Mg_2	no cEs	40	0.157	0.185
	a/b,Mg_2	no S0s	39	0.114	0.250
	a/b,a_4	Full	31	0.313	0.049
	Mg_2,a_4	Full	31	0.109	0.288
	a/b,Mg_2,a_4	Full	31	0.058	0.386

† The following test pairs show no correlation: L_B–$\delta\kappa_3$, L_X–$\delta\kappa_3$, L_6–$\delta\kappa_3$, a_4–$\delta\kappa_3$

Figure Captions

1. κ_1 vs. a) κ_2, and b) κ_3. Symbols are coded as in Bender *et al.* (1992): Squares are giant ellipticals; Triangles are intermediate ellipticals; Diamonds are dwarf ellipticals; Crosses are S0 bulges; M32, a compact dE is shown as a solid circle. The arrows in a) are from Bender *et al.* (1992), and show the directions that various processes will move objects in the κ_1–κ_2 plane. The dashed line in b) shows the equation of the fundamental plane from Bender *et al.* (1992).

2. κ parameters vs. L_B. Symbols as in Figure 1.

3. κ_1 vs. a) κ_2, and b) κ_3. Symbols are coded in quartiles of L_B, with the solid circles being the most optically luminous galaxies, then the squares, then the triangles. The diamonds are the optically faintest galaxies in our sample.

4. κ parameters vs. L_X. Symbols as in Figure 1 for x-ray detections. Open symbols for x-ray upper limits (+-signs for x-ray upper limits on S0 bulges).

5. κ_1 vs. a) κ_2, and b) κ_3. Symbols are coded as in Figure 3, but in quartiles of L_X, with open symbols for systems with upper limits in L_X.

6. κ parameters vs. L_6. Symbols as in Figure 4.

7. κ_1 vs. a) κ_2, and b) κ_3. Symbols are coded as in Figure 5, but in quartiles of L_6, with open symbols for systems with upper limits in L_6.

8. κ parameters vs. Mg_2. Symbols as in Figure 4.

9. $\delta\kappa_3$ vs. $\log(\sigma_v)$. Symbols as in Figure 4.

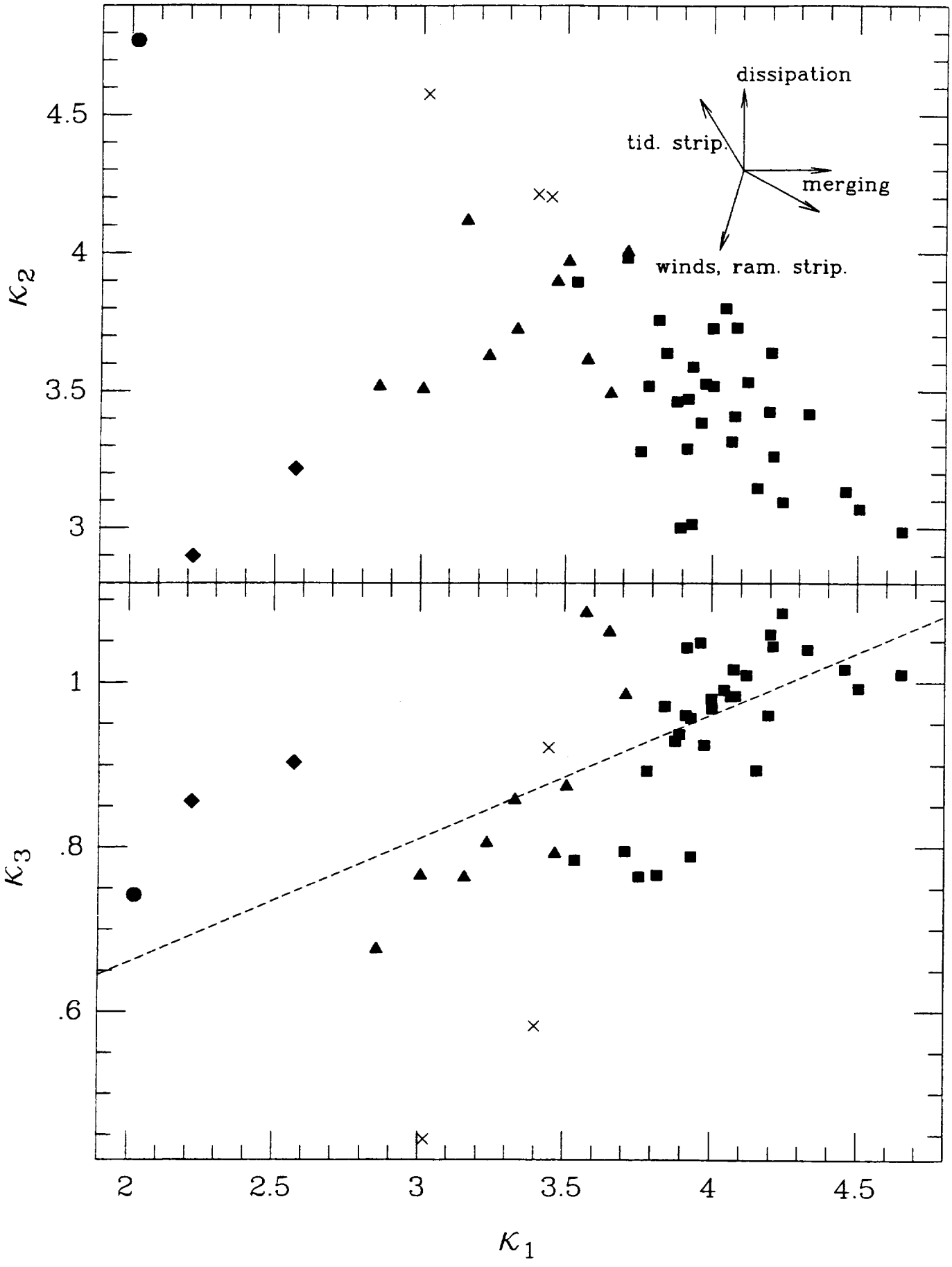

Figure 1a

Figure 1b

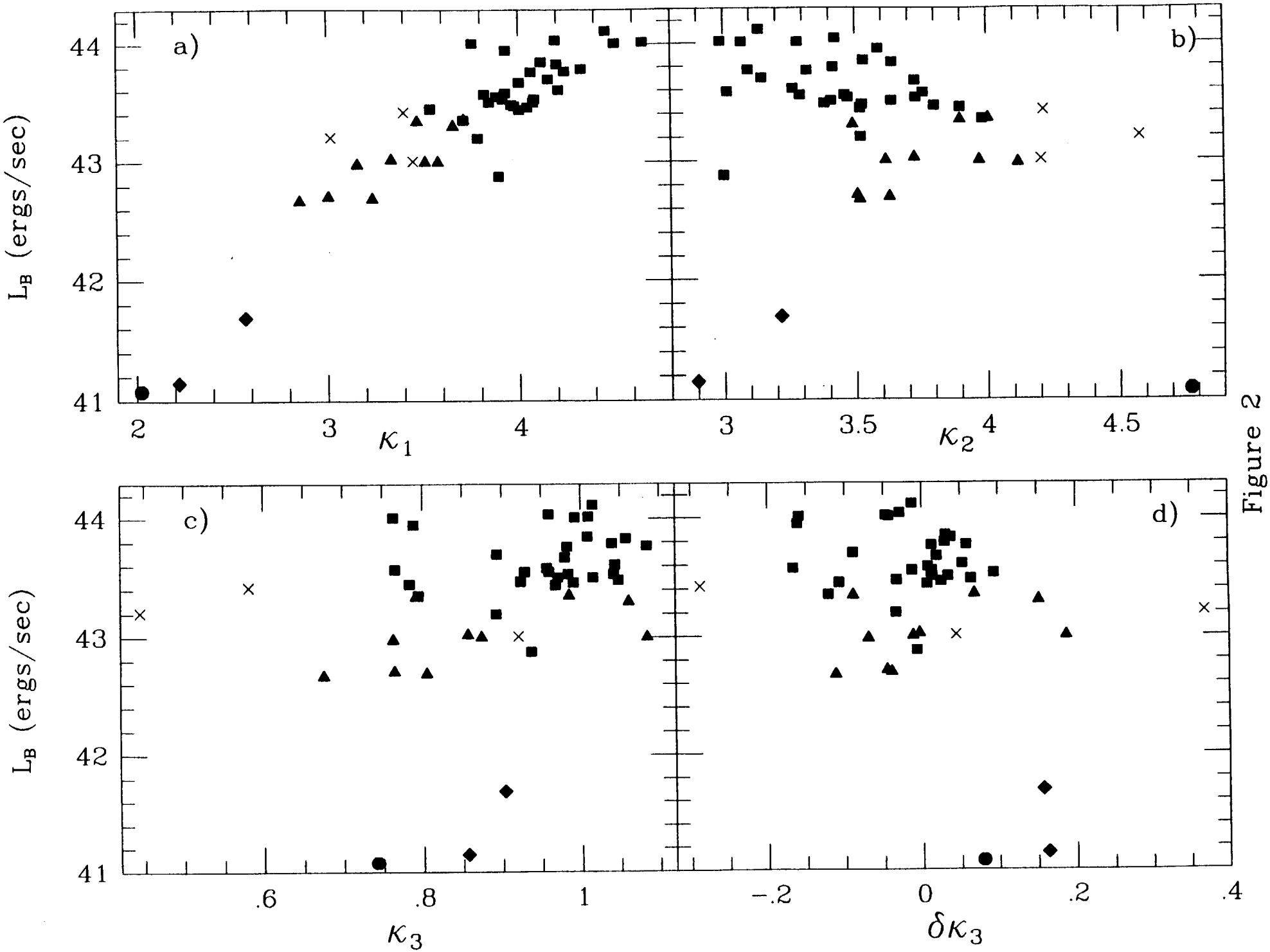
a)
b)
c)
d)
L_B (ergs/sec)
44
43
42
41
2
3
4
κ_1
3
3.5
4
4.5
κ_2
.6
.8
1
κ_3
-.2
0
.2
.4
$\delta\kappa_3$

Figure 2

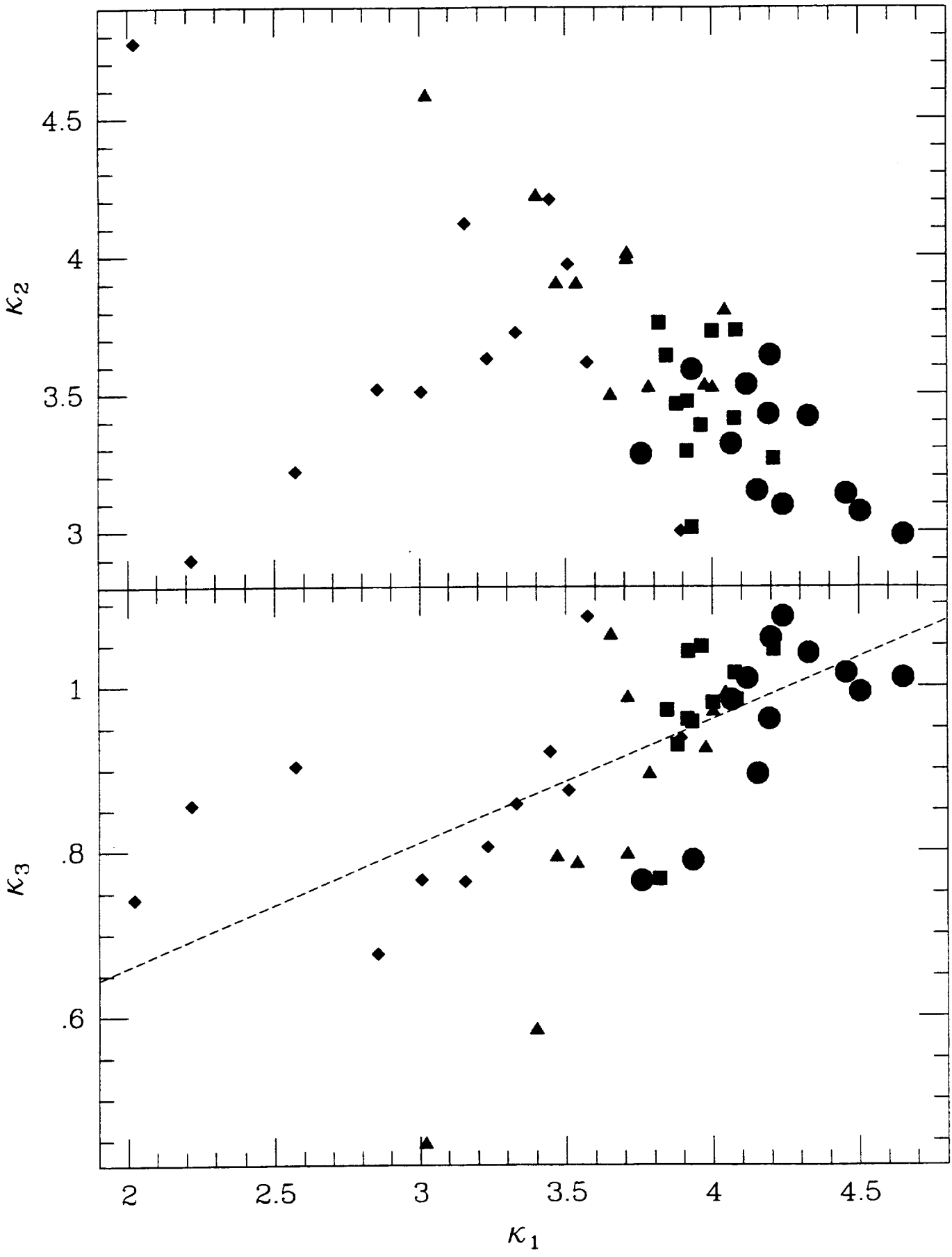

Figure 3a

Figure 3b

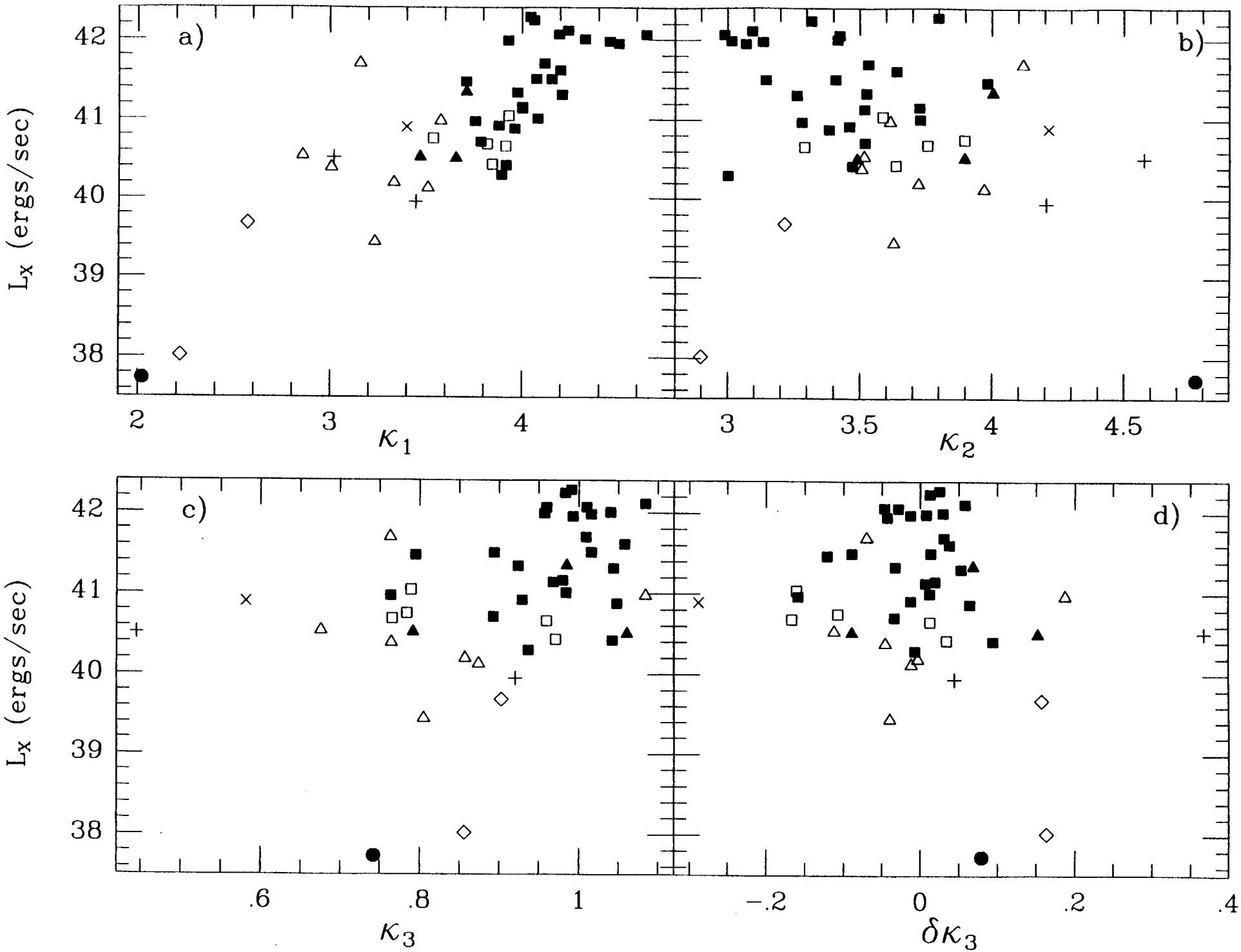
a)
b)
c)
d)
L_X (ergs/sec)
42
41
40
39
38
2
3
4
κ_1
3
3.5
4
4.5
κ_2
.6
.8
1
κ_3
−.2
0
.2
.4
$\delta\kappa_3$

Figure 4

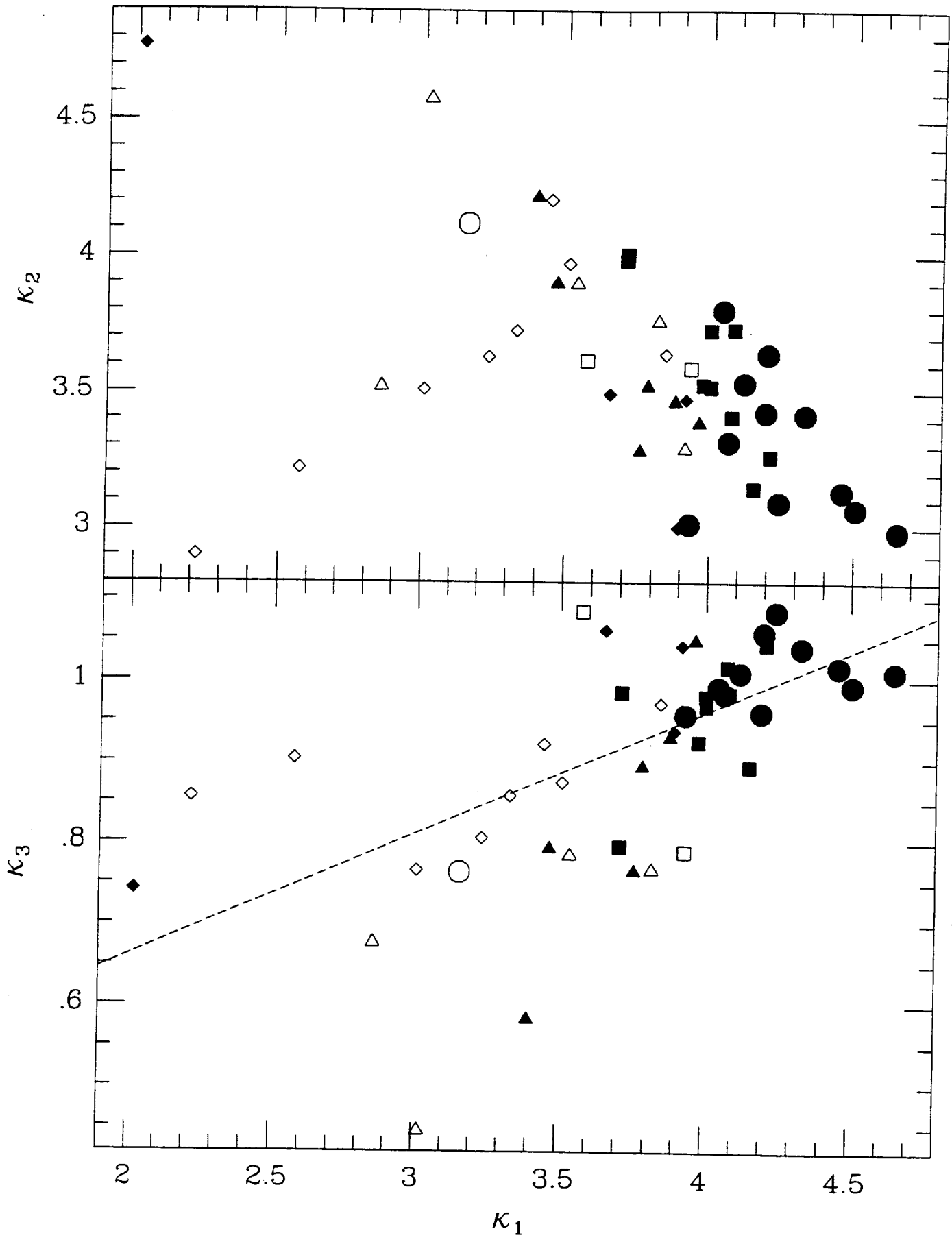

Figure 5a

Figure 5b

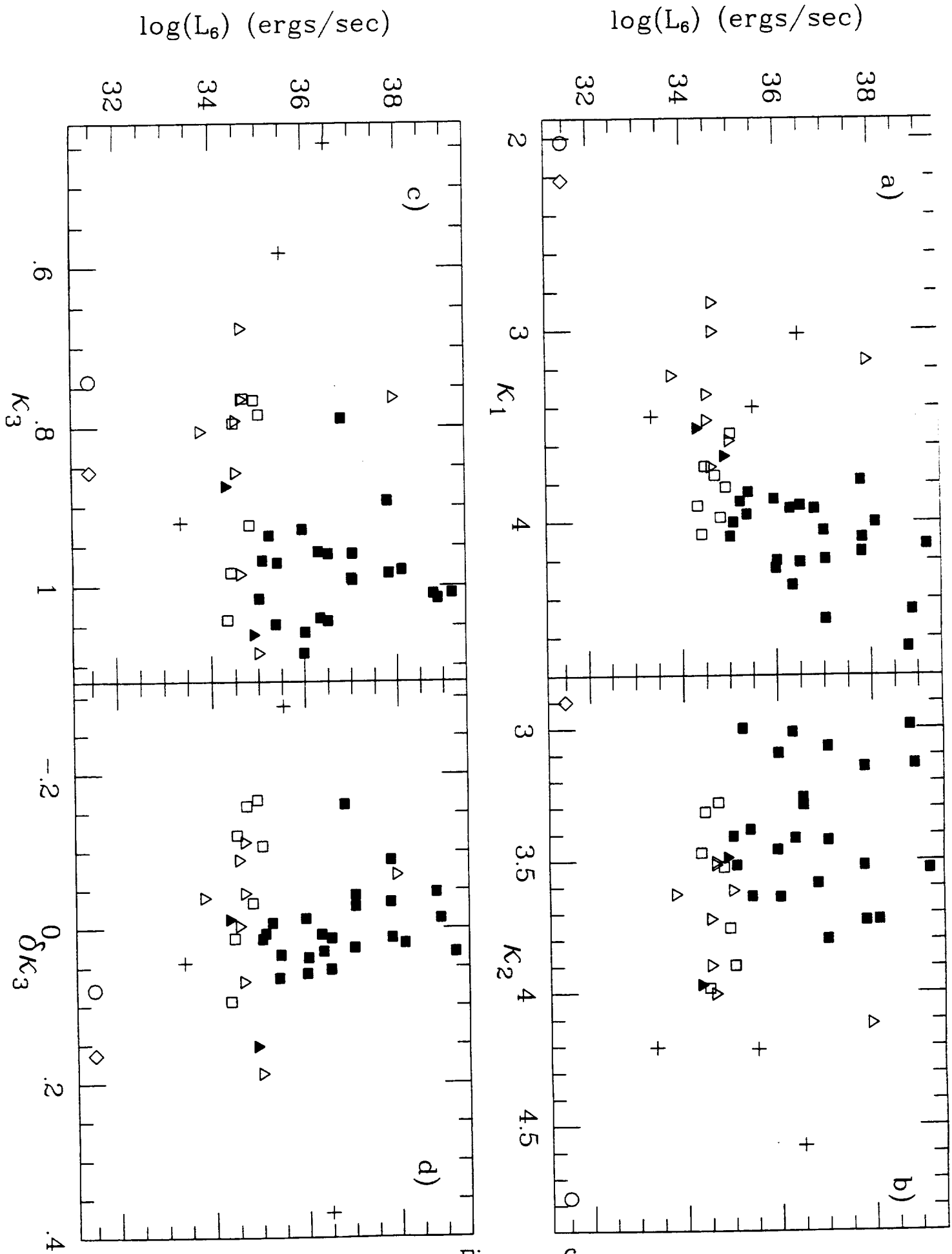

Figure 6

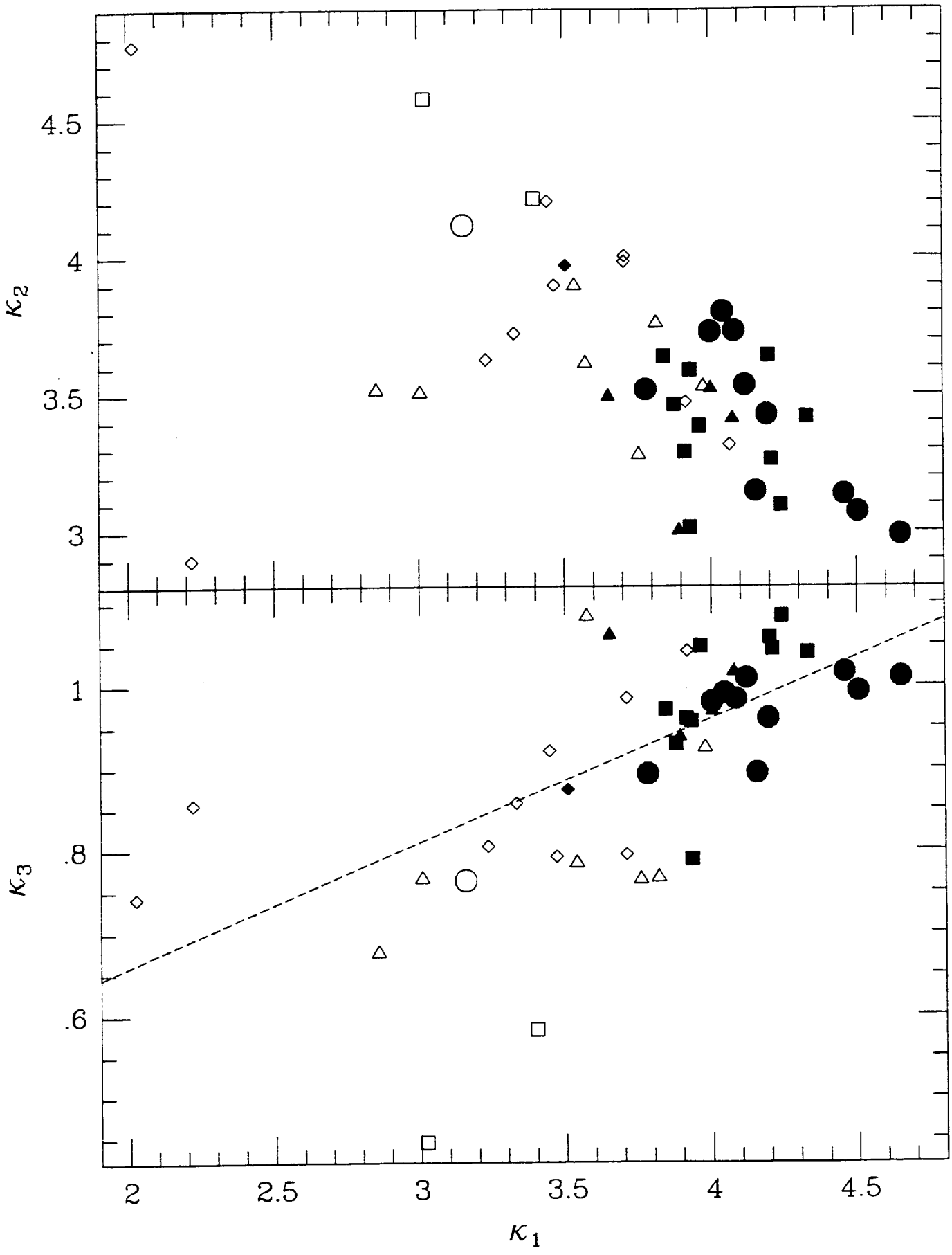

Figure 7a

Figure 7b

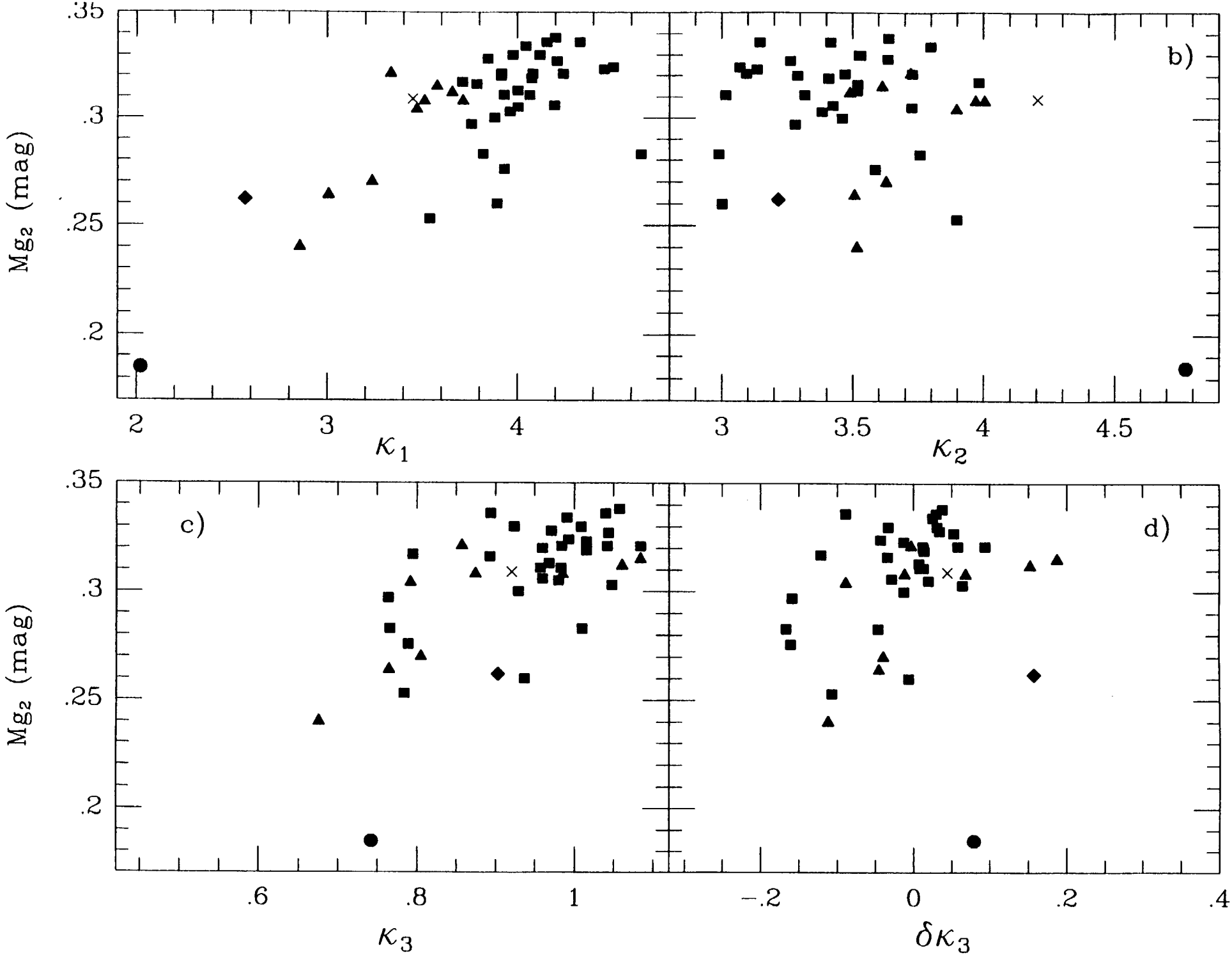
b)
c)
d)
Mg_2 (mag)
.35
.3
.25
.2
2
3
4
κ_1
3
3.5
4
4.5
κ_2
.6
.8
1
κ_3
−.2
0
.2
.4
$\delta\kappa_3$

Figure 8

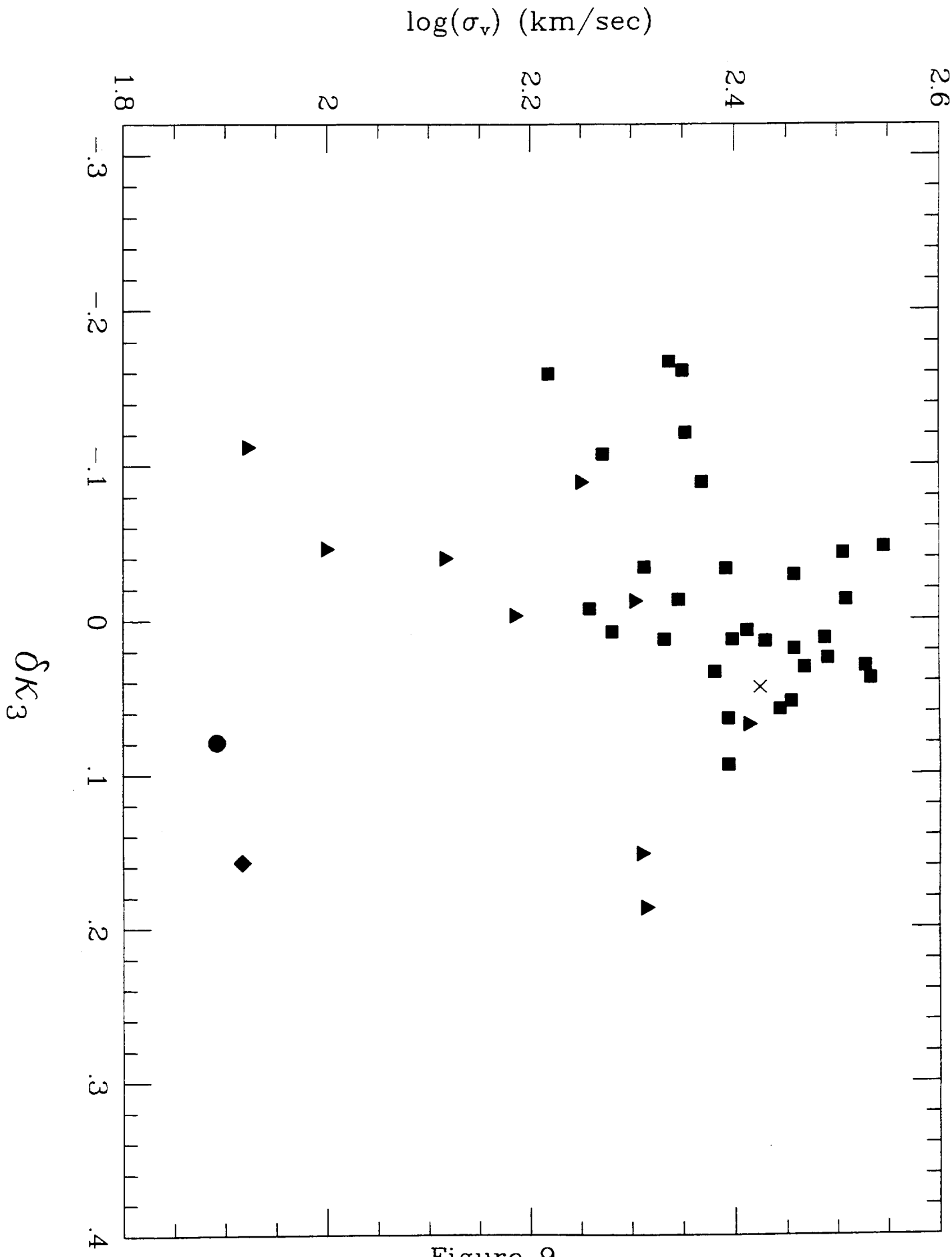

Figure 9

Harvard-Smithsonian Center for Astrophysics

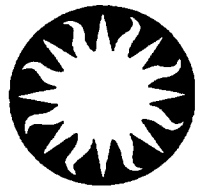

Preprint Series

No. 3947
(Received September 19, 1994)

ROSAT PSPC OBSERVATIONS OF THE EARLY TYPE GALAXIES NGC 507 AND NGC 499: CENTRAL COOLING AND MASS DETERMINATION

Dong-Woo Kim
Harvard-Smithsonian Center for Astrophysics
and
Chungnam National University, South Korea

and

G. Fabbiano
Harvard-Smithsonian Center for Astrophysics

To appear in
The Astrophysical Journal
March 1, 1995

HARVARD COLLEGE OBSERVATORY SMITHSONIAN ASTROPHYSICAL OBSERVATORY
60 Garden Street, Cambridge, Massachusetts 02138

Center for Astrophysics
Preprint Series No. 3947

ROSAT PSPC Observations of the Early Type Galaxies NGC 507 and NGC 499: Central Cooling and Mass Determination

Dong-Woo Kim
Harvard-Smithsonian Center for Astrophysics
and
Chungnam National University, S. Korea

G. Fabbiano
Harvard-Smithsonian Center for Astrophysics

To appear in
The Astrophysical Journal
March 1, 1995

ABSTRACT

We present the results of a deep observation of NGC 507 and NGC 499 with the ROSAT PSPC. The X-ray emission of NGC 507 is extended at least out to 1000 arcsec (458 kpc at a distance of 94.5 Mpc). The radial profile of X-ray surface brightness goes as $\Sigma_X \sim r^{-1.8}$ outside the core region. The radial profile is a function of energy such that the softer X-rays have a smaller core radius and a flatter slope. Spectral analysis reveals that the emission temperature, with an average of 1 keV, peaks at an intermediate radius of 2-3 arcmin and falls toward the center (possibly decreases outward as well). The absorption column density is consistent with the Galactic line-of-sight value. The X-ray emission of NGC 499 is extended to 300 arcsec and suggests a similarly cooler core. The cooler cores of NGC 507 and NGC 499 are strong evidence of the presence of cooling flows in these galaxies. Assuming hydrostatic equilibrium outside the cooling radius, the estimated mass to light ratio of NGC 507 is 97 $\pm$ 16 within 458 kpc, indicative of the presence of a heavy halo. Similarly the mass to light ratio of NGC 499 is 89 $\pm$ 14 within 137 kpc. Near the edge of the X-ray emitting region of NGC 507 we detect 19 soft, unresolved sources. These sources do not have optical counterparts and are significantly in excess of the expected number of background serendipitous sources. We speculate that they may represent cooling clumps in the halo of NGC 507. If there are many undetected cooling clumps distributed at large radii, then the radial profile of the X-ray surface brightness does not directly reflect the potential, adding uncertainty to the measurement of the binding mass; the gas mass could also be overestimated.

1. INTRODUCTION

Soon after the *Einstein* Observatory's discovery of X-ray emitting hot gas in early type galaxies, a debate ensued on the physical status of these halos and on using them as a tool for measuring the mass of the galaxies (for a review, see Fabbiano 1989). Initially, cooling flows were invoked to explain X-ray observations of early type galaxies (for example, Fabian, Nulsen and Canizares 1984; Sarazin and White 1987). These models reproduce observed global properties such as X-ray luminosity and emission averaged temperature. However, until recently there has not been any direct evidence of the presence of cooling, with the exception of a few clusters of galaxies like Virgo and Perseus (e.g., Canizares, Market and Donahue 1988), where X-ray spectroscopic observations revealed emission lines originating from the cooling gas. If cooling flows really take place in X-ray–bright early type galaxies, the gas temperature should decrease within the cooling radius as the gas is falling toward the center. An important consequence of the presence of gaseous halos is the ability to measure the galaxy mass if these halos are in hydrostatic equilibrium. In many X-ray emitting galaxies, these mass estimates suggested the existence of a large amount of dark matter. However, the uncertainties on the radial behaviour of emission temperature and surface brightness, intrinsic to *Einstein* data, resulted in large uncertainties (Trinchieri, Fabbiano and Canizares 1986). In particular, if the radial behaviour of the temperature is not known, the presence of high external pressure could lead to the erroneous conclusion of the presence of large heavy halos (Vedder, Trester and Canizares 1988; Bertin, Pignatelli and Saglia 1993). External pressures are typically not considered in the derivation of these masses.

Accurate measurements of emission temperature and surface brightness distribution are necessary to confirm the existence of cooling flows in these galaxies and study their properties, and to measure their binding mass. To obtain these measurements, we have acquired deep ROSAT PSPC observations of NGC 507 and report the spatial/spectral behaviour of its X-ray properties in this paper.

NGC 507 is the brightest member of a group of galaxies belonging to a poor cluster, the Pisces cluster, which contains several subgroups (e.g., the NGC 383 group and the NGC 507 group). This cluster in turn belongs to the long, narrow main ridge of the Pisces-Perseus supercluster (see Wegner, Haynes and Giovanelli 1993 for a large scale distribution of galaxies in this region). Within its optical radius, NGC 507 (also Arp 229 and VV 207) has a close companion elliptical galaxy with a similar redshift, NGC 508 which is 90 arcsec north of NGC 507, and there may be interaction between the two galaxies (Arp 1966). NGC 507 has a weak radio core (Parma et al. 1986) and it may have a dust lane in the center (Ebneter, Djorgovsky and Davis 1988).

NGC 507 is one of the most luminous, extended X-ray sources among early type galaxies (Fabbiano, Kim and Trinchieri 1992) and its X-ray luminosity ($\sim 10^{43}$ erg sec^{-1}) is comparable to those of poor clusters (Kriss, Cioffi and Canizares 1983). The ROSAT PSPC observation was motivated by the suggestion, based on the *Einstein* IPC data, that NGC 507 may have relatively a cool, absorbed core of X-ray emission (Kim and Fabbiano 1992; see Fabbiano 1993). We indeed find the signature of cooling in this galaxy core

with the ROSAT PSPC, but do not confirm the excess absorption. The *Einstein* IPC image (Fabbiano, Kim and Trinchieri 1992) shows that while NGC 507 is the dominant X-ray source, another relatively strong source is associated with the elliptical galaxy NGC 499. We describe observational results for spatial and spectral analyses of both galaxies in section 2, and we compare these results with the *Einstein* data in section 3. We estimate the deprojected density and gravitational mass and discuss the implications of the observational results in section 4. Finally, we summarize our results in section 5.

2. OBSERVATIONS AND DATA ANALYSIS

The NGC 507 and NGC 499 field was observed by the ROSAT PSPC at two separate times, Aug. 9-10, 1992 and Jan. 8-9, 1993. The net exposure time is about 20500 seconds (5600 and 14900 seconds each). The observational parameters and basic physical parameters of the galaxies are listed in Table 1. The *raw* PSPC image of NGC 507/499 (the second, longer observation) is shown in Figure 1. Although no correction was applied, it is clear that extended diffuse emission is present inside the 20 arcmin circle of the detector supporting structure. In addition, several point-like sources are visible within the field of view.

Because of pointing uncertainty, the X-ray centroids of the two observations are not at the same sky coordinates once the data are aspect-corrected. For this reason, we have analyzed the two observations separately to determine radial profiles and spectral distribution for each. We then combined the counts in each radial bin relative to the centroid of the emission from the two observations to generate a radial profile. Similarly, the spectral counts from each channel were added to generate the total spectral distribution. We used the IRAF/XRAY package (developed at SAO) for the data analysis. We also used the program XSPEC (provided by the NASA-HEASARC) for the spectral analysis.

2.1 Background Subtraction

The standard ROSAT PSPC analysis software (SASS) provides background estimates for each observation. However, this background map does not represent the real field background when a very extended source is present as in this observation (see also Trinchieri et al. 1994). In Figure 2a, we compare the radial distribution of the background map with that of the exposure map, also generated by SASS. The latter contains the effect of telescope vignetting and shadowing by the window supporting structures. The exposure map can be considered as a flat-field for a given observation. It is clear that in the center of the field the background map contains excess emission over that expected from a uniformly extended background. This is also demonstrated by Figure 2b, where we show the observed data (source+background profile) divided by the exposure map (solid line), compared with a similarly treated background map (dashed line). Both unsubtracted data profile and background map profile flatten out at radius $r > 30'$ from the field center. However, the SASS background profile is not flat throughout the field, but increases between $\sim 5'$ and $30'$. This demonstrates the inclusion of residual source emission in the background map. We adopt the dashed line (i.e., the flat surface brightness) as our background level.

This corresponds to a background level determined locally at r=30-40 arcmin from the field center where the count rate per unit area becomes flat. The background subtracted data are shown as points with error bars in Figure 2b.

A detailed discussion of the different PSPC background components can be found in Snowden et al. (1994). In summary, this background consists of a particle component (which is not vignetted) and X-ray component (auroral, scattered solar X-ray, cosmic X-ray etc.), which is vignetted. In our background subtraction analysis, we have implicitly assumed that the field background is vignetted (see above). This is not a bad assumption in our case, since we estimate that the particle contribution is $\sim$1% of the total background (estimated from the master veto rate, see Plucinsky et al. 1993). Moreover, we have checked the time variation of our data to exclude short-term enhancements and scattered solar X-rays in the background. These, however, would be vignetted, so our analysis would subtract them correctly. Another background term, mentioned by Snowden et al. (1994) is afterpulse background. The afterpulse is present in PI channels near 11 after cosmic ray hits. We do not use these low energy channels in our analysis (see below).

To estimate the uncertainties of our background determination, and how it would affect the derived surface brightness profile of NGC 507, we used background maps generated from other observations which do not contain extended sources. As done in Trinchieri et al. (1994), we used 4 representative PSPC pointing observations: rp600009, rp600008, rp600017, and rp600520. In all of these observations, the second PSPC (PSPC-B) was used and the gain was at a low state. The radial profiles of the four background maps (pi=7-240) produced by the standard SASS processing are very similar to each other and also similar to that of the NGC 507 exposure map (see Figure 3). Only one observation (rp600520) results in systematically lower counts in the central region (about 10%). Using different observed background templates, we find that the net source radial surface distribution does not change appreciably. When these differences are translated in errors in the parameterization of the surface brightness profile (see §2.4) we obtain estimates of a core radius and slope all within 1% of each other, except the case of rp600250 which produces a $\sim$3% flatter slope. All these values are well within the error bars of our estimates.

2.2 Surface Brightness Distribution – Contour Map

The X-ray contour map of the NGC 507 region is shown in Figure 4. The broad band image (0.1-2.4keV), after exposure-correction and background-subtraction, is binned in 15″ bins, and smoothed with a Gaussian of σ=30″. The contours are plotted in units of counts arcmin^{-2} ksec^{-1}. The lowest plotted contour is roughly at the 2σ level, corresponding to 0.4 counts arcmin^{-2} ksec^{-1}; other contours follow at 0.5 mag interval (i.e., a factor of 1.585). The figure shows two strong X-ray sources, the strongest is at the center of the field, corresponding to the optical position of NGC 507; the second strong source coincides with NGC 499 at 13.6 arcmin to north-west of NGC 507. Both sources were also detected with the *Einstein* IPC (Fabbiano, Kim, Trinchieri 1992). Four more prominent point sources are present in the ROSAT PSPC field: one at 7 arcmin to SW of NGC 507, one at 18 arcmin to SW of the NGC 507, and the other two outside the central 20 arcmin circle (see Figure 1). Also noticeable are many less intense peaks of emission near the edge of

the X-ray emitting halo of NGC 507. While the X-ray image of NGC 507 is in general spherically symmetric, the X-ray isophotes at 2-3 arcmin are less steep toward the 1st quadrant (PA=270-360°) than that in the other directions.

2.3 Source Detection and Count Rates

X-ray count rates for NGC 507 and NGC 499 were extracted from circular regions centered at their X-ray centroids from the background-subtracted, exposure-corrected image (as above). The X-ray centroids are (7668.2,7622.9) and (8349.2, 9104.9) in pixels and the radii are 1000″ and 300″, respectively (the radius was determined from the radial profiles in §2.4). All point-like sources detected in the observed field (described below) are excluded if they are within these radii. We obtain 17627 ± 196 counts and 5813 ± 82 counts for NGC 507 and NGC 499, respectively.

The SASS detection method found more than 100 sources. But it often found multiple detections for many sources particularly near the center of NGC 507 and NGC 499 probably because of the presence of the diffuse extended emission. A different method was followed to determine the existence of individual sources. To detect sources, we first generated an error map, which gives the statistical errors corresponding to the smoothed map. By dividing the smoothed map by the error map pixel by pixel, we then generated a signal-to-noise ratio (S/N) map. We selected sources at above 5 sigma in several 15x15″ pixels by eye-examining this S/N map. In this way we find 21 sources. The X-ray positions of these 21 sources are listed in RA order in Table 2. These sources are marked in Figure 4 with their source numbers taken from Table 2. All the sources we detect were also found by the SASS method except for source 1, which is partly hidden by the detector support structure.

Recently, Prestwich et al. (1994) and White et al. (1994) pointed out that the filamentary features in A2029 found with the ROSAT HRI by Sarazin, O'Connell and McNamara (1992) may be not real and caused by applying an inadequate analysis technique. These filaments in A2029 are small-scale features ($\lesssim$10 arcsec) in the central 30″ region with strong diffuse emission and White et al. (1994) suggested that these may have been resulted by a circularly symmetric modeling of the elliptically shaped diffuse emission. However, the White et al. (1994) approach, while explaining away the filaments in A2029, is not necessarily a unique representation of the astrophysical object. In our case, we detect a number of prominent point-like sources, far away from the central (almost circular) halo. It is very hard to imagine how these could be produced by projection effects. Furthermore, the average PSPC spectrum of these sources differs from that of the surrounding emission (§2.5.2), proving that our detected sources are not produced by an artifact of data analysis.

The count rate for each source is extracted from the circle centered on the source. The diffuse emission relevant to that position is then subtracted from the source counts. The count rate of the diffuse emission and its error were estimated using the radial profile at a given radius (see §2.4). For sources 19 and 21 (at 28′ and 42′ away from the center), background counts extracted from the annuli surrounding the sources were subtracted from the source counts. The results are summarized in Table 2. Within the PSPC position uncertainty, these sources do not match with any known SIMBAD object except for sources

2 and 21. A star, HD8216, and a galaxy, Z0119.4+3300, are within 1.4 and 1.3 arcmin from source 2. A galaxy, EQ0123+328, is within 3.4 arcmin from the center of source 21 (its source size $\simeq$ 5 arcmin). We will discuss the possible nature of these sources in §4.

2.4 Surface Brightness Distribution – Radial Profiles

2.4.1 NGC 507

Assuming circular symmetry, we derived a radial profile of the X-ray surface brightness measured in concentric rings centered on the X-ray centroid. Regions of NGC 499 (radius= 300″) and all the detected sources (radii and centers from Table 2) were excluded. Due to the serious position uncertainty at the lowest PI channels, known as the electronic ghost effect (Plucinsky et al. 1993), we used only PI channels above 20, which corresponds to 0.2 keV. However the radial profile is almost the same as that with all channels in our case. Due to the recent report of the ghost effect which may affect up to PI channel 25 (Fabbiano, Kim and Trinchieri 1994), we also derived a profile with PI channels above 27 but the results are exactly the same. We also tried non-uniform radial bins to make a signal to noise ratio at each radial bin similar, but the results again do not differ greatly. The radial profile is shown in Figure 5a. The emission is extended at least out to 1000 arcsec. We fitted the observed radial profiles (r $<$ 1000″) to the analytic King approximation model, $\Sigma_X \sim (1+(\frac{r}{a})^2)^{-3\beta+0.5}$, after convolving this model with the PSPC point response function appropriate for a 1 keV source. The best fit parameters and 90% confidence regions (in parenthesis) are: core radius, a = 39.7″(37.6″ $\sim$ 42.5″) and slope, β = 0.449 (0.445 $\sim$ 0.457). Given the $\sim$25″ spatial resolution of the PSPC, the estimate of the core radius is very uncertain. However, the power law slope outside the core radius can be relatively well determined from the emission outside the core region. Where $r >> a$, the X-ray emission falls as $\Sigma_X \sim r^{-1.69(1.67\sim1.74)}$.

This best fit is not acceptable, yielding χ^2=116 for 29 degrees of freedom. The fit residuals (Figure 5a) show departures of the observed data from the model at r=90-150″ (too high), at r=150-350″ (too low) and at r=450-650″ (too high again). The most significant is the bump at r=450-650″. To search for substructures in this radius range, we derived a ratio map by dividing the image by a model image generated with the best fit radial profile (Figure 6). Indeed many small clumps are seen in this region, implying that the bump at r=450-650″ is likely to be due to the faint sources below the detection threshold. To confirm that the the excess emission in this bump is not localized to a particular part of the image, we divided the region into 4 angular sectors (4 quadrants) and regenerated radial profiles for each angular bin. The bump exists in all 4 bins. It appears strongest in the 1st quadrant (PA=270-360°) and weakest in the 4th quadrant (PA=180-270°). In the first quadrant, there may exist enhanced diffuse emission between NGC 507 and NGC 499 (see Figure 4 and 6). However, the best fit parameters of a radial profile obtained by excluding the first quadrant remain within the estimated error.

We fitted the profile of the region r=0-450″ and r=650-1000″ to exclude the bump. The best fit slope is β = 0.461 (0.454 $\sim$ 0.469), which corresponds to $\Sigma_X \sim r^{-1.77(1.72\sim1.81)}$. Such a flat radial profile is also found in the ROSAT observations of NGC 4636 (Trinchieri

et al. 1994) and NGC 1399 (Kim et al. in preparation). $\Sigma_X \sim r^{-2}$ is excluded at the 99% level. $\Sigma_X \sim r^{-2}$ was suggested to be the typical surface brightness profile of X-ray bright ellipticals from the analysis of the Einstein data, although the *Einstein* range encompasses $\Sigma_X \sim r^{-(1.4-2.6)}$ (e.g., Trinchieri, Fabbiano and Canizares 1986; Fabbiano 1989). The minimum χ^2 is significantly reduced to 44 for 22 degrees of freedom and even the observed data at the outer region (r=650-1000″) are well reproduced by the model. The major differences are at the 90-120″ and 120-150″ bins which contribute χ^2=18 (see Figure 5b).

To explore energy dependencies of the surface brightness distribution, we derived radial profiles for two different energy bands: 0.2-1.0 keV and 1.0-2.4 keV. This choice of energy bins divides the counts roughly in half. Proceeding as above, we find that the acceptable parameter ranges for the soft and hard energy bins are clearly disjoint at the 99% level (Figure 7). The soft energy radial profile (the best fit is $\beta = 0.442$ for the whole region and 0.454 for the region excluding r=450-650″) is flatter than the hard energy profile ($\beta = 0.461$ for the whole region and 0.472 for the region excluding r=450-650″). The 90% confidence intervals on the best fit core radius are 34-37″ for the soft energy and 48-51″ for the hard energy, indicating that the soft X-rays are more centrally concentrated than the hard X-rays.

This finding is not affected by the energy dependent point response function (PRF) and energy dependent exposure map (vignetting effect). We checked the PRF effect by reestimating the best fit parameters using a 0.5 keV PRF for the soft band and a 1.5 keV PRF for the hard band instead of a 1 keV PRF. We also checked the vignetting effect by generating exposure maps at 7 different energy bands (Snowden et al. 1994) and applying each exposure map separately to a given energy band. Both effects cause the observed difference between the soft and hard energy band to be even stronger but do not change the results more than the error of our estimates. As remarked in §2.1, uncertainties in the background subtraction will not affect our results appreciably. In summary, the radial profile of the surface brightness is a function of energy in such a way that the softer X-ray photons are concentrated in the center more strongly and fall less steeply in the outskirts. This is also consistent with the spectral fitting results (§2.5).

2.4.2 NGC 499

In a similar fashion, we made a radial profile of the X-ray surface brightness of NGC 499, using concentric rings centered on its X-ray centroid and excluding sources 7 and 12. We again used PI channels between 20 and 240. The X-ray emission in NGC 499 is extended to ~300″. As done for NGC 507, we fitted the King approximation model to the observed data. The best fit model (Figure 8) yields χ^2=8.3 for 7 degrees of freedom with β=0.60 (0.58-0.63) and core radius=42.9″ (39-46). The radial distribution of the X-ray emission is much steeper than that of NGC 507 ($\Sigma_X \sim r^{-2.6}$ at r >> a in NGC 499). A similar steep X-ray surface brightness distribution was found in NGC 4649 with the Einstein IPC (Trinchieri, Fabbiano and Canizares 1986).

2.5 Spectral Analysis

To extract the net source counts for the spectral analysis, we also need to subtract

the field background. However, we cannot use the method of §2.1, because the vignetting is a function of energy. Therefore, we have first determined background counts for each spectral channel from source-free regions not hidden by the detector supporting structure, at 30-40 arcmin from the field center. Then we have applied energy dependent vignetting corrections to these counts, before subtracting them. Particle background was subtracted separately but its contribution is very small. We tried different background regions, and we found that the uncertainty in the background could only affect our results in determining the absorbing column density for the outer region of the NGC 507 emission (see also Trinchieri et al. 1994).

We used the IRAF/XRAY spectral software package, which bins the 256 pulse height channels into 34 channels. To fit the observed spectra to models, we used the Raymond thermal gas emission model (1992) and the Morrison and McCammon absorption model (1980). We also used XSPEC for an independent check of the results and to be able to add together low energy channels with low statistics. The two software packages produce slightly different results but they are consistent within the error ranges when their abundance tables are adjusted to have the same value.

2.5.1 NGC 507

The spectral distribution of the background-subtracted counts extracted from a circle with r=1000″ containing NGC 507 (after excluding NGC 499 and the detected sources listed in Table 2) shows a strong peak at $\sim$ 1 keV (Figure 9), indicating that the emission is mainly from thermal emission lines. This spectrum, however, cannot be fitted with a single temperature Raymond model with low energy absorption and 100% cosmic abundance (χ^2=63 for 21 degrees of freedom). A similar result was found by Trinchieri et al. (1994) for NGC 4636.

As was done in NGC 4636, we divided the emitting region into several concentric rings to determine if there are radial changes in the spectral parameters. NGC 499 and other sources in Table 2 were excluded as above. The results of the fit to a single temperature Raymond model with 100 % cosmic abundance (Allen 1973) are listed in Table 3 and the best fit parameters and their ranges at the 90% level (for two interesting parameters, Avni 1976) as a function of radius are shown in Figure 10. The spectral fits of the subregions are statistically acceptable with reduced χ^2 close to 1. The two innermost radial bins have the highest reduced χ^2 of $\sim$1.4. On the average, the emission temperature is close to $\sim$ 1 keV (0.9 – 1.4 keV) as seen in other X-ray bright elliptical galaxies (Kim, Fabbiano and Trinchieri 1992; Trinchieri et al. 1994) and the absorption column density is close to the Galactic line-of-sight value (see Table 1).

The emission temperature increases from the center to the 2-3 arcmin bin (from 1 keV to 1.3 keV). The temperature difference between the 1st and 3rd radial bin is significant at 3.5 σ. After 3 arcmin, the temperature appears to decrease, but the decrease is marginally significant (about 2 σ). These results are consistent with the energy dependence of the surface brightness radial profile discussed in §2.4, which shows a smaller core radius and a flatter radial slope for the lower energy range.

The absorbing column density remains constant out to 5 arcmin and similar to the Galactic line-of-sight value, $5.3 \times 10^{20} cm^{-2}$, or $\log N_H = 20.72$ (Stark et al. 1992). The column density appears to decrease after 5 arcmin but is consistent with the Galactic value within the 90% error.

We tried fitting the data with a two component Raymond spectrum and with a single component spectrum, leaving the abundance free to vary. The fitting parameters are given in Table 4. In both instances we do not find appreciably better values of χ^2 and the radial dependence of kT seen in Figure 10 remain the same. The metal abundance is not well constrained with these data. It may be lower than solar (down to $\sim$ 30%) but the acceptable range does not exclude solar abundance. The data only constrain the abundance not to be much higher than the solar value.

2.5.2 *Point-like* Sources

Near the edge of the X-ray emitting region of NGC 507 we have detected 19 sources. Sources 19 and 21 are far from NGC 507 (r $\gtrsim$ 30′) and may be not related with it. We tried to see if these sources have different spectral properties from those of the diffuse emission surrounding them. Since these sources are weak, we co-added their spectra by summing the counts in each spectral channel to increase the statistical significance (we exclude source 1, 2, 3, and 6 because they are partly hidden by the detector structure). The combined spectrum still contains emission from the extended gas in NGC 507 as well as the emission from the sources. This composite spectrum is compared with that of the diffuse emission from the r=420-700″ radial bin in Figure 11 a and b. The best fit model prediction for the radial bin r=420-700″ (from Table 3) is plotted as a solid line in both figures. It is clear that this model (with normalization as a free parameter) can not fit the combined spectrum of the point sources, yielding $\chi^2 = 66$ for 24 degrees of freedom (Figure 11b). This point source spectrum definitely contains excess emission at the low energies, indicating that the sources have softer spectral property than the surrounding diffuse gas.

Assuming that the spectrum at r=420-700″ is representative of the diffuse emission, we subtract this spectrum from that of Figure 11b, after normalizing it to match its extraction area to the total point source extraction area. This assumption is reasonable because the spectra of the last three radial bins do not differ significantly from each other (see Table 3). We also used a spectrum taken from source-free regions close to each source (having the same area as the source region) and we reached similar results. The net spectrum after subtracting the diffuse emission is shown in Figure 11c. This spectrum is soft and is similar to that of ellipticals with the lowest L_X/L_B (Kim, Fabbiano and Trinchieri 1992; Fabbiano, Kim, Trinchieri 1994). As found by Fabbiano, Kim and Trinchieri (1994), this spectrum can be fitted either with a thermal gas model with a low abundance or a two-temperature gas model with 100% solar abundance. In Figure 11c, the best fit low abundance model is plotted as a solid line. The best fit parameters are kT = 0.52 (0.28 - 0.86) and abundance = 0 (0-0.02) solar, yielding $\chi^2 = 6.7$ for 9 degrees of freedom. The parameters of the two-component model are not well constrained. A model with kT_1 = 0.1-0.5 keV and $kT_2 > 1$ and with similar fluxes from the two components fits well the

spectrum.

2.5.3 NGC 499

The results of spectral fitting to the NGC 499 data are summarized in Table 5. The emission from the whole NGC 499 (r < 300 arcsec) is not compatible with a single temperature fit with 100% solar abundance, resulting in a best fit χ^2=47.6 with 23 degrees of freedom. To explore radial changes in the spectral properties as seen in NGC 507, we extract spectral data from regions with r < 2′ and r=2-5′. When these data are analyzed we find that the temperature decreases toward the center, as seen in NGC 507. The best fit column density is consistent with the Galactic line-of-sight value. If the abundance is allowed to vary, the minimum χ^2 value are somewhat reduced in the central bin, where the abundance is constrained to be 18 - 60% solar. A similar lower value of χ^2 in the central bin is achieved by allowing the presence of two different temperature components with solar abundance.

2.6 Fluxes and Luminosities

The X-ray fluxes of NGC 507 and NGC 499 were calculated for each radial bin used for the spectral analysis with the appropriate best fit kT and N_H (Table 3 and 5). In the energy range of 0.1-2.4 keV, $F_X = 1.3 \times 10^{-11}$ erg sec^{-1} cm^{-2} within r < 1000 arcsec for NGC 507; $F_X = 4.0 \times 10^{-12}$ erg sec^{-1} cm^{-2} within r < 300 arcsec for NGC 499. The total X-ray luminosity of NGC 507 (adopted distance is 94.5 Mpc) is 1.45×10^{43} erg sec^{-1}, which makes this galaxy one of the X-ray brightest early type galaxies and comparable to poor clusters. The X-ray luminosity of NGC 499 is 5.3 x 10^{42} erg sec^{-1}, lower but in the range of gas dominated ellipticals (Fabbiano, Gioia and Trinchieri 1989; Kim, Fabbiano and Trinchieri 1992).

The flux of the point sources is given in Table 2. It was calculated by assuming a Raymond thermal gas model with T=0.5 keV and the Galactic line-of-sight absorption N_H=5.3 x 10^{20} cm^{-2} (Starks et al. 1992). These sources, if they are at the same distance as NGC 507, would have X-ray luminosities of $10^{40} - 10^{41}$ erg sec^{-1}.

3. COMPARISON WITH EINSTEIN RESULTS

The NGC 507/499 field was previously observed with the *Einstein* IPC for ~9000 seconds. The IPC data of NGC 507 and NGC 499 (Fabbiano, Kim and Trinchieri 1992; Kim, Fabbiano and Trinchieri 1992) are consistent with the PSPC estimates in terms of the X-ray flux and overall spectral distribution. However, the spectral results of the two observations differ. The most puzzling discrepancy between the two observations is in the measurement of the low energy absorption. The IPC spectrum (Kim and Fabbiano 1992; see Fabbiano 1993) requires excess absorption over that expected from the Galactic line-of-sight N_H, while the PSPC spectrum (this paper) is consistent with the Galactic value. The two spectra are compared in Figure 12, where the best fit model predictions for the PSPC data (two-temperature thermal model with kT_1=0.7 KeV, kT_2=1.3 keV and *Log* N_H=20.7) are plotted on the data to illustrate the difference. We consider two possibilities: (1) an

extra absorbed, hard emission component or (2) an unknown systematic error. There may be a very absorbed, hard emission component (perhaps associated with the active nucleus) which is seen in the IPC observation, but not in the PSPC observation due to the different energy response of the two instruments. This would effectively mimic the excess absorption required by the IPC data. We used various models such as multiple components, edges, and partial covering to imitate such an effect. These complex models considerably reduce χ^2 in the joint fitting but the fit is still not acceptable ($\chi^2 = 48$ for 27 degrees of freedom). Another possibility is that the IPC data are affected by unknown systematics. Fiore et al. (1994) compared ROSAT and *Einstein* spectra of a quasar sample and found a systematic discrepancy similar to that in Figure 12. ASCA and AXAF observations with response up to ~10 keV may resolve the inconsistency. For the moment, we can only conclude that no excess absorption is required to explain the ROSAT PSPC data.

4. DISCUSSION

The intensity and extent of the X-ray emission of NGC 507 and NGC 499 and their spectral properties strongly argue for a centrally cooling hot extended halo. Both emission components from stellar sources in NGC 507 and NGC 499 (see e.g., Kim, Fabbiano and Trinchieri 1992) and X-ray emission from the active nucleus of NGC 507 (Fanti et al. 1987; we assume a typical X-ray–radio ratio, see Fabbiano, Gioia and Trinchieri 1989) would not be detected with our data.

Although we are fairly confident of the radial behaviour of the temperature of the X-ray emitting gas in both cases, our measurements cannot set very strong constraints on the metal abundance of this medium, although solar values are allowed. There is a basic uncertainty in the interpretation of PSPC spectra (see Fabbiano, Kim and Trinchieri 1994 and Trinchieri et al. 1994), which do not permit a unique choice of emission model. Only in the inner regions of both NGC 507 and NGC 499, a thermal gas model with low abundance can reproduce the observed spectra slightly better (slightly reduced minimum χ^2) than the model with solar abundance. However a similar good fit can be obtained with two-temperature thermal models with solar abundance. To accurately measure abundance (without ambiguity of model dependency), a high spectral resolution observation of individual lines which will be provided by ASCA and AXAF is crucial.

In the following sections, we will discuss the implications of our results for the physical status of the hot ISM and for the measurement of the binding masses of NGC 507 and NGC 499. We will also discuss possibilities for the nature of the population of unresolved sources found surrounding NGC 507.

4.1 Gas Parameters

To estimate the 3-dimensional density distribution of the X-ray emitting gas, we have used the deprojection scheme described in Kriss, Cioffi and Canizares (1983). To do this, we implicitly assume that the hot gas is homogeneous i.e., the physical status of gas in a given radius can be represented by one temperature and density. The deprojected density profile of NGC 507 is shown in Figure 13a. To derive this profile the best fit temperatures

determined by the spectral analysis for each annulus (in Table 3) were used. To exclude the bump at r=450-650″, the surface brightness at this radius was interpolated using the best fit parameters (§2.4.1). The solid line is the best fit model, $n_e \sim (1+(\frac{r}{a})^2)^{-1.5\beta}$ with $\beta = 0.463$. This slope is consistent with the radial surface brightness distribution, since the gas temperature does not vary significantly. The shoulder at 90-150″ seen in the surface brightness profile (Figure 5) is even more pronounced in the density profile. This is partly because the temperature at this radius is highest so that the cooling function is lowest.

Using these density and temperature distributions, we estimate the cooling time as a function of radius (Figure 13b). The cooling time is given as $\tau_c = 1.5\frac{nkT}{n_e n_H \Lambda}$, where n, n_e and n_H are the total particle density, electron density, and Hydrogen density, respectively and Λ is the cooling function. The constant is in the range of 1 to 2.5, depending on its definition (see Sarazin 1988). The cooling time in the center is $\sim 10^9$ years, smaller than the Hubble time. The cooling radius (i.e., the radius at which the cooling time is equal to the Hubble time, $t_H = 10^{10}$ years) is ~200 arcsec (~ 92 kpc).

Since the X-ray emitting gas temperature of NGC 499 does not change greatly as a function of radius, we assume isothermality in this case to estimate the electron density and cooling time. We find that the electron density at the center is $\sim 4 \times 10^{-3}$ cm^{-3} and then falls radially as $\sim r^{-1.8}$. The central cooling time is $\sim 10^9$ years and the cooling radius is ~3′(~82 kpc).

4.2 Dark and Visible Mass

Using the spatially resolved spectra, we have determined temperature and density as a function of radius (Figure 10 and 13a). With these measurements we can derive an accurate estimate of the gravitational mass outside the core region.

To determine the total gravitational mass, we use power law descriptions for density and temperature gradients which are reasonable approximations in our case in the region well outside the core radius. If we assume $T \sim r^{-\alpha}$ and $N_e \sim r^{-3\beta}$, at a given radius r the binding mass will be given, assuming hydrostatic equilibrium (e.g., Fabricant et al. 1983), by

$$M_T(M_\odot) = 1.8 \times 10^{12}\,(3\beta+\alpha)(\frac{T}{1keV})(\frac{r}{10^3 arcsec})(\frac{d}{10Mpc}).$$

Similarly, the mass to light ratio scales as

$$\frac{M_T}{L_B} = 1.16 \times 10^{-2}\,10^{B/2.5}\,(3\beta+\alpha)(\frac{T}{1keV})(\frac{r}{10^3 arcsec})(\frac{d}{10Mpc})^{-1}.$$

In both equations r is the radius within which the mass is determined and T is the temperature of the X-ray emitting gas at this radius. In these equations we implicitly assume that the external pressure is negligible. Although in absence of a measured radial dependence of T the presence of high external pressure could lead to the erroneous conclusion of the

presence of massive dark halos (Vedder, Trester and Canizares 1988; Bertin, Pignatelli and Saglia 1993), this is not the case in NGC 507 because a radial temperature profile has been measured. There is no evidence for an outwardly increasing temperature, which would be appropriate for the model with significant external pressure.

We estimate a mass outside of 3 arcmin, where the density and temperature gradients are almost constant and are not seriously affected by the unresolved, cooling core. We take $\beta = 0.461$ (0.454 - 0.469) from §2.4 and we determine $\alpha = 0.1$ (0.05 - 0.2) at r=180-1000″ from Figure 10. The estimated total mass within r, $M_T(< r)$ is shown in Figure 14. The error bars include the errors in temperature and its gradient as well as the error in density gradient. Since the temperature gradient is small, $M_T(< r)$ increases almost linearly as r. The total mass within the outermost radius (1000″) is 2.2×10^{13} ($1.8 - 2.6 \times 10^{13}$) $M_\odot$, which corresponds to $M_T/L_B = 97$ (81 - 113), where L_B includes the optical luminosity of NGC 508. We used H=50 km sec^{-1} Mpc^{-1} for the adopted distance. If we used H=100, the mass would be half and the mass to light ratio double.

Similarly, to estimate the gravitational mass of NGC 499, we used $T = 0.9$ keV at $r = 300''$, $\beta = 0.62$ and $\alpha = 0$ (i.e., isothermal). The total mass is then 9.5 x 10^{12} (8.2 - 11.0 x 10^{12}) $M_\odot$ within $r = 300''$ (137 kpc) and the mass to light ratio is 89 (76 - 104).

Our estimates indicate large amounts of dark matter in both NGC 507 and NGC 499. If the mass-to-light ratio of stellar matter is 8, the estimated stellar mass of NGC 507 (including NGC 508) is $M(\mathrm{star}) = 1.8 \times 10^{12}$ $M_\odot$ which is ~8% of the total mass. The estimated total gas mass of NGC 507 is $\leq 2.4 \times 10^{12}$ $M_\odot$, ≤11% of the total mass. For NGC 499, the stellar and gas mass are $\sim 8.5 \times 10^{11}$ $M_\odot$ and $\leq 2.3 \times 10^{11}$ $M_\odot$, which are about 9% and 2% of the total mass, respectively. The gas mass estimated with the X-ray data is an upper limit because we assumed a filling factor of 1. Since the X-ray emissivity depends on a square density, the gas mass for the same X-ray flux can vary largely depending on the unknown volume filling factor ($\sim f^{1/2}$). We will show in §4.3 and 4.4 that the hot gas may be clumpy within the cooling radius as well as outside the cooling radius. Therefore the above can be used to derive upper limits of the baryonic fraction of ~19% and ~11% in NGC 507 (r < 458 kpc) and in NGC 499 (r < 137 kpc), respectively.

As it has been frequently noted (for example see Forman, Jones and Tucker 1985; Trinchieri, Fabbiano and Canizares 1986), the mass estimated using X-ray data strongly depends on the radius to which X-ray emission can be detected. This radius is ~1000 arcsec in NGC 507 and two other galaxies with very extended X-ray emission observed with ROSAT (NGC 1399 and NGC 5044; Jones et al. 1994 and David et al. 1994), because this radius is just inside the PSPC detector supporting structure (see Figure 15). The circular PSPC support structure at ~20′ prevents an accurate estimate of X-ray emission outside this position. Until the background of the PSPC is better understood, the X-ray emission outside the 20′ circle is very uncertain. The masses quoted in these three studies are almost proportional to the radius quoted. If one estimates the mass within a certain linear distance (say, 100 kpc) from the center, then the masses are almost the same (a few times 10^{12} $M_\odot$) because all three galaxies have similar gas temperature and their gas is almost isothermal. The different density gradients make the masses different by ~60%. Note that

the slope of the surface brightness distribution may not directly reflect the binding mass in the case of inhomogeneous cooling flow (see §4.3 and 4.4). If this is the case in NGC 507, an additional uncertainty on the mass measurement is present.

These uncertainties and the uncertainty on the filling factor of the X-ray emitting gas (which could be clumpy, see §4.3 and 4.4) make very tentative any conclusions based on the baryon fraction of these galaxies. As remarked by Briel, Henry and Bohringer (1992) and David et al. (1994), baryon fraction $\gtrsim 6\%$ would be inconsistent with $\Omega = 1$, if $\Omega_b h_{50}^2 = 0.05 \pm 0.01$ (Walker et al. 1991). Recent measurement of the deuterium abundance reduces $\Omega_b h_{50}^2$ to 0.02, making the discrepancy more serious (Songaila et al. 1994). David et al.'s (1994) measurement of NGC 5044 and our measurement of NGC 507 suggest larger baryon fractions. However, for the above reasons these measurement are really upper limits (see also Ponman and Bertram 1993).

It is not clear how much of the dark halo of NGC 507 is bound to the galaxy and how much belongs to the galaxy group. The mass estimated by the observed X-ray data is larger than for the typical isolated early type galaxy, for example NGC 4636 where the mass to light ratio is ~ 30 (Trinchieri et al. 1994). The X-ray luminosity is at the highest end of those of the observed galaxies (Fabbiano, Kim and Trinchieri 1992) and comparable to those of poor clusters (Kriss, Cioffi and Canizares 1983). The emission temperature is typical of early type galaxies and much lower than that of rich clusters (for example, David et al. 1993) and at the lowest end of the poor clusters temperature distribution (Kriss, Cioffi and Canizares 1983). The almost isothermal temperature gradient is also similar to that of typical elliptical galaxies (e.g., NGC 4636 Trinchieri et al. 1994; NGC 4472 Forman et al. 1994) and is in contrast to a large positive gradient found in clusters, for example in the Virgo cluster around M87 (e.g., Fabricant and Gorenstein 1983). The velocity dispersion of the NGC 507 group is about 600 km sec^{-1} (Wegner, Haynes and Giovanelli 1993). The virial mass is then $2.5 \times 10^{14}\ M_\odot$ within 1 Mpc. Although the virial mass is uncertain, it is an order of magnitude larger than the mass estimated with the X-ray data. The emission-averaged temperatures of clusters of galaxies are well correlated with their velocity dispersions (Edge and Steward 1991; Lubin and Bahcall 1993), indicating that the hot gas is in hydrostatic equilibrium under the gravitational potential specified by the velocity dispersion. The group velocity dispersion of the NGC 507 group (595 km sec^{-1}, Wegner et al. 1993) is far in excess to that expected for its temperature ($\sim$1 keV) from this relationship ($\sim$330 km sec^{-1} is expected for 1 keV). This may imply that the observed hot gas may be bounded mainly by the galaxy gravitational potential, including the heavy halo. In the outer region, some of the group potential may play a role, but not all the mass in the group seems to work to hold the observed hot gas.

4.3 Implications for Cooling Flow Models

The temperature decrease toward the center found in NGC 507 (also possibly in NGC 499) is clear evidence that the gas is cooling. Indeed the cooling time in the center of NGC 507 and NGC 499 is $\sim 10^9$ years, much shorter than the Hubble time. Unless it is being reheated, the gas must flow in.

In the case of homogeneous inflow (i.e., no mass deposition), the hydrodynamic equations can be written as

$$\frac{1}{r^2}\frac{d}{dr}(r^2\rho v) = 0 \ \ (or, \ \ \dot{M} = 4\pi r^2 \rho v)$$

$$\frac{dP}{dr} = -\frac{GM}{r^2}\rho$$

$$\rho v \frac{dE}{dr} - \frac{P}{\rho} v \frac{d\rho}{dr} = -\rho^2 \Lambda.$$

Here ρ, v, P, and E are the density, flow velocity, pressure, and thermal energy ($\frac{3}{2}\frac{kT}{\mu m_H}$) of the gas. M is the total binding mass within r and Λ is the cooling function. We assume a steady-state condition which is valid within the cooling radius, where the flow time (cooling time) is shorter than the age, i.e., $t_c < t_H$. The first equation (continuity equation) mean a constant mass inflow rate, the second one is the equation of hydrostatic equilibrium and the third one is the equation of energy conservation. Since the gas is almost isothermal (which is valid down to the position of the temperature peak), then the energy equation is simply reduced to

$$\frac{P}{\rho} v \frac{d\rho}{dr} = \rho^2 \Lambda,$$

or, after substituting the gravitational pressure gradient with the potential gradient,

$$\rho v \frac{GM}{r^2} = -\rho^2 \Lambda,$$

This equation simply means that the potential energy gain of the inflowing gas is balanced with the radiative loss by the X-ray emission. If we write the gas density and velocity as $\rho \sim r^{-n}$ and $v \sim r^{n-2}$, making them satisfy the continuity equation, then from the energy equation, $\rho \sim r^{-1.5}$, which corresponds to $\Sigma_X \sim r^{-2}$. This equation is valid in the case of a homogeneous, isothermal, steady-state inflow (i.e., inside the cooling radius and outside the region where the temperature is decreasing). Outside the cooling radius, the steady-state condition is not valid because the flow time is very large. On the other hand, the assumption of homogeneity and isothermality is not valid in the cooling region where the temperature decreases inward.

Combining the three hydrodynamic equations, one can write the constant mass inflow rate, $\dot{M} = 4\pi r^2 \rho^2 \Lambda \, / \, \frac{GM}{r^2}$ (see also equation 1 of Canizares, Steward and Fabian 1983). The mass inflow rate at the cooling radius of NGC 507 is $\dot{M} \simeq 40 \ M_\odot \ \mathrm{year}^{-1}$. Similarly, we can estimate the average cooling rate within the cooling radius by dividing the energy

loss rate by the enthaphy of the gas, $\dot{M} = \frac{2\,\mu\,m_H\,L_X}{5\,kT}$, where L_X is the bolometric X-ray luminosity inside the cooling radius. The average cooling rate of NGC 507 is $\sim 35\ M_\odot$ year^{-1}. The mass inflow rate at the cooling radius of NGC 499 is $\dot{M} \simeq 30\ M_\odot$ year^{-1} and the average cooling rate is $\sim 20\ M_\odot$ year^{-1}.

If all the cooling gas is falling into the center, we would have a central peak of the surface brightness much more pronounced than observed. Some of the hot gas will cool locally and drop out of the overall inflow and hence the actual inflow rate inside the cooling radius will become smaller as gas flows toward the center. The local excess at r=90-150″ (41-69 kpc) seen in both surface brightness and density of NGC 507 could be an example of the increased local cooling within the cooling radius. High resolution spectral/spatial observations are necessary to confirm this hypothesis. The detailed process of how mass deposition occurs as a function of radius is not easily determined because a priori knowledge of the distribution of the gravitating mass (i.e., the potential) is needed (Arnaud 1988; see also David et al. 1994). With our data we can determine this well only outside the cooling radius (see Figure 14 and §4.2).

To assess how much the potential varies particularly inside the cooling radius, we compare the X-ray surface brightness profile of NGC 507 with those of two other galaxies in poor groups. This comparison suggests that the mass deposition rate and the shape of the potential may vary widely from galaxy to galaxy. These three galaxies (all observed with the ROSAT PSPC) are NGC 507, NGC 1399 (Jones et al. 1994) and NGC 5044 (David et al. 1994). They are similar in many respects, for example cluster richness (all three are poor in clusters or galaxy groups), X-ray temperature (all three have kT $\simeq$ 1 keV) and central cooling core (all three show temperatures decreasing toward the center). However their surface brightness distributions differ widely. Beyond the core radius, $\Sigma_X \sim r^{-1}$ in NGC 1399 (Jones et al. 1994) and $\Sigma_X \sim r^{-2.2}$ in NGC 5044 (David et al. 1994), while we find $\Sigma_X \sim r^{-1.8}$ in NGC 507 (§2.4.1). The X-ray radial profiles of the three galaxies are compared in Figure 15, where the profiles are plotted against the linear distance from the center (as those authors, we adopted D = 24 Mpc and 52.2 Mpc for NGC 1399 and NGC 5044, respectively). We marked with three large, filled symbols in each radial profile the position of the temperature peak, the cooling radius and the outermost radius ($\sim$ 1000 arcsec) where the X-ray emission can be accurately measured.

These three positions divide the surface brightness profiles into four subregions: (1) within the temperature peak (down to a few kpc) where the temperature decreases inward, i.e., the cooling gas is mainly deposited, (2) between the point where the temperature stops decreasing and the cooling radius where the assumption of steady state, homogeneous and isothermal flow may be valid, (3) between the cooling radius and the outermost radius ($\sim$1000″), where the binding mass can be well determined by the X-ray data, and (4) outside $\sim$1000″, where the X-ray data are very uncertain.

In region (2), between the temperature peak and the cooling radius, the slopes of the radial profiles are similar. Within this region, the uncertainty in our measurement is such that temperature could be constant, and the gas could still be in cooling flow regime. These slopes are close to $\Sigma_X \sim r^{-2}$ as expected for a homogeneous, isothermal gas flow.

However, if there is a real temperature peak (i.e., the temperature is decreasing radially), this result may be just coincidental. In this case, a cooling flow would be restricted only to the region within the temperature peak.

In the region where the gas temperature decreases inward (region 1), the X-ray profiles begin to differ and keep the trend down to a few kpc radius. Inside a few kpc, the PSPC data of NGC 1399, the galaxy closest to us, suggest a change in slope. The ROSAT HRI observations of NGC 1399 confirm this central peak (Kim et al. 1994). NGC 5044 and NGC 507 may also contain such a central peak which would be unresolved with the ROSAT PSPC. HRI observations are required to test this.

It is difficult to interpret the radial profile in region (1) from the position of the temperature peak to a few kpc (excluding the central peak of NGC 1399, because we do not have comparable data for the other two galaxies). If one assumes that the shape of the potential is similar in the three cases, the different X-ray radial profiles may imply that the cooling flow of NGC 1399 deposits mass at large radii while that of NGC 5044 deposits mass mainly at the center; NGC 507 would be an intermediate case. Qualitatively this argument may be correct. However, the exact amount of mass deposition as a function of radius may differ from this simple scenario because the determination of the mass deposition process is closely coupled with the shape of the potential, which we can not determine with the X-ray data.

Outside the cooling radius (region 3), the gas is not in a steady state because the flow time is much larger than the Hubble time. However, the equation of hydrostatic equilibrium is valid because the sound crossing time of the $\sim$ 1 keV gas is short. This justifies the use of this equation in determining the binding mass in §4.2. The different slopes of the X-ray radial profiles reflect the difference in the binding mass. However the gas may not be homogeneous even outside the cooling radius. We will discuss this possibility in §4.4. Then the different slopes represent mixed effects of different binding masses and inhomogeneities.

The possibility that the potential in region (4) ($r \gtrsim 1000''$) where X-ray data cannot determine a mass, may vary is suggested by a comparison of the optical velocity dispersion of group galaxies in the three cases with the stellar velocity dispersion of each dominant galaxy. The Fornax group where NGC 1399 resides has the lowest group velocity dispersion ($\sim$ 325 km sec^{-1}; Ferguson and Sandage 1990) while the NGC 507 and NGC 5044 groups have higher velocity dispersions (595 km sec^{-1} and 474 km sec^{-1}, respectively; Ferguson and Sandage 1990 and Wegner et al. 1993). The ratio of the group velocity dispersion to the galaxy velocity dispersion may be used as a measure of the shape of the potential in the region between the galaxy scale and the group scale. NGC 1399 has the lowest ratio ($\sim$1) and NGC 5044 has the highest ratio ($\sim$2) while NGC 507 is intermediate ($\sim$1.6). A recent measurement using globular clusters confirms the low velocity dispersion of the NGC 1399 group (Grillmair et al. 1994). Unless the optical measurements are contaminated by non-group members or the velocity is not isotropic, the wide range of the velocity dispersion ratios indicates that the group velocity dispersion measures the potential in a much larger scale than the outer limit of the gas distribution. To confirm the difference in the shape

of the potential in a larger scale suggested by the optical data, X-ray data in such a larger scale are necessary. These may be obtained by better understanding the field background and/or obtaining long off-center exposures of these galaxies.

The X-ray surface brightness of NGC 499 is quite in contrast to those of the three galaxies mentioned above in that its X-ray distribution is very steep ($\Sigma_X \sim r^{-2.6}$). The steepness is at the highest end of those measured with *Einstein* in X-ray bright early type galaxies (see Fabbiano 1989). The hot gas in NGC 499 is likely maintained by the steep galaxy potential (i.e., the potential of the NGC 507 group does not have a significant effect). This is also indicated by the relatively small extent of the X-ray gas. The steep surface brightness distribution of NGC 499 may imply that most of gas is falling toward the center before condensing at a large radius, as suggested by the presence of a possible cool core and the short cooling time at the center. It may also be interpreted as a stripped gas distribution due to tidal interaction with NGC 507.

4.4 The Unresolved Sources in the Halo of NGC 507

As discussed in §2.3 (see Table 2) 19 faint point-like sources are detected above 5 σ near the edge of the X-ray emitting gas. The number of sources found in this observation is about twice that expected by chance in the corresponding area of sky with a comparable flux threshold (estimated using deep survey field data by Hasinger et al. 1993), indicating that many of the detected sources are related with NGC 507 or its group.

Except for a few very bright sources (such as sources 6, 10, 19, and 21), the X-ray luminosities of these sources are in the range of 10^{40} to 10^{41} erg sec^{-1} assuming they are at the distance of NGC 507. These values are far in excess of those expected for binary stars or globular clusters associated with NGC 507 (e.g., Fabbiano 1989). Their average spectrum is also soft (Figure 11c) in contrast to the hard spectrum expected from X-ray accretion binaries. The composite spectral distribution of these sources is reminiscent of that of elliptical galaxies with the lowest L_X/L_B (Kim, Fabbiano and Trinchieri 1992; Fabbiano, Kim and Trinchieri 1994). However, given their luminosities, it is highly unlikely that they could be due to the integrated emission of the soft stellar sources invoked to explain the emission of X-ray faint ellipticals (Fabbiano, Kim and Trinchieri 1994). With the possible exception of two of them, these sources do not have any obvious optical counterpart (see §2.3). In this they are similar to otherwise more luminous sources found near the clusters of galaxies A1367 (Bechtold et al. 1983) and A2256 (Henry and Briel 1991).

We speculate that these sources may be cooling clumps in the cooling flow even though they lie outside the cooling radius. A local high density blob will cool more rapidly than the surrounding gas and the cooler clumps are then dropped out of the general inflow and remain at large radii. The spectral properties of these sources indicate that they are cooler than the diffuse gas at the same radius (Figure 11). The fainter substructures (see Figure 6) causing a bump in the radial profile at 450-650″ (see Figure 5) may also be due to local cooling. The spectral behaviour of the surface brightness (Figure 7) is in agreement with the hypothesis of mass deposition at large radii. The cooling gas at large radii will produces much stronger soft emission in the outer region (see White and Sarazin 1987b; Vedder, Trester and Canizares 1988; Sarazin and Ashe 1989). This is what our

observations suggest, i.e., the radial profile is flatter in the soft energy band (0.2-1.0 keV) than in the hard energy band (1.0-2.4 keV).

It is not clear how density fluctuations are originally introduced into the hot gas and how cooling clumps form and evolve through thermal instability (Balbus and Soker 1989; Loewenstein 1989; see Fabian, Nulsen and Canizares 1991 for a review). In particular, Balbus and Soker (1989) have shown that the linear thermal instability does not grow and produces just a buoyant oscillation. Fabian, Nulsen and Canizares (1991) suggested that density inhomogeneities might be initiated by some dynamical effects (such as stripping of gas, winds, infall, etc.). In NGC 507, there is some evidence of dynamical perturbations. Within its optical radius, there is a possible interacting galaxy, NGC 508, at 1.5 arcmin away (5 time less bright than NGC 507). Optical observations of the surface brightness distribution reveal shell features around NGC 507 (Arp 1966; Prugniel, Davoust and Nieto 1989), which are often interpreted as evidence of interaction (e.g., Malin and Carter 1983; Schweizer 1990). The density inhomogeneities may also be related to the tidal interaction with NGC 499.

However, these sources look like unresolved point sources rather than like filaments as seen in the central regions of cooling flow clusters, 2A 0335+096 and A2029 (Sarazin, O'Connell and McNamara 1992a, b). If these sources are cooling clumps, their electron density must be larger than $\sim 10^{-3}$ cm^{-3} for the cooling time to be shorter than the Hubble time. Then the upper limits of their size and mass are $\sim$14 kpc and 3×10^8 $M_\odot$. At the distance of NGC 507, the angular size would be $\lesssim$0.5 arcmin, therefore it would appear as a point-like source with the PSPC. High resolution spatial/spectral observations will be very important to establish if they are cooling clumps.

5. SUMMARY AND CONCLUSIONS

We have observed the field containing NGC 507 and NGC 499 with the ROSAT PSPC for a total of $\sim$ 20,000 sec. With this deep observation we have studied in detail the X-ray properties of these galaxies. Our results are summarized below:

1) In both galaxies the L_X/L_B ratio is far higher than that expected from the integrated emission of a population of X-ray emitting stellar sources, suggesting that the emission is dominated by hot gaseous components. In both cases the average spectral distribution of the PSPC counts support this conclusion, presenting a very pronounced peak near 1 keV, which can be explained with the blended contribution of thermal line emission. The X-ray halo of NGC 507 is also far more radially extended than its optical stellar emission.

2) We detect a total of 17600 counts from NGC 507, corresponding to an X-ray flux of 1.3×10^{-11} erg sec^{-1} cm^{-2} within 1000 arcsec (458 kpc) and luminosity of 1.45×10^{43} erg sec^{-1} in the energy range of 0.1 - 2.4 keV (D = 94.5 Mpc).

3) NGC 499 is detected with 5800 counts within 300 arcsec (137 kpc), corresponding to $F_X = 4.0 \times 10^{-12}$ erg sec^{-1} cm^{-2} and $L_X = 5.3 \times 10^{42}$ erg sec^{-1}.

4) The X-ray emission of NGC 507 is extended at least out to 1000″ (458 kpc at a distance of 94.5 Mpc). The surface brightness distribution outside the core region of NGC 507 declines as $\Sigma_X \sim r^{-1.8}$. Both core radius and gradient of the surface brightness are function of energy such that the surface brightness is both more centrally concentrated and flatter at the outer radii for softer rather than harder X-rays.

5) The X-ray emitting temperature of NGC 507 is near ∼1 keV but there is clear cooling at the center and possibly at the outer radii. The temperature peaks at a radius of 2-3′ (55-82 kpc). The absorption column density is consistent with the Galactic line-of-sight value at all radii. We cannot set a strong constraint on the metal abundance of the X-ray emitting gas. Values ranging from 30% up to 100% of solar value are acceptable. A better definition of the spectral parameters and of emission model will require higher resolution data (see also Trinchieri et al. 1994).

6) We detected 19 weak point-like sources near the edge of the X-ray emitting region of NGC 507. Their spectrum is on average softer (∼0.5 keV) than that of the X-ray emission at a similar radius from the center. Their fluxes are in the range of 10^{-14} – 10^{-13} erg sec^{-1} cm^{-2} and if they are associated with NGC 507, their luminosities are in the range of 10^{40} – 10^{41} erg sec^{-1}. The number density of these sources is well in excess to that of the expected background sources, indicating that a good fraction of them ($\sim \frac{1}{2}$) are associated with NGC 507.

7) The surface brightness distribution of NGC 499 is steep ($\Sigma_X \sim r^{-2.6}$), in contrast to that of NGC 507, but in the range of those measured with *Einstein* in X-ray bright early type galaxies (see Fabbiano 1989). Its emission temperature is also near 1 keV and there is a suggestion of cooler core. The choice of the spectral model is more uncertain than in NGC 507; both a low abundance model and a two-temperature solar abundance one give a better fit to the core emission. This is reminiscent of the results on NGC 4636 (Trinchieri et al. 1994).

These results suggest that:

1) Both NGC 507 and NGC 499 contain large amounts of dark matter; total binding masses are 2×10^{13} $M_\odot$ within 458 kpc and 9×10^{12} within 137 kpc, respectively, yielding $M_T/L_B = \sim$100 in both cases. The baryonic mass (including stellar and gas masses) is $\lesssim$19% for NGC 507 and $\lesssim$11% for NGC 499. The upper limits are due to the unknown volume filling factor of the hot gas which could be clumpy.

2) Both galaxies are experiencing cooling flows. The central cooling time is $\sim 10^9$ years in both cases, shorter than the Hubble time. The cooling radius is at ∼200″ (∼92 kpc) in NGC 507 and ∼180″ (82 kpc) in NGC 499. Within the cooling radius, the cooling rate is roughly 30-40 $M_\odot$year^{-1} in NGC 507 and 20-30 $M_\odot$year^{-1} in NGC 499.

3) By comparing the NGC 507 X-ray surface brightness with those of two other galaxies observed with the PSPC, NGC 5044 and NGC 1399, we find that the surface brightness distributions vary widely in otherwise similar galaxies. Only in the region between the point where the temperature stops decreasing and the cooling radius (where

one may assume the isothermal, homogeneous, steady-state condition), the radial profiles of the three galaxies are similar to $\Sigma_X \sim r^{-2}$, as expected. This wide variation of radial profiles may indicate significant variation in the mass deposition rate as a function of radius. However, the shape of the potential may vary as well in the cooling regions where X-ray data cannot accurately measure the binding mass (and potential gradient). A comparison of stellar and galaxy velocity dispersions in the three cases also suggest differences in their potentials in the radius range between the galaxy scale and the group scale.

4) We speculate that the unresolved, soft sources are cooling clumps. An excess of the surface brightness distribution seen at r = 450–650″ could be due to an unresolved population of similar sources. The inhomogeneous cooling flow may be dynamically affected by the nearby companion galaxies, NGC 508 and NGC 499. The relatively flat radial profile of X-ray surface brightness, and the different slope as a function of energy are consistent with this interpretations. If there is a large number of undetected cooling clumps in a wide range of radii, then the radial profile does not directly represent the potential, and a further uncertainty must be added to the measurement of the binding mass. The presence of cooling clumps could be confirmed by detection of extended emission with high resolution ROSAT HRI observations.

5) The relatively steep distribution of X-ray surface brightness of NGC 499 as well as the relatively small extent of its gas distribution suggests that the hot gas of NGC 499 is trapped by the galaxy potential well, not by the potential of the NGC 507 group. The data could also suggest that the hot gas may be stripped by the tidal force of NGC 507.

In a following paper, we will describe quantitatively the detailed radial behaviour of mass deposition and the shape of the gravitational potential as a function of radius, and discuss their implications for the nature of cooling flows.

ACKNOWLEDGMENTS

This work was supported by NASA grant NAG 5-2152 (ROSAT), NAGW 2681 (LTSA), NASA contract NAS8-39073 (AXAF Science Center) and KOSEF international program. We thank Claude Canizares, Martin Elvis, Paul Eskridge and Glen Mackie for useful discussions and comments.

References

Allen, C. W. 1973, "Astrophysical Quantities" (3rd ed.; London: Athlone).

Arnaud, K. A. 1988, in "Cooling Flows in Clusters and Galaxies" ed. by A. C. Fabian, p31, (Kluwer Academic Publishers: Dordrecht).

Arp, H. 1966, ApJ Suppl, 14, 1.

Avni, Y. 1976, ApJ, 210, 642.

Balbus, S. and Soker, N. 1989, ApJ, 341, 611.

Bertin, G., Pignatelli, E., and Saglia, R. P. 1993, AA. 49, 137

Bechtold, J., Forman, W., Giacconi, R., Jones, C., Schwarz, J., Tucker, W., and Van Speybroeck, L. 1983, ApJ, 265, 26.

Briel, U.G., Henry, J. P., and H. Bohringer 1992, AA, 259, L31.

Canizares, C. R., Steward, G. C. and Fabian, A. C. 1983, ApJ, 272, 449.

Canizares, C. R., Fabbiano, G. Trinchieri, G. 1987, ApJ, 312, 503.

Canizares, C. R., Markert, T. H., and Donahue, M. E. 1988, in "Cooling Flows in Clusters and Galaxies", ed. A. C. Fabian, p63, (Kluwer Academic Publishers: Dordrecht).

David, L. P., Slyz, A., Jones, C., Forman, W., Vrtilek, S. D. and Arnaud, K. A. 1993, ApJ, 412, 479.

David, L. P., Jones, C., Forman, W. and Daines, S. 1994, preprint.

Ebneter, K. Djorgovsky, S., and Davis, M. 1988, AJ, 95, 422.

Edge, A. C. and Steward, G. C. 1991, MNRAS, 252, 428.

Fabbiano, G. 1989, ARAA, 27, 87.

Fabbiano, G. 1993, in *Structure, Dynamics and Chemical Evolution of Elliptical Galaxies*, ed I. J. Danziger, W. W. Zeilinger and K. Kjar, ESO Conf. Proc. No. 45, p.617.

Fabbiano, G., Gioia, I. M., and Trinchieri, G. 1989, ApJ, 347, 127.

Fabbiano, G., Kim, D.-W., and Trinchieri, G. 1992, ApJ Suppl 80, 531.

Fabbiano, G., Kim, D.-W., and Trinchieri, G. 1994, ApJ, 429, 94.

Fabricant, D. and Gorenstein, P. 1983, ApJ, 267, 535.

Fabian, A. C., Nulsen , P. E. J. and Canizares, C. R. 1984, Nature, 310, 733

Fabian, A. C., Nulsen , P. E. J. and Canizares, C. R. 1991, AA Rev, 2, 191.

Fanti, C., Fanti, R., de Ruiter, H. R., and Parma, P. 1987, AA Suppl. 69, 57.

Ferguson, H. C. and Sandage, A. 1990, AJ, 100, 1.

Fiore, F., Elvis, M., McDowell, J. C., Siemiginowska, A., and Wilkes, B. J. 1994, ApJ, in press.

Forman, W., Jones, C., David, L., Franx, M., Makishima, K. and Ohashi, T. 1993, ApJ Lett, 418, L55.

Grillmair, C. J., Freeman, K. C., Bicknell, G. V., Carter, D., Couch, W. J., Sommer-Larsen, J. and Taylor, K. 1994, ApJ Lett, 422, L9.

Hasinger, G., Burg, R., Giacconi, R., Hartner, R., Schmidt, M., Trumper, J and Zamorani, G. 1993, AA, 275, 1.

Henry, J. P. and Briel, U. G. 1991, AA, 246, L14.

Jones, C., Stern, C., Forman, W., Breen, J., David, L., Tucker, W., Franx, M. and Fabian, A. C., 1994, preprint.

Kim, D.-W., and Fabbiano, G. 1991, BAAS, 23, 1402.

Kim, D.-W., Fabbiano, G., and Trinchieri, G. 1992, ApJ 393, 134.

Kim, D.-W., et al. 1994 in preparation.
Kriss, G. A., Cioffi, D. F., and Canizares, C. R. 1983, ApJ 272, 439.
Loewenstein, M. 1989, MNRAS, 283, 15.
Lubin, L. M. and Bahcall, N. A. 1993, ApJ Lett, 415, L17.
Malin, D. F. and Carter, D. 1983, ApJ, 274, 534.
Morrison, R., and Mccammon, D. 1983, ApJ 270, 119.
Parma, P., de Ruiter, H. R., Fanti, C., and Fanti, R. 1986, AA Suppl. 64, 135.
Pellegrini, S., and Fabbiano, G. 1994 ApJ in press.
Plucinsky, P. P., Snowden, S. L., Briel, U. G., Hasinger, G., and Pfeferman, E. 1993, ApJ 418, 519.
Ponman, T. J., and Bertram, D. 1993, Nature, 363, 51.
Preswitch, A., H., Guimond, S.J., Luginbuhl, C., and Joy, M. 1994, ApJ, accepted.
Prugniel, P., Davoust , E. and Nieto, J.-L. 1989, AA, 222, 5.
Sarazin, C. L. 1988 "X-ray emissions from clusters of galaxies" (Cambridge University press).
Sarazin, C. L., and White, R. E. 1987, ApJ 320, 32.
Sarazin, C. L., and Ashe, G. A. 1989, ApJ 345, 22.
Sarazin, C. L., O'Connell, R. W., and McNamara, B. R. 1992a, ApJ 397, L31.
Sarazin, C. L., O'Connell, R. W., and McNamara, B. R. 1992b, ApJ 398, L59.
Schweizer, F. 1990, in *Dynamics and Chemical Evolution of Elliptical Galaxies*, ed R. Wielen (Heidelberg: Springer), P60.
Snowden, S. L., McCammon, D., Burrows, D. N., and Mendenhall, J. A. 1994, ApJ, Submitted.
Songaila, A., Cowie, L. L., Hogan, C. J., and Rugers, M. 1994, Nature, 368, 599.
Stark, A. A., Gammie, C. F,. Wilson, R. W., Bally, J., Linke, R. A., Heiles, C., Hurwitz, M. 1992, ApJ Suppl. 79, 77
Tammann, G. A. 1982, in *Supernovae: A Survey of Current Research*, ed M. Rees and R. Stoneham (Dordrecht: Reidel) p.371.
Thomas, P. A., Fabian, A. C., Arnaud, K. A., Forman, W., and Jones, C. 1986, MNRAS, 222, 655.
Trinchieri, G., Fabbiano, G., and Canizares, C. R. 1986, ApJ, 310, 637.
Trinchieri, G., Kim, D.-W., Fabbiano, G. and Canizares, C. R. 1994, ApJ, 428, 555.
van den Bergh, and S. Tammann, G. A. 1991, ARAA 29, 363.
Vedder, P. W., Trester, J. J., and Canizares, C. R. 1988, ApJ 332, 275
Walker, T. P., Steigman, G., Schramm, D. N., Olive, K. A. and Kang, H. 1991, ApJ, 376, 51.
Wegner, G., Haynes, M. P., and Giovanelli, R. 1993, AJ, 105, 1251.
White, R. E., and Sarazin, C. L. 1987a, ApJ, 318, 621.
White, R. E., and Sarazin, C. L. 1987b, ApJ, 318, 629.
White, D. A., Fabian, A. C., Allen, S. W., Edge, A. C, Crawford, C. S., Johnstone, R. M., Stewart, G. C., and Vogue, W. 1994, MNRAS, 269, 589.
Whitmore, B. C., McElroy, D. B., and Tonry, J. L. 1985, ApJ Suppl, 59, 1.

Table 1

Basic parameters

	NGC 507	NGC 499
RA (J2000)[a]	1 23 40.1	1 23 11.6
DEC (J2000)[a]	33 15 22	33 27 36
B_T^o (mag)[a]	12.19	12.79
D (Mpc)[b]	94.5	94.5
D_{25} (arcsec)[a]	185	97
N_H (cm^{-2})[c]	5.3 x 10^{20}	5.3 x 10^{20}
PSPC Observed Date[d]	Aug 9-10, 1992	Aug 9-10, 1992
PSPC On Time (sec)[d]	5728	5728
PSPC Exp Time (sec)[d f]	5600	5410
PSPC Observed Date[e]	Jan 8-9, 1993	Jan 8-9, 1993
PSPC On Time (sec)[e]	15290	15290
PSPC Exp Time (sec)[e f]	14900	13920
σ_* km sec^{-1} [g]	301	–
σ_{group} km sec^{-1} [h]	595	–
Log Fx (IPC) erg sec^{-1} cm^{-2} [i]	9.4 x 10^{-12}	3.0 x 10^{-12}

a. Right Ascension (RA), declination (DEC), total face-on B magnitude (B_T^o), and major isophotal diameter measured at B = 25 magnitude $arcsec^{-2}$(D_{25}) taken from de Vaucouleeurs et al. 1991 (RC3)

b. Distance estimated by using H = 50 km sec^{-1} Mpc^{-1} and an average group velocity of 4725 km sec^{-1} (Wegner et al. 1993).

c. Galactic line of sight H column density from Starks et al. 1992.

d. Sequence number rp600254.

e. Sequence number rp60025401.

f. average exposure time within 3 arcmin circle.

g. stellar velocity dispersion from Whitmore et al. 1985.

h. group velocity dispersion from Wegner et al. 1993.

i. IPC flux from Fabbiano et al. 1992. Fluxes were estimated in a energy range of 0.2–4.0 keV and kT=1keV was assumed. The count extraction radii are r=630″ and r=210″ for NGC 507 and 499, respectively.

Table 2

Other Sources

source number	X pixel	Y pixel	radius arcsec	source[a] cnt rate	diffuse emission[a] cnt rate	net[a] cnt rate	net error[a] cnt rate	fx[b]
1[c]	10219.70	6997.40	90	7.94	1.01	6.93	1.28	0.94
2[c]	9981.20	7685.90	90	11.07	1.26	9.81	1.30	1.34
3[c]	9598.10	8046.20	90	7.49	1.72	5.77	1.13	0.79
4	9398.00	7733.30	60	3.60	0.98	2.61	0.71	0.36
5	9366.20	7307.90	90	6.60	2.11	4.49	1.00	0.61
6[c]	9196.10	6058.10	120	24.44	2.47	21.98	1.96	3.00
7	8629.70	8522.60	60	7.45	1.54	5.91	0.85	0.81
8	8440.10	7637.00	60	5.45	3.92	1.53	0.77	0.21
9	8371.40	8155.70	60	6.56	3.28	3.28	0.83	0.45
10	8343.20	7119.20	90	20.32	7.81	12.51	1.45	1.71
11	8028.80	8307.80	60	7.08	3.98	3.10	0.84	0.42
12	8025.50	8865.50	60	8.14	1.44	6.70	0.86	0.91
13	7508.60	8918.00	60	4.81	1.63	3.18	0.74	0.43
14	7273.40	8628.50	60	4.87	2.07	2.81	0.72	0.38
15	7023.20	6724.40	60	4.57	2.19	2.38	0.72	0.32
16	6895.40	7208.00	60	5.28	3.25	2.03	0.76	0.28
17	6887.60	8434.70	60	5.79	2.08	3.71	0.78	0.51
18	6625.40	6462.20	90	5.93	2.55	3.37	0.96	0.46
19[c]	6387.20	4544.60	180	106.78	2.83	103.95	3.93	14.18
20	6217.40	6906.50	90	6.83	2.44	4.39	1.00	0.60
21	2700.50	6720.50	300	215.14	1.40	213.74	5.45	29.15

a. Counts rate are in units of cnt $ksec^{-1}$. The diffuse emission is subtracted from the source counts. Its count rate and error were estimted using the radial profile at a given radius (see section 2.4). For sources 19 and 21, background counts extracted from the annuli surrounding the sources were subtracted from the source counts.

b. Flux was calculated by assuming T=0.5 keV and N_H=5.3 x 10^{20} cm^{-2} and is in unit of 10^{-13} erg sec^{-1} cm^{-2}.

c. Source 1 2 3 6 and 19 are partly hidden by the detector structure.

Table 3

Spectral parameters (1T fit)

region	channel used	$\log N_H$ (90%) (cm^{-2})	kT (90%) (keV)	χ^2	degrees of freedom
0 – 60	5-30	20.71 (20.64-20.81)	0.98 (0.94-1.01)	32.40	23
60 – 120	5-30	20.65 (20.60-20.71)	1.06 (1.02-1.11)	31.93	23
120 – 180	5-30	20.73 (20.65-20.83)	1.32 (1.21-1.46)	17.93	23
180 – 300	6-30	20.64 (20.56-20.74)	1.17 (1.11-1.26)	25.60	22
300 – 420	5-30[a]	20.66 (20.52-20.83)	1.11 (1.07-1.20)	23.72	19
420 – 700	6-30[b]	20.60 (20.47-20.77)	1.08 (1.04-1.11)	22.75	20
700 –1000	7-30[c]	20.49 (20.16-20.95)	1.04 (0.96-1.10)	14.29	18

a. Channels (5,6) and (7,8,9,10) are combined.

b. Channels (6,7,8) are combined.

c. Channels (8,9,10,11) are combined.

Table 4

2-Component fit[a]

region	logN_H (cm^{-2})	kT Primary	kT Second	Norm[b]	χ^2	degrees of freedom
adding a hard component (1.5 to 3.0 keV)						
0 – 60	20.73	0.95	3.00	-0.50	30.47	21
60 – 120	20.69	0.95	2.99	0.11	18.38	21
120 – 180	20.76	0.86	1.52	1.13	15.54	21
180 – 300	20.69	1.05	3.00	0.11	17.49	20
300 – 420	20.49	0.89	1.51	0.54	14.54	16
420 – 700	20.52	0.95	2.95	0.07	12.31	18
700 –1000	20.23	0.99	2.62	-0.57	11.73	14
adding a soft component (0.1 to 0.5 keV)						
0 – 60	20.72	0.98	0.46	-2.00	32.40	21
60 – 120	20.68	1.13	0.49	-1.32	26.22	21
120 – 180	20.74	1.32	0.10	-2.00	18.00	21
180 – 300	20.70	1.19	0.23	-1.41	22.16	20
300 – 420	20.50	1.21	0.45	-1.26	13.52	16
420 – 700	20.51	1.13	0.45	-1.21	13.41	18
700 –1000	20.23	1.03	0.25	-1.94	11.61	14

With Varying Abundance

region	logN_H (90%)[c] (cm^{-2})	kT (90%)[c] (keV)	Abundance (90%)[c]	χ^2	degrees of freedom
0 – 60	20.71 (20.43-20.88)	1.01 (0.94-1.07)	0.99 (0.45-)	32.13	22
60 – 120	20.74 (20.61-20.86)	1.08 (1.02-1.12)	0.53 (0.29-1.00)	23.38	22
120 – 180	20.77 (20.63-20.95)	1.35 (1.17-1.55)	0.70 (0.31-1.52)	16.68	22
180 – 300	20.76 (20.61-20.93)	1.14 (1.09-1.30)	0.47 (0.26-0.95)	18.24	21
300 – 420	20.80 (20.58-21.10)	1.09 (1.96-1.18)	0.37 (0.12-0.98)	18.14	18
420 – 700	20.76 (20.56-21.05)	1.05 (0.94-1.11)	0.38 (0.16-0.84)	14.67	19
700 –1000	20.55 (-21.24)	1.04 (0.87-1.11)	0.73 (0.14-)	14.03	17

a. In 2-component model fitting, the acceptable ranges are not well determined.

b. Logarithm of the relative normalization to the first component.

c. 90% confidence range with 3 interesting parameters.

Table 5

Spectral parameters (NGC 499)

region	channel used	logN_H (90%) (cm^{-2})	kT (90%) (keV)	χ^2	degree of freedom
0-300	5-30	20.76	0.81	47.59	23
0-120	6-30	20.65 (20.57-20.77)	0.77 (0.74-0.80)	29.90	22
120-300	6-30[a]	20.74 (20.51-21.43)	0.92 (0.80-0.99)	19.69	16

2-Component Fit[b]

region	logN_H (cm^{-2})	kT Primary	kT Second	Norm[c]	χ^2	degree of freedom
adding a hard component (1.5 to 3.0 keV)						
0-120	20.74	0.66	1.73	-0.12	12.84	20
120-300	20.30	0.89	3.00	-0.08	17.84	14
adding a soft component (0.1 to 0.5 keV)						
0-120	20.77	0.95	0.50	-0.22	16.58	20
120-300	20.00	0.99	0.50	-1.14	20.04	14

With Varying Abundance

region	logN_H (90%)[d] (cm^{-2})	kT (90%)[d] (keV)	Abundance (90%)[d]	χ^2	degrees of freedom
0 – 120	20.86 (20.71-21.02)	0.72 (0.67-0.77)	0.29 (0.18-0.60)	14.78	21
120 – 300	20.92 (20.75-21.53)	0.88 (0.81-0.99)	0.46 (0.17-1.63)	16.94	15

a. Channels (6,7,8,9) and (10,11,12) are combined.

b. In 2-component model fitting, the acceptable ranges are not well determined.

c. Logarithm of the relative normalization to the first component.

d. 90% confidence range with 3 interesting parameters.

Figure Captions

Figure 1. The raw PSPC image of NGC 507/499 field. No correction was applied.

Figure 2. Comparison of background map and exposure map. (a) The radial profile of the background map (dashed line) and that of the exposure map (solid line) are plotted in unit of counts per unit area, but the normalization is arbitrary to easily compare two profiles. (b) The rate as a function of radius is made by dividing the image by the exposure map. The solid line is the source rate, the dashed line is the rate taken from the background map, the dotted line is the adopted background rate and circles with error bars are the net rate.

Figure 3. Comparison of background map obtained from other PSPC observations. From the top, they are rp600009, rp600008, rp600017, and rp600520. The dotted line is the radial profile of the exposure map of this observation (rp60025401). The bottom two lines are radial profiles of the background maps of this observations (rp600245 and rp60025401). Normalizations are arbitrary.

Figure 4. Contour plot of X-ray image of NGC 507 and NGC 499. The lowest contour is 2 sigma level (0.4 counts arcmin^{-2} ksec^{-1}) and the step size is a factor of 1.585 (0.5 mag interval). The source number of 21 detected small sources is sorted by RA.

Figure 5. Radial profiles of NGC 507 X-ray surface brightness. (a) Radial profile was made excluding NGC 499 and all the sources in Table 2, and the data at r $< 1000''$ was fitted to $\Sigma_X \sim (1+(\frac{r}{a})^2)^{-3\beta+0.5}$, and (b) same as (a) but fitting is to the data at r=0-450$''$ and r=650-1000$''$.

Figure 6. A model image was made by the best fit radial profile of NGC 507 and the image was divided by this model image, then smoothed with a Gaussian σ=30$''$. The small circles mark detected sources and the large annulus indicates the region (r=450-650$''$) where the excess emission is seen.

Figure 7. Contour plot of acceptable parameter ranges for the radial profiles of soft and hard X-rays. The contours are at the 66%, 90% and 99% confidence levels.

Figure 8. Radial profiles of NGC 499 X-ray surface brightness.

Figure 9. Spectral fit of the whole region of NGC 507 (r $< 1000''$) with a single temperature model with cosmic abundance.

Figure 10. Best fit kT and N_H for various radial bins. The error bars are at the 90% confidence level.

Figure 11. (a) Spectrum taken from r=420-700$''$ and (b) combined spectrum taken from the point-like sources. The solid lines both in (a) and (b) are the same best fit model prediction for the spectrum in (a). (c) Net source spectrum. A normalized diffuse spectrum is subtracted from the source spectrum.

Figure 12. Comparison of (a) the ROSAT PSPC and (b) Einstein IPC spectra of NGC 507. The best fit model for the PSPC spectrum is plotted in both figures.

Figure 13. (a) Deprojected density profile and (b) cooling time as a function of radius. The best fit temperature at each radial bin is used. The last point in both figures is an artifact of the deprojecting routine.

Figure 14. Radial dependence of binding mass of NGC 507.

Figure 15. Comparison of radial profiles of X-ray surface brightness of NGC 1399 (open circle), NGC 5044 (cross) and NGC 507 (open square). The big filled circles, triangles and squares indicate positions at r=1000 arcsec from the center (outer set), positions of the cooling radius (middle set) and positions where the measured temperature peaks (inner set) for NGC 1399, NGC 5044 and NGC 507, respectively. The dips at 140 kpc for NGC 1399, 300 kpc for NGC 5044 and 580 kpc for NGC 507 are due to the detector structure.

NGC 507/499 ROSAT PSPC

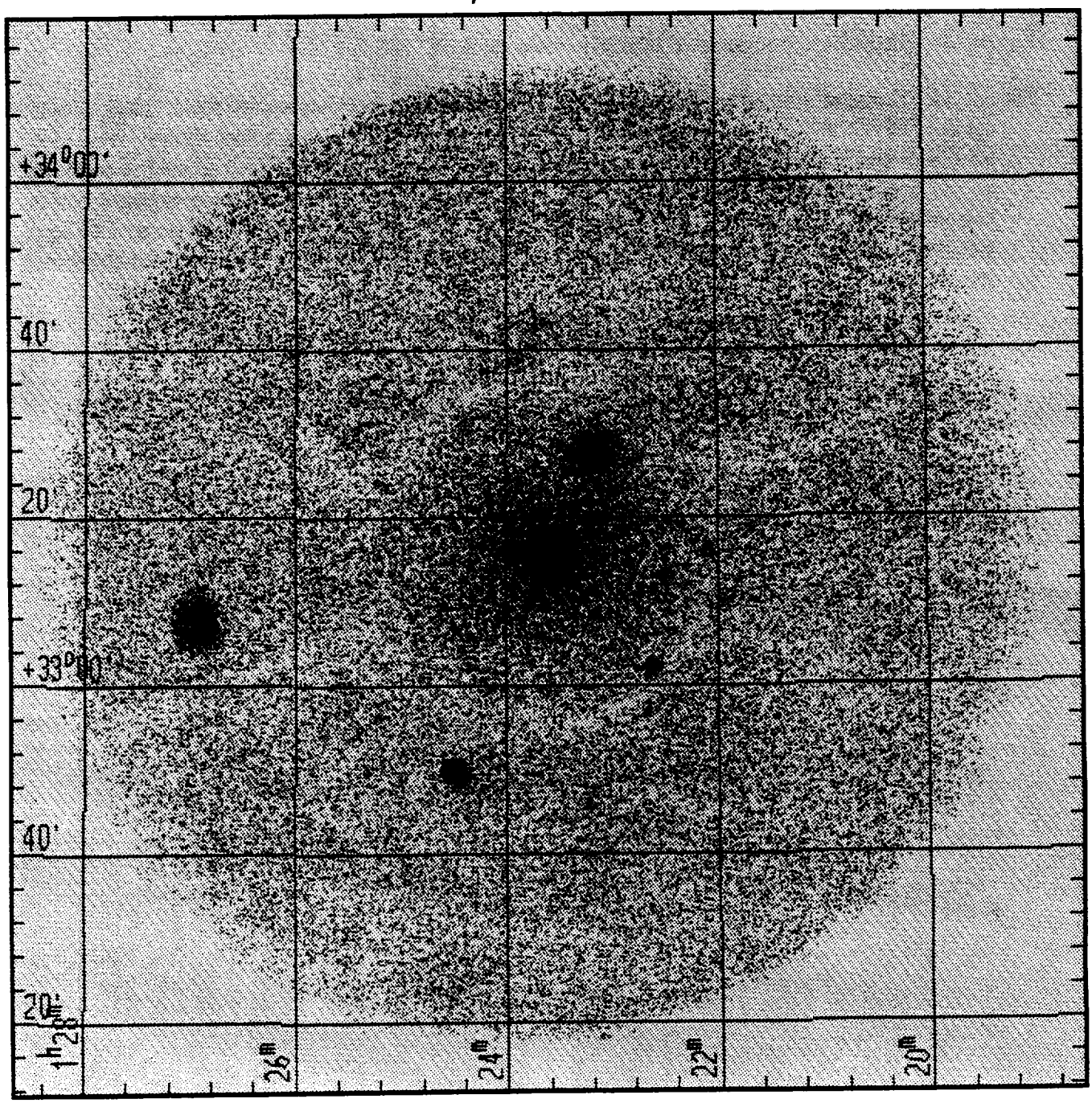

Fig. 1

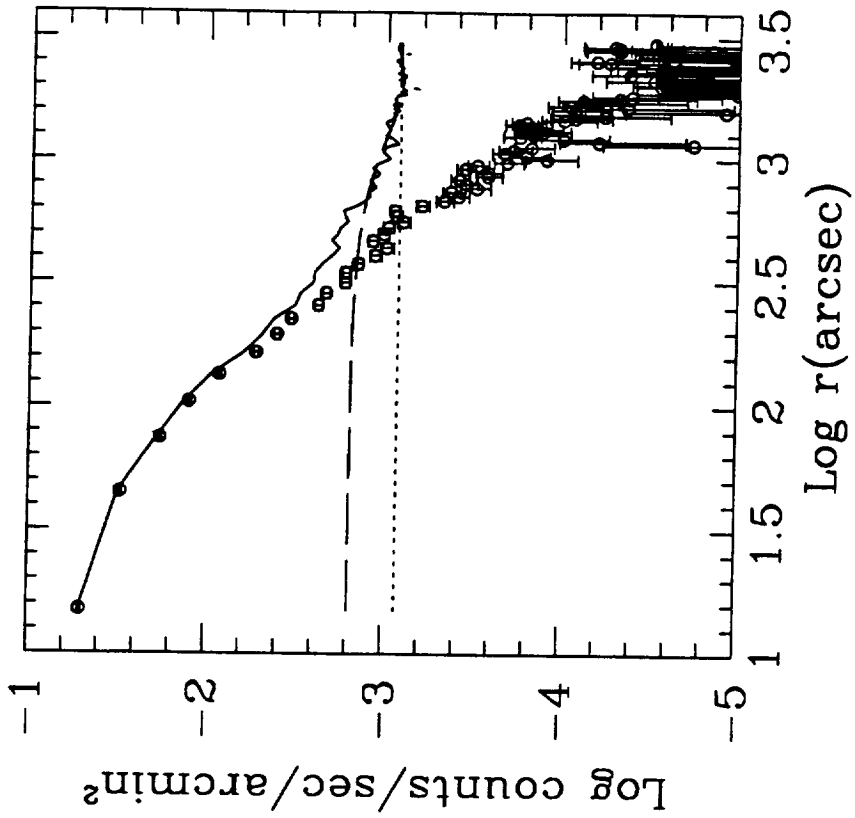
Log counts/sec/arcmin²
−1
−2
−3
−4
−5
1
1.5
2
2.5
3
3.5
Log r(arcsec)

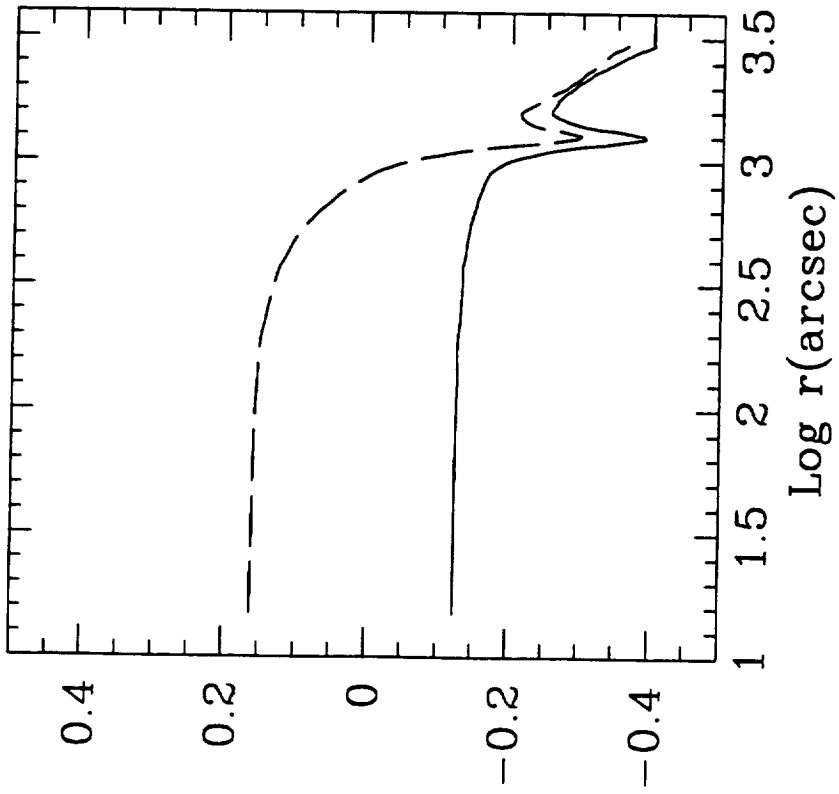
Log counts/arcmin² + constant
0.4
0.2
0
−0.2
−0.4
1
1.5
2
2.5
3
3.5
Log r(arcsec)

Fig. 2

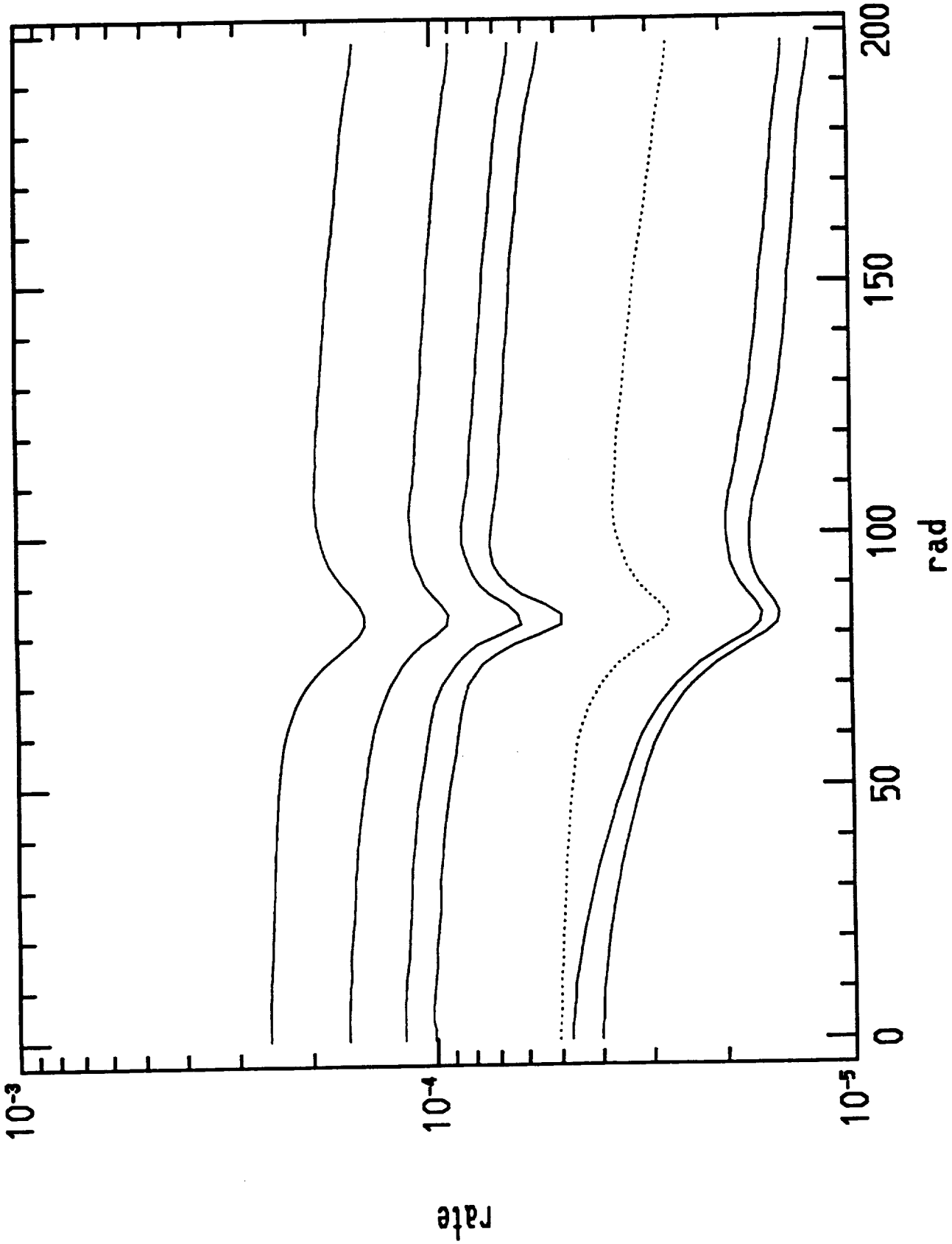

Fig. 3

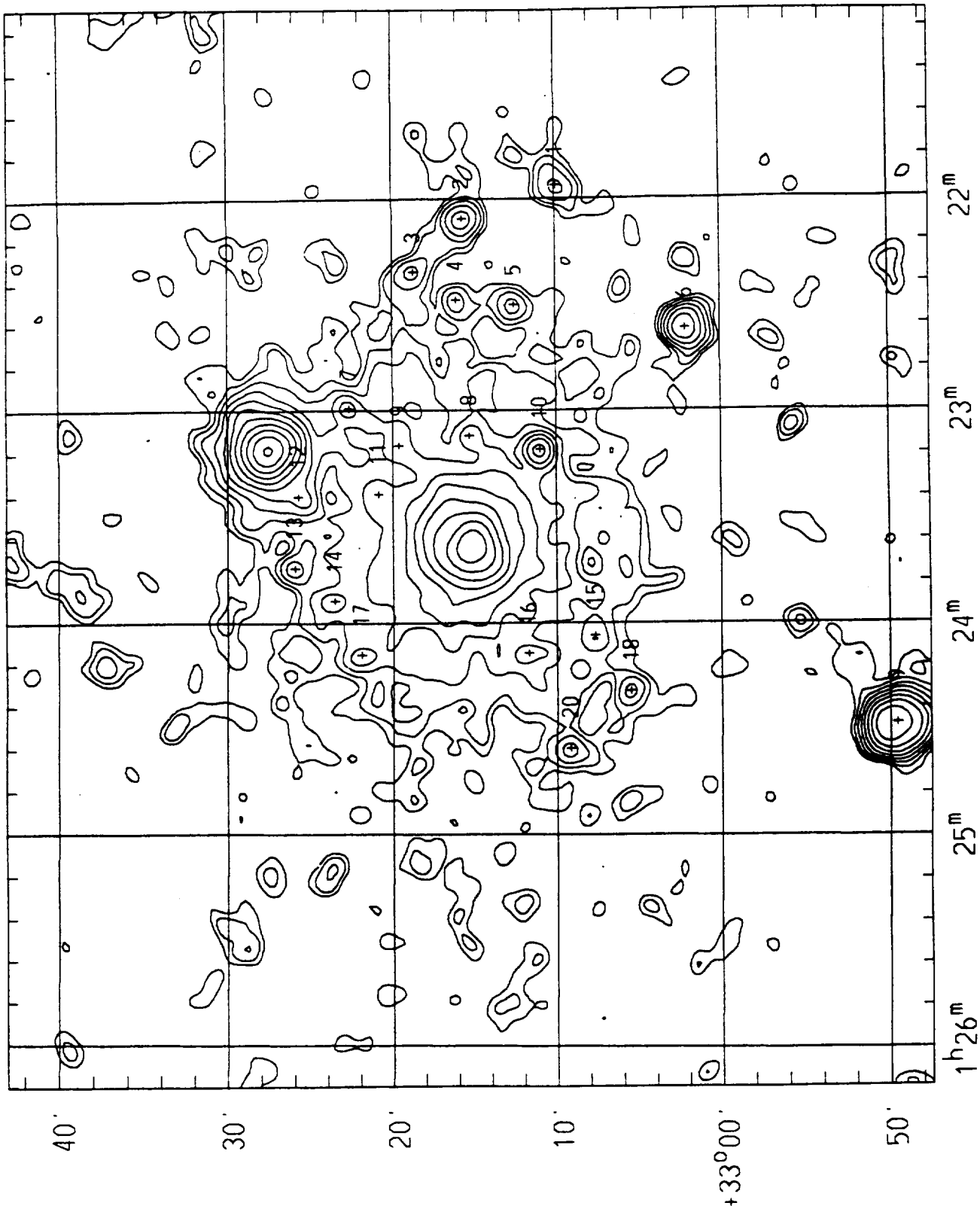

Fig. 4

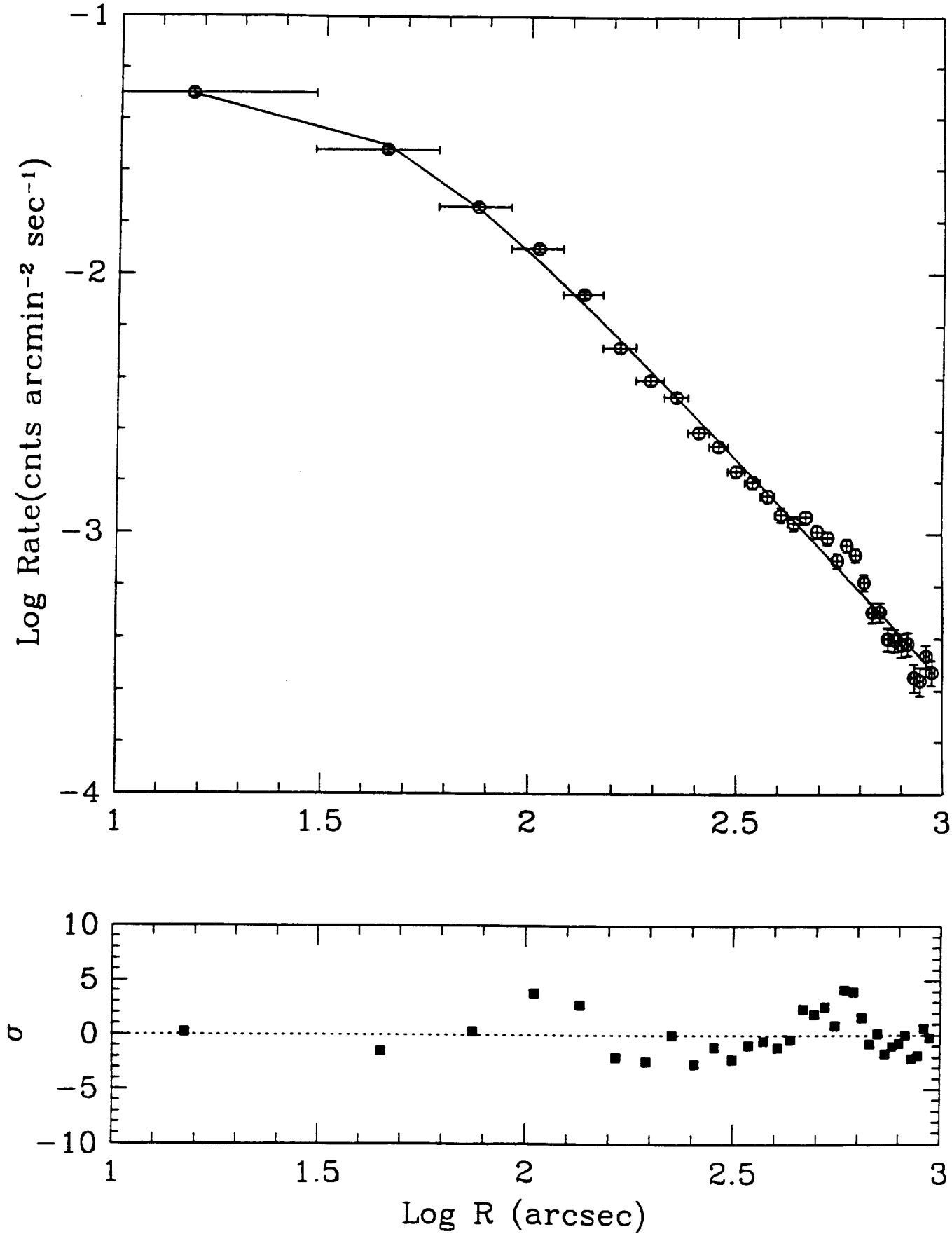
Log Rate(cnts arcmin^{-2} sec^{-1})
−1
−2
−3
−4
1
1.5
2
2.5
3
σ
10
5
0
−5
−10
Log R (arcsec)

Fig. 5a

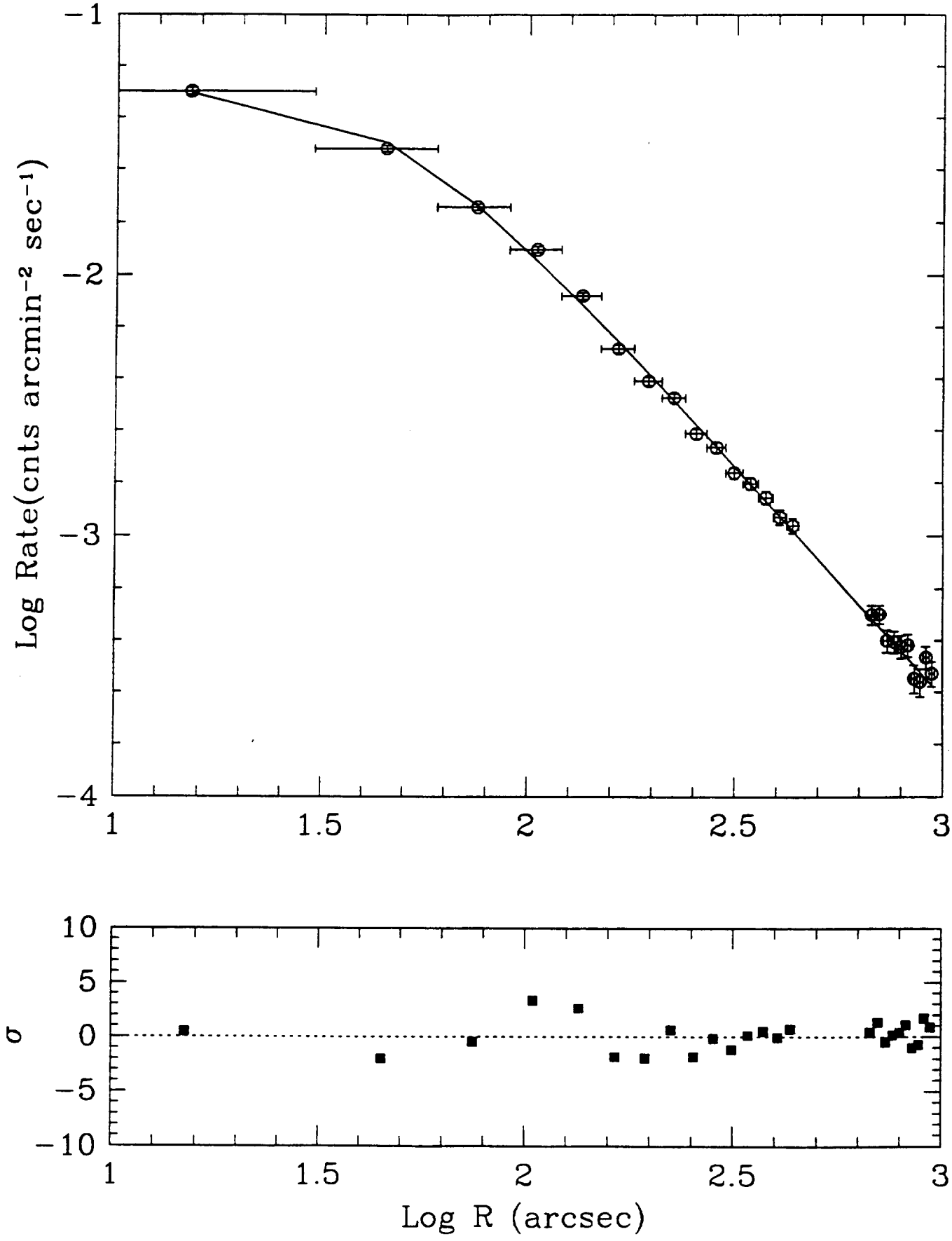
Log Rate(cnts arcmin^{-2} sec^{-1})
−1
−2
−3
−4
1
1.5
2
2.5
3
σ
10
5
0
−5
−10
Log R (arcsec)

Fig. 5b

NGC 507 model-divided

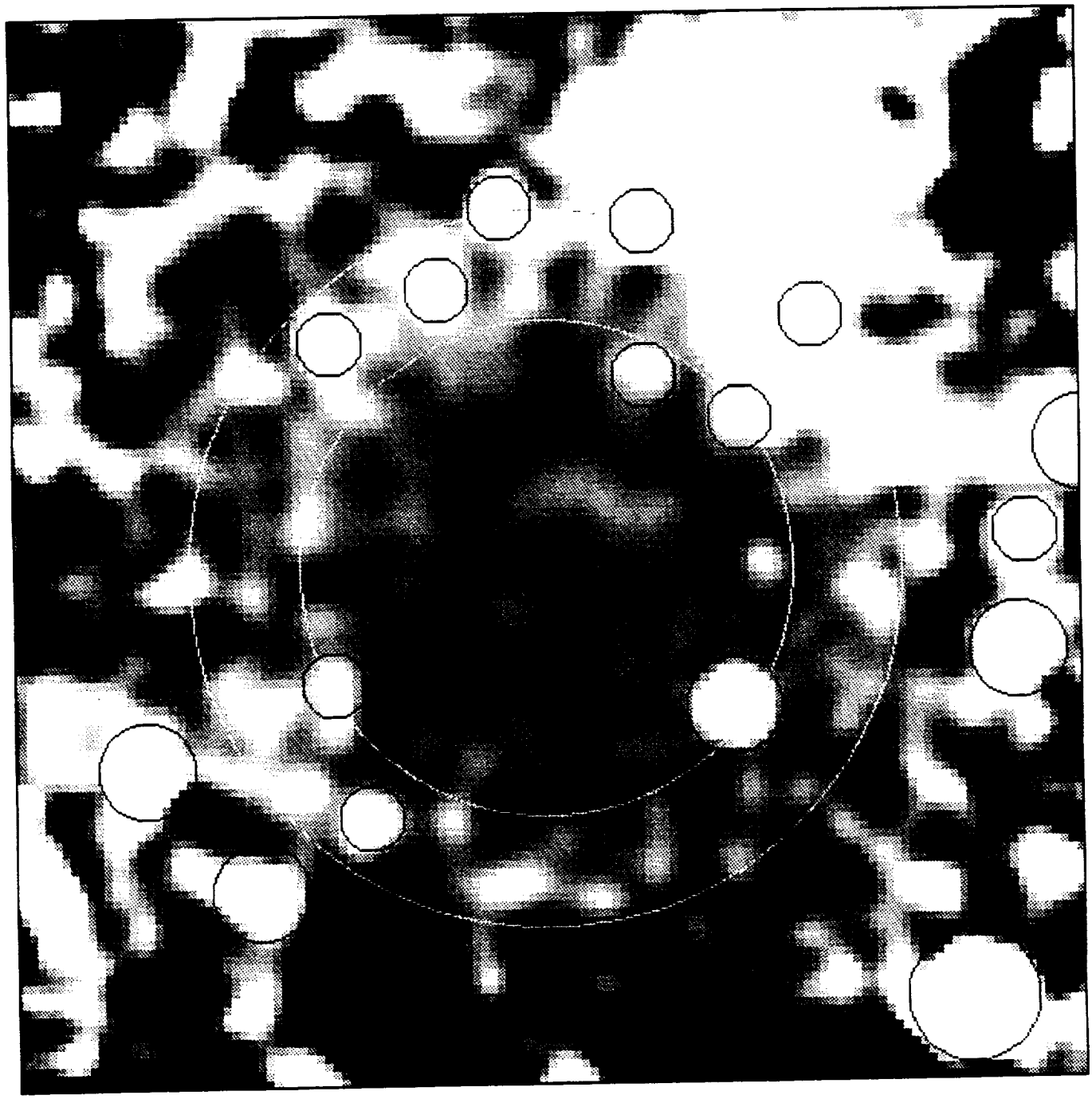

Fig. 6

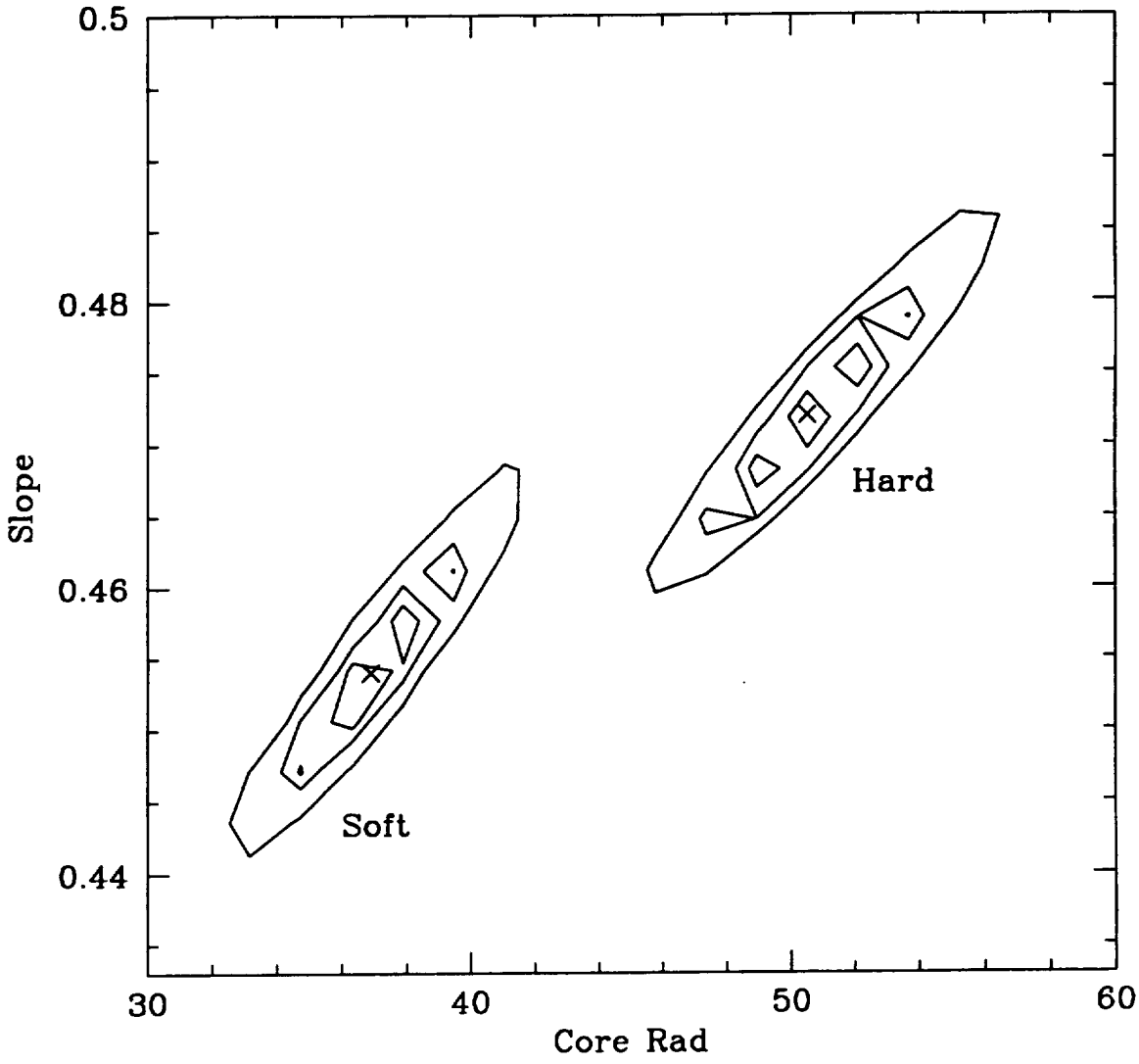

Fig. 7

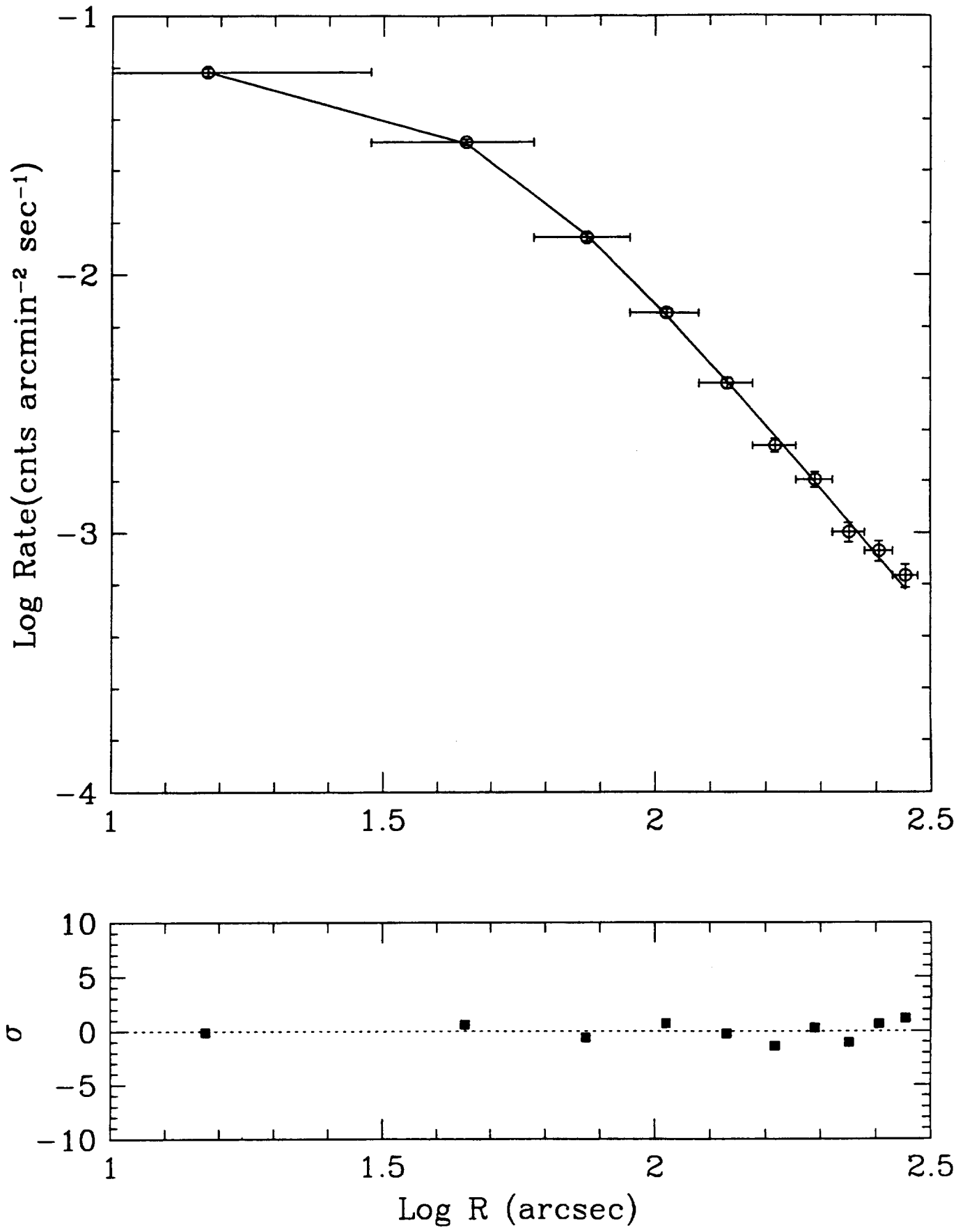
−1
−2
−3
−4
Log Rate(cnts arcmin⁻² sec⁻¹)
1
1.5
2
2.5
10
5
0
−5
−10
σ
1
1.5
2
2.5
Log R (arcsec)

Fig. 8

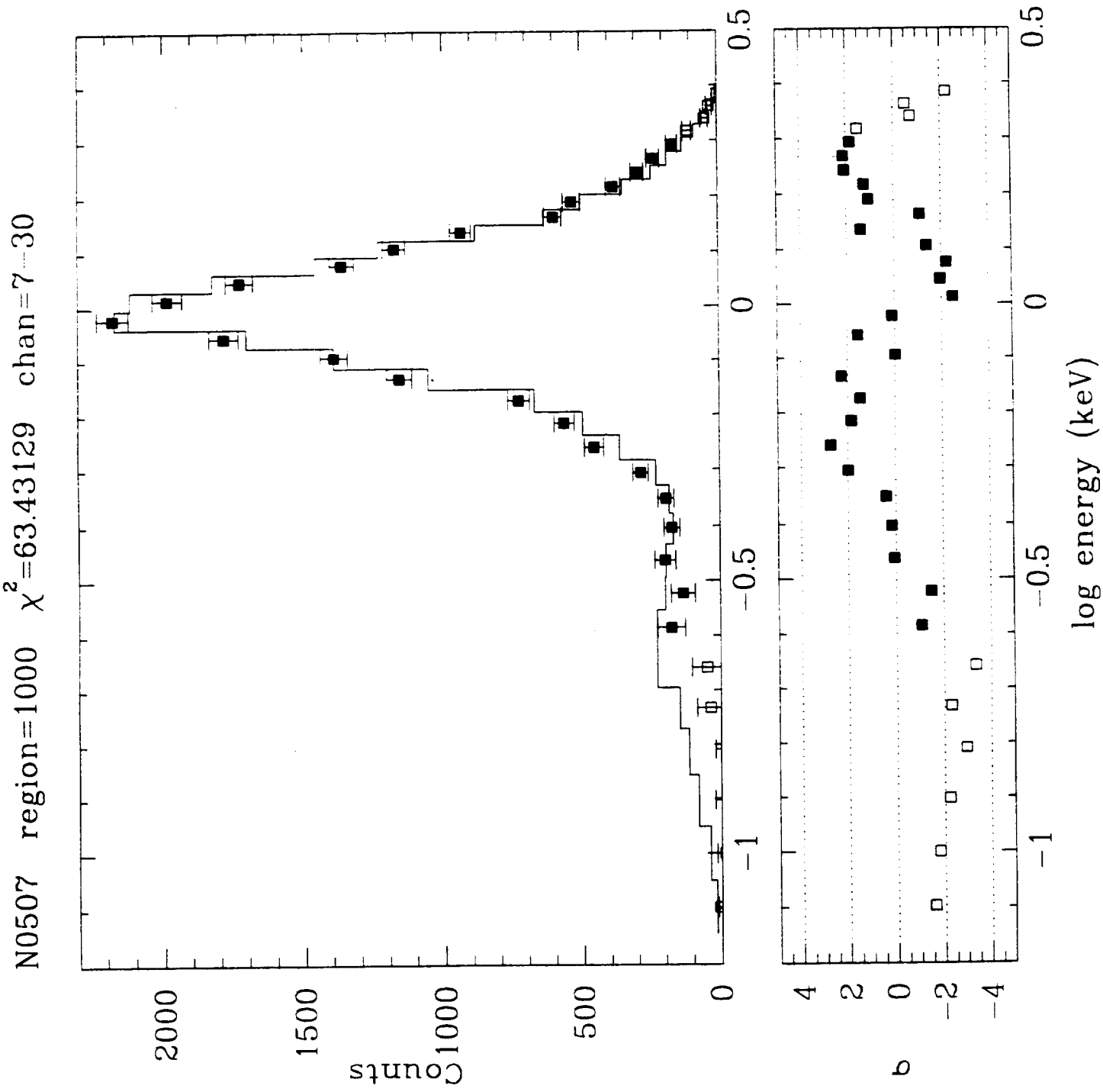

Fig. 9

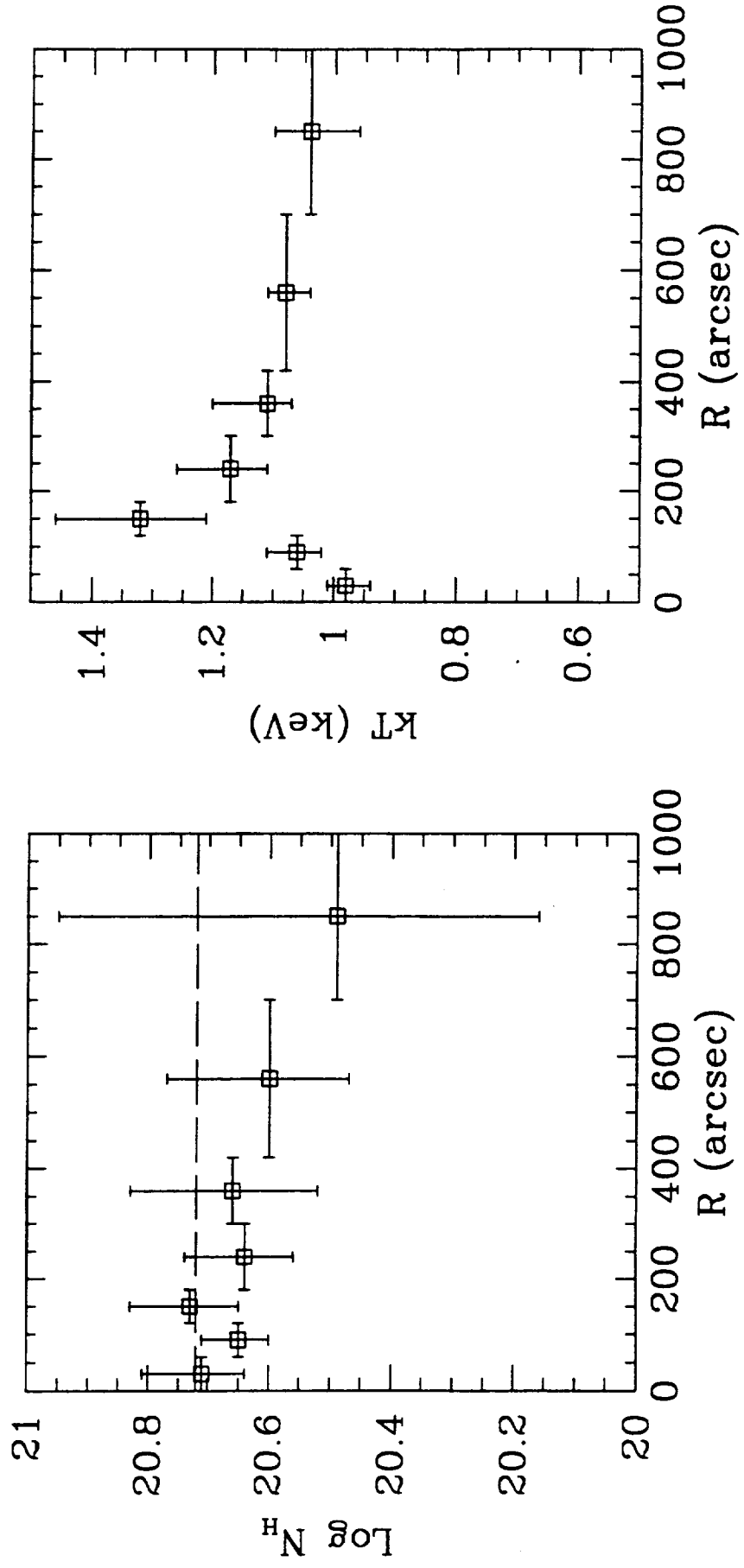
kT (keV)
1.4
1.2
1
0.8
0.6
0
200
400
600
800
1000
R (arcsec)
Log N_H
21
20.8
20.6
20.4
20.2
20
0
200
400
600
800
1000
R (arcsec)

Fig. 10

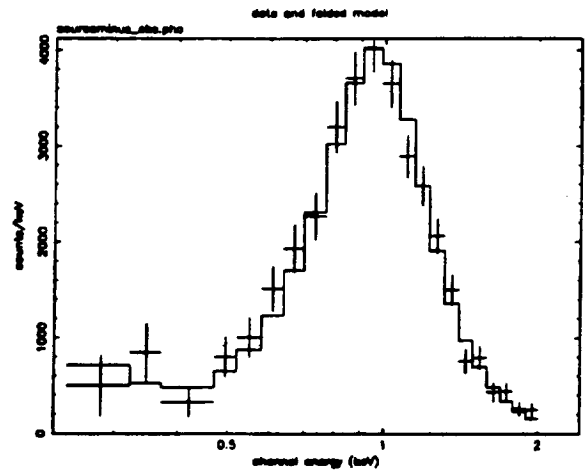
data and folded model
counts/keV
channel energy (keV)

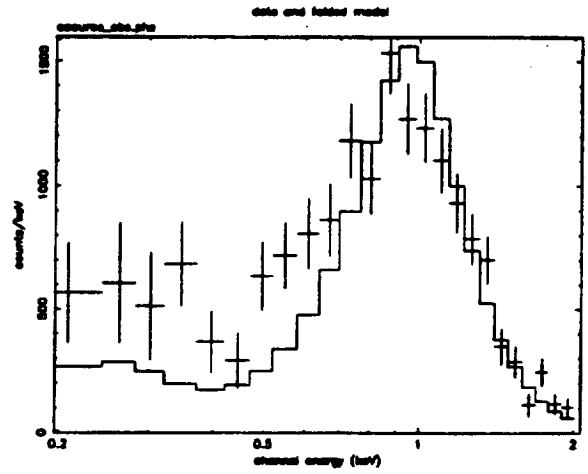
data and folded model
counts/keV
channel energy (keV)

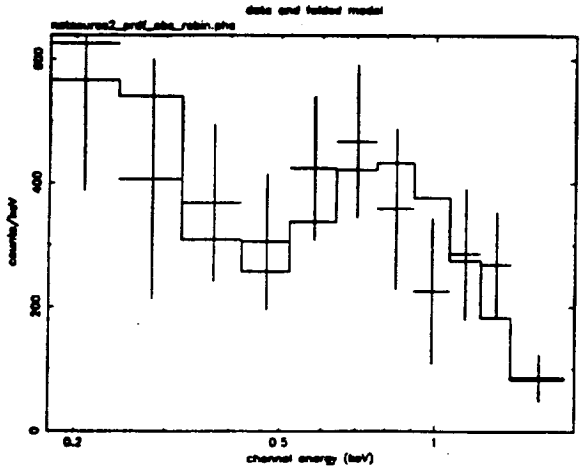
data and folded model
counts/keV
channel energy (keV)

Fig. 11

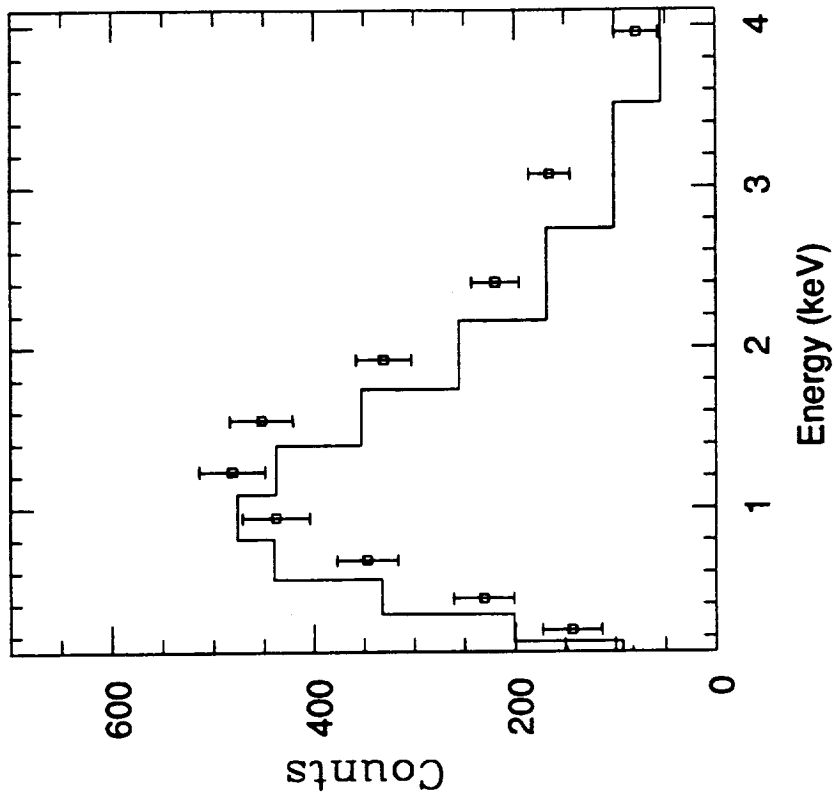
Counts
0
200
400
600
Energy (keV)
1
2
3
4

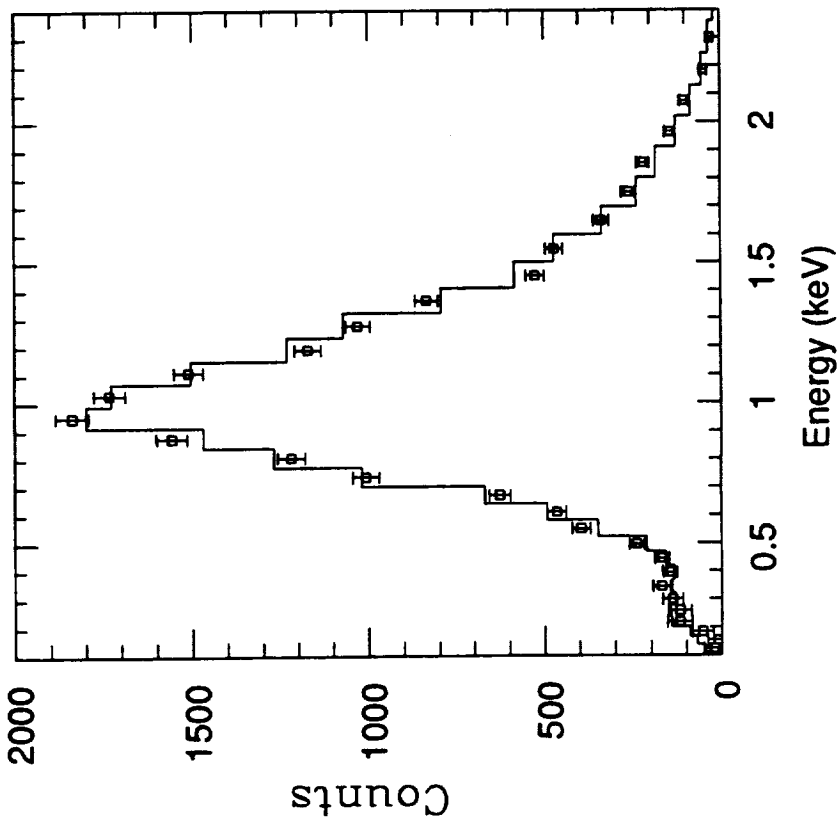
Counts
0
500
1000
1500
2000
Energy (keV)
0.5
1
1.5
2

Fig. 12

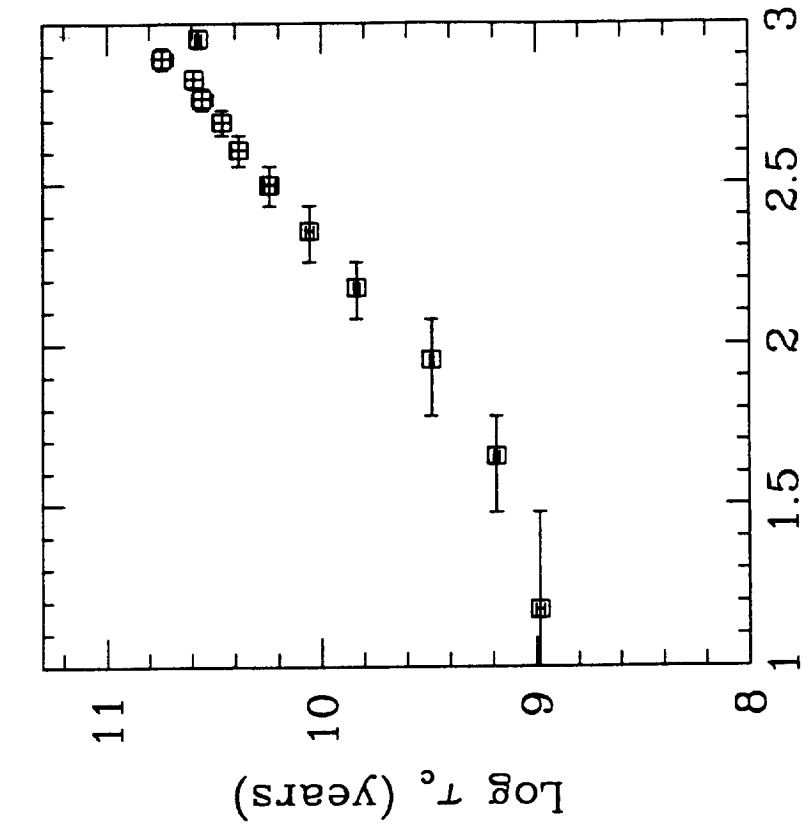
Log τ_c (years)
11
10
9
8
1
1.5
2
2.5
3

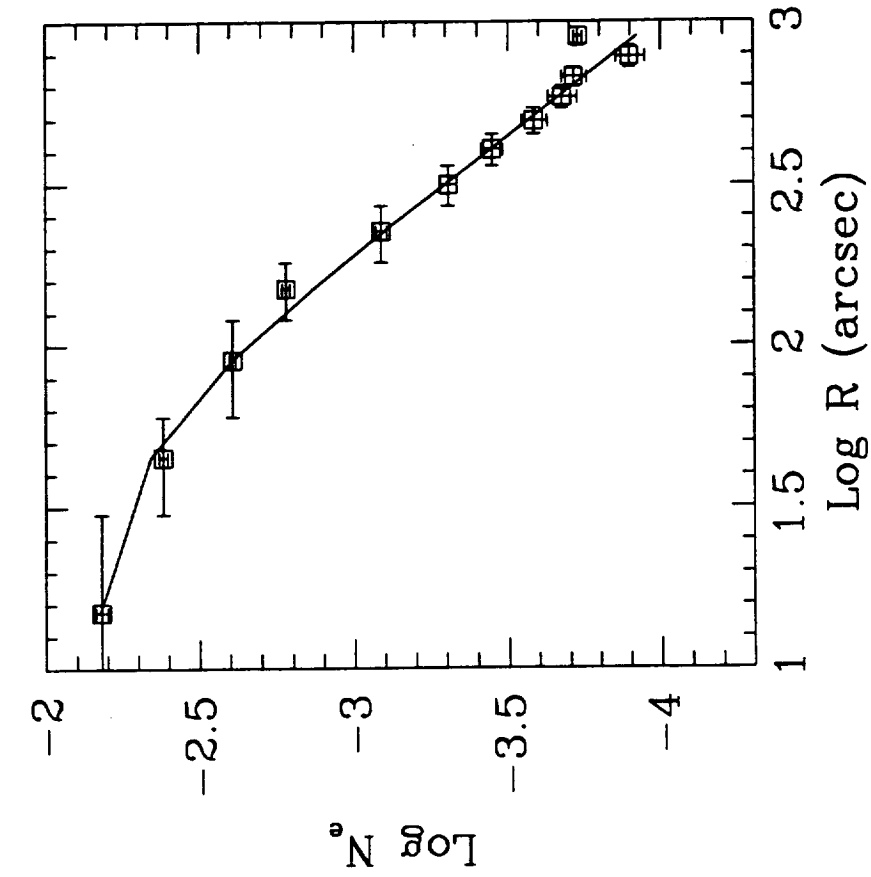
Log N_e
−2
−2.5
−3
−3.5
−4
1
1.5
2
2.5
3
Log R (arcsec)

Fig. 13

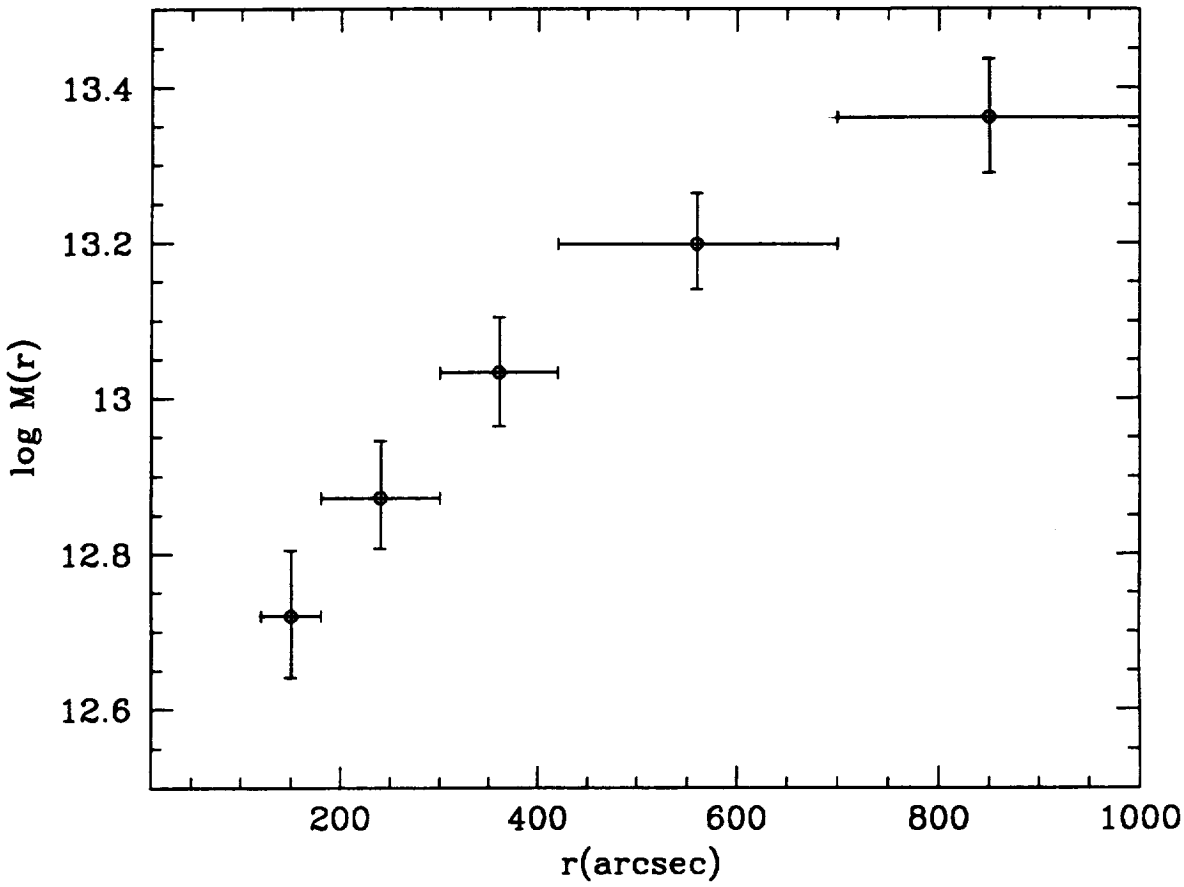

Fig. 14

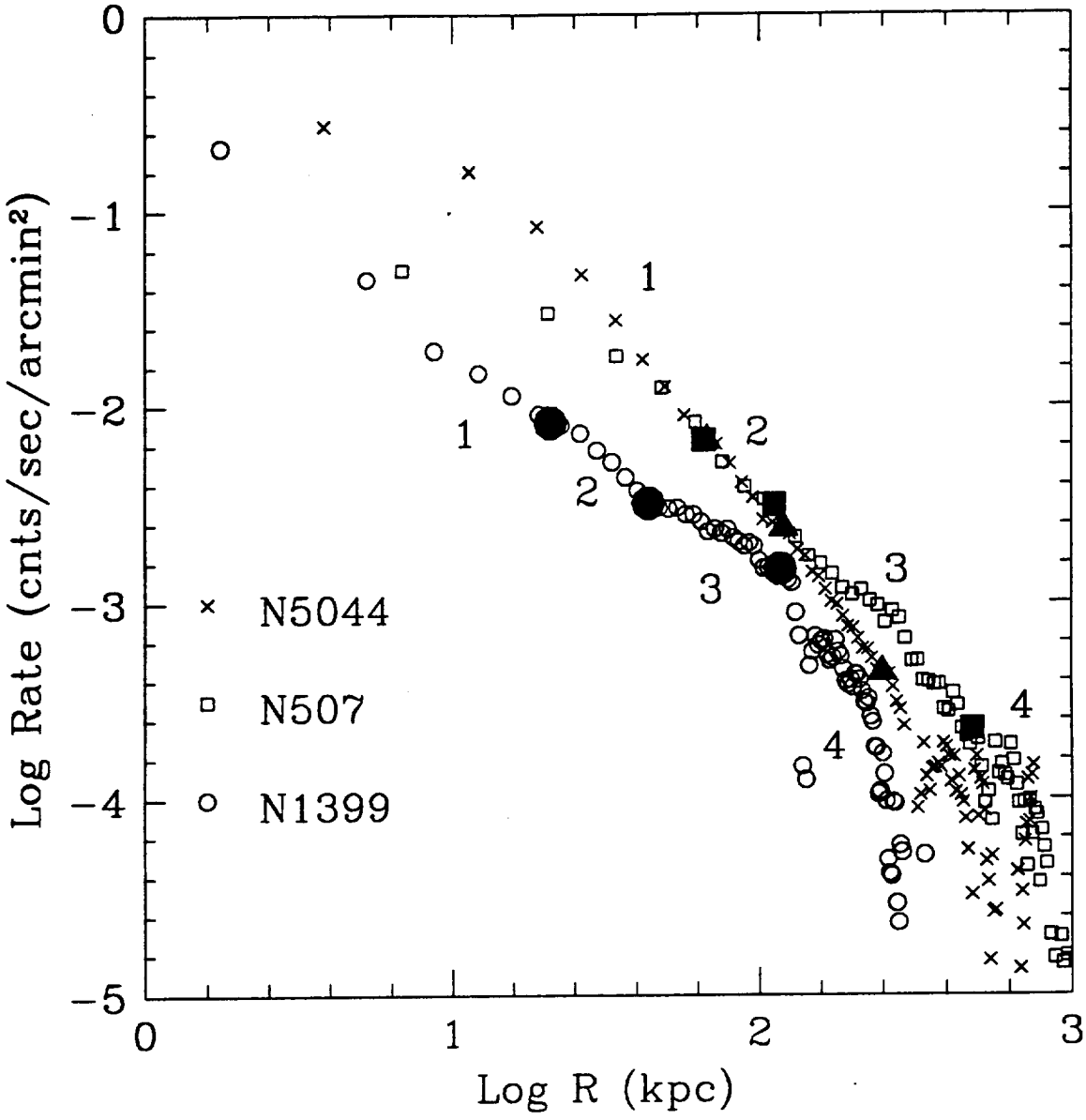
Log Rate (cnts/sec/arcmin²)
Log R (kpc)
N5044
N507
N1399
0
−1
−2
−3
−4
−5
0
1
2
3
1
2
3
4
1
2
3
4

Fig. 15

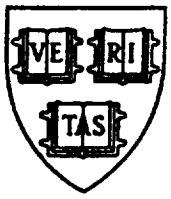

Harvard-Smithsonian Center for Astrophysics

Preprint Series

No. 4026
(Received January 26, 1995)

ROSAT PSPC OBSERVATIONS OF TWO DYNAMICALLY YOUNG ELLIPTICAL GALAXIES: NGC 4125 AND NGC 3610

G. Fabbiano
Harvard-Smithsonian Center for Astrophysics

and

François Schweizer
Department of Terrestrial Magnetism, Carnegie Institution of Washington

To appear in
The Astrophysical Journal
July 10, 1995

HARVARD COLLEGE OBSERVATORY SMITHSONIAN ASTROPHYSICAL OBSERVATORY
60 Garden Street, Cambridge, Massachusetts 02138

Center for Astrophysics
Preprint Series No. 4026

ROSAT PSPC Observations of two Dynamically Young Elliptical Galaxies: NGC 4125 and NGC 3610

G. Fabbiano
Harvard-Smithsonian Center for Astrophysics
60 Garden St., Cambridge, MA 02138

and

François Schweizer
Department of Terrestrial Magnetism, Carnegie Institution of Washington
5241 Broad Branch Road, N.W., Washington, DC 20015-1305

TO APPEAR IN THE ASTROPHYSICAL JOURNAL
JULY 10, 1995

Abstract

We present the results of ROSAT PSPC X-ray observations of NGC 4125 and NGC 3610. These two galaxies are among the best representatives of a newly recognized class of elliptical galaxies that may be the product of recent mergers. NGC 4125 shows two plumes or disks crossing at right angles; NGC 3610 has the richest fine structure of all ellipticals catalogued by Schweizer and Seitzer. Our X-ray observations show that these galaxies do not retain large gaseous halos, contrary to the suggested link between merging and X-ray brightness. Their X-ray luminosities (0.1 –2 keV) are in the range $10^{40-41} ergs\ s^{-1}$, low compared with those of hot-gas-rich ellipticals. The X-ray to optical ratio of NGC 3610 is in the range of those of X-ray faint ellipticals, consistent with the value found for the bulge of M31, where the X-ray emission is dominated by low-mass binaries; its X-ray spectrum is also comparable with those of X-ray faint ellipticals, presenting significant very soft excess emission. The X-ray to optical ratio of NGC 4125 is larger, and might suggest the presence of some hot ISM. This suggestion is supported by the spectrum of NGC 4125, which shows evidence of Fe L emission. This spectrum can be fitted with either a low abundance single temperature Raymond model, or with a two-temperature model with solar abundances. Further work is needed to firmly resolve the question of gaseous versus stellar X-ray emission in NGC 4125.

1. Introduction

Recent work has focused on a newly recognized class of elliptical galaxies that either may be the products of recent mergers or may have accreted major companions. These ellipticals exhibit much 'fine structure' in their images, including ripples or shells, plumes of luminous matter, boxy isophotes, and X-shaped structures. A catalog of such and other types of fine structure in 74 early-type galaxies has been assembled by Schweizer & Seitzer (1995). Correlations between the fine-structure index Σ and optical line strengths (Schweizer et al. 1990) and UBV colors (Schweizer & Seitzer 1992) suggest that ellipticals with much fine structure may be relatively young ($\leq$7 Gyr) merger remnants. Besides morphological signatures characteristic of mergers, these ellipticals feature also enhanced Hβ absorption and systematically bluer UBV colors that suggest the presence of intermediate-age stellar populations stemming from aging starbursts. Clearly, such dynamically young ellipticals are promising objects for studies of galaxy evolution.

We report here the results of observations of two of these ellipticals, NGC 4125 (E6) and NGC 3610 (E5), with the Position Sensitive Proportional Counters (PSPC, see Pfeffermann et al. 1987) of the Roentgensatellit (ROSAT, see Trümper 1983). These two ellipticals are among the best representatives of their class because their rich fine structure points toward *major* mergers of disk galaxies in their recent past as opposed to mere accretion of dwarf companions. NGC 4125 shows two plumes or disks crossing each other at nearly right angles (Bertola 1972, 1981; Schweizer & Seitzer 1995); and NGC 3610 has the richest fine structure of all catalogued ellipticals (Seitzer & Schweizer 1990). Both galaxies have enhanced Hβ absorption, unusually weak Mg and CN features, and blue $U-B$ and $B-V$ color indices when compared to the mean indices computed from color–magnitude relations. Based on these color indices, Schweizer & Seitzer (1992, hereafter SS92) estimated merger ages of 3–7 Gyr via a two-burst model of population evolution.

A central question is the fate of the gas in disk galaxies that collide and merge. Observations of infrared-luminous mergers (e.g., Young et al. 1984; Joseph & Wright 1985; Sanders et al. 1988; Solomon, Downes, & Radford 1992) and $\sim$1 Gyr old merger remnants (Schweizer 1990), and N-body simulations of disk–disk mergers that include gas hydrodynamics (Hernquist & Barnes 1991; Barnes 1994; Mihos & Hernquist 1994; see also Hibbard & Mihos 1995) all suggest that part of the gas falls to the center where it forms a dense molecular disk. Such dense, central gas disks can rotate at any angle and are the likely precursors of oddly rotating cores in ellipticals (Wang, Schweizer, & Scoville 1992). On the other hand, new VLA observations of the merger remnant NGC 7252 suggest that neutral hydrogen survives mainly in the outskirts and tails of this remnant, leaving a large intermediate region between the central molecular-gas disk and the outskirts free of cold gas (Hibbard et al. 1994). Several questions arise: What happens to the gas at intermediate radii (3–15 kpc in NGC 7252) ? Is it being heated to low X-ray temperatures by cloud–cloud collisions, or is it being heated even

further by supernovae and blown out by galactic winds? In other words, is this ISM to be found in an X-ray emitting phase, as observed in many other early-type galaxies (see review by Fabbiano 1989), or has it already escaped the galactic potential well?

Models of merging galaxies (e.g., Barnes 1992, 1994; Mihos & Hernquist 1994) suggest that random motions during mergers are of the order of 300 km s^{-1}. Therefore, the ISM of the parent galaxies will experience cloud–cloud collisions with similar velocities, which will shock-heat the gas to temperatures of *a few* million degrees. These temperatures are, of course, similar to those derived from random stellar motions in giant ellipticals. If this simple gravitational scenario holds, the potential of the remnant galaxy should be able to retain the hot ISM. However, there is the distinct possibility that supernovae of the induced starburst will heat the ISM further (e.g., Ciotti et al. 1991; David, Forman & Jones 1991) to the point where most of it escapes from the system. In summary, the status of the hot ISM in merger remnants is likely to depend on many parameters, including the amounts of gas present in the parent galaxies, the SN rates resulting from the induced starbursts, and the depth of the gravitational potential of the remnants. Depending on the interplay of these parameters, dynamically young ellipticals may be among the most X-ray luminous ellipticals, or among the faintest ones.

In the following, we first present the ROSAT observations of NGC 4125 and NGC 3610 and then discuss their implications for our understanding of the gas phases in dynamically young ellipticals. As we shall describe, our observations exclude the presence of large X-ray luminous halos of hot gas in both galaxies and suggest that these two ellipticals may have X-ray properties similar to those of other X-ray faint, early-type galaxies (Kim, Fabbiano & Trinchieri 1992a and b; Fabbiano, Kim, & Trinchieri 1994; Pellegrini and Fabbiano 1994; Pellegrini 1994; Schweizer, Fabbiano, & Seitzer 1995).

2. Observations, Data Analysis, and Results

Table 1 summarizes the characteristics of NGC 3610 and NGC 4125 and gives the ROSAT PSPC observation log. The data were analyzed using the *xray* package of IRAF, developed at SAO for the analysis of X-ray data, and the spectral-fitting package XSPEC provided by the NASA archival center for high-energy astrophysics (HEASARC). The procedures followed are very similar to those described by Fabbiano et al. (1994). A difference here is that both galaxies were observed during several distinct time periods. For the analysis we merged the individual observations of each galaxy, using tools in the *xray* package. To make sure that uncertainties in the nominal field centers would not affect the quality of the merged images, we used the centroids of various sources in the field as reference points.

2.1 Background Subtraction and Extraction of Source Counts

To extract counts for flux determination and spectral analysis, and to study

the radial behaviour of the X-ray surface brightness, the field background must be subtracted from the images. Following Fabbiano et al. (1994), we used the broad-band images provided by the ROSAT pipeline processing. First, we subtracted all strong point sources detected in the fields by excluding circular areas centered on these sources. The sources were chosen both by inspection of the source list resulting from the pipeline processing of the data and by visual inspection of the images. This done, radial profiles of the two fields were obtained by binning the data within circular annuli centered on the peaks of galaxy emission (which lie at the centers of the fields). These radial profiles were then compared with similarly binned profiles of the field background and of the exposure maps. Both background and exposure maps are included in the ROSAT PSPC processed data package. The field-background and exposure-map profiles closely follow each other, implying that there is no extended residual emission in the field (for a more detailed discussion, see Trinchieri et al. 1994). Figure 1 shows the case of NGC 4125. Both for it and for NGC 3610 it was evident that the radial profiles flatten to a constant level at radii where mirror vignetting effects are still minor. Because of the relatively small source extents, we derived the background locally by using source-free annuli surrounding the galaxy emission.

To increase the statistical significance of our detections, we inspected the count distributions (see §2.4) and extracted source counts from the energy band in which the source appears to be above the noise. Table 2 summarizes the parameters used for count extraction and the results. This procedure yielded 891.8±43.3 net counts for NGC 4125 and 109.2±21.6 net counts for NGC 3610.

To calculate count rates, we also need to estimate the average exposure times in the regions of interest. Since each of our sources lies at the center of its field, where the average exposure is relatively uniform, we used the live-time estimates provided by the standard processing. These exposure times are typically within a few percent (±2%) of times derived from the exposure maps and are given in Table 2.

2.2 Contour Plots

Figure 2 shows contour plots of the central parts of the two PSPC images containing the target galaxies. In both cases, data from the 'source extraction' energy bands were used (Table 2). The data were then binned in 5" pixels and smoothed with a 20" Gaussian, comparable in width with the PSPC Point Response Function (PRF). As Figure 2a shows, extended X-ray emission is clearly detected in NGC 4125. Comparison between the isophotes of a point-like serendipitous source present in the field — near the northern edge of the portion of the field shown in the figure — and those of NGC 4125 demonstrates qualitatively that the latter is not point-like. In the NGC 3610 field there are no nearby strong point sources available for comparison, and the detection is much weaker. In both cases the X-ray isophotes lie well within the optical extent of the galaxies, indicated by ellipses marking the $B = 26.5$ mag arcsec^{-2} isophotes. The X-ray surface-brightness distribution of NGC 4125 suggests

an East-West elongation, in accord with the orientation of the optical isophotes. Similarly, the X-ray isophotes of NGC 3610 may be elongated in the direction of P.A. $\approx 135°$, consistent with the orientation of the optical inner disk. However, in this case we need a statistically more significant X-ray image before concluding that this elongation is real.

In both galaxies the general appearance of the X-ray contour map does not change significantly if only Pulse-Invariant (PI) spectral channels $\geq$26 are used. This choice of PI channels avoids the "ghost image" problem, which tends to spread the detection of soft X-ray events between adjacent PSPC wires (Hasinger et al. 1992). However, in the case of NGC 3610 exclusion of the first 25 channels lowers the signal-to-noise ratio of the image considerably.

2.3 Surface-Brightness Profile of NGC 4125

We computed surface-brightness profiles of NGC 4125 by binning the data in concentric, 15" and 30" wide annuli centered on the peak of the surface brightness distribution. The location of this peak was determined with the aid of isointensity contour maps (see Fig. 2 and Table 2), and the background was subtracted as described above. Because of the "ghost image" problem described above, we used only data from PI, gain-corrected spectral channels 26–140 (0.27–1.41 keV).

Figure 3 displays the resulting surface-brightness profile. Also plotted is the instrumental PRF (Hasinger et al. 1992) appropriate for a 0.7 keV spectrum (see below) and binned in concentric, 15" wide annuli as well. Obviously, the X-ray emission of NGC 4125 is extended. From the observed brightness profile and after correcting for the width of the PRF in quadrature, we estimate the intrinsic core radius (= half width at half maximum) of this emission to be $r_c = 19" \pm 3"$ (3.5 ± 0.6 kpc).

In analogy with what was done for X-ray bright ellipticals (Fabbiano 1989 and refs. therein; Kim & Fabbiano 1995), we parameterized the X-ray surface brightness of NGC 4125 by fitting it to a model of the form

$$\Sigma_X(r) = \Sigma_X(0) \times [1 + (r/a_X)^2]^{-3\beta+1/2}$$

convolved with the PSPC PRF. We obtain a best-fit $\chi^2 = 5.3$ for 8 degrees of freedom, a best-fit core radius $a_X = 15.5"$ (11"–21" at 90% confidence for two interesting parameters), and a best-fit $\beta = 0.53$ (0.49–0.60 at 90% confidence). The latter exponent corresponds to an X-ray surface brightness decreasing as $r^{-(1.9-2.6)}$ and lies within the range of exponents determined for X-ray bright E and S0 galaxies with the *Einstein Observatory* (Fabbiano 1989).

For comparison, Figure 3 also shows the optical surface-brightness profile of NGC 4125. This profile was derived from an image in the R passband obtained

with the KPNO 0.9 m telescope and CCD camera (Schweizer & Seitzer 1995). To facilitate intercomparison with the X-ray profile, we convolved the R image with the PSPC PRF and extracted the brightness profile from concentric apertures identical to those used for the ROSAT data. As the figure shows, the X-ray and optical profiles are remarkably similar.

The restricted energy range (0.27–1.41 keV) and limited count statistics do not allow us to explore the energy dependence of the profile. However, within the quoted energy range we would not expect any significant variations even in a multi-component spectral model as described below, because both components would be represented equally throughout the spectral range.

NGC 3610 was detected with far fewer counts, a good fraction of which occur in the lowest spectral channels ($\leq$25). With these data we cannot derive a meaningful radial profile.

2.4 Spectral Analysis

Global counts for spectral analysis were extracted from the regions defined in Table 2 above. We fitted the resulting spectra with different models using both the IRAF/*xray* spectral routines and XSPEC. The spectral data extraction program in *xray* rebins the counts from the original 256 PI bins into 34 bins, covering the energy range 0.07–2.48 keV. These spectra are then compared via χ^2 fits to model spectra that have been convolved with the instrument and mirror response functions. Because the software uses a Gaussian approximation to calculate statistical uncertainties, we excluded from the fits bins with fewer than $\sim$10 counts at the upper end of the ROSAT spectral range (see Table 2). We also excluded the two lowest bins because the response function of the PSPC is less well determined in this spectral range (Hasinger et al. 1992). In all cases, the counts in the excluded bins turn out to be consistent with our best-fit predictions.

A combination of Raymond models (Raymond & Smith 1977), which include both continuum and line contributions from an optically thin, metal-enriched thermal plasma, and simple Bremsstrahlung emission models were fitted to the data. (See Fabbiano et al. 1994 for a discussion of the relative merits of these models and of the intrinsic uncertainties of ROSAT PSPC spectral results.) Line-of-sight absorption was calculated using the Morrison-McCammon (1983) cross sections. We used the January 1993 spectral matrix to derive these values. Using the March 1992 response matrix instead would not affect our results (within the quoted error range) because the uncertainties are dominated by count statistics.

2.4.1 NGC 4125

Table 3 summarizes the results of our spectral analysis for NGC 4125. In all fits we used the line-of-sight N_H (Stark et al. 1992) as a fixed value for the absorption parameter. Figure 4a shows the observed PSPC spectral count distribution

for NGC 4125 together with the best-fit Bremsstrahlung model. This distribution is reminiscent of those of the X-ray faint galaxies NGC 4365 and NGC 4382 (Fabbiano et al. 1994). However, contrary to the results for NGC 4365 the Bremsstrahlung model here does not give an acceptable fit to the data. (In the case of NGC 4382, the data had less statistical significance and the results were less constrained.) Most of the large residuals are concentrated in the region just below 1 keV, where the Fe L lines would occur. The Bremsstrahlung model gives an acceptable χ^2 only if N_H is free to vary, in which case the best-fit N_H is higher than the line-of-sight value, thus reducing the $\sim$0.7 keV excess in the emitted spectrum.

A single-temperature Raymond model is also unacceptable, unless the metal abundance is relatively low but not zero, which would be the Bremsstrahlung approximation. This can be seen from the confidence contours shown in Figure 5a and from the parameters given in Table 3.

Two-temperature Raymond models with cosmic abundance and Raymond + Bremsstrahlung models both give good fits. The data and best-fit two-temperature Raymond model are shown in Figure 4b. The corresponding confidence contours for the temperatures are shown in Figure 5b and those for a Raymond + Bremsstrahlung model in Figure 5c. In the two-temperature Raymond model, the two components have best-fit values of kT $\approx$ 0.16 keV and 0.6 keV, respectively. The Raymond + Bremsstrahlung model yields similar temperatures (kT $\approx$ 0.3–0.4 keV) for the two components. This last model is equivalent to adding an extra continuum component (i.e., lowering the allowed line contribution, as in the case of the low-abundance fit).

2.4.2 NGC 3610

NGC 3610 was detected with too few photons to attempt a spectral analysis comparable to that of NGC 4125. However, the distribution of spectral counts again suggests a soft spectrum, possibly consistent with that of NGC 4125. We rebinned the spectral data (see Table 2) into six bins to increase the signal-to-noise ratio of each data point. Using the line-of-sight N_H given in Table 1 as a fixed parameter, these six data points were fitted with a Raymond spectrum for cosmic abundance. The best-fit temperature and 90% confidence range — for one interesting parameter — are kT = 0.18 keV and 0.13–0.24 keV, respectively, with a best-fit $\chi^2 = 1.73$ for 4 degrees of freedom. The data and best-fit model are shown in Figure 6. Given the poor count statistics and limited spectral range of the data, it does not seem meaningful to discuss spectral models any further or to comment on possible multiple components.

2.5 Fluxes and Luminosities

Table 4 gives fluxes and luminosities in the 0.1–2.0 keV range for both galaxies. For NGC 3610, the flux is derived from the best-fit Raymond model with solar abundance. For NGC 4125, fluxes are presented as derived from three different

models: the best-fit ~8% abundance, single-temperature Raymond model, the cosmic-abundance Raymond + Bremsstrahlung model, and the cosmic-abundance, two-temperature Raymond model. All three models yield consistent values of the flux in the range 7.7–8.1$\times 10^{-13}$ergs s^{-1} cm^{-2} for the entire detected emission. In the two-component models, the flux is almost equally divided between the two components. Although the uncertainty in the 0.1–2.0 keV flux introduced by different choices of best-fit models is small, the uncertainty in the relative contributions of each of the two spectral components is large. An assessment of this uncertainty can be made by using the errors of the relative normalizations of the two components (see Table 3).

The corresponding X-ray luminosities of NGC 3610 and NGC 4125 lie in the range 10^{40-41}ergs s^{-1} (for $H_0 = 50$ km s^{-1} Mpc^{-1}), comparable with those of X-ray faint ellipticals. The X-ray to optical luminosity ratios, calculated as in Kim, Fabbiano, & Trinchieri (1992b), put NGC 3610 in their lowest L_X/L_B bin (Group 1) and NGC 4125 at the boundary between Group 1 and Group 2.

3. Discussion

Figure 7 shows the positions of NGC 3610 and NGC 4125 in the $L_X - L_B$ diagram of E and S0 galaxies (taken from Fabbiano, Kim & Trinchieri 1992). The present two galaxies are clearly X-ray faint. They lie in the region of the diagram where the X-ray emission of early-type galaxies can be explained by the presence of a population of X-ray sources similar to those in spiral bulges and does not require the presence of extensive, hot, gaseous halos (Trinchieri & Fabbiano 1985; Fabbiano, Gioia & Trinchieri 1989; Eskridge, Fabbiano & Kim 1995).

The $L_X - L_B$ diagram has been used as a tool for understanding the properties of gaseous halos in early-type galaxies (see review by Fabbiano 1989). The most striking property of this diagram, apart from the rather steep correlation between X-ray and optical luminosities, is the large range of X-ray luminosity at any given optical luminosity: X-ray to optical flux ratios may range from the low values observed in the X-ray-binary dominated bulge of M31 and in spiral galaxies to the ~50–100 times higher values observed in galaxies rich in hot gas. The source of this large scatter is not clear. Models have been developed in which the X-ray faint galaxies are stripped of their ISM by galactic winds (e.g., Ciotti et al 1991). Alternatively, the hot ISM could be removed by (i) ram-pressure stripping within an intra-cluster or intra-group medium, (ii) by ram-pressure stripping during interactions with neighboring galaxies, or (iii) by galactic winds following mergers (White & Sarazin 1991).

Our ROSAT measurements of the X-ray fluxes of NGC 3610 and NGC 4125 cannot adjudicate unambiguously between these various possibilities. Although NGC 3610 and NGC 4125 appear relatively isolated, each being separated by more than 10 diameters from any nearest neighbor, they both are members of the very extended, rich group GH 94 (Geller & Huchra 1983). We conclude that any ram-

pressure stripping through interactions with neighbor galaxies during the past 1 Gyr seems unlikely. A similar conclusion has been reached by Pellegrini (1994) for the X-ray faint S0 galaxy NGC 5866. However, two possibilities remain: ram-pressure stripping through some intra-group medium and gas removal through recent mergers. Since we have no information about the intra-group medium of GH 94, we cannot assess the likelihood of its having caused ram-pressure stripping. On the other hand, the rich fine structures and bluish colors of both NGC 3610 and NGC 4125 strongly suggest major mergers during the past 3–7 Gyr (SS92), making gas removal through winds induced by starbursts a likely explanation for the paucity of gas.

Using *Einstein* IPC data, Kim, Fabbiano & Trinchieri (1992b) found a dependence of the average spectral properties of E and S0 galaxies on their position in the $L_X - L_B$ plane. They divided this plane into four distinct regions, as shown in Figure 7. While the average X-ray spectra of X-ray bright galaxies (Groups 4 and 3, which have X-ray to optical ratios well in excess of those expected from a population of 'bulge' X-ray sources; see Trinchieri & Fabbiano 1985, Canizares, Fabbiano & Trinchieri 1987) could be fitted with $\sim$1 keV Raymond models, the average X-ray emission temperature was found to be higher in Group 2 galaxies. In these galaxies a hard component similar to that present in spiral galaxies and bulges (Fabbiano, Trinchieri & Van Speybroeck 1987) dominates the emission. These results all support the notion that in X-ray faint galaxies the hot ISM is relatively depleted.

However, a surprising result was the discovery of very soft X-ray emission in the group of galaxies with the lowest values of L_X/L_B (Group 1). Recent ROSAT PSPC observations of the two Group 1 galaxies NGC 4365 and NGC 4382 confirm these earlier results (Fabbiano, Kim & Trinchieri 1994; see also Fig. 7 here). Their spectra cannot be fitted with a single-temperature Raymond model with solar abundances. To obtain acceptable fits either very low (near zero) abundances or two-component models are needed. Very low abundances appear implausible on astrophysical grounds if the emission is of gaseous origin: the Bremsstrahlung model results in a best fit kT=0.7 keV; this result could be understood only by postulating a new class of X-ray emitting sources (see Fabbiano et al. 1994). Two-component models yield a very soft component of kT $\sim$ 0.2 keV and a hard component with kT $>$ 1 keV. While the hard component could easily be justified by the presence of a population of bulge-type X-ray sources, the origin of the soft component is more debatable and could be explained either by the existence of soft stellar sources or, in part, by a hot ISM (Pellegrini & Fabbiano 1994).

Of the two galaxies studied in this paper, NGC 3610 belongs to Group 1. Not much can be said about its PSPC spectrum, except that it is very soft, in general agreement with the PSPC spectra of the X-ray faint Group 1 galaxies discussed above (see also Pellegrini 1994). As stated already, these PSPC spectra differ significantly from those of X-ray bright galaxies, which tend to peak near 1 keV (Fabbiano et al. 1994; Trinchieri et al. 1994; Kim & Fabbiano 1995). Note that the $\sim$1 Gyr old

merger remnant NGC 7252 is also relatively X-ray faint (Hibbard et al. 1994), with an L_X/L_B ratio placing it in Group 1 as well.

The other galaxy, NGC 4125, falls near the boundary between Groups 1 and 2 as defined by Kim et al. (1992b). Its PSPC spectrum is also soft, but — in contrast with those of the other few X-ray-faint E and S0 galaxies studied with the PSPC so far — it cannot be fitted with a simple Bremsstrahlung model. As shown in Table 3 and Figure 4, a line contribution near 1 keV is needed to fit this spectrum, suggesting the presence of metal enriched hot gas. If the emission is isothermal, the metal abundance of the emitting medium would be less than ~15% of the cosmic value. However, significantly higher metal abundances would be allowed if several emission components with different temperatures coexist. In the two-component model fits, however, the temperature of the harder component is lower than in NGC 4365 and NGC 4382 (Fabbiano et al. 1994). This result suggests that this harder emission (if present) is not dominated by the output of a M31-bulge type, X-ray binary population. When fitted with a Bremsstrahlung model, such a population would yield a kT of a few keV (Fabbiano, Trinchieri & Van Speybroeck 1987).

Instead, the PSPC spectrum of NGC 4125 suggests the possible presence of some hot ISM in this galaxy. The fact that the X-ray and optical surface-brightness distributions trace each other (Fig. 3), as would be expected if the X-ray emission were mostly of stellar origin, does not necessarily argue against a sizeable gaseous component. A similar behaviour was found in a number of X-ray bright, gas-dominated galaxies with *Einstein* (Trinchieri, Fabbiano & Canizares 1986; Fabbiano 1989).

Clearly, further observational and theoretical work is needed to firmly resolve the question of gaseous vs. stellar X-ray emission in NGC 4125. Observationally, a higher-resolution spectrum covering a longer energy baseline, such as ASCA can provide, will let us firmly establish the presence or absence of gaseous emission and will give us a better handle for identifying different spectral components. Theoretically, models need to be explored that can reproduce in a self-consistent way the observed spectra and surface-brightness profiles. In the previously studied case of NGC 4365, the data were compared with the results of hydrodynamical simulations based on the D'Ercole et al. (1989) and Ciotti et al. (1991) code (Pellegrini & Fabbiano 1994). This work suggested a model for NGC 4365 with a ~0.6 keV hot ISM, which was consistent — given the quality of the data — with both the PSPC spectrum and the radial surface-brightness profile. This model, however, predicted an X-ray surface-brightness distribution intrinsically more extended than the stellar one. While in NGC 4125 the X-ray surface-brightness distribution does not appear more extended than the optical distribution, higher-resolution X-ray observations will be needed to carry out a proper comparison in the inner 20"–30", where the present X-ray data are limited by the resolution of the PSPC.

4. Conclusions

ROSAT PSPC observations of the dynamically young ellipticals NGC 3610 and NGC 4125 have shown that these galaxies are X-ray faint compared to other ellipticals of similar optical luminosity. This result suggests that NGC 3610 and NGC 4125 are relatively depleted of hot ISM. Since the optical properties of these ellipticals suggest that they are the remnants of relatively recent mergers (SS92), winds induced by starbursts may temporarily have depleted these remnants of their hot gas. Such winds have, in fact, been detected both optically and via X-rays in nearby starbursting galaxies (e.g., in M82 and NGC 253: McCarthy et al. 1987; Fabbiano 1988).

The L_X/L_B ratio of NGC 3610 is particularly low (Table 4), consistent with the ratios of star-dominated systems (e.g., bulges of spiral galaxies). This ratio is also similar to that of the merger remnant NGC 7252 (Hibbard et al. 1994). The L_X/L_B ratio of NGC 4125 is 3–4 times larger, although still lower than the ratios observed in halo-dominated X-ray-bright ellipticals. The spectrum of NGC 4125 suggests the presence of some hot ISM. We cannot tell whether this ISM stems from stellar ejecta due to normal stellar evolution during the post-merger phase, or whether it stems from merger detritus falling into the remnant. Numerical models (e.g., Barnes 1992; Hibbard & Mihos 1995) show that material ejected into the tails remains largely bound and will fall back over several Gyr. If this material shock heats as it falls into the potential well, it may act to slowly increase the amount of hot gas in the galaxy. We note that in NGC 1316, another post-merger early-type galaxy (Schweizer 1980), there is also evidence both from imaging and from spectra for the presence of some hot ISM (Kim, Fabbiano & Mackie 1995).

Further work is needed to confirm our conclusion that winds may temporarily have depleted NGC 3610 and NGC 4125 of hot gas, and to explore the relation between galactic mergers and X-ray emission in general. Although our results suggest gas depletion in relatively recent merger remnants, a correlation between X-ray luminosity and central boxiness in elliptical galaxies (Bender et al. 1989; Eskridge, Fabbiano & Kim 1995) has long been interpreted as suggesting a connection between the presence of a large amount of hot ISM and past mergers. Thus, our conclusion appears to be in puzzling contradiction to these earlier results. One solution to this perhaps only apparent contradiction might be that, if galactic winds subside after the starburst, aging merger remnants may be slowly replenishing their hot gas through mass loss from evolving stars and/or gas returning from previously ejected tails. To further explore these possibilities, we need to assemble and study a larger sample of early-type galaxies and to compare their X-ray properties with age estimates for past merger events. This will be the subject of future work.

ACKNOWLEDGEMENTS

We thank Dong-Woo Kim and Glen Mackie for their help and useful discussions. We also thank the referee, Chris Mihos, for interesting and helpful comments. This work was supported by NASA grants NAG 5-1937 (ROSAT), NAG 5-2281 (ROSAT), and NAGW-2681 (LTSA), and by NASA contract NAS8-39073 (AXAF Science Center).

REFERENCES

Barnes, J.E. 1992, ApJ, 393, 484

Barnes, J.E. 1994, in The Formation of Galaxies, ed. C. Muñoz–Tuñón (Cambridge: Cambridge Univ. Press), in press

Bender, R., Surma, P., Döbereiner, S., Möllenhof, C., & Madejski, R. 1989, AA, 217, 35

Bertola, F. 1972, Communicazioni dell'Osservatorio di Padova, No. 98, 199

Bertola, F. 1981, in Structure and Evolution of Normal Galaxies, ed. S.M. Fall & D. Lynden-Bell (Cambridge: Cambridge Univ. Press), 13

Canizares, C. R., Fabbiano, G. & Trinchieri, G. 1987, ApJ, 312, 503

Ciotti, L., D'Ercole, A., Pellegrini, S., & Renzini, A. 1991, ApJ, 376, 380

David, L. P., Forman, W., & Jones, C. 1991, ApJ, 369, 121

D'Ercole, A., Ciotti, L., Pellegrini, S., & Renzini, A. 1989, ApJ, 341, L9.

Eskridge, P., Fabbiano, G., & Kim, D.-W. 1995, ApJS , in press.

Fabbiano, G. 1988, ApJ, 330, 672.

Fabbiano, G. 1989, ARA&A, 27, 87

Fabbiano, G., Gioia, I. M., & Trinchieri, G. 1989, ApJ, 347, 127

Fabbiano, G., Kim, D.-W. & Trinchieri, G. 1992, ApJSup, 80, 531

Fabbiano, G., Kim, D.-W. & Trinchieri, G. 1994, ApJ, 429, 94

Fabbiano, G., Trinchieri, G., & Van Speybroeck, L. 1987, ApJ, 316, 127

Geller, M.J., & Huchra, J.P. 1983, ApJS, 52, 61

Joseph, R.D., & Wright, G.S. 1985, MNRAS, 214, 87

Hasinger, G., Turner, J. T., George, I. A., & Boese, G. 1992, OGIP Calibration Memo CAL/ROS/92-001, NASA-GSFC

Hernquist, L., & Barnes, J.E. 1991, Nature, 354, 210

Hibbard, J.E., Guhathakurta, P., van Gorkom, J.H., & Schweizer, F. 1994, AJ, 107, 67

Hibbard, J.E., & Mihos, J.C. 1995, preprint

Kim, D.-W., & Fabbiano, G. 1995, ApJ, in press

Kim, D.-W., Fabbiano, G., & Trinchieri, G. 1992a, ApJSup, 80, 645

Kim, D.-W., Fabbiano, G., & Trinchieri, G. 1992b, ApJ, 393, 134

Kim, D.-W., Fabbiano, G., & Mackie, G. 1995, in preparation

McCarthy, P.J., Heckman, T., & van Breugel, W. 1987, AJ, 93, 264

Mihos, J.C., & Hernquist, L. 1994, ApJ, in press

Morrison, R., & McCammon, D. A. 1983, ApJ, 270, 119

Pellegrini, S. 1994, Astro. Ap., in press

Pellegrini, S. & Fabbiano, G. 1994, ApJ, 429, 105

Pfeffermann, E. et al.1987, Proc. SPIE, 733, 519

Raymond, J. C., & Smith, B. W. 1977, ApJSup, 35, 419

Renzini, A., Ciotti, L., D'Ercole, A., & Pellegrini, S. 1993, ApJ, submitted

Sanders, D.B., Scoville, N.Z., Sargent, A.I., & Soifer, B.T. 1988, ApJ, 324, L55

Schweizer, F. 1980, ApJ, 237, 303

Schweizer, F. 1990, in Dynamics and Interactions of Galaxies, ed. R. Wielen (Heidelberg: Springer), p. 60
Schweizer, F., Fabbiano, G., & Seitzer, P. 1995, ApJL, in preparation
Schweizer, F., Seitzer, P., Faber, S.M., Burstein, D., Dalle Ore, C.M., & Gonzalez, J.J. 1990, ApJ, 364, L33
Schweizer, F., & Seitzer, P. 1992, AJ, 104, 1039 (SS92)
Schweizer, F., & Seitzer, P. 1995, in preparation
Seitzer, P., & Schweizer, F. 1990, in Dynamics and Interactions of Galaxies, ed. R. Wielen (Heidelberg: Springer), p. 270
Solomon, P.M., Downes, D., & Radford, S.J.E. 1992, ApJ, 387, L55
Trinchieri, G. & Fabbiano, G. 1985, ApJ, 296, 447
Trinchieri, G., Fabbiano, G., & Canizares, C. R. 1986, ApJ, 310, 637
Trinchieri, G., Kim, D.-W., Fabbiano, G., & Canizares, C. R. 1994, ApJ, 428, 555
Trümper, J. 1983, Adv. Space Res., 2, No. 4, 241
Wang, Z., Schweizer, F., & Scoville, N.Z. 1992, ApJ, 396, 510
White, E.W. III & Sarazin, C.L. 1991, ApJ, 367, 476
Young, J.S., Kenney, J., Lord, S.D., & Schloerb, F.P. 1984, ApJ, 287, L65

Table 1. Galaxy and Observation Parameters

Name (NGC)	Type	M_B	RA,Dec (J2000)	D[a] (Mpc)	N_H [b] (cm^{-2})	Observing Dates Start/Stop	Time in Image (sec)
3610	E5	−21.37	11 18 26 +58 47 14	39	7.2×10^{19}	92 Nov 30/92 Dec 04 93 May 10/93 May 11	4610 6209
4125	E6	−22.28	12 08 07 +65 10 22	38	1.8×10^{20}	92 Dec 02 93 Oct 15	5709 4329

[a] from

[b] from Stark et al. (1992)

Table 2. Source Count Extraction

Galaxy (NGC)	PI	Energy (keV)	Source x,y (pixels);	radius (")	Background[a] radii (")	Net counts	Live Time (sec)	Rate (cts/s)
3610	14–83	0.14–0.84	7710,7640;	250	300–600	109.2±21.6	10419	0.01
4125	11–140	0.11–1.41	7660,7640;	510	600–1050	891.8±43.3	9665	0.09

[a]Serendipitous sources were excluded from the background annulus.

Table 3. Spectral Results for NGC4125

Model	Fit Parameters	Best Fit Values[a]
Bremsstrahlung	N_H (cm^{-2})	1.8×10^{20}, fixed
	kT (keV)	0.71
	χ^2, ν	41.9, 19
Raymond	N_H (cm^{-2})	1.8×10^{20}, fixed
	kT (keV)	0.25
	Abundance	100%, fixed
	χ^2, ν	42.7, 20
Raymond	N_H (cm^{-2})	1.8×10^{20}, fixed
	kT (keV)	0.37 (0.29–0.50)
	Abundance	7.4% (3.4%–15.5%)
	χ^2, ν	12.1, 19
Ray(1)&Ray(2)	N_H (cm^{-2})	1.8×10^{20}, fixed
	kT_1 (keV)	0.16 (0.08–0.20)
	Abundance	100%, fixed
	kT_2 (keV)	0.61 (0.35–1.00)
	$Norm^{(2)}/Norm^{(1)}$	0.39±0.24
	χ^2, ν	13.0, 17
Ray(1)&Brem(2)	N_H (cm^{-2})	1.8×10^{20}, fixed
	kT_1 (keV)	0.34 (0.23–0.53)
	Abundance	100%, fixed
	kT_2 (keV)	0.46 (0.13–0.93)
	$Norm^{(2)}/Norm^{(1)}$	4.6±3.8
	χ^2, ν	11.5, 18

a) The 90% confidence levels (for 2 interesting parameters) on temperatures and abundance are given in parentheses. The errors on the normalization ratios were derived using 1σ average errors (for 2 interesting parameters) on each normalization value.

Table 4. (0.1–2.0) keV Fluxes and Luminosities[a]

NGC 3610

Model	f_x (erg $cm^{-2}s^{-1}$)	L_x (ergs s^{-1})	$\log(L_x/L_B)$ (ergs $s^{-1}/L_\odot$)
Raymond 100% cosmic	8.6×10^{-14}	1.6×10^{40}	29.5

NGC 4125

Model	f_x (erg $cm^{-2}s^{-1}$)	L_x (ergs s^{-1})	$\log(L_x/L_B)$ (ergs $s^{-1}/L_\odot$)
Raymond free abundance	7.7×10^{-13}	1.3×10^{41}	30.0
Ray(1)+Ray(2)	8.1×10^{-13}	1.4×10^{41}	30.1
Ray(1)	4.3×10^{-13}	7.4×10^{40}	
Ray(2)	3.8×10^{-13}	6.6×10^{40}	
Ray+Brem	8.0×10^{-13}	1.4×10^{41}	30.1
Ray	3.9×10^{-13}	6.8×10^{40}	
Brem	4.1×10^{-13}	7.2×10^{40}	

a) Luminosities are calculated using the distances from Table 1. $L_B/L_\odot = dex[-0.4(M_B - 5.41)]$, where M_B are listed in Table 1.

FIGURE CAPTIONS

Figure 1: Radial distribution of X-ray surface brightness in the central part of the NGC 4125 field after subtraction of other sources in the field, compared with the radial distribution of the background map. The radius is in units of 15" pixels.

Figure 2: Contour plots of the X-ray emission of (a) NGC 4125 and (b) NGC 3610. Contours are spaced logarithmically from 6% to 100% of peak value in (a), and from 30% to 100% of peak value in (b). Ellipses mark optical extent of galaxies at $B = 25$ (dotted) and 26.5 (dashed) mag arcsec^{-2} isophotes. Coordinates are for J2000.

Figure 3: Radial X-ray surface-brightness profile of NGC 4125. The dashed line approximates the point response function of the PSPC. The solid line represents the optical surface brightness in the R passband, measured from CCD images in a manner analogous to the X-ray measurements; for details, see main text.

Figure 4: Comparison between the observed spectral distribution of PSPC counts for NGC 4125 and (a) thermal Bremsstrahlung best-fit model and (b) two-temperature Raymond best-fit model. The residuals are shown in the bottom panel of each figure.

Figure 5: Confidence contours (60%, 90%, and 99%) for two interesting parameters: (a) kT versus abundance for the single-temperature Raymond model; (b) kT_1 versus kT_2 for the two-temperature Raymond model; (C) kT_1 versus kT_2 for the Raymond + Bremsstrahlung model.

Figure 6: Comparison between the observed spectral distribution of PSPC counts of NGC 3610 and the best-fit cosmic-abundance Raymond model.

Figure 7: X-ray luminosity of ~140 E and S0 galaxies plotted versus their optical luminosity. *Filled circles* mark NGC 3610 and NGC 4125, while *squares* mark two other X-ray faint E and S0 galaxies. *Lines* delineate boundaries between Groups 1, 2, 3, and 4 introduced by Kim et al. (1992b). For details, see text.

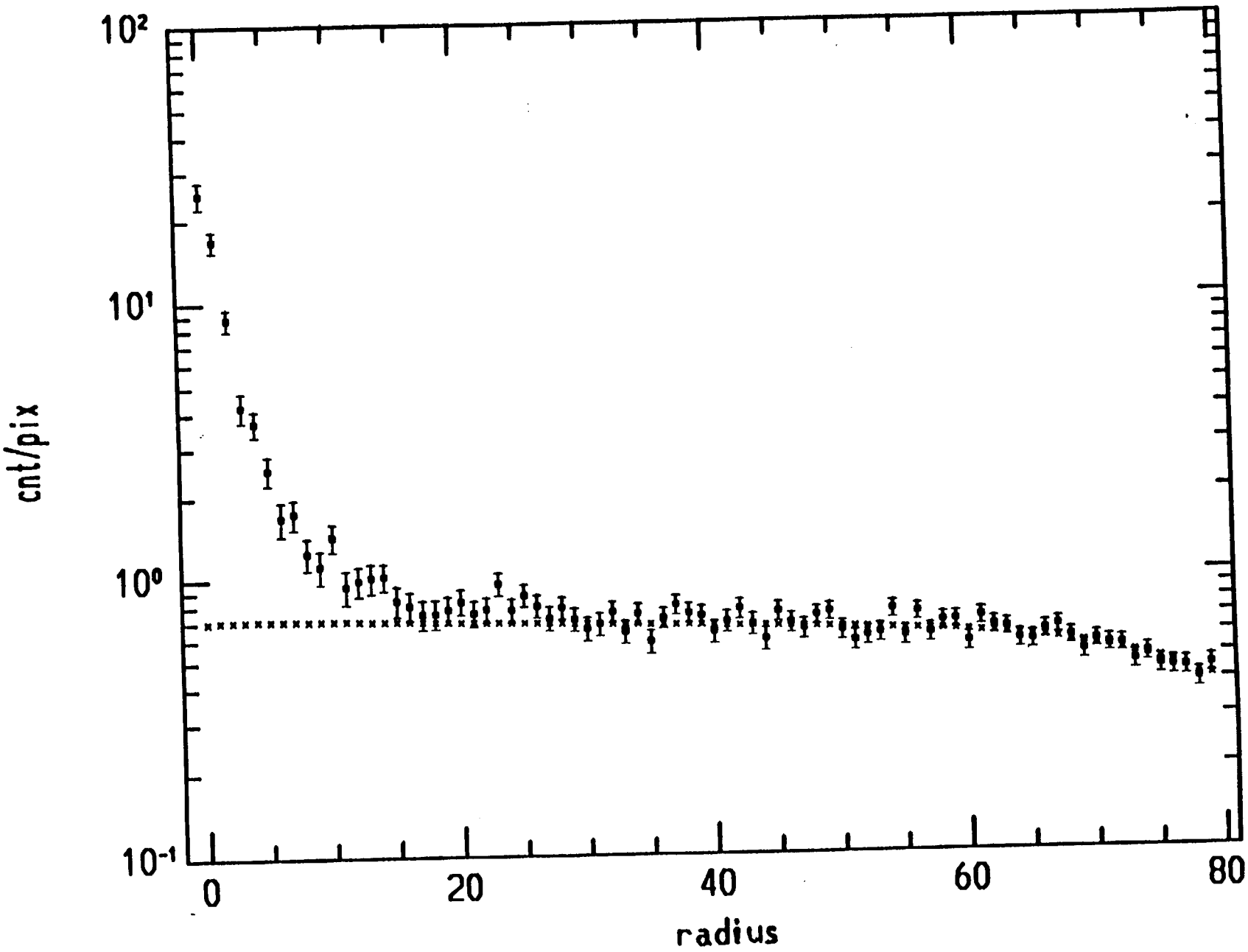

Fig. 1

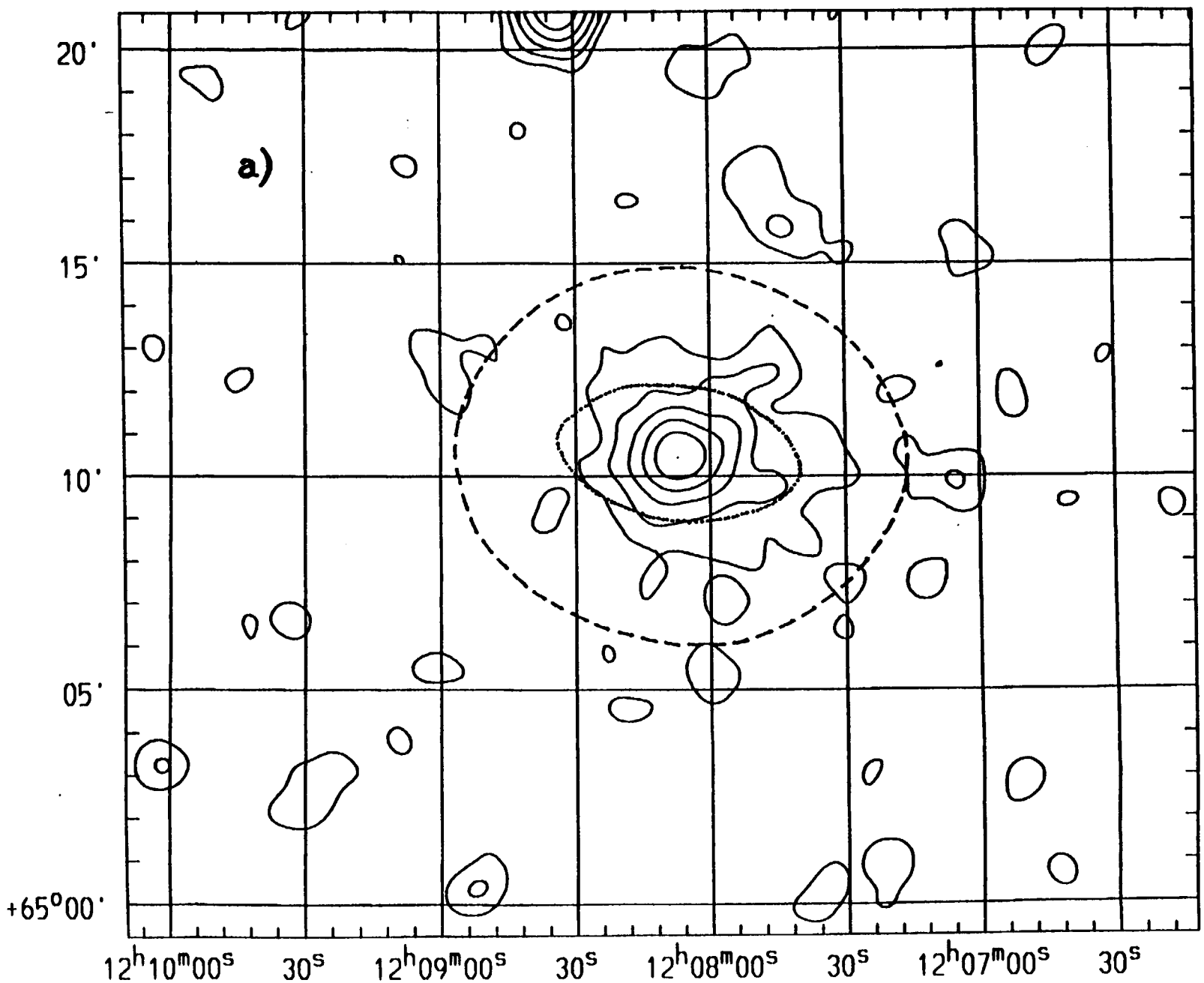
a)
20'
15'
10'
05'
+65°00'
12h10m00s
30s
12h09m00s
30s
12h08m00s
30s
12h07m00s
30s

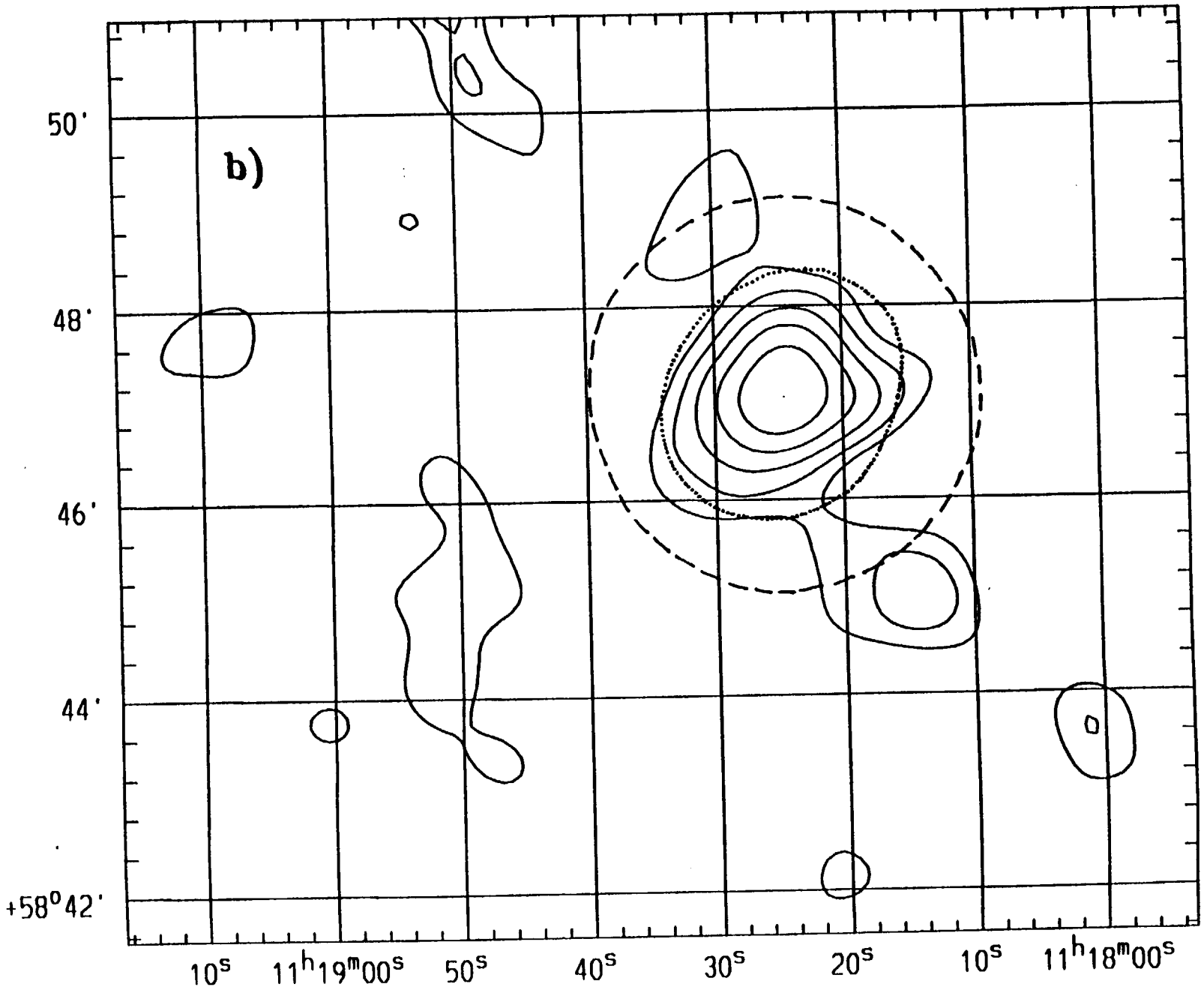

Fig. 2b

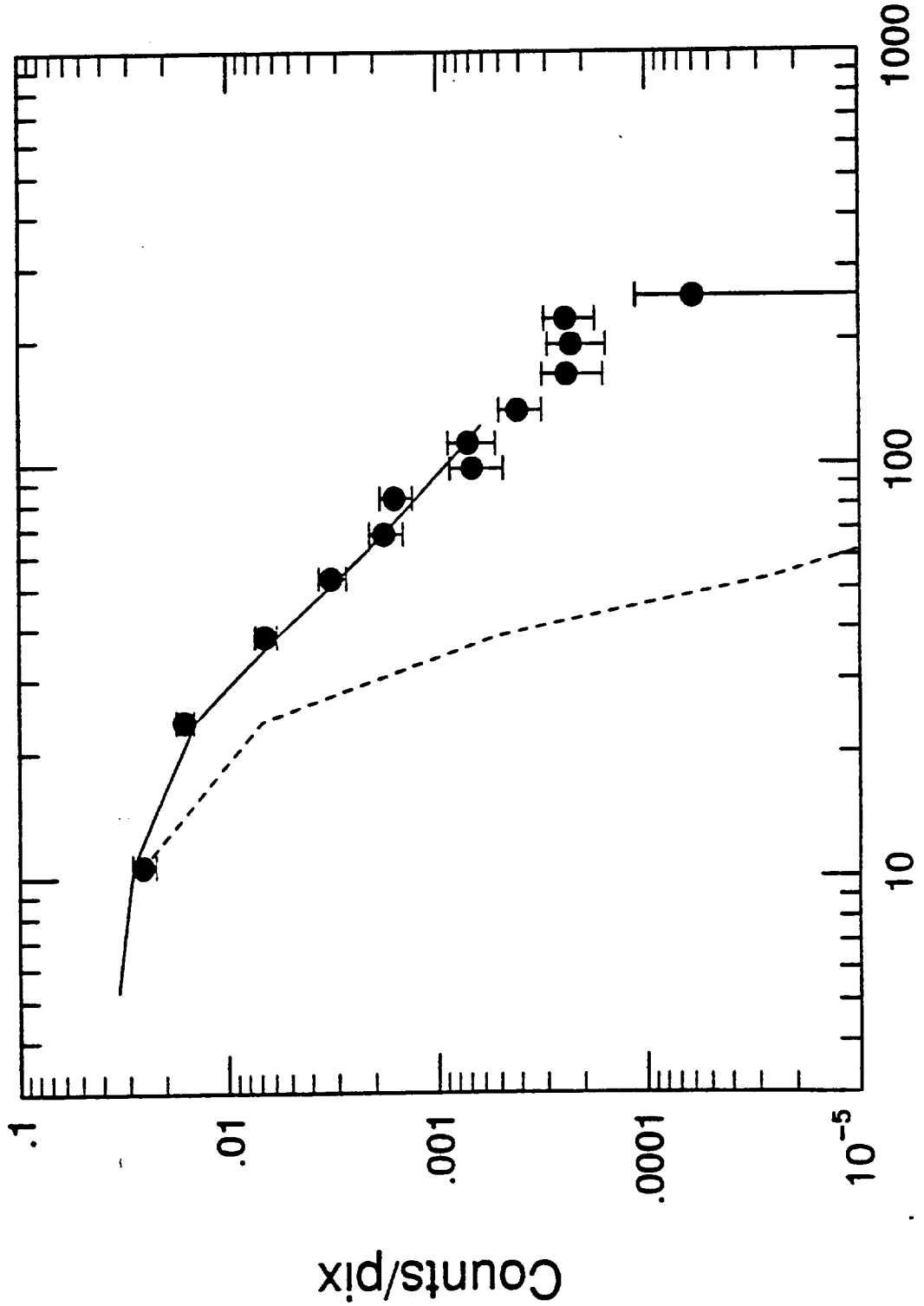

Fig. 3

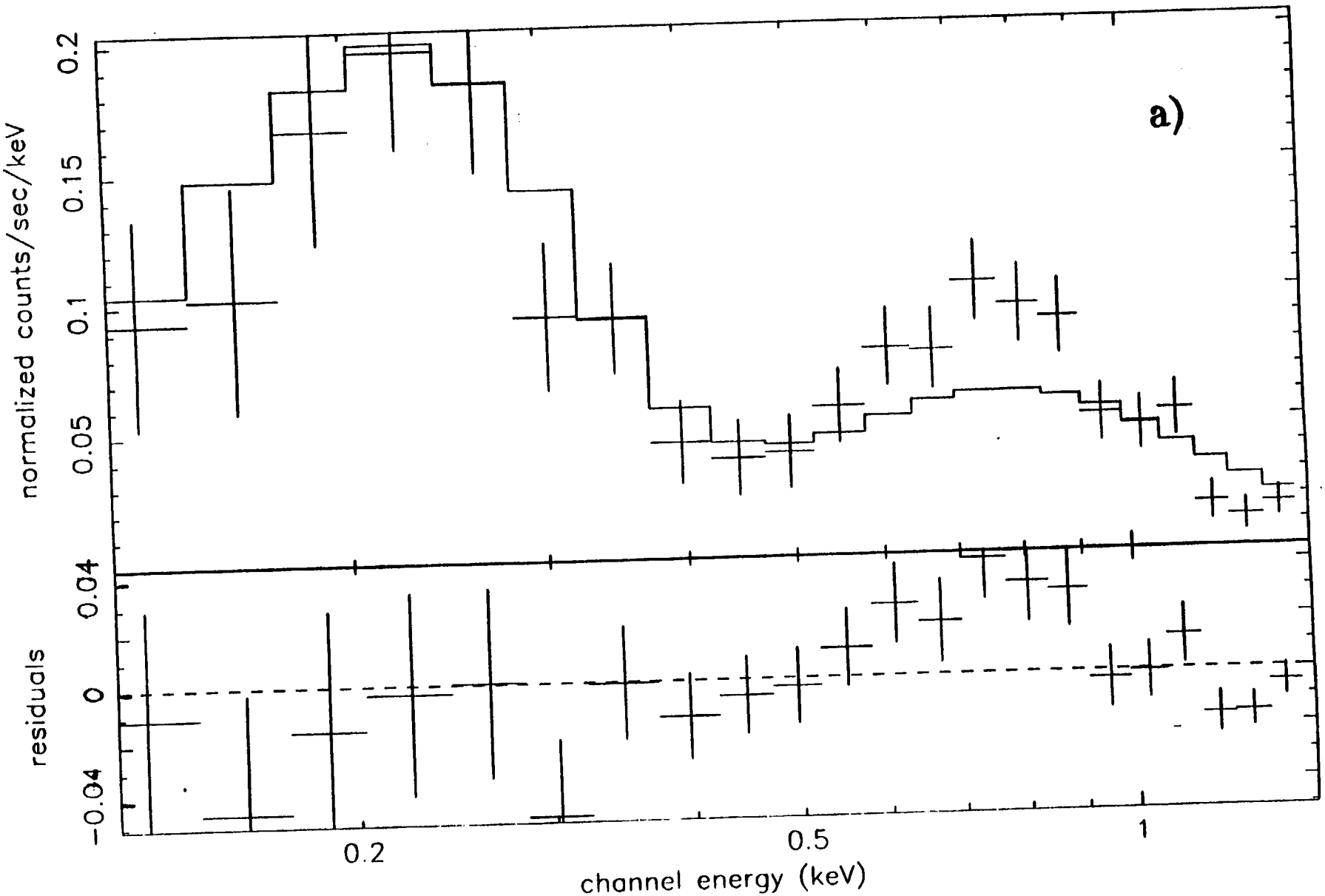
a)
normalized counts/sec/keV
0.2
0.15
0.1
0.05
residuals
0.04
0
-0.04
0.2
0.5
1
channel energy (keV)

Fig. 4a

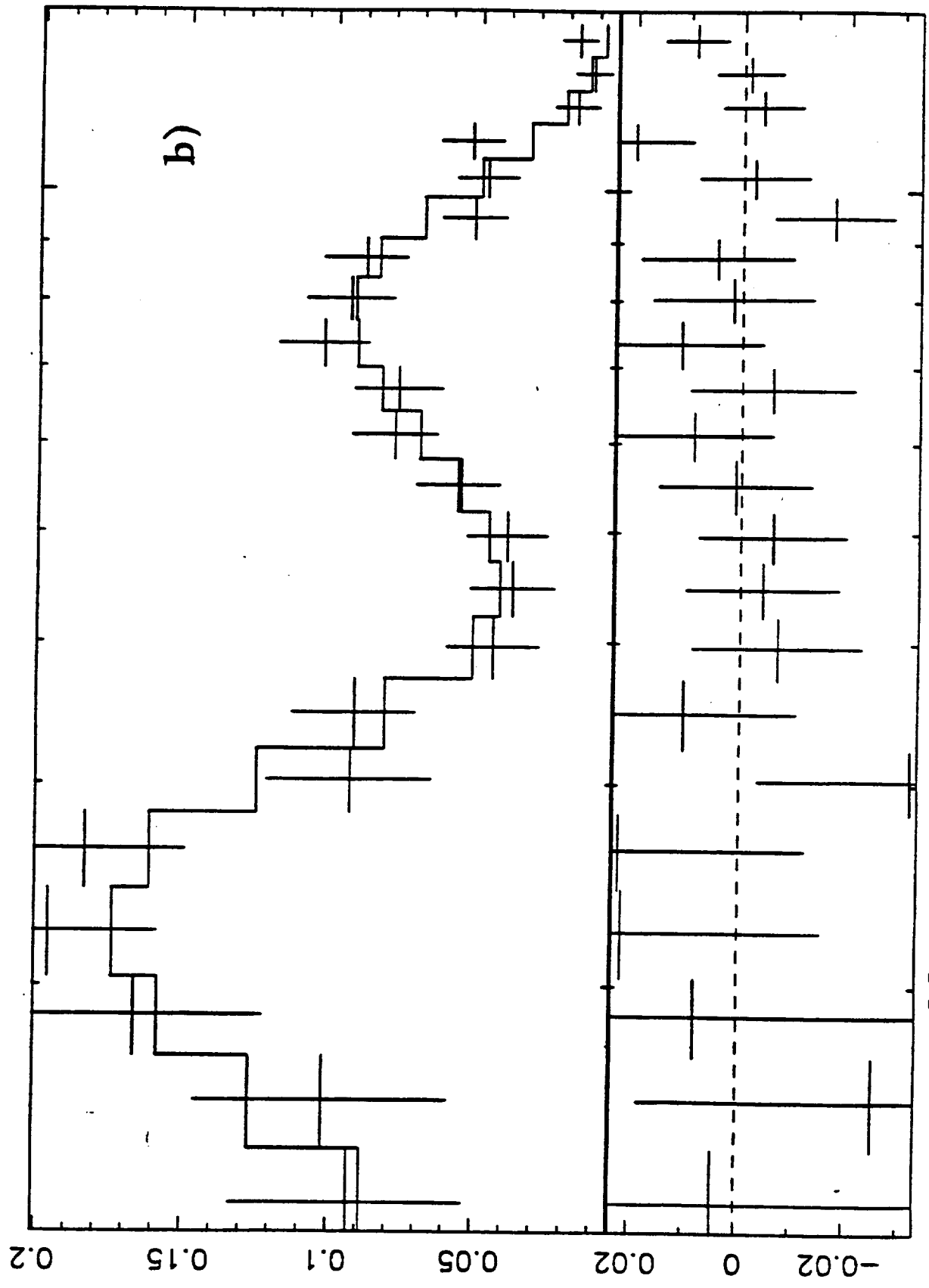
b)
normalized counts/sec/keV
0.2
0.15
0.1
0.05
0.02
0
−0.02
0.2
0.5
1
channel energy (keV)

Fig. 4b

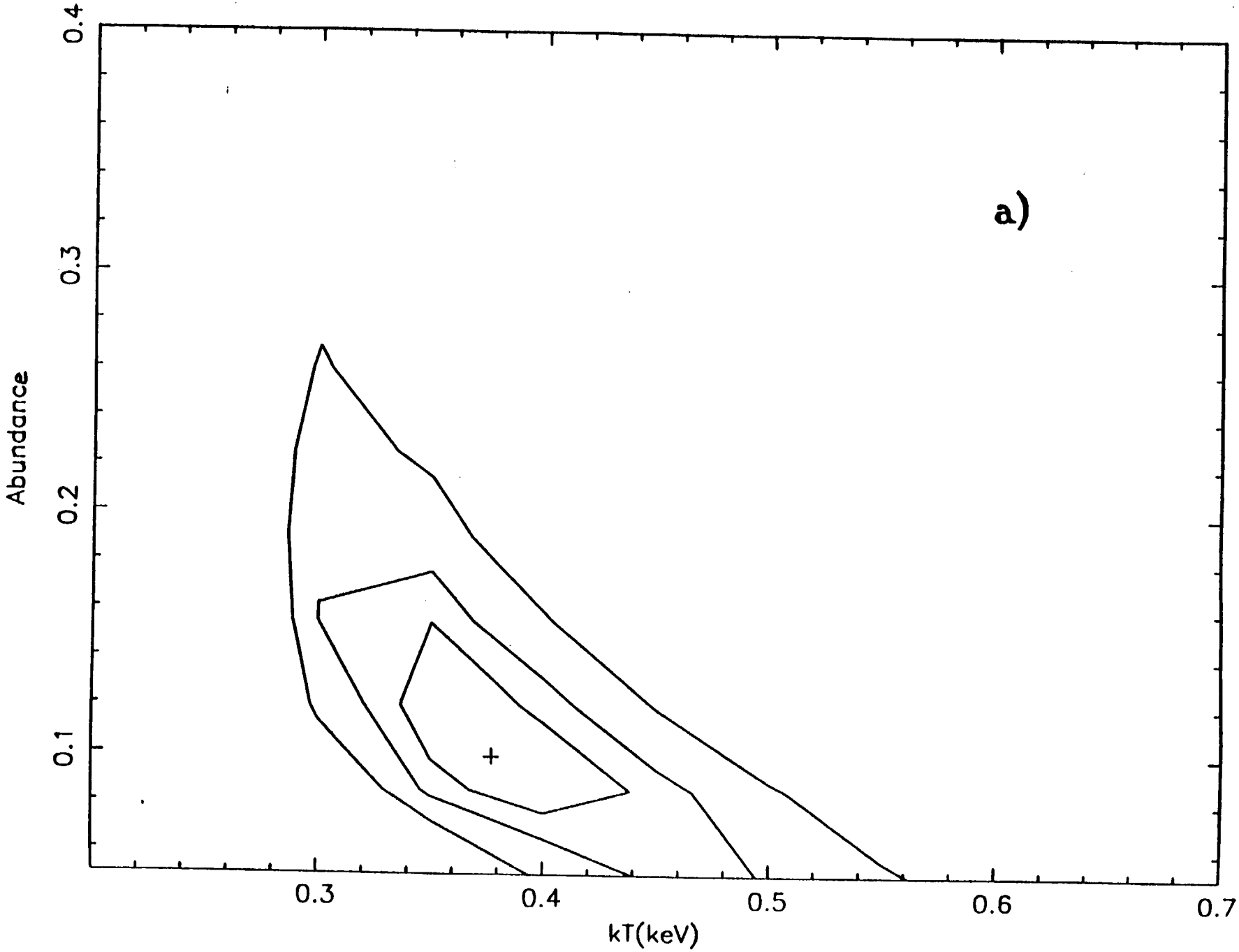

Fig. 5a

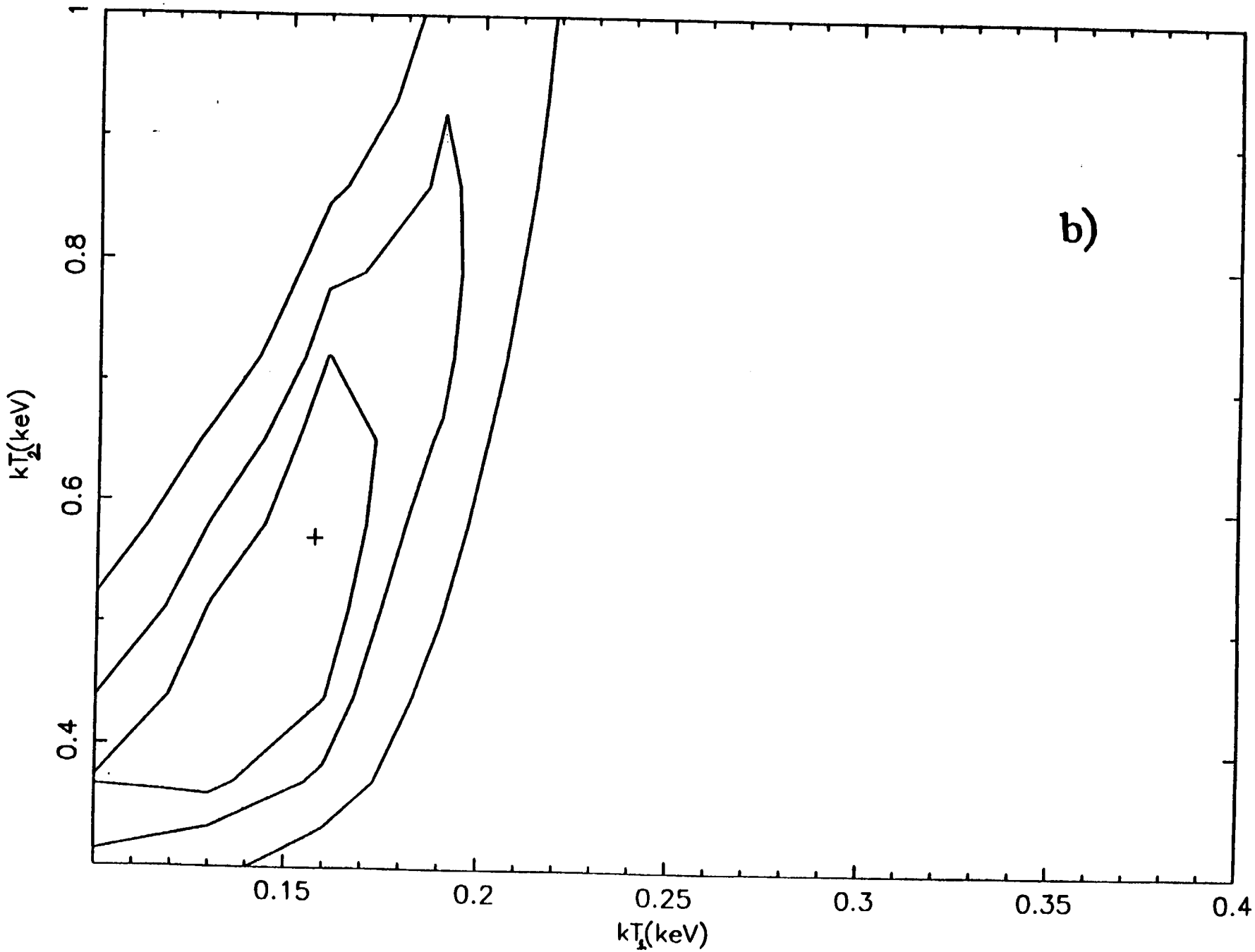

Fig. 5b

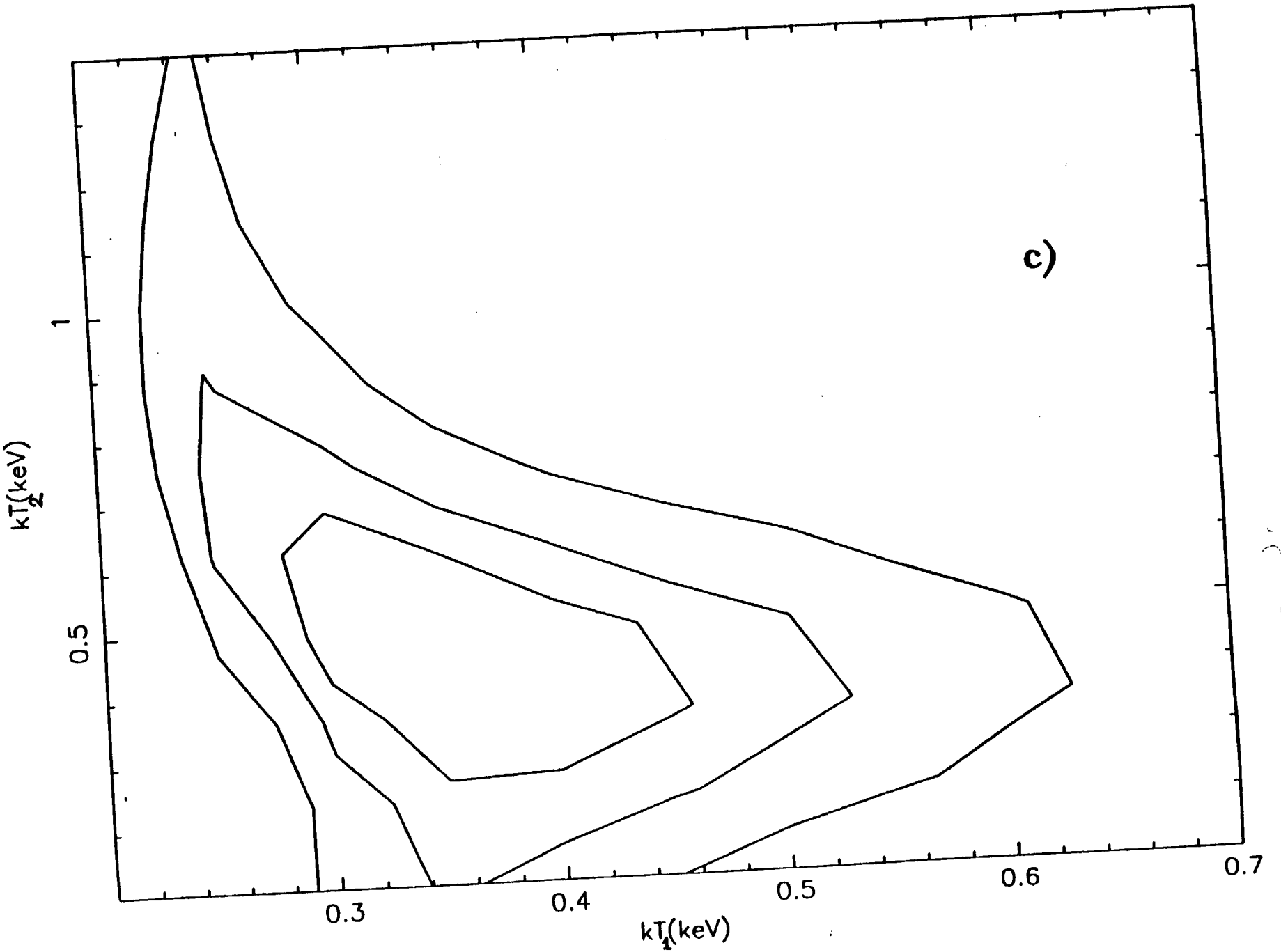

Fig. 5c

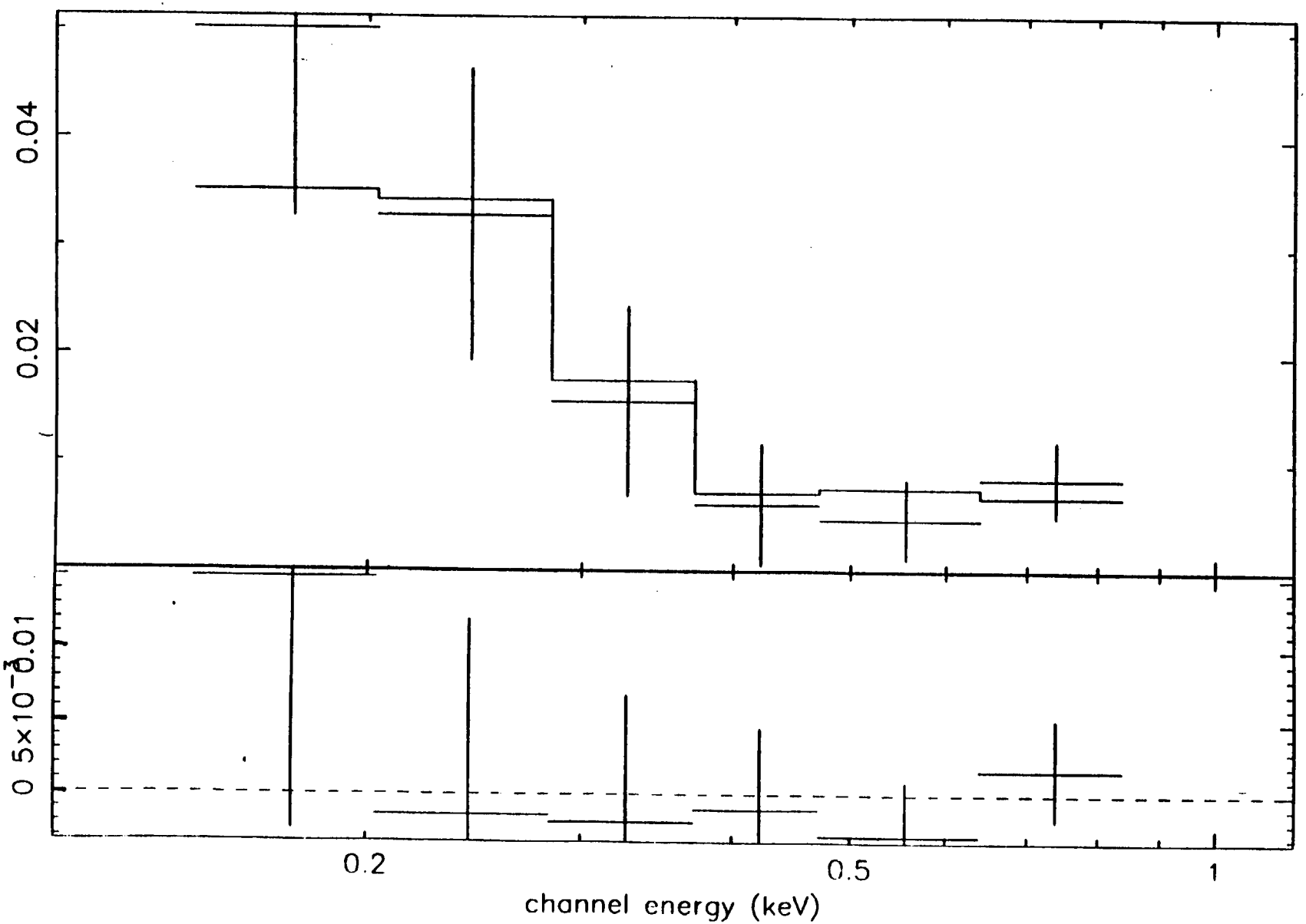

Fig. 6

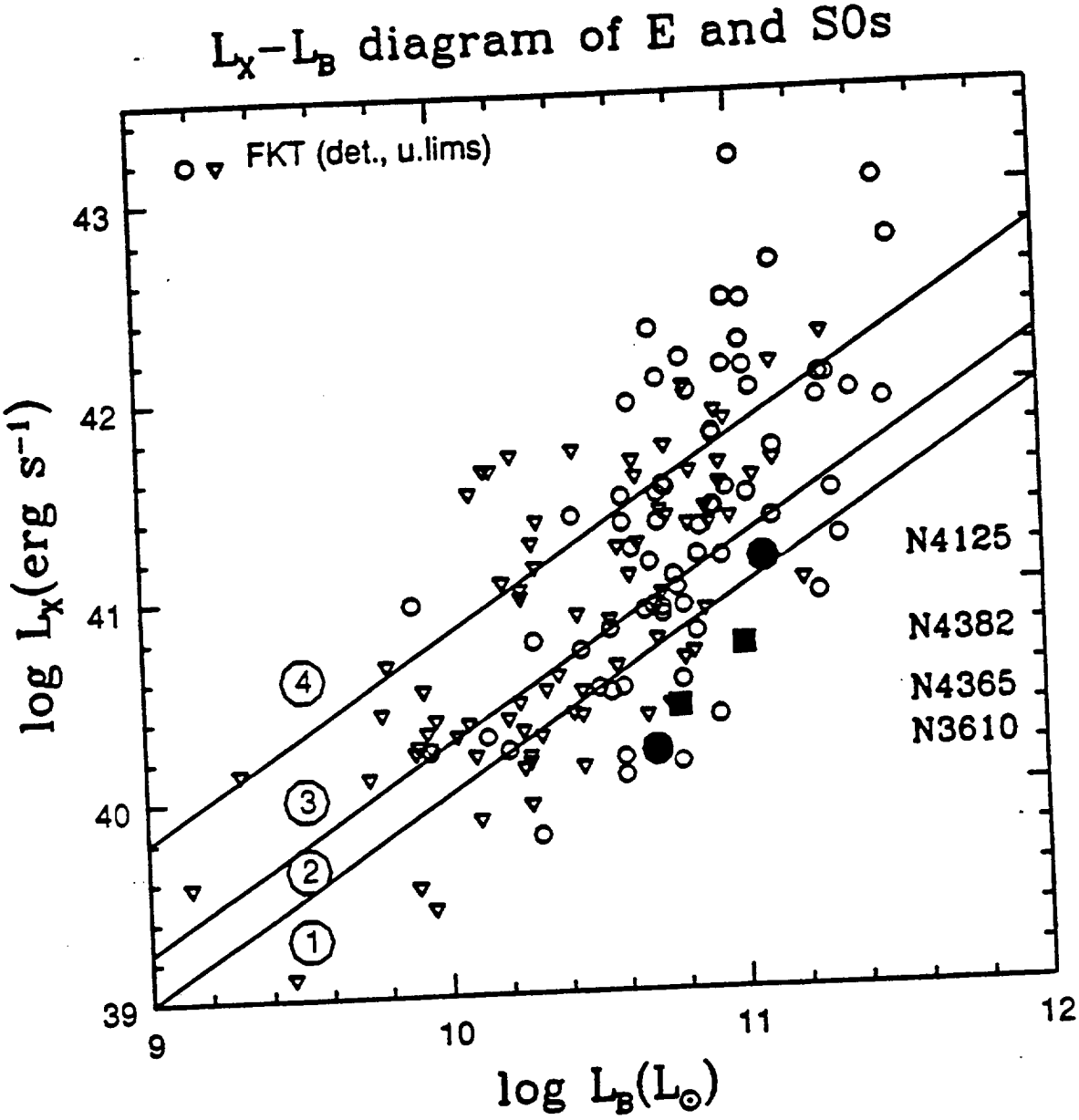
L_X–L_B diagram of E and S0s
FKT (det., u.lims)
N4125
N4382
N4365
N3610
4
3
2
1
43
42
41
40
39
9
10
11
12
log L_X(erg s^{-1})
log L_B($L_\odot$)

Fig. 7